Dipartimento di Fisica "E. Amaldi"

Università degli Studi Roma Tre

Dottorato in Fisica XIX ciclo

PHASE TRANSITIONS IN TRANSITION METAL OXIDES STUDIED BY X-RAY ABSORPTION SPECTROSCOPY

Claudia Monesi

Chairperson
of the Ph.D. School
prof. Orlando Ragnisco

Supervisor
prof. Settimio Mobilio

A.A. 2005 - 2006

Contents

Introduction

In a system, phase transitions are macroscopic effects due to the interactions among atomic constituents, when the external conditions, such as temperature, pressure or external fields, are varied. In such cases, the free energy of the system changes smoothly and continuously and if variations in structural details of the phase are associated to this change, a *phase transformation* or *phase transition* is said to occur. Such transformations are useful to have an insight of the physics of the system and also for technological applications. Although thermodynamic treatment of phase transitions is very useful to describe the characteristics of these phenomena, nevertheless it not always provides a picture of the microscopic changes accompanying a transition. Therefore another essential part of the study of a phase transition in solids involves a detailed understanding of crystal chemistry, in terms of atomic arrangements, bonding and electron energy. In this work I will deal with solid systems characterized by phase transitions of peculiar interest. In particular I will consider some transition metal oxides, which are object of great interest because they present peculiar electronic, magnetic and transport properties, mainly arising from electron correlations. When electron correlations are not negligible, the one-electron description of the system fails and much more sophisticated theoretical models that take into account the interactions among the electrons must be used. In this thesis I will consider two examples of transition metal oxides: the manganese oxides with perovskite structure ($LaMnO_3$ and $CaMnO_3$) and the vanadium oxide (V_2O_3).

The $LaMnO_3$ and $CaMnO_3$ systems are the end compound of the $La_{1-x}Ca_xMnO_3$ series, which has been studied since the '50s because of its interesting properties. Manganese oxides's peculiar properties arise from the strong interplay between ferromagnetic double-exchange interaction among Mn ions, antiferromagnetic superexchange interaction among the same ions and strong electron-phonon interaction, which results in a complex phase diagram in terms of structural, magnetic and electronic properties as a function of composition, temperature and pressure. These compounds, in fact,

show very different properties according to the pressure, temperature and La/Ca concentration conditions: when the Ca concentration x is between 0 and 0.15 the materials are insulating for every T, with a paramagnetic (P) phase at high T and a ferromagnetic (F) one at low T; when $0.15 < x < 0.5$ they show a P insulating (I) phase at room temperature, while they are F and metallic (M) below a critical temperature. The coupling of the magnetic transition with the metal-insulator one originates a very important effect, the negative colossal magnetoresistance phenomenon (CMR): when a magnetic field is applied, there is a drop in resistivity of about 100% with respect to the value without the external magnetic field. This effect is of great importance because it occurs at temperatures near, or even above, room temperature, therefore it is of large interest for technological applications. When $x \geq 0.5$ the ground state instead is antiferromagnetic insulating (AFI) and at low temperature charge ordering appears. Finally, the end compounds $LaMnO_3$ and $CaMnO_3$ are PI at room temperature and AFI at low temperature. Since their discovery, these compounds have been a challenge both for experimentalists and for theoreticians and new physical concepts have been introduced to explain some aspects of their complex phase diagram. In fact they are the prototype of highly correlated electronic systems, where charge, spin, orbitals and structural degrees of freedom simultaneously play together. For example, it was demonstrated that the local atomic structure around Mn ions plays a crucial role in determining these complex phenomena, since the electron-phonon coupling involves a dynamical Jahn-Teller (JT) deformation of the Mn local surroundings. From the structural point of view these systems are rather complex, too, because the ideal simple cubic structure, which describes the perovskite compounds, is distorted and becomes pseudo-cubic, characterized by different distortions. One of the distortions is connected to the Jahn-Teller effect, which exists when the ground state has degenerate partially occupied orbitals. In our case the Mn^{3+} ion is the JT atom; the effect is the elongation of the Mn-O apical bonds in the MnO_6 octahedron. The study of the local structure around Mn in $LaMnO_3$ and $CaMnO_3$ is important because its local deformation determines the conductive mechanism in the $La_{1-x}Ca_xMnO_3$ systems and hence it affects the properties of the phase diagram of manganites. Diffraction and X-ray absorption spectroscopy studies are reported in literature which describe the crystallographic and the local structure of $LaMnO_3$, $CaMnO_3$ and of the doped compounds. For what concerns the structural description of the mixed samples $La_{1-x}Ca_xMnO_3$, it is much more complex than the one in the end compounds, because it is not clear yet what is the charge state of the Mn ion in these systems. Actually, there are two main hy-

pothesis: the Mn atoms could have a valence intermediate between +3 and +4 and dependent on the Ca concentration, or the Mn ion could be either in the +3 or in the +4 state, therefore the octahedra centered on Mn^{3+} would be distorted whereas those centered on Mn^{4+} would not. These two extreme situations imply two different models to describe the transport properties: in the first case, the conduction electrons of Mn^{3+} would be delocalized and they would contribute to the conduction in the compounds with PM-FM transition; in the second case, instead, the external electron moves by hopping from a Mn^{3+} ion to a Mn^{4+} one.

In this context it is important to set which is the local structure around the Mn atom in the end compounds $LaMnO_3$ and $CaMnO_3$, to further determine how they affect the $La_{1-x}Ca_xMnO_3$ systems. To this purpose, we performed X-ray absorption spectroscopy (XAS) experiments at the Mn K-edge in $LaMnO_3$ and $CaMnO_3$, at room temperature, at the European Synchrotron Radiation Facility (ESRF) in Grenoble. XAS spectroscopy, in fact, is a local probe that allows to investigate the structure of a sample near the absorbing atom. The X-photons are absorbed and electrons are emitted from the ionized atoms. These electrons interact with the other atoms surrounding the absorber, in this way they bring information about the distribution of the ions around the central atom and about its electronic state. The original aspect of our study is the use of a new method of analysis to the XANES region of the absorption spectra (i.e., the region of the spectrum corresponding to the absorption edge), by means of the recent MXAN code. This software allows to perform a complete fitting of the experimental data in the XANES region, using the theory of the Full Multiple Scattering (FMS). In this way we can achieve a compete structural refinement of the local structure of our systems, starting from the crystallographic structure found by diffraction. Actually, previous studies, reported in literature, on the edge region of the absorption spectra analyzed XANES with a qualitative approach; just few examples exist of quantitative numerical simulations. In this way, instead, we try to achieve a quantitative result by a real fitting of the experimental data. Our final goal is to apply our method, in the future, to the mixed compounds $La_{1-x}Ca_xMnO_3$.

Vanadium sesquioxide V_2O_3 is another transition metal oxide that shows a complex and still unexplained phase diagram. It has been identified in the past as the prototype of Mott-Hubbard systems, due to the metal-insulator transitions exhibited by the phase diagram: one from a paramagnetic metallic (PM) phase to an antiferromagnetic insulating one, at 160 K; the other from the PM to a paramagnetic insulating phase at higher temperature (above 500 K). Moreover a change in the crystallographic structure

accompanies the first transition: the system has trigonal symmetry above the transition temperature- the structure of the system in this case is like an honeycomb, with hexagonal basal plane- but below the transition temperature the symmetry is monoclinic. The structural transition is accompanied by the volume increase of the unit cell. Finally, a more complex phase diagram is obtained varying the pressure or doping the system, in particular substituting part of the V atoms with Cr atoms.

Mott advanced a theory of the transition at T=160 K, arguing that it would be possible for a metal to transform into an insulator simultaneously with the onset of magnetic order when the distance between the atoms in the lattice increases. By 1970 there was a large number of experimental work which led to a large debate about these transition mechanisms; however, up till now a detailed microscopic picture of the Mott theory does not exist. About that time V_2O_3 began to be doped with other $3d$ transition metals to induce variations in the lattice parameters and to study the effects on the transition. However, the effects of doping on the phase transitions were much more complex than expected, so that a big experimental effort continued on this problem. In the meanwhile, several theories were elaborated to explain the experimental evidences. According to recent theoretical models, the fundamental unit in V_2O_3 is formed by two vanadium atoms which couple along the vertical axis of the hexagonal cell, each V atom has spin equal to 1 and the total spin of this molecule is 2.

The mechanism which guides these structural, magnetic and electronic transformations has not been clearly identified, yet, but resonant X-ray scattering experiments showed that there is a strong correlation between orbital degrees of freedoms and structural properties. Moreover, experiments performed by means of this technique suggested that the structural transition could not be a first-order one; according to this hypothesis, the structure would start changing at temperatures higher than the transition temperature, as if monoclinic domains would form and grow as the temperature decreases. Another hypothesis is that the local structure around the V atom is monoclinic but all the monoclinic domains at high T are differently oriented in such a way to give, on the whole, a trigonal structure.

Given the fundamental role the local structure plays in V_2O_3, we used X-ray absorption spectroscopy to study vanadium sesquioxide. We performed absorption measurements at the V K-edge at many different temperatures, below and above the transition temperature, in a Cr doped V_2O_3 sample. The absorption spectra were collected considering three orthogonal polarization directions, to study the local environment along the three different symmetry axis of the system. The aim was twofold; first we want

to understand which is the origin of the dichroism measured in V_2O_3 and reported in literature, as due to structural anisotropies. Then we analyzed the EXAFS signal, that is the high energy region of the absorption spectra, to study the evolution with temperature of the local structure surrounding the V absorbing atom. In this way we try to follow the local structural changes and to determine the symmetry of the system during the transition and above the transition temperature, to state if monoclinic precursors form above the transition temperature. Finally, we studied also the local environment of the Cr atom, to establish how the Cr ions arrange themselves in the cell of V_2O_3; in fact, in spite of the huge amount of publication on V_2O_3 and its phase diagram, we could find just very little investigation about the role of chromium in Cr-doped samples. In most cases, the problem is dealt with only qualitatively, by stating that the role of Cr is to increase the average cation-cation distance, which leads to the mechanism for the metal-insulator transition traditionally described by Mott.

The thesis is articulate as follows: in the first two chapters, I will introduce the problem of phase transitions in solids and describe the main properties of the systems we studied, i.e. maganites and V_2O_3. Then I will discuss the theoretical framework of the analysis of our experimental data, that is the multiple scattering theory which is the basis of the theoretical interpretation of the X-ray absorption spectroscopy data. The experimental set-up and a brief description of the European Synchrotron Radiation Facility are reported in Chapter 4. Finally, the details of the analysis we performed on manganites and V_2O_3 and the discussion of the results we obtained are treated in the last chapter.

Chapter 1

Phase transitions in solids

An assembly of atoms or molecules may be homogeneous or nonhomogeneous. The homogeneous parts of such a system, called phases, are characterized by thermodynamic properties like volume, pressure, temperature and energy. An isolated phase is stable only when its free energy is a minimum for the specified thermodynamic conditions. If the phase is a local minimum of free energy separated from lower minima by energy barriers, the system is said to be in a metastable state. If barriers does not exist, the state is unstable and the system moves into a stable or equilibrium state, characterized by the lowest possible free energy. As the temperature, pressure or any other variable, like an electric or a magnetic field acting on the system, is varied, the free energy of the system changes smoothly and continuously. Whenever such variations of free energy are associated with changes in structural details of the phase, a *phase transformation* or *phase transition* is said to occur.

Phase transformations are classified by the kind of discontinuity in the Gibbs free energy. First order phase transitions involve discontinuous changes in the first derivatives of Gibbs free energy such as entropy and volume; their features are satisfactorily understood by the classical Clapeyron equation. On the other hand, second or higher-order transitions are not readily explained by classical thermodynamics. Unlike the case of first-order transitions, where the surface of constant free energy of the two phases intersect sharply at the transition temperature, it is difficult to visualize the behaviour of the free energy surfaces in second- or higher-order transitions.

Although it is convenient to classify phase transitions as first- or second-order, actually many real transformations are of mixed order, exhibiting features of both. In general in thermal transformations the high temperature phase is of higher symmetry and higher disorder. Therefore it is often useful to examine phase transitions in terms

of changes in order or disorder.

While the thermodynamic treatment of phase transitions is very useful, it does not provide a picture of the microscopic changes accompanying a transitions. Therefore another essential part of the study of a phase transition in solids involves a detailed understanding of crystal chemistry, in terms of atomic arrangements, bonding and electron energy. For example the transition can be accompanied by a change in the coordination, brought out either by a reconstructive mechanism or by some other one; it could present a change in the electronic structure or in the bond type. It is important, therefore, the study of the microscopic structure of the transformed phases.

In addition thermodynamics alone cannot account for different rates at which phase transitions take place. Phase transitions in many solids occur through the process of nucleation and propagation, and each of these processes is associated with a specific activation energy. Generally, the activation energy of the nucleation process, which involves the formation of nuclei of critical size of the transformed phase, is higher than that of propagation. There are many examples of nucleation-growth transformations in metallic and non-metallic solids, and many of the transformations from metastable states to stable states proceed by this mechanism.

Since perfect order in solids is not realized at any temperature other than 0 K, it is necessary to talk of the extent of order or disorder content as mentioned before. Three main kinds of disordering transitions are generally found: positional disordering, orientational disordering and disordering of electronic or nuclear spins. The entropy change in an order-disorder transition is mainly configurational in origin, and is given by $k \ln(\omega_2/\omega_1)$, where ω_1 and ω_2 are the number of configurations in the ordered and disordered states. Many systems show positional or orientational order-disorder transitions: magnetic transitions (like ferromagnetic-paramagnetic) or dielectric transitions (ferroelectric-paraelectric) are such cases. There are also transitions involving disordering of defects like vacancies. The subject of this kind of transitions is very large.

Order parameters. In second-order transition the long-range order parameter, characteristic of the ordered phase, decreases to zero as the critical temperature is approached. It is also possible to define a short-range order parameter in such a way that it approaches a limiting value defined by the long-range order parameter. In real situation, any physically observable quantity which varies with temperature can be taken as an experimental order parameter. Thus, polarization in a ferroelectric material or magnetization in a ferromagnetic material, for example, have been taken as order parameters.

One of the most interesting features of phase transitions is the similarity in behavior encountered in the variation of physical properties near the critical temperature. In general, the dimensionless quantity, $\epsilon = (T - T_c)/T_c$, is related to the long-range order parameter by the equation

$$p(\text{or } M) = A(-\epsilon)^{\lambda} \tag{1.1}$$

where p and M refer to the order parameters in order-disorder and magnetic transitions respectively, and the exponent λ is always about 1/3. Such a similarity in the behaviour of different systems indicates that the basic physical processes leading to the transition are similar. The transitions are cooperative and are caused by the interaction of many particles. Thus, small changes in temperature give rise to large fluctuations in the order parameter near the critical temperature, since the energy of disordering depends on the extent of disorder already accrued. In order to understand critical phenomena, statistical mechanics is employed. The Ising model is one of the most widely used approaches to examine order-disorder transitions. A one-dimensional Ising model does not give rise to phase transitions, but a two-dimensional model does. Apart from rigorous methods such as the Ising models, approximate models have been employed to investigate magnetic and order-disorder transitions. For example, effective field theories [44] satisfactorily predict the general behaviour of three-dimensional systems, although not the details of critical behaviour.

Material properties. Phase transitions in solids are accompanied by interesting changes in many properties of the materials. Measurements of any sensitive property across the phase transition, in principle, provides a means of investigating the transition. Changes in properties at the phase transition are often of technological interest. In magnetic properties, in addition to the transitions from a magnetically ordered state to the paramagnetic state, Jahn-Teller distortions and spin-state transitions are also quite interesting. For the electrical properties, insulator-metal transitions [56] (including Mott transitions) are of great interest; a number of oxides and sulfides are known to exhibit these transitions. Another aspect of high interest is also the cooperative Jahn-Teller effect [57].

Applications. Following Goodenough [75], applications of phase transitions may be classified into groups: those utilizing (i) the formation or motion of mobile boundaries between two or more phases which coexist below a critical temperature, (ii) changes in physical properties as the temperature approaches the critical temperature, (iii) changes in properties at the critical temperature and (iv) metastable phases

obtained by control of the kinetics of nucleation or diffusion required for the transformation to stable the phases. In the first category one makes use of changes in the net material properties by controlling nucleation or movement of domain boundaries;such category includes large classes of materials like ferroelectrics, ferroelastics, ferromagnets, liquid crystals and superconductors, which are important also in our work. In next chapters in fact we will talk about manganese oxides and vanadium oxide, which show ferromagnetic or antiferromagnetic phases in certain conditions. In ferromagnets, long-range magnetic order below the Curie temperature induces a spontaneous magnetization; many magnetic domains are present each with a vector oriented in a direction different from that of adjacent domains. The adjacent domains are separated by domain walls within which the magnetization vector rotates from one orientation to the other. The net magnetization is determined by an external magnetic field which forces the domains to become parallel.

1.1 Order-Disorder transitions

When the position and orientation of every atom in a system is fixed according to the crystallographic structure, the state of the system corresponds to perfect order. Perfect order is, however, never realized in materials at any temperature other than 0 K. This is due to the thermal agitation in materials at non-zero temperatures, which enables atoms and groups to assume other positions and orientations so diminishing the order. For this reason we speak of the degree of order or disorder in materials. This is usually done by using order parameters, which are defined in such a way that they are equal to unity in the perfectly ordered state and zero in the completely disordered state.

In continuous order-disorder transitions, disorder is a function of temperature and there is a finite value of the order parameter at each temperature; the order parameter of relevance here is the long-range order parameter (LRO). In the case of positional disordering (if more than one chemical species is present), when disordering sets in, correlation between distant neighbours disappears and LRO is reduced to zero, but the preference for unlike neighbours continues to operate because of energy requirements. This leads to the presence of short-range ordering (SRO), that often persists even beyond the transition temperatures in most order-disorder transitions. The equilibrium value of LRO is not attained instantaneously when the material is brought to the appropriate temperature and the rate at which the full value of the disorder or order is attained is generally different in different directions. For this reason any mea-

sured property which depends on disorder reaches its proper value with a characteristic kinetics.

In general, the transition may take place discontinuously as a first-order change at a particular temperature and may involve simultaneous change of volume as well. It may also occur in the manner of a lambda transition (continuously as in higher-order cooperative transitions) over a range of temperature during which the order vanishes to zero. An important aspect of such cooperative transitions is that the energy required for disordering is a progressively decreasing function of the disorder itself.

Three main kinds of disordering transitions may be distinguished: (i) positional disordering, (ii) orientational disordering and (iii) disordering associated to electronic and nuclear spin states. Positional disordering arises either when atoms or ions occupy inappropriate sublattice positions, or when more positions are available for the atoms than those necessary. Orientational disorder can take place in situations where the ions or the basic units occupying the lattice sites contain more than one atom. In this situation more than one distinguishable orientation becomes possible for the ions in the lattice. If these orientations correspond to very small differences in energy, then the disordering can occur by thermal excitation. Even in this case, it is possible that a low-temperature phase may have no disorder while the high-temperature phase which forms after a first-order transition may correspond to very high disorder.

Another large class of order-disorder transitions is provided by the disordering of spins. By virtue of the presence of unpaired electrons or spins, atoms or ions behave as tiny magnets and give rise to a magnetic moment when they are in a parallelled ordered state. This spontaneous magnetic polarization of materials is known as ferromagnetism. As the temperature increases, the elementary magnets on the lattice flip over to other orientations, decreasing the magnetism, until the disorder is complete and the system becomes paramagnetic. Spins in a paramagnetic state tend to align under the influence of an external magnetic field. The ordered state can also correspond to antiparallel (antiferromagnetic) alignment of spins on two sublattices giving rise to a zero net magnetic moment. Antiferromagnetic materials also undergo disordering transitions to a paramagnetic state. The magnetic polarization of the overall lattice may still be non zero if the spins on the two sublattices are unequal (ferrimagnetism). Also in this case, a fully disordered state is paramagnetic. Transition metal and rare earth ions, by virtue of the presence of unfilled d and f shells, impart magnetic properties to their compounds in the solid state and provide a host of magnetic order-disorder transitions.

By analogy with these magnetic transitions, there are order-disorder transitions in-

volving electric dipoles (ferroelectricity). Metal-insulator transitions in which localized electrons become itinerant can also be discussed as order-disorder transitions.

When we consider the thermodynamics and kinetics of order-disorder transitions, we must take into account the entropy variation occurring during the transformations. The increase in entropy, ΔS, in an order-disorder transition is mainly related to positional disorder; in fact the total increase in entropy is made up of electronic, vibrational, rotational and configurational contributions. The electronic term can generally be ignored except in metal-insulator or similar transitions. The vibrational entropy term is considerable only when the change in volume at the transition is very high and when the disordered state has a different crystal symmetry. The rotational entropy term becomes important only if free rotation occurs. Therefore the configurational entropy is the real dominant term in most order-disorder transitions, so we can approximate

$$\Delta S \simeq \Delta S_{conf} = k \ln(\omega_2/\omega_1) \tag{1.2}$$

where ω_1 and ω_2 are the number of configurations in the ordered and disordered states.

1.2 Cooperative Jahn-Teller effect

Another example of phase transition is the cooperative Jahn-Teller effect. According to the Jahn-Teller theorem, if the ground state of an ion in a crystal is orbitally degenerate, the crystal will distort to a lower symmetry in order to remove the degeneracy. Jahn-Teller distortion is observed only if the orbital angular momentum is quenched by ligand fields. I will illustrate the JT effect with an example: the case of $LaMnO_3$. This manganese lanthanum oxide undergoes a distortion due to the presence of the Jahn-Teller ions Mn^{3+}. The $3d$ electronic levels of Mn^{3+} are not fully occupied: there are three electrons in the lower three-fold degenerate t_{2g} levels and one electron in the two-fold degenerate e_g levels. To remove the degeneracy of the half occupied e_g orbitals, the systems undergoes a tetragonal distortion. The distortion preserves the center of gravity of the e_g level of the cation, and hence the ion can obtain equal stabilization through distortion to tetragonal symmetry. The system could resonate between two stable configurations unless one of them is preferred for some reason. This happens if there is a coupling between vibrational modes and low-frequency electronic motion and the effect is then referred to as the dynamic Jahn-Teller effect. The cooperative Jahn-Teller effect is therefore a phase transition driven by the interaction between the electronic states of one of the ions in the crystal and the phonons. The transition can

be first- or second-order, in either case there will be a lowering in the symmetry of the lattice distortion and the splitting of the electronic levels. Since the crystal distortion requires cooperative distortions around the Jahn-Teller ion, the concentration of these kind of ions must be quite large for such transitions.

Jahn-Teller effect is a correction to the Born-Oppenheimer approximation. If the JT contribution to the hamiltonian is added and the elastic energy is included, the potential energy exhibits two minima for two different ligand geometry around the JT atom. If experimental observations are made in a short time, a distortion is observed. An average of a number of observations would indicate a lowering of symmetry and this is the situation in the static JT effect. Dynamic effect, instead, can arise from thermal fluctuation. If $\hbar\omega \ll E_{JT}$, and at low temperatures $kT \ll E_{JT}$, the system will be situated at the bottom of the potential well (static case). At higher T, $kT \geq E_{JT}$, thermally induced fluctuation from one potential well to another can occur (dynamic case). A more important case of dynamic JT effect occurs when $\hbar\omega \geq E_{JT}$. In this situation, even at the lowest temperature, there will be no stabilization of one distortion. Since the mechanism of JT effect involves interactions between ligand displacements due to the elastic properties of the lattice, an entire crystal can become unstable with respect to the distortion if the concentration of JT ions is large. Phase transitions resulting from such interactions can result in a parallel or some other alignment of all the distortions. Since an isolated JT ion drives a local distortion, there would be some JT stabilization energy for an assembly of ions and this would not make any contribution to the cooperative effect. To evaluate the cooperative effect it is necessary to subtract this self-energy from the total energy.

1.3 Metal-Insulator transitions

An insulator is a substance with a vanishing electrical conductivity in a (weak) static electrical field at zero temperature. The transport of electrical charge in the solid state is provided by electrons that are subjected to the Coulomb interaction with the ions and the other electrons. A first category of insulator can be understood in terms of band theory as single electrons that interact with the electrostatic field of the ions. Mott insulators, instead, constitute a second category, where the insulating behaviour is explained as a cooperative many-electrons phenomenon.

To understand the insulating behaviour of a material at zero temperature we may consider only static ion configurations. Insulators described by a single-electron theory

belongs to three types, namely: (i) Bloch-Wilson or band insulators, due to electrons' interaction with the periodic potential of the ions; (ii) Peierls insulators, due to electrons' interaction with the static lattice deformations; (iii) Anderson insulators, due to the presence of disorder (e.g., lattice imperfections, impurities, etc.). The Mott insulators are conceptually different, due to electron-electron interaction. In this case in fact it is necessary to solve a many-electron problem to explain the material insulating properties. In real materials the interactions used in this classification scheme are always simultaneously present: although a single interaction can drive the transition, its nature may be strongly affected by the others, therefore the classification of experimentally observed insulators is not always so straightforward.

The formation of a gap that characterizes an insulator and drives a metal-insulator transition can be understood according to two different pictures: the first considers the MI transition as a quantum phase transition that results from the competition between electrons' kinetics and the potential energies. The second way to explain the formation of a gap is offered by thermodynamic phase transitions: the competition between the internal energy and the entropy favors an ordered state at low temperatures and the symmetry-broken state may display a gap for charge-carrying excitations that causes an insulating behaviour below the critical temperature.

If we take into account the first mechanism, in the case of solid-state physics the electrons, on the one hand, prefer to spread over the entire crystal to optimize their kinetic energy. On the other hand, their various interactions tend to localize them in order to minimize their potential energy. It is the competition between these two tendencies that determines their conducting properties at zero temperature. The ground state can display dominantly either the electrons' itinerant (metallic) or localized (insulating) features. This energy balance can be externally shifted by the application of a pressure to the specimen, for example, to induce a metal-insulator transition. The concept of quantum phase transition is strictly limited to zero temperature and so are the notions of a metal and an insulator. In reality, both of them display a finite conductivity at $T > 0$ and it is better to discriminate between "good" and "bad" conductors. The generic situation for a system with a quantum phase transition as a function of an external parameter λ is sketched in Fig.1.1.

We observe a crossover regime from good to bad conductivity. In real experiments a very sharp increase in the resistivity can still be observed in a metal-to-insulator transition since temperature often is a small energy scale compared to electronic energies such that the system behaves as if the zero temperature limit was reached.

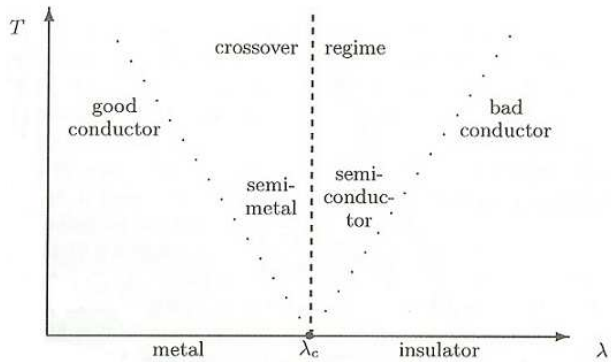

Figure 1.1: A metal-insulator transition as quantum phase transition: the gap for one-electron excitation opens at the critical interaction λ_c and separates the semi-metallic and semiconducting phases.

Thermodynamic phase transitions are the consequence, instead, of the competition between the internal energy and the entropy of a system such that a low-entropy (ordered) state is formed at low enough temperatures, which breaks a (continuous) symmetry of the Hamiltonian. The formation of an ordered state also influences the conducting properties. The most celebrated example is superconductivity. The formation of an ordered state in a thermodynamic phase transition may also result in a gap for charge excitations. Since in this kind of transition the conducting properties change because of a shift in the energy-entropy balance, the control parameter for the thermodynamic transition is the temperature. The essential difference from the quantum phase transition lies in the fact that an increase in temperature allows the gap to close, that is it allows to transform the insulator at T=0 K into a "true" metallic state at $T > T_c$. Along the line $T = T_c(\lambda)$ we observe a transition from the symmetry-unbroken into the ordered phase (Fig.1.2). At finite temperature there is always a finite region around the transition line within which the values for the critical exponents can be obtained from a classical statistical mechanics [1.13,1.14]. This region shrinks to zero at the so-called "quantum critical point" ($\lambda = \lambda_c$, T=0) where the critical exponents in the whole transition region must be obtained from a quantum-mechanical approach.

However, one must be aware of the fact that the signatures of both quantum and thermodynamic phase transitions will be often present in experimentally determined phase diagrams.

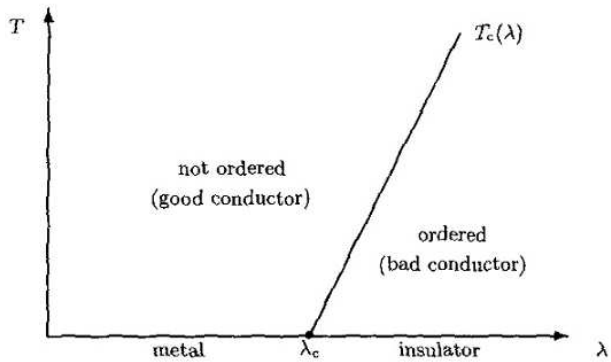

Figure 1.2: A metal-insulator transition as a thermodynamic phase transition: the gap for one-electron excitations opens at the critical temperature T(λ) and separates the non-ordered metal from the ordered insulating phase.

1.3.1 Mott insulators

In Mott insulators the electron-electron interaction cannot be neglected and on the contrary dominates the properties of the system. In general, the repulsive electron-electron interaction tends to keep the electrons apart from each other. This localization tendency is in conflict with the electrons' kinetic energy that tries to spread out the electrons over the whole crystal. To asses the "true" strength of these interactions, it is important to define a significant measure for their relative strength. We consider s electrons with spin $\sigma =\uparrow,\downarrow$ and write the average potential energy for the Coulomb interaction between these electrons:

$$\langle \hat{V} \rangle = \sum_{\sigma,\sigma'} \int d\vec{r} d\vec{r'} \frac{e^2}{|\vec{r} - \vec{r'}|} \langle \hat{\psi}^+_\sigma(\vec{r}) \hat{\psi}^+_{\sigma'}(\vec{r'}) \hat{\psi}_{\sigma'}(\vec{r'}) \hat{\psi}_\sigma(\vec{r}) \rangle, \tag{1.3}$$

where $\langle ... \rangle$ denotes a thermal average over the quantum-mechanical states. To determine the strength of the electron-electron interaction, we need to know the probability to find a σ' electron at $\vec{r'}$ when there is a σ electron at $\vec{r}$. This information is contained in the pair correlation function:

$$g_{\sigma,\sigma'}(\vec{r}, \vec{r'}) = \langle \hat{\psi}^+_\sigma(\vec{r}) \hat{\psi}^+_{\sigma'}(\vec{r'}) \hat{\psi}_{\sigma'}(\vec{r'}) \hat{\psi}_\sigma(\vec{r}) \rangle - \langle \hat{n}_\sigma(\vec{r}) \rangle \langle \hat{n}_{\sigma'}(\vec{r'}) \rangle. \tag{1.4}$$

This quantity differs from the expectation value we need for the evaluation of (1.3) by the subtraction of a product of a two-fermion expectation values ($\hat{n}_\sigma(\vec{r}) = \hat{\psi}^+_\sigma(\vec{r}) \hat{\psi}_\sigma(\vec{r})$ is the density particle operator). Hence $g_{\sigma,\sigma'}(\vec{r}, \vec{r'})$ measures the correlations in the system. There are two different contributions to the pair correlation function, namely the effect of the particle statistics (Pauli exclusion principle) for the electrons with the

same spin and the electron correlations induced by the electron-electron interaction.

a) Exchange. For fermions the Pauli principle guarantees that two electrons of the same spin cannot occupy the same orbital. Hence, the pair correlation function for electrons with the same spin is different from zero even if no electron-electron interaction takes place. The Pauli principle itself thus reduces the probability to find a σ electron in the vicinity of another σ electron. For electrons with different spin quantum numbers there is no exclusion principle and we find $g_{\sigma,-\sigma}(\vec{r},\vec{r'}) = 0$. Since electrons with the same spin are already kept apart from each other by the Pauli principle, this in turn reduces their mutual Coulomb interaction. To lowest order in perturbation theory the electron wave functions remain unchanged such that the electron-electron interaction among σ electrons is reduced compared to the interaction between σ and $-\sigma$ electrons. The corresponding "energy gain" is called "exchange interaction". In atoms the exchange interaction is responsible for the parallel orientation of the electron spins in open shells, whereas in solid-state physics this energy contribution is invoked to explain ferromagnetism in transition metals.

b) Correlations. The correlation function $g_{\sigma,-\sigma}(\vec{r},\vec{r'})$ between electrons of different spin accounts for the contributions beyond the exchange effect, that is it contains the true many-body effects. As mentioned above, the Fermi statistics of the electrons gives rise to " exchange" between electrons of the same spin, which is signaled by a non-vanishing pair correlation function for equal spins. We refer to systems with a non-vanishing pair correlation function between $\uparrow$ and $\downarrow$ electrons as "correlated electron systems". Naturally, the interaction also changes the correlation function between electrons of the same spin. If the pair correlation functions for electrons of the same spins and electrons of opposite spin are comparable in size, the system is termed " strongly correlated". In general a σ electron will not only be surrounded by an exchange hole but also by a correlation hole, since the repulsive electron-electron interaction will also prevent electrons of different spin to come close to each other.

In this context, Mott emphasizes the significance of correlations for the comprehension of the metal-insulator transition. Moreover, a proper description of the metal-insulator transition where the low-energy (Fermi-liquid) picture breaks down must necessarily include the effects of local magnetic moments. Mott himself describes a Mott insulator as a material that would be a metal if no moments were formed. The moments appear since the electrons try to avoid each other in order to minimize their Coulomb repulsion. These consideration lead to the following definition of a Mott insulator [32]: for a Mott insulator, the electron-electron interaction leads to the occurrence

of (relative) local moments. The gap in the excitation spectrum may arise either from the long-range order of the pre-formed moments (Mott-Heisenberg insulator) or by a quantum phase transition induced by charge or spin correlations (Mott-Hubbard insulator).

1.3.2 Mott-Hubbard insulators

Considering a simplified atomic model, we can assume that the effective electron-electron interaction will be local. The intra-atomic energy, that is the ionization energy minus electron affinity, is called the "Hubbard" U energy. In this picture the electrons dominantly sit *on* and not *between* the lattice sites. We further assume that the electrons may hop between neighbouring atoms. This tight-binding approximation for independent electrons results in a cosine dispersion relation $\epsilon(\vec{k}) = -2t\sum_l cos(k_l a)$ (being a the lattice constant), with a bandwidth $W \propto 2t$ and $t > 0$ is the tunnel amplitude. At large distances between the atoms, the overlap between the atomic wave functions is small, which implies $W \ll U$. In the ground state every lattice site will be singly occupied since we are at half band-filling. The energy $\mu^+(N) = E_0(N+1) - E_0(N)$ necessary to add another electron is given by $U - W_1/2$ since charge excitations with energy U are mobile such that they form a band of width W_1; this band is called the "upper Hubbard band", which is generally not a one-electron band. Instead, it describes the spectrum of charge excitations for an extra electron added to the ground state of the half-filled electron system. Analogously, the energy required to remove an electron, $\mu^-(N) = E_0(N) - E_0(N-1)$, is given by $W_2/2$. The corresponding spectrum for the removal of a charge from the half-filled ground state constitutes the "lower Hubbard band". At half band-filling and for $(W_1+W_2)/2 \ll U$ one expects that a gap for charge excitations occurs and the system is an insulator. If now the distance between the atoms is reduced, the overlap of the atomic wave functions increases and gives rise to an enhancement of the electrons' tendency to delocalize. The combined bandwidth of the upper and lower Hubbard band $W_1 + W_2$ increases accordingly: the two bands finally overlap and the gap for charge excitations vanishes. For $W \gg U$ the system is a paramagnetic metal. For intermediate values, $U \approx W$, we expect a metal-insulator transitions: the transition is a consequence of electron correlations. These considerations lead to the following definitions: for a Mott-Hubbard insulator the electron-electron interactions leads to the formation of a gap in the spectrum for single charge excitations; the correlations force a quantum phase transition from a correlated metal to a paramagnetic Mott-

Hubbard insulator, in which the local magnetic moments do not display long-range order. In this case we will observe drastic changes in the resistivity even at finite temperatures when going through the quantum phase transition value for the external parameters that control the relative strength of the electrons' kinetic and potential energy, U/W. For temperatures small compared to the single-electron gap we may then speak of a "Mott-Hubbard insulator" in practical terms even at finite temperatures. Until now we have not considered the possibility of an ordering of magnetic moments. Thus, the concept of the Mott-Hubbard insulator must be supplemented by that of Mott-Heisenberg insulator for which the insulating state displays long-range order. In fact the exchange interaction between localized spins must be considered. Even for $U \gg W$ the tunnelling of electrons to neighbouring sites is allowed ("virtual" hopping processes). In this case (that is, large interactions) if the the energy scales for charge excitations ($\Delta\mu \approx U - W$) and spin excitations ($J \sim t^2/U$) are well separated, then the system is in the Mott-Hubbard insulating regime since the gap due to the quantum phase transitions is finite. The spin energy scale, however, cannot be ignored for temperatures around or below that of the corresponding exchange interaction. The local magnetic moments in the Mott-Hubbard insulator, in fact, can become long-range ordered at the temperature $k_B T_N = O(ZJ) \ll \Delta\mu$. The system goes over from the Mott-Hubbard insulator into the antiferromagnetic Mott-Heisenberg insulator in a thermodynamic phase transition at $T = T_N$. According to Mott [1.1] the size of the local moments does not change much in the transition through the Néel temperature. For small interactions the Mott-Hubbard gap is absent but correlations for all $U > 0$ lead to preformed magnetic moments. In this case also these moments may become ordered on a long-range dimension at the Néel temperature and a thermodynamic phase transition from a paramagnetic (correlated) metallic state into the (antiferromagnetic) Mott-Heisenberg insulating phase is observed. From these considerations follows the definition of Mott-Heisenberg insulator [32]: the Mott-Heisenberg insulating state is the result of a thermodynamic phase transition in which the pre-formed local magnetic moments (antiferromagnetically) order below the critical Néel temperature. Above T_N the Mott-Heisenberg insulator goes into a paramagnetic phase, which can be either a correlated metal or a Mott-Hibbard insulator.

1.4 Mott-Hubbard transition

As we discussed above, the interactions between electrons leads to magnetic moments. In general, as pointed out by Mott [7.1,7.2], these moments have formed at temperatures above $T_N(U)$. A material can effectively remain insulating (Mott-Hubbard insulator) even above T_N where the order of the moments ceases to exist. Such behaviour can be understood as the consequence of a quantum phase transition at zero temperature: even if the long-range order of the moments was absent, the electron correlations will drive the metal into the Mott-Hubbard insulator at some finite interaction strength U_c. The canonical (U,T) phase diagram for an undoped system then displays three generic phases and their respective transitions; an AF Mott-Heisenberg insulator below $T_N(U)$, a correlated metal above $T_N(U)$ and for sufficiently low interaction strengths, finally a paramagnetic Mott-Hubbard insulator above $T_N(U)$ and for larger interaction strengths. We must note that there is no sharp distinction between the paramagnetic metal and the paramagnetic Mott-Hubbard insulator for $T > T_N$ since these are not two distinct phases in the sense of statistical physics. Instead, there is a crossover as a function of the interaction strength at finite temperatures. The phase diagram of vanadium sesquioxide (Fig.2.17 [48]) for example displays these three canonical phases. It also confirms that a correlated electron approach is the proper starting point for a theoretical investigations of these materials. A complicated band structure, band degeneracies, the influence of impurities and the electron-phonon interaction often blur the basic mechanism behind the Mott metal-insulator transition. The Hubbard model is the simplest model to describe interacting itinerant lattice electrons, for this reason it is the natural starting point study the Mott transition. Then other approximation schemes provide complementary views on the various metallic and insulating phases [32]. In infinite dimensions the Hubbard model is able to describe the generic (U,T) phase diagram at half-band filling and the corresponding Mott transitions. However, important details of the Mott-Hubbard transition remain to be clarified. For example, it is still an open question whether this zero-temperature quantum phase transition is discontinuous or continuous, and whether or not there is a line of first-order transitions at finite temperatures.

In the following chapter we will discuss about still open problems regarding the phase transitions in vanadium sesquioxide and manganite perovskites, which are correlated electron systems.

V_2O_3 is considered the prototype of the Mott-Hubbard system, since it shows, at about 160 K, a phase transition from a paramagnetic-metallic high temperature phase

to an antiferromagnetic-insulating low temperature phase. Therefore the electronic and transport properties of this system are strictly connected to the magnetic ones. As we will see in the following, this is just one aspect of the complex phase diagram associated to V_2O_3, because the system shows also, together with the magnetic transition, a structural transition between two different spatial symmetries.

For what concerns manganites, these compounds have a transition between different magnetic and conductive phases. Moreover these systems show also the cooperative Jahn-Teller effect, because the manganese ions in the $LaMnO_3$compound have +3 valence state and hence there are $3d$ electronic levels with e_g symmetry which are not completely occupied. As we said in the previous section, the system tends to remove the degeneracy by distorting the structure. These properties are treated in the next chapter.

Chapter 2

Transition metals oxides: manganites and V_2O_3

2.1 Manganites

Mixed valence manganites with perovskite structure, like $La_{1-x}Ca_xMnO_3$, are obtained by substitution of La ions (+3 valence) in $LaMnO_3$with Ca ions (+2 valence). These compounds are studied since the '50s because of their interesting electric and magnetic properties, showed in the proper conditions of temperature, pressure, external magnetic field and doping x. The most significant effect discovered in manganites is a huge magnetoresistance effect (MR), the so-called colossal magnetoresistance (CMR). Such effect in manganites is much higher than that usually observed in metals, where it is due to a magnetic dependent electron mean free path: actually, in these materials with a very high purity and regular crystal lattice, the application of an external magnetic field forces the electrons to move in orbits, thus reducing their mean free path. In manganites the CMR arises from the competition between different ground states, metallic and insulating, and it is actually due to a magnetic field driven metal to insulating transition. These materials are of large interest also for application because CMR occurs at temperatures near, or even above, room temperature.

Since their discovery, these compounds have been a challenge both for experimentalists and for theoreticians, because they show a very complex phase diagram; to explain some aspects of it new physical concepts have been introduced, such as the *double exchange* and the *Jahn-Teller polaron*. In spite of this effort a complete and satisfactory knowledge of manganites has not been achieved yet. Nowadays, apart from the interest due to their potential technological application, these materials are a challenge

in solid state physics because they are the prototype of highly correlated electronic systems where spin, charge, orbitals and structural degrees of freedom simultaneously play together, in determining the physical properties of the material.

In this section I will shortly illustrate the most important aspects of the behaviour of $La_{1-x}Ca_xMnO_3$, in particular I will consider their structural, electronic and the transport properties.

2.1.1 Magnetic properties

Magnetic and electric properties of $La_{1-x}Ca_xMnO_3$strongly depend on the doping x and on the temperature. In a wide range of x values these materials show a phase transition from a paramagnetic (PM) phase to a ferromagnetic (FM) one on cooling, with a simultaneous sharp decrease of the resistivity (metal-insulator transition). The metal-insulator transition temperature depends also on the applied magnetic field and this origins the colossal magnetoresistance phenomenon. The MR is defined as

$$MR = \frac{\rho(H) - \rho(0)}{\rho(0)} \tag{2.1}$$

and when a magnetic field is applied in manganites the drop in resistivity induces a MR of -100%. In Fig.2.1 the phase diagram of the series $La_{1-x}Ca_xMnO_3$is reported.

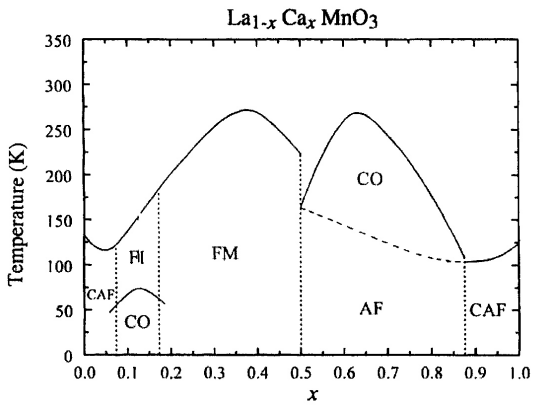

Figure 2.1: Phase diagram of manganites as a function of temperature and doping. CO = charge ordered; CAF = canted antiferromagnetic; FI = ferromagnetic insulator; FM = ferromagnetic metallic; AF = antiferromagnetic

For $0 < x < 0.15$ the system is insulating for all the temperatures and show a PM phase at high temperature and a FM one at low T.

For $0.15 < x < 0.45$ it undergoes an insulating-to-metal transition (M-I) and a PM-FM one when the temperature decreases below the Curie temperature T_c; the M-I

transition temperature is close to T_c and depends on the magnetic field. In this doping interval the material shows the CMR behaviour: sharp decrease of the resistivity and the changes of the magnetization M are strictly connected to the FM transition of the magnetization M (Fig. 2.18).

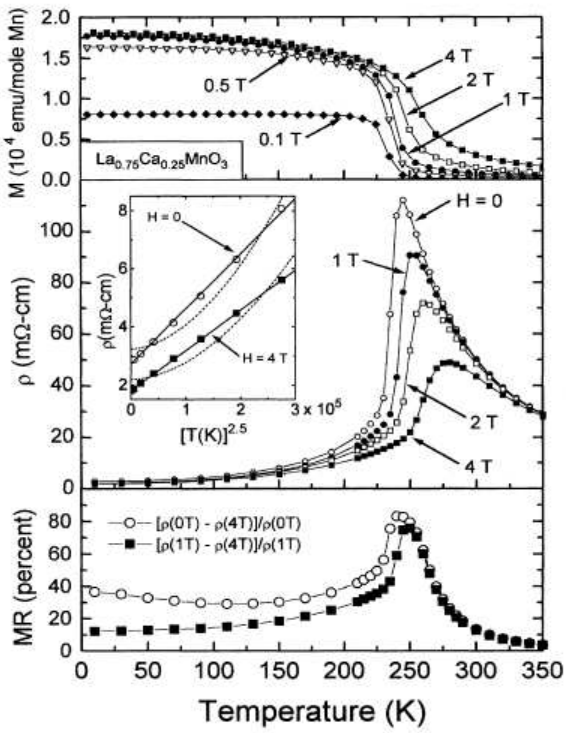

Figure 2.2: Trend of magnetoresistance and resistivity when the temperature and the applied magnetic field vary.

For $x = 0.5$ the ground state becomes antiferromagnetic (AFM) insulating: this is the most complex situation, because there are three possible configurations which are electrostatically equivalent and the system has more phase transitions (PM-FM-AFM) when T varies. Moreover charge ordering effects (CO) emerge at some T. When $x > 0.5$ the solid is AFM insulating at low temperature. In this range of x values there are not differences in M(T) if the sample is cooled or heated and this fact suggests that the magnetic transitions are second-order.

The M-I transition in manganites is atypical because the low temperature phase is metallic instead of the high T one. This is due to the character of the double-exchange coupling which is the basic mechanism underlying the magnetic and transport properties of the material (see Par.2.1.4): when a magnetic field is applied, magnetic

order and charge mobility increase and as a consequence the resistivity decreases.

In these materials remarkable hysteresis magnetic and thermic effects are observed, above and below the resistivity maximum. In the magnetic case, varying the external field from zero until a maximum value and then again to zero, the sample "remembers" the maximum value reached by the field and the resistivity assumes the 40% of its value at H=0 T [88]. Moreover a temporal relaxation of the resistivity at constant T is also observed.

The transport properties of manganites are anomalous and still not fully explained: different authors, in fact, report different resistivity trend. Anyway they agree that the charge carriers form dielectric polarons (as we will see in the following), observed for the first time from the pair distribution function of $La_{1-x}Ca_xMnO_3$ with $x = 0.12$ [8]. The polaronic hopping gives a resistivity law

$$\rho = \frac{kT}{ne^2D}\exp(\frac{E_0}{kT}) \tag{2.2}$$

where n is the charge carriers density and D is the polaronic diffusion constant. The contributions to E_0 can have magnetic, elastic (Jahn-Teller) and coulombian origin. The influence of a magnetic field above T_c on resistivity suggests that the polarons have, at least partially, a magnetic origin [15].

2.1.2 Crystal structure

Ideal perovskite structure Manganites with general chemical formula $AMnO_3$, where A is a metallic ion with valence +2 or +3, have a perovskite-like structure which derives from the space group $Pm3m$. In the ideal structure the unitary cell is cubic with a lattice parameter of $\sim$ 3.90 Å. The cation A (La, Ca) is placed at the center of the cell (in the site with coordinates $\frac{1}{2}, \frac{1}{2}, \frac{1}{2}$); the Mn cation occupies the vertexes of the perovskite cube, surrounded by oxygen octahedra that share their vertexes. every Mn ion is the center of an octahedron. The oxygen ions are in the middle of the cubic sides (Fig. 2.3).

The octahedron MnO_6 at the cube's vertexes makes the structure very stable. In the ideal cubic cell the angle of the bond Mn-O-Mn is 180°.

Distorted perovskite structure Actually the real structure of manganites is not ideal but it is a pseudo-cubic lattice characterized by different kinds of distortions. The first cause of distortion is the so-called "size-mismatch": this effect is due to the central atom that is smaller than the free space available inside the cubic cell. To evaluate the entity of the distortion we define a tolerance factor

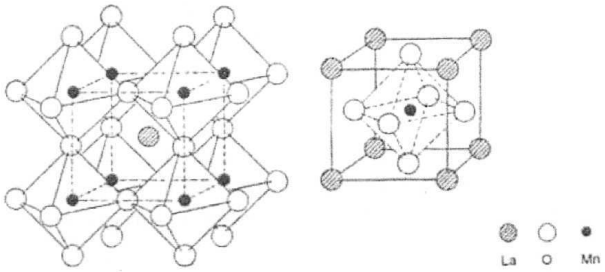

Figure 2.3: The ideal perovskite structure.

$$t = \frac{r_{La,Ca} + r_O}{\sqrt{2}(r_{Mn} + r_O)} \tag{2.3}$$

which represents the importance of the distortion; this factor is equal to 1 for the ideal structure. Since oxygen octahedra are very stable structures, the system reduces the size-mismatch by titling the octahedra with respect to the cell axis, rather than changing the lattice parameter (Fig. 2.4). The Mn-O-Mn angle thus is reduced to $\sim 155°$.

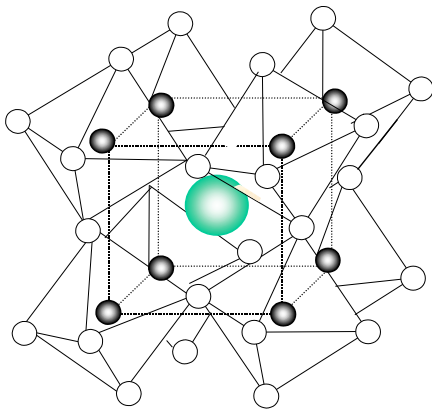

Figure 2.4: Reduction of the size-mismatch: the O octahedra are tilted. Different tilting configurations are possible: in the figure, the octahedra are titled by the same angle alternatively clockwise and counterclockwise from one site to the other. In the figure the white circles are O atoms, The black ones are Mn, the big central atom is La/Ca.

The second distortion is connected to the Jahn-Teller effect (see Par.1.2). This is a common effect for ions having partially filled outer electronic states with a high degree of degeneration. In this case a distortion of the local lattice around the Mn ion occurs, which lowers the crystal symmetry so to remove the degeneration. This is the case of the e_g and t_{2g} bands of the Mn^{3+} ion, which derive from the 3d orbitals for

the octahedral crystalline field. These levels are two-fold and three-fold degenerate, respectively, therefore they are "unstable" in a perfect cubic geometry. The distortion of the octahedra splits the degenerate energy levels by a quantity E_{JT}. This effect does not acts in Mn^{4+} ions because the t_{2g} levels are completely filled and the e_g band is empty. Therefore Mn^{4+} ions are not accompanied by any JT distortion.

The Jahn-Teller distortions results in the elongation of the apical octahedral bonds from an average value of ~ 1.95 Å up to a value ~ 2.20 Å, with respect to the planar ones ($\sim 1.90 - 1.95$ Å). Therefore the resulting coordination geometry is anisotropic (Fig.2.5)

Due to this distortion the unitary cell is not cubic anymore, therefore the description of the intermediate crystallographic phases ($La_{1-x}Ca_xMnO_3$) requires unitary cells with different symmetry: cubic, rhombohedral, orthorhombic and monoclinic.

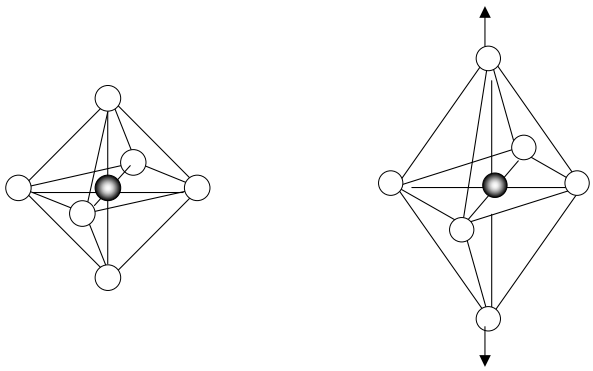

Figure 2.5: On the right, the distorted Mn^{3+} ion. The distortion acts upon one axis and induces the other Mn-O ligands to follow the new configuration. On the left, the Mn^{4+} ion does not present this distortion.

The pure $LaMnO_3$compound

Experiments performed by Huang [35] show that at room temperature different samples of $LaMnO_3$ have different symmetry: in some cases it is monoclinic or orthorhombic, in others it is rhombohedral. These structural changes refer to sample prepared with different methods. Using X-ray and neutrons diffraction Huang and Elemans [22] determined the oxygen positions, highlighting that the MnO_6 octahedra are not only distorted but also tilted, and observed an antiferromagnetic arrangement of the magnetic moments. The Mn-O distances at T=300 K are 1.91 Å and 2.18 Å in the a-b plane and 1.97 Åalong the c axis: this is the Jahn-Teller distortion; the La atoms are

displaced along the cube's diagonal. The Mn-Mn distance is 3.99 Å along the apical axis of the octahedron and 3.85 Å along c-axis.

At T=1020 K the orthorhombic distortion disappears and the sample becomes rhombohedral (almost cubic). This phenomenon can be interpreted as an order-disorder transition, where the local JT distortions become spatially uncorrelated but do not disappear [57]. At this temperature the frequency of electronic hopping exceeds that of the JT distortion optical phonons [72].

The intermediate compounds

The doping of manganites concerns the substitution of the rare earth ion (La, Pr, ...) by divalent metals such as Ca, Sr, ... In this way the $La_{1-x}Ca_xMnO_3$series is obtained. Since the Ca^{2+} substitutes La^{3+}, the manganese ion must change its valence from 3+ to 4+ to balance this charge deficit and hence the system has a mixed valence. Moreover, since the Mn^{4+} have not degenerate occupied states, their levels are not separated by JT effect, hence the sites around the Mn^{4+} are not distorted. For this reason in the mixed valence compounds there should be the presence of both distorted sites and non-distorted ones. Actually the situation is much more complex, as we will see in next sections.

In the intermediate compounds there are three factors which contribute to the structural changes when x and T vary: the passage from a static JT distortion to a dynamic one, the transition from charge ordered states to disordered ones and the transformation from states with localized charge carriers to states where the carriers are free to move. The different magnetic ordering for different x values depends on the charge ordering in the perovskite lattice [15]; a simple set of rules can be deduced by mean of comparison of the charge and magnetic ordering: the exchange coupling is FM between Mn^{3+} and Mn^{4+} ions, AFM between two Mn^{4+} ions and FM or AFM between two Mn^{3+}.

2.1.3 Electronic structure

For what concerns the electronic structure, the manganese ions are the relevant atoms in manganites. The electronic configuration of Mn is [Ar]$3d^5 4s^2$. According to Hund's rule, the four 3d electrons have parallel spin, resulting in a non-zero magnetic moment. In the ideal case, the 3d orbitals split into two sublevels due to the crystalline field created by the oxygen octahedra: the three-fold degenerate t_{2g} level and the two-fold degenerate e_g level (see Fig.2.6).

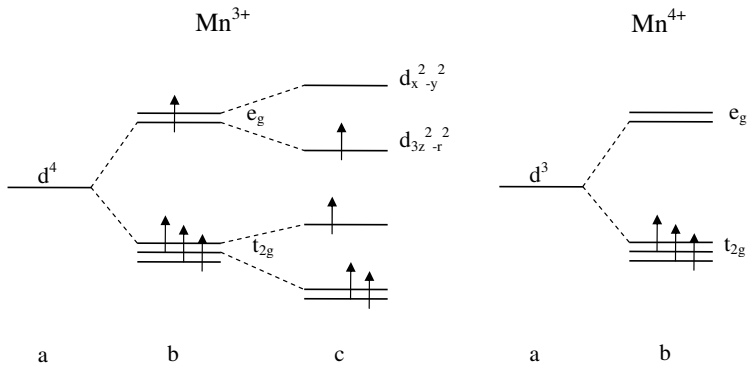

Figure 2.6: On the left, a) the $3d^4$ five-fold degenerate Mn^{3+} electronic levels; b) $3d$ level splitting due to the crystal field; c) further splitting due to the JT effect. On the right, a) the $3d^4$ Mn^{4+} levels; b) crystal field splitting.

A Mn^{4+} atom has 3 valence electrons which completely occupy the t_{2g} symmetry level, giving rise to a non degenerate ground state; therefore the Mn^{4+} ions do not experience the JT effect. On the contrary, Mn^{43+} ions have one electron in the double degenerate e_g state; therefore the JT distortion occurs and further splits the energy levels removing the degeneration. At the end of this process, we have two σ-type orbitals ($d_{x^2-y^2}$ and $d_{3z^2-r^2}$) and three π-type orbitals with symmetry d_{xy}, d_{xz} andd_{yz}. The orbitals obtained from the further splitting are pictured in Fig.2.7.

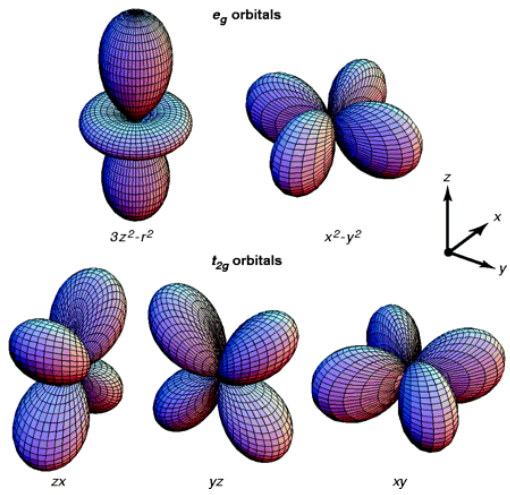

Figure 2.7: 3d orbitals wave functions.

In mixed valence compounds the average number of 3d electrons per manganese ion is 4-x, where x indicates the nominal occurrence of Mn^{3+} ions with respect to the Mn^{4+} ones. Three of these electrons fill up the t_{2g} levels which form a core with total

spin S=3/2. The remaining $1-x$ electrons occupy the e_g symmetry level that has a bandwidth of $\sim$ 2.5 eV. Moreover, due to the large Hund coupling strength, the spin of the e_g electrons is parallel to the spin of the core.

The energy scale of the interactions present in these materials is of the order of the electronvolts. The interactions that determine its electronic properties are the following:

- the Mott-Hubbard interaction strength U_{dd}, which represents the energy needed to create an excited state $d^{n+1}d^{n-1}$ in a d^n ions lattice;
- U_{pd}, the energy occurred to transfer a p electron from the oxygen site to the nearest-neighbour Mn ion ($p^6d^{n+1} \rightarrow p^5d^n$);
- the transfer integral t, which quantify the wave functions overlapping between adjacent ions and determines the energy bandwidth of the d electrons;
- the on-site exchange interaction U_{ex}, that splits the up and down spin electrons and represents the energy required to rotate the spin;
- the crystalline filed interaction δ_{cf}, that acts in the splitting of the $3d$ levels into t_{2g} and e_g symmetry states;
- the JT interaction δ_{JT}, which gives rise to the further splitting of the t_{2g} and e_g levels.

Since the e_g symmetry orbitals have wave function lobes oriented in the direction of the oxygen p orbitals (Fig.2.8), their energy levels will lye above the t_{2g} ones, that are differently oriented, due to the higher electrostatic Coulomb repulsion. The energy splitting is $\sim$ 1.5 eV. Moreover, the stretching of the apical bonds in the MnO_6 octahedra, originated from the JT effect, stabilizes the e_g $d_{3z^2-r^2}$ orbitals with respect to the $d_{x^2-y^2}$ ones. The t_{2g} orbitals instead are scarcely overlapped with the p oxygen orbitals and tend to form a localized core, whereas the direct overlapping of the e_g states and p oxygen states forms an anti-bonding band.

In the $LaMnO_3$, the Fermi level is in the middle of the gap opened by the JT effect between the e_g sublevels, which contain one delocalized electron. Therefore both the end compounds $LaMnO_3$and $CaMnO_3$are insulating, because they have an entirely filled or a totally empty conduction band, respectively. On the contrary, mixed valence systems have a partially filled anti-bonding e_g band and thus can be conductive. In next section we will see how the conduction process takes place via the hopping of the electrons from one manganese ion to the other.

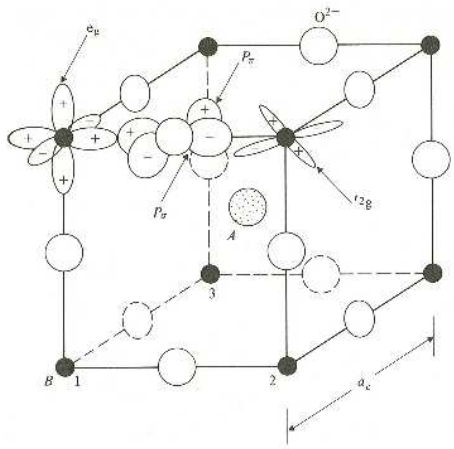

Figure 2.8: (Ideal) Perovskite structure (ABO_3). A is the La/Ca cation and B is the Mn ion.

2.1.4 Transport theories

The original theory of the exchange interactions in solids is based on the direct exchange interaction, described by the effective Heisenberg Hamiltonian

$$H = -2J(S_1 \cdot S_2) \tag{2.4}$$

where J is the exchange integral and S_1 and S_2 are the atomic spins. Anyway this model is not always appropriate because the magnetic cations, such as Mn, are often not nearest-neighbours , but they are separated by non-magnetic anions. This means that their wave functions barely overlap therefore the exchange integral is negligible. Moreover the direct exchange predicts a ferromagnetic interaction among the spins, while we know $LaMnO_3$is antiferromagnetic.

The super-exchange (SE) theory overcomes this problem because it describes an indirect magnetic interaction among the transition metal ions via the covalent bonds of the ligand atoms: if we consider two Mn atoms separated by an O one, the overlapping between the Mn d orbitals and the 2p O wave functions gives rise to covalent bonds. The net effect is to partially transfer one electron from O to Mn; due to the Pauli exclusion principle, the transferred electron will have opposite spin with respect to the one in the d orbital. On the contrary, the other metal ion should receive an electron with spin opposite to the one transferred to the other Mn. This may happen only if the two metals have un-paired electrons with antiparallel spins. As a consequence, the covalency of the two Mn atoms induces an antiferromagnetic ordering of their magnetic moments (Fig.2.9).

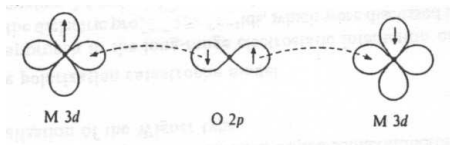

Figure 2.9: The super-exchange induces an antiferromagnetic arrangement of the ions with the participation of an anion.

Nevertheless, this model is not able to account for the complex phase diagram of systems such as $La_{1-x}Ca_xMnO_3$. For this reason a new transport theory was developed in the attempt to explain the conduction properties of manganites. This is the double-exchange (DE) model, which considers the degeneration of the Mn energy levels.

The Double-Exchange model

The nature of the low-temperature ferromagnetic metal phase and the coupling between T_c and the metal-insulator transition were discussed in 1951 by Zener [91, 92], who proposed the so-called double-exchange (DE) mechanism. In Zener's model the electronic transport is driven by the transfer of the charge carriers between Mn^{3+} and Mn^{4+} cations via the O^{2-} anion. There two antagonist mechanism that take place: the ferromagnetic ordering, which favors the charge carriers hopping, and the thermal disorder which destroys the FM order and is therefore responsible for the FM-PM transition. On the other hand, the application of an external magnetic field favors the metallic behaviour even at temperatures higher than T_c.

Now we consider two identical magnetic ions, each one with total spin S=3/2 and an extra electron (in our case e_g) with spin s=1/2, which can be on one of the two ions; between the two magnetic ions there is a different atom with zero total spin. Since the wave functions of the magnetic atoms do not overlap, there is no be direct exchange. In our case the magnetic ions are two Mn atoms and the ion with S=0 is an O. Zener made three assumption in his model: (i)the intra-atomic exchange is so strong that only the configurations where the spin of each carrier is parallel to the local ionic core spin are relevant; (ii) the carriers preserve their spin during the motion: this means that they can move, by hopping from one ion to the next, only if the two ionic spins are parallel; (iii) when hopping is allowed, the ground state energy is lowered because the carriers take part in the bonding.

In doped manganese oxides, there are two possible configurations that describes the ground state and they are degenerate:

$$Mn^{3+} \quad O^{2-} \quad Mn^{4+} \Rightarrow (\psi_1) \tag{2.5}$$

$$Mn^{4+} \quad O^{2-} \quad Mn^{3+} \Rightarrow (\psi_2) \tag{2.6}$$

The two states are connected by the double-exchange matrix. The system resonates between the states ψ_1 and ψ_2 for a merely quantum phenomenon. Since the two states are degenerate, the exact wave functions should be a linear combination of ψ_1 and ψ_2:

$$\psi_\pm = N_\pm(\psi_1 \pm \psi_2). \tag{2.7}$$

If we denote the energy difference of the two states in eq.(2.7) by 2ε, the conduction electron will resonate with frequency $\nu = 2\varepsilon/h$. The exchange energy ε is given explicitly by the integral

$$J = \int \bar{\psi_1}(H - E_0)\psi_2 d\tau \tag{2.8}$$

where H is the Hamiltonian of the system and E_0 the energy associated to one of the states ψ_1 or ψ_2. The integral is over all the coordinates and the spin of all the electrons.

In the exchange integral only the electronic functions are important, therefore we can write:

$$\psi_1 = (\psi_d^1 \psi_p) \tag{2.9}$$

where ψ_d^1 is the Mn 3d electron's wave function and ψ_p is the O 2p electron's one. Thus J becomes

$$J = \int \bar{\psi_d^1}\bar{\psi_p}(H - E_0)\psi_d^2\psi_p d\tau. \tag{2.10}$$

This matrix element arises from the transfer of one electron from Mn^{3+} to the central O^{2-} simultaneously with the transfer of one electron from O^{2-} to Mn^{4+}: there is a double exchange (see Fig.2.10).

Zener underlines how this mechanism is different with respect to the usual SE, because in that case only the excited states are degenerate, whereas in DE the whole system is degenerate due to the presence of the Mn ions with different charge. Moreover also the probability of the process is different, because if t is the electron hopping probability to go from one Mn to the other, then the probability of DE the achievement is proportional to t, while the probability of the SE one is proportional to t^2.

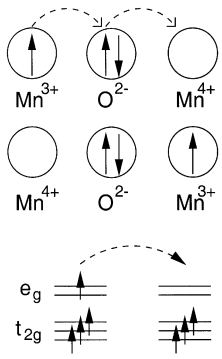

Figure 2.10: Schematic picture of the double-exchange mechanism: one e_g electron on Mn^{3+} is transferred to the O ion and at the same time another one goes from O to Mn^{4+}.

As we said, the coupling of degenerate states removes the degeneracy and system resonates between ψ_d^1 and ψ_d^2 leading to a conducting ferromagnetic state. Moreover, since the strong intra-atomic Hund's coupling is assumed, the exchange integral has a non-negligible value only when the core magnetic moments of the Mn ions, involved in the electron hopping, are parallel. On the contrary, a certain energy would be necessary to rotate the spin of the e_g conducting electron in order to align its spin with the core spin of the ion it is hopping to: the FM order of the Mn ions comes with an increase in the rate of migration of the Mn^{4+} ions and hence of the electrical conductivity. On the other hand, DE occurs only when the spins of the metal ions point in the same direction; since the stationary ground state is described be one of the two linear combinations (2.7), the DE raises the energy of ψ_d^1 and lowers that one of ψ_d^2, or viceversa. At low temperatures the energy of the system therefore will be lowered by a parallel alignment of the spins, that is by FM. Summarizing Zener found that the electronic transfer is favored by a FM arrangement while, on the other hand, a FM ordering itself is favored by the electronic transfer.

The magnitude of the exchange energy ε determines the rate of electron jumping from a Mn^{3+} to an adjacent Mn^{4+} across the O anion. The diffusion coefficient of the Mn^{4+} ion is thus given by

$$D = \frac{a^2 \varepsilon}{h} \tag{2.11}$$

where a is the lattice parameter. From the Einstein relation, $\sigma = ne^2 D/kT$, among the electrical conductivity σ, the diffusion coefficient D and the number of Mn^{4+} per unit volume n, the conductivity becomes:

$$\sigma = \frac{xe^2}{ahkT} \tag{2.12}$$

where x is the fraction of Mn ions with 4+ charge. If we consider that the Curie temperature T_c is approximately $kT_c \sim \varepsilon$, we find:

$$\sigma = \frac{xe^2}{ah}\frac{T_c}{T} \tag{2.13}$$

which describe the relation between conductivity and ferromagnetism.

Anderson and Hasegawa [1] used and bettered the model of Zener with a more quantitative approach: they treated classically the core spin of each Mn and quantum mechanically the mobile electron. In this way they found that the transfer integral t_{eff}, that is the matrix element of the single particle Hamiltonian between the wave functions localized on two nearest-neighbours ions, is equal to

$$t_{eff} = b\cos\frac{\theta}{2} \tag{2.14}$$

where the θ is the classical angle between the core spins. Here b is the transfer matrix element. In the hypothesis of strong Hund coupling ($J \cdot S \gg t_{eff}$), the energy of the state is given by

$$E = -J \cdot S - t_{eff} \tag{2.15}$$

Where J is the Hund's exchange on-site energy and $S = S_1 + S_2$. This relation means that the energy lowers when the itinerant electron's spin is parallel to the total spin of the Mn cores. Moreover, since t_{eff} depends on θ, the ferromagnetic arrangement favors the electronic transfer which lowers the energy: this process leads to a metallic and ferromagnetic ground state. The authors also show that the classical assumption about the spin can be replaced by the substitution of $\cos\frac{\theta}{2}$ with $(S_0 + 1/2)(2S + 1)$, where S_0 is the total spin of the two Mn and the mobile electron, while S is the core spin.

In 1960 de Gennes [16] approached the problem considering the DE when the lattice is AFM. He considered a layered model with N magnetic ions per unit volume, each of them has the spin coupled ferromagnetically to z' neighbours in the same plane, with exchange energy J', and antiferromagnetically to z neighbours on adjacent layers with energy exchange J. The Zener's carriers can hop both in the same layer (with transfer integral b') and from one layer to another (with b). When the angle between

the magnetization vectors of successive layers is Θ the energy exchange of the system becomes:

$$\frac{E_{ex}}{N} = -z'J'S^2 + zJS^2 \cos\Theta. \tag{2.16}$$

The double-exchange contribution is calculated in the tight-binding approximation:

$$\frac{E_{de}}{N} = -xb'\gamma'_k + b\gamma_k \cos\frac{\Theta}{2} \tag{2.17}$$

where γ'_k and γ_k are the sum of phase factors over the z and z' nearest-neighbours, and x is the Mn^{4+} concentration. In this case, the ferromagnetic state is stable at all temperatures is $x > 4JS^2/b$. At lower concentrations there is alow-temperature transition to a canted state that extends to $x = 0$; the canting angle between the successive ferromagnetic planes is given by $\Theta_0 = 2\cos^{-1}(\frac{bx}{4JS^2})$, reaching π if $x \to 0$. Therefore the canted state aligns ferromagnetically or antiferromagnetically according to the x value. The border between FM and AFM state is found for $\Theta_0 = 103°$. When $x < 2.5JS^2/b$ the canted state gives rise to AFM alignment along a critical line, while for $2.5JS^2/b < x < 4JS^2/b$ the state is FM.

Finally, in 1972 Kubo and Ohata [40] considered a fully quantum mechanical approach to DE. They introduced the now standard Hamiltonian

$$H = -J \sum_{i,\sigma,\sigma'} (\vec{S}_i \cdot \vec{\sigma}_{\sigma,\sigma'}) c^+_{i\sigma} c_{i\sigma'} + \sum_{i,j,\sigma} t_{ij} c^+_{i\sigma} c_{j\sigma} \tag{2.18}$$

where $c^+_{i\sigma}$and $c_{i\sigma}$ are the creation and annihilation operators for an e_g electron with spin σ on a Mn site and t_{ij} is the transfer matrix element; The spin of the core t_{2g} electrons is $\vec{S}_i$; $\vec{\sigma}$ is the Pauli matrix and J the intra-atomic Hund's exchange energy.

As a consequence of this model, the ferromagnetism enhances the conductivity, which on the other hand lowers the energy and favors the entire process. The DE model qualitatively explains the M-I transition and the negative MR effects: when the temperature decreases the thermic disorder also decreases and so does the angle θ between the spins of adjacent ions: in this way the transfer amplitude of the e_g electron between the two atoms increases. Even the application of an external magnetic field makes t_{eff} increase, favoring the spin alignment.

For many years this model had been considered satisfactory, but in 1995 Millis et al. underlined how in manganites the predictions of this model disagree with the experimental data on a quantitative basis: in particular, the resistivity calculated by mean of the DE model is some orders of magnitude lower than the experimental one,

it has a too weak dependence on the x doping concentration and it has not the correct behaviour for $T < T_c$ or in an applied magnetic field, showing that some new physical aspect must be included.

Recent transport theories

In 1995 Millis et al. [56] demonstrated that the DE model does not describe satisfactorily the experimental data; they proposed a correction to the DE that considers a strong electron-phonon interaction, caused by the Jahn-Teller effect. They introduced in the transport theory of manganites the concept of charge localization by means of electric or magnetic fields. The idea of self-trapped charge carrier was introduced for the first time by Landau in 1933 to explain the properties of alkaline metals. They suggested that free charges could localize in potential wells produced by the displacement of ions from their equilibrium position. Charges can be excited out of the potential wells they are trapped in, by photoabsorption or by thermal effects. Once free, they can hop from one site to another and in this way the medium becomes conductive. In strong polar solids, due to the Coulomb interaction, an unbalanced charge is accompanied in its motion by the polarization of the surrounding lattice. Crystal physical properties can be described by considering the quasi-particle formed by the charge itself, plus the "cloud" of virtual phonons surrounding it. Such an entity is called "polaron". A polaron can be viewed as a quasi-particle formed by a charge and by the local distortion it induces in the surrounding lattice. This distortion has both an electrostatic and a magnetic origin and it is usually accompanied by a cooperative mechanic strain of the lattice [56, 57, 58, 59]. Materials that can stabilize polarons have a peculiar conductivity behaviour due to the enhanced effective mass of the polarons. This behaviour is more evident at high temperatures.

Millis et al. suggested that for $x > 0.2$ and $T > T_c$ the strong coupling between electron and phonon makes the electrons of the conduction band become polarons at $T > T_c$ and that the polaronic effect disappears with temperature decreases below T_c, so that a metallic state forms. The competition between the electronic mobility and the self-entrapment is driven by the ratio λ of the Jahn-Teller stabilization energy E_{JT} and the energy of electronic delocalization given by the hopping matrix element t_{eff}. When $T = T_c$ the spins order and the value of t_{eff} increases with respect to E_{JT}, as a consequence λ decreases. Therefore this parameter varies in a wide range and strongly depends on T and H.

The complete Hamiltonian used by Millis is

$$H = H_{el} + H_{de} + H_{JT} + H_{ph} \tag{2.19}$$

where

- H_{band} describes the electronic transfer:

$$H_{band} = -\sum_{<ij>,a,b,\alpha} t_{ij}^{ab} c^{+} ja\alpha cja\alpha \tag{2.20}$$

  i and j indicating the sites where the electron hops between; α and β represent the spin of the a and b orbitals; t_{ij} is the transfer matrix element (t_{eff}); c and c^{+} are the annihilation and creation operators for a single electron.

- H_{de} is the double-exchange Hamiltonian for the itinerant electrons:

$$H_{de} = -J_H \sum_{i,a,b,\alpha,\beta} \vec{S}_c^i \cdot c^{+} ia\alpha \vec{\sigma}_{\alpha\beta} c_{ib\beta} \tag{2.21}$$

  where $\vec{S}_c^i$ is the core spin of site i that is coupled to the itinerant electron through the Hund strength J_H; $\vec{\sigma}_{\alpha\beta}$ are the Pauli matrixes that describe the spin of the itinerant electron.

- H_{JT} represents the electron-phonon interaction:

$$H_{JT} = g \sum_{i,a,b,\alpha} \vec{r_i} \cdot d_{ia\alpha}^{+} \vec{\tau}_{ab} d_{ib\alpha} \tag{2.22}$$

  here g is the electron-phonon coupling constant; $\vec{r_i}$ the vector which parameterizes the distortion and $\vec{\tau}_{ab}$ the Pauli matrixes in the orbital space.

- H_{ph} describes the independent lattice vibrations (phonons):

$$H_{ph} = \frac{1}{2} \sum_i K r_i^2 \tag{2.23}$$

  where K is the elastic constant of the harmonic oscillators.

The Hamiltonian is solved under the assumption of strong magnetic coupling between the spin core and the itinerant electron ($S_c \cdot J_H \rightarrow \infty$). Three behaviours are distinguished by Millis below the Curie temperature:

- weak coupling, $\lambda \ll 1$: there is a small lattice distortion even at low temperature and, as in metals, the resistivity grows linearly by lowering the temperature;

- intermediate coupling, $\lambda \approx 1$: there is a finite distortion even at T=0 but the amplitude of the distortion is not sufficient to localize carriers near the Fermi level. The resistivity grows when the temperature decreases but remains finite when reaching T=0 (like in metals);

- strong coupling, $\lambda \gg 1$: the distortion of the lattice due to the polaron formation is sufficiently important to open a gap in the spectral function. This induces an insulating behaviour : the resistivity becomes infinite when the temperature reaches 0.

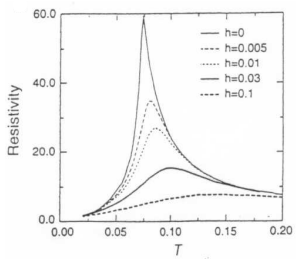

Figure 2.11: Expected resistivity in the Millis' model (double exchange + JT coupling). h is the applied magnetic field expresses as: h=$0.1T_c$.

Models which include electron-phonon interaction agree better with the experimental results: in Fig.2.11 the calculated resistivity is shown. To reproduce even better the real behaviour other ingredients should be taken into account. These are the on-site Coulombian interaction that enhances the localization of the carriers due to the strong Hund coupling; the so-called "breathing mode" distortion of the oxygen octahedra, which acts on the planar bonds; the phonon and the spin core quantum fluctuations and the phonon correlations between adjacent Jahn-Teller distorted sites [57].

Magnetic polarons

In 1960 de Gennes already considered the possibility that in magnetic materials the effect of charge localization is originated not only by the electron-phonon interaction (dielectric polaron) but also by the localization of charges whose magnetic moment polarizes the surrounding ions spin (magnetic polaron).

A charge carrier, belonging to the conduction or valence band in a semiconductor, can move through the crystal interacting with the magnetic moments of the lattice ions. This interaction usually has a ferromagnetic character, since the energy of the system is reduced in the case of parallel orientation of the spins. In 1979 Mott and

Davis described this phenomenon quantitatively. They considered the Hund coupling between the conduction electron and the on-site spin, J_1, and the interaction between spins belonging to different ionic sites, J_2. They considered the case $J_1 \gg J_2$, as occurs in manganites. The charge polarizes the surrounding magnetic moments in a region having radius r_p where it is localized. Thus the kinetic energy is

$$E_c = \frac{\hbar^2 \pi^2}{2m^* r_p^2} \tag{2.24}$$

while the total energy of the charge plus the ferromagnetic cluster it induces is given by:

$$E_{tot} = \frac{\hbar^2 \pi^2}{2m^* r_p^2} + \frac{4\pi r_p^3 J_2}{3a^3} - J_1 \tag{2.25}$$

where the second term represents the energy required to break an antiferromagnetic bonds in the volume $\frac{4\pi r_p^3}{3}$ and $-J_1$ the energy gained through alignment of the core spins with the conduction electron spin. Minimizing the energy with respect to r_p we find:

$$r_p^5 = \frac{\hbar^2 \pi a^3}{4m^* J_2} \tag{2.26}$$

that is the polarization effect of the charge increases with decreasing J_2. In this way the total energy becomes

$$E_{tot} = \frac{5\hbar^2 \pi^2}{6m^*} (\frac{4m^* J_2}{\hbar^2 \pi a^3})^{\frac{2}{5}} - J_1. \tag{2.27}$$

when this quantity is negative there is the formation of a magnetic polaron: inside it, the moments are parallel to the one of the charge. The spin lattice out of the polaron will experiment this cluster with a different ordering as a defect and it will create a distorted region surrounding the polaron, where the spins are tilted of a certain angle, in order to minimize the magnetic dipole energy ("spin canted"). The polaron's energy is strictly connected to the exchange interaction between the magnetic moment of the ions and the charge spin, which favors a FM arrangement. In this way FM domains form with radius r_p; the spin of the adjacent domains are not necessarily parallel among themselves: thus the charge is localized in each of these clusters until a magnetic ordering takes place in the whole system, due for example to a PM-FM or PM-AFM transition or to an external magnetic field which will inhibit the formation of magnetic polarons.

From a theoretical point of view, Roder et al. [75] studied the combined influence of double-exchange and Jahn-Teller coupling when a magnetic polarization exists in $La_{1-x}A_xMnO_3$ perovskites. They show that the strength of the JT coupling modifies the magnetic transition and is the cause, as it increases, of the decreasing of the maximum transition temperature one can obtain, as a function of the doping. When the temperature increases through T_c, the spin-polaronic effect increases the localization of the lattice polarons. At low temperature the magnetization, that is induced by the localized electron, is reduced to a small region surrounding the central site; at higher temperatures the disorder effects become more important and the magnetopolaron is even more localized, so that there is a reduction of the magnetization of the adjacent sites (small magnetic polaron). Basically, when T increases the dimensions of the magnetic domain reduce. Therefore the high-temperature regime is where magnetic correlations become negligible and electric charge-lattice interplay is dominant.

If the carrier, together with the associated crystalline distortion, is comparable in size to the cell parameter, the object is called a small polaron. The electron-phonon interaction has both a short and long range component. The short one is due to the interaction between the charges and the on-site crystalline field and gives rise to the formation of small polarons. The long range component is due to the Coulombian potential that couples the charge with electric dipoles of a ionic solid. This contribution gives rise to large polarons because the distortion is spread over more lattice sites. The large polarons have an itinerant character due to their small effective mass ($m^* \sim 2-4$) and the lattice distortion is extended over a wide spatial range. On the other hand, the small polarons could move only by tunnelling or thermally activated hopping between locally distorted lattice sites, because of the large effective mass ($m^* \sim 10 - 100$) and the distortion of the lattice extended over a domain of one or few atomic sites.

In manganites the situation is quite complex, because the presence of polarons is not only limited to the high temperature/paramagnetic phase. In fact clear evidences of the presence of polarons across the metal to insulator transition (and even well inside the metallic phase) exist.

2.1.5 XAS spectroscopy results

The EXAFS oscillations in the absorption coefficient of an atom give information about the local structure around the absorber, on the distances between the central atom and the surrounding atoms and on their number. The fine structures near the absorption edge moreover contain information about the electronic structure of the absorbing site

and the topology of the local surrounding. At even lower energy, in the pre-edge region, the information about the potential is contained (see Chapter 3).

In the following, a short review of the results obtained by means of XAS measurements on manganites is reported. In particular the EXAFS experiments concentrated on the local structural problem and the effects of disorder, while XANES analysis focused on the determination of the electronic structure and the valence state of Mn in $La_{1-x}Ca_xMnO_3$. The big question studied by XAS concerns the actual charge state of Mn in $La_{1-x}Ca_xMnO_3$. The main hypothesis about the manganese valence is: (i) the valence of Mn is the same for all the sites and intermediate between 3+ and 4+ according to the doping x; (ii) there are different percentages of Mn^{3+} and Mn^{4+} sites. From a theoretical point of view, these two situations should be distinguished by X-ray absorption spectroscopy, since in one case there is only one valence state, which should correspond to a unique absorption edge (only one resonance), while in the second situation one would expect two resonances, that is two different absorption edges corresponding to the Mn^{3+} and Mn^{4+} sites. Actually it is not so simple to discriminate between these two cases and the results are still ambiguous.

XANES

The analysis of XANES spectra is rather difficult, as we will see also in Chapter 3, since the low energy region of the spectrum contains the effect of all the scattering events subdued by the photoelectron (full multiple scattering). For this reason it is not possible to describe analytically all the fine structures of the spectrum. In literature, the XANES studies on manganites give in general a qualitative analysis of the spectra (Subìas et al., Booth et al., Tyson et al.), while only few quantitative studies were reported [74]. The work on these materials was aimed to determine the geometrical local structure around the manganese site and its charge distribution and the results obtains are often in disagreement among themselves.

In 1996 Tyson et al. [86] measured the absorption coefficient at the manganese K-edge in $La_{0.67}Ca_{0.33}MnO_3$ at temperatures above and below the critical temperature $T_c = 270$ K; they found an energy shift of the edge (Fig.2.12) when T varies from 293 K down to 80 K, that is the absorption peak moves towards higher energies as the sample is cooled. They interpreted this fact as the effect of changes in the local electronic structure and in the atomic structure through the transition. The Mn-O bond distance distribution found by Tyson is very different for $T < T_c$ or $T > T_c$ (see Fig.2.12) and this difference cannot be explained as the effect of thermic disorder, since

ligands have typical Debye temperatures of the order of 500 K. A possible explanation of the data could be that the distribution of the bond lengths for $T > T_c$ is not simply the consequence of the Mn^{3+} and Mn^{4+} sites distribution. On the contrary Booth et al. [10] did not observed any energy shift of the edge cooling the sample.

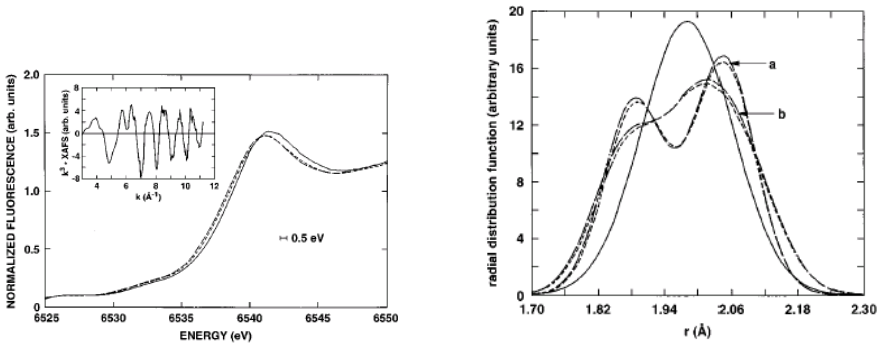

Figure 2.12: First picture: Mn K-absortpion edge at 80 K (continuous line), 273 K (short lines) and 293 K (long lines). Second picture: radial distribution of Mn-O at different temperatures.

A conclusion similar to that of Tyson was reached by Subìas et al.[80, 81, 82], who found a chemical shift of the edge position when the dopant concentration varies, for x between 0 and 1 (Fig.2.13). From this observation they deduce that the compounds are characterized by an intermediate valence of Mn. Anyway the chemical shift does not allow to discriminate between the existence of two different Mn ions (Mn^{3+} and Mn^{4+}) or a single Mn site which fluctuates between two states.

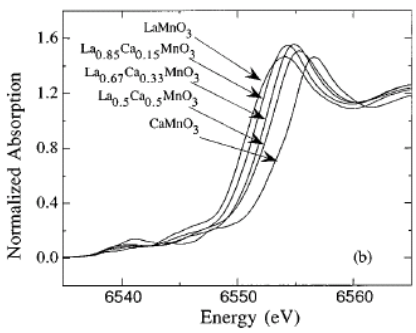

Figure 2.13: XANES spectra at the Mn K-edge at room temperature, for $La_{1-x}Ca_xMnO_3$(x=0, 0.15, 0.33, 0.5, 1).

In another work [31], in 2001, the authors find that the chemical shift is almost linear with the formal valence of Mn; they tried to reproduce the XANES data of

doped samples as the weighted sum of the spectra of the two end compounds and they obtained the correct edge position but with big differences in the slope of the spectrum. Moreover in the calculated spectra two structures appear in the main peak, that are not observed in the experimental data. This fact is in agreement with the hypothesis of a single electronic state, which gives rise, in the photoabsorption spectrum, to only one resonance with a width sharper than that calculated for a mixture of two atoms with different oxidation states. Their conclusion was that the electronic charge localization spreads upon more atoms, giving rise to the segregation of local phases and to molecular polarons or also to low-dimensional conductive states.

A study of the variations of the XANES features when T changes has been performed also by Garcìa et al.[31]. In this case they consider the x=0.33 compound at different temperatures (T=50, 140, 160, 170, 190, 210 K), comparing the spectra. They found that no significant change is evident through the MI transition, showing that the electronic structure of Mn remains unchanged through the phase transformation; they concluded that the MR and the MI transition are no driven by the charge localization on Mn atom.

It is noteworthy that in XAS studies the analysis of the electronic state of Mn ions is strictly connected to the local geometrical structure around Mn. In fact the local distorted structure of the Mn^{3+} ion, due to the Jahn-Teller effect, strongly modifies the charge distribution in the various phases. The XANES structures are dependent both on the local order and on the charge distribution around Mn, therefore it is very difficult to discriminate charge effects and structural ones. Booth et al. [10] tried to discriminate among different models based on charge and/or structural effects. They considered three possible models:

- JT distortions;
- charge disproportion (CD);
- ionic polaron (IP).

In a JT distortion every Mn^{3+} ion will have two O atoms at ~ 1.90 Å, two atoms at ~ 1.97 Å and two at ~ 2.15 Å; in the CD model a certain amount of Mn^{3+} ions separates into Mn^{2+} and Mn^{4+} ions (with $d_{Mn-O} = 2.18$ Å for Mn^{2+}, 1.99 Å for Mn^{3+} and 1.88 Å for Mn^{4+}); finally, in the IP model a very localized charge induces a symmetric distortions of the oxygens (breathing mode): in this case all the $Mn^{3+}-O$ distances are ~ 1.97 Å and the $Mn^{4+}-O$ are ~ 1.90 Å.

The authors considers first the simplest hypothesis: there are different manganese sites with valence +3 and +4. According to them, in the compounds with intermediate concentration the structure behaves as a linear combination of the end compound ($LaMnO_3$ and $CaMnO_3$), therefore the amount of the distortion is consistent with a model where the Mn^{3+} atoms, which are near La, have JT distortions, while the others are not deformed. Neither the CD or the IP model behaves in this way. To quantify the effect of the different distortions, Booth et al. used the FEFF6 [90] package to simulate the XAFS amplitude of the Mn-O peak in $LaMnO_3$(Fig.2.14): it is evident that the amplitude's trend in the CD, CD+JT or IP models is too different with respect to the JT one, therefore the CD, CD+JT and IP models are excluded as the main origin of the distortions.

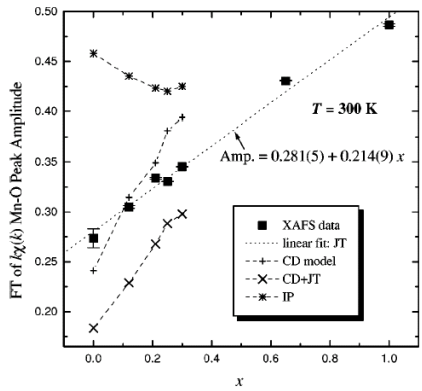

Figure 2.14: Mn-O peak's amplitude at T=300 K.

From their analysis the authors conclude that the distortions which are measured above T_c are local JT distortions around the Mn^{3+} atoms, even if a small contribution of CD effect (10%) cannot be excluded.

An important step towards the quantitative analysis of the XANES spectra have been carried out by Quian et al. in 2001 [51], who calculated theoretically the absorption coefficient of $LaMnO_3$(both distorted and undistorted) and $CaMnO_3$to determine the octahedron's structure of MnO_6. The simulations of the absorption coefficient were calculated using the RELXAS software [87]; the potential is determined for perovskite structures with 142 atoms, with a non-selfconsistent method, and in muffin-ton approximation. The XANES spectra are calculated for atomic clusters made of 7, 21, 51 and 87 (or 85 for distorted $LaMnO_3$) atoms. The calculations take into account also the hybridization effects by means of the overlapping of the adjacent atoms' potential. They compared the ideal perovskite model of $LaMnO_3$(d_{Mn-O} = 2.018 Å)

with a distorted structure ($d_{Mn-O} = 1.968, 1.907, 2.178$ Å) and then these two models with the orthorhombic structure of $CaMnO_3$($d_{Mn-O} = 1.895, 1.900, 1.903$ Å). They observe (Fig.2.15) that the main peak appears in clusters with at least 21 atoms for the undistorted $LaMnO_3$ and 51 for $CaMnO_3$and $LaMnO_3$ JT-distorted; moreover in the case of $LaMnO_3$ cubic and $CaMnO_3$ it is sharp and narrow, while in distorted $LaMnO_3$ it is less intense and more broadened. By comparison of these simulations with the experimental spectra they concluded that the JT distortions are fundamental to determine the shape of the edge. Also from the pre-edge region they obtained useful information about the electronic structure: the calculations for undistorted $LaMnO_3$ give only one sharp peak before the edge, which represents the absorption from an e_g state, whereas the simulations for JT-distorted $LaMnO_3$ show a splitting of e_g into two levels, in agreement with the experimental data.

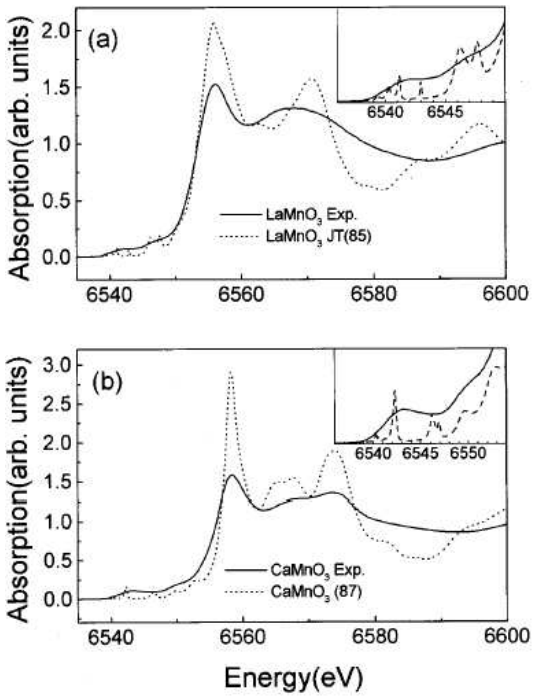

Figure 2.15: Comparison between the experimental spectrum (continuous line) and the simulated ones for $LaMnO_3$(a) and $CaMnO_3$(b).

The analysis of the XANES spectra I will show in Chapter 5 is developed in this framework, since it starts from the results of Quian et al. and aims to determine the structural features of $LaMnO_3$ and $CaMnO_3$ by means of calculations of the XANES spectra at room temperature. Our approach, however, is innovative because we performed fittings of the experimental data, using a recent software named MXAN [5, 6,

7]. In this way we are able to refine the structural and potential parameters previously obtained from diffraction experiments, by means of an optimization procedure. This method allows to gain the structural information about the local surrounding of the Mn atoms in $LaMnO_3$ and $CaMnO_3$ in a more complete way, since the XANES spectra reflect not only the pairs distribution function of the Mn absorber and its surrounding atoms, but also the topology of the structure around Mn (distances and angles).

EXAFS

Many EXAFS papers dealt with the local structure around the manganese atom in $La_{1-x}Ca_xMnO_3$. In 1998 Subìas et al. [81] showed that in the ferromagnetic-metallic phase the Mn ion is surrounded by a regular oxygen octahedron with a Debye-Waller factor σ^2_{Mn-O} similar to the $CaMnO_3$ one, where the JT distortions are absent. Anyway, other authors (Meneghini et al. [52], Booth et al. [10] and Lanzara et al. [43]) concluded that distortions remain in the low-temperature phase but much reduced with respect to the high-temperature state. It should be noted that, although all of them reached similar conclusions, their works strongly differ about the microscopic interpretation of the results.

Meneghini investigated the local structure surrounding Mn in samples with x=0.2 and x=0.4, varying T. They used a single coordination shell model to describe the data with an increasing Debye-Waller factor. This parameter showed a peculiar temperature dependence, with respect to that of MnO and $LaMnO_3$: in the doped compounds there is an evident change at the transition temperature, that is not explained by means of a simple Debye model (or Debye plus a static disorder). The anomalous deviation of σ^2_{Mn-O} from the expected trend was interpreted as the consequence of the formation of small polarons in the PMI phase.

From the analysis of samples with x=0.21, 0.25, 0.3, Booth et al. conclude that at low temperature (50 K) almost the 70% of the distortions have been removed. In the $CaMnO_3$ instead they find the same Mn-O distance through the transition. Finally, in 1998 Lanzara et al. try to quantify the octahedral distortion in $La_{0.75}Ca_{0.25}MnO_3$ in a wide range of temperatures. They find an asymmetric Mn-O distribution: at low T, the distribution has two distances at $R_1 \sim 1.92$ Å and $R_2 \sim 2.01$ Å; at T=170 K a third contribution appears, at $R_3 \sim 2.13$ Å, whose weight increases until T=240 K; in the same interval the second peak decreases until it reaches the same weight of the third one. The authors describe the local structure around the absorber for $T < T^*$ ($200K < T^* < T_c$) by means of octahedra with four 1.92 Å bonds in the

plane and two 2.01 Åbonds along the apical axis, therefore there would be only a small JT distortion. In the insulating phase, instead, the system is more distorted, with a longer ligand in R_3: according to them this lattice distortion is connected to small polarons. They conclude that the CMR transition presents simultaneously large and small polarons (Fig.2.16). Actually, even if this model is very good, the experimental data have been probably overestimated.

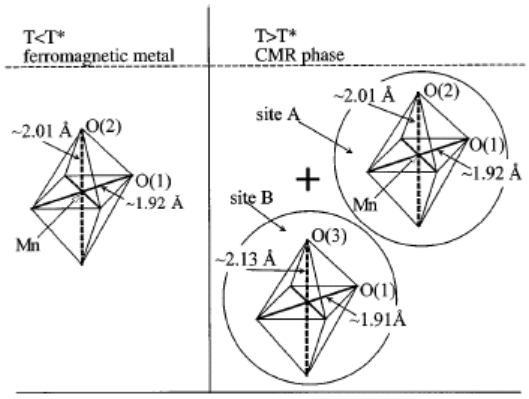

Figure 2.16: Local distortions of MnO_6 in the metallic and insulating phases [43].

Another important aspect of $LaMnO_3$ is studied in a very recent paper by M.C. Sánchez et al. [76]. The authors study the structural phase transition of $LaMnO_3$ at T_{JT}=750 K, above which the orbital ordering disappears. In order to analyze the JT distortion below and above the transition, they measure the absorption spectra of Mn K-edge in $LaMnO_3$ from 300 up to 920 K. From the XANES region they observe that the spectra at different temperatures are alike, indicating that no large changes of the local electronic structure occur between 300 and 920 K. The largest difference in the pre-edge and XANES spectra corresponds to the 650K-750K temperature range, close to T_{JT}, giving direct signature of the phase transition. The analysis of the EXAFS spectra shows that there is not discontinuity crossing T_{JT}, indicating a similar local structure for the Mn^{3+} ions above and below T_{JT}. The EXAFS spectra show that the MnO_6 octahedra are tetragonally distorted both for $T>T_{JT}$ and for $T<T_{JT}$: this fact means that below T_{JT} the tetragonal local distortion is ordered in space and gives rise to the known Pbnm crystallographic structure, while above T_{JT} the local distortions are dynamically distorted and the average lattice is cubic. Thus the phase transition at T_{JT} can be classified as an order-disorder phase transition, where the statistical occupation in the disordered phase corresponds to the three possible orientations of the

tetragonal distortions on each octahedron. A very important point is that the authors conclude that the orbital ordering proposed for $LaMnO_3$ origins from the ordering of local JT distortions and they exclude a direct electronic origin for orbital ordering, such as the cooperative Jahn-Teller mechanism with simultaneous local distortion. In this framework, the conduction mechanism cannot be considered as polaronic, because the e_g electron jumps between the degenerate three orbitals on each Mn^{3+} for $T>T_{JT}$ and can also jump to the orbitals of the nearest neighbour Mn because of the covalent Mn-O bond. At $T<T_{JT}$, instead, the e_g electrons are ordered and localized and they cannot jump between adjacent octahedra.

2.2 Vanadium sesquioxide

The metal-insulator phase transition in vanadium sesquioxide (V_2O_3) has been largely studied in the last fifty years, both from a theoretical and an experimental point of view. Metal-insulator transitions and phase transitions, in general, have always attracted great interest, since the explanation of the driving mechanisms of these phenomena enlightens us on the nature of the forces in play. A good theory of a phase transition, in fact, must not only explain the mechanisms that drive the transformation, but it must also identify the physical properties of both the phases involved. The great interest in the V_2O_3 system is due to the large number of phase transitions it shows as a function of temperature, pressure and dopant content (for instance Cr, Ti, etc.), as it will be shown later on.

In the forties a first-order metal-insulator transition was observed in V_2O_3 as the temperature was lowered below 160 K and some years later Mott advanced a theory of this transition, arguing that it would be possible for a metal to transform into an insulator simultaneously with the onset of magnetic order when the distance between the atoms in the lattice increases.

By 1970 there was a large number of experimental work which led to a debate about the transition mechanisms, even though a detailed microscopic picture of the Mott theory didn't exist yet. About that time V_2O_3 began to be doped with other $3d$ transition metals, in order to induce variations in the lattice parameters and study the effects on the transition. For instance, the system doped with Ti showed exactly the same behaviour as the pure system under hydrostatic pressure; doping with Cr acted as a negative pressure on the lattice. However, the effects of doping on the phase transitions were much more complex than expected, so that a big experimental effort

continued on this problem. In the meanwhile, several theories have been elaborated to explain the experimental evidences. Nevertheless the description of the driving forces involved in the transitions observed in these systems is still incomplete.

2.2.1 Phase diagram: pure and doped V_2O_3

The phase diagram of V_2O_3 (Fig.2.17) [48] is characterized by three different regimes. At the lowest temperatures the material is stable in a monoclinic antiferromagnetic ordered phase (AF) and it is insulating. At about 160 K this phase transforms to a metallic one with trigonal symmetry and without any magnetic order. Then, at ~550 K the new phase undergoes another change to a second metallic phase with no variation of lattice symmetry.

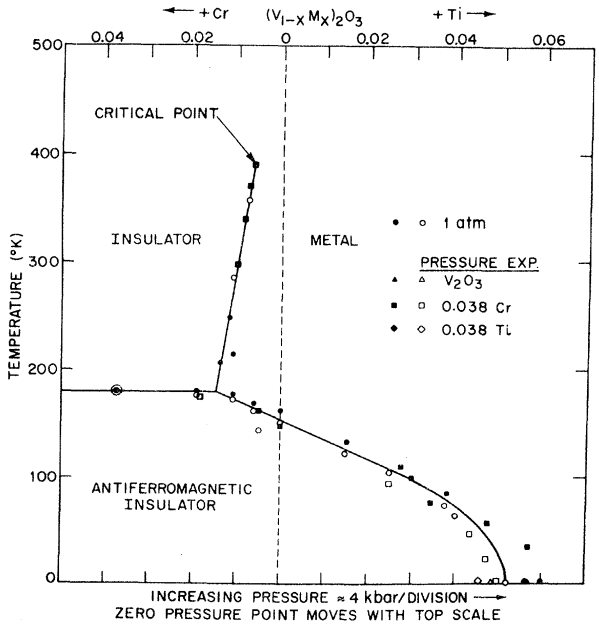

Figure 2.17: Phase diagram of V_2O_3 as a function of temperature, pressure and dopant concentration [51].

The presence of an antiferromagnetic order in the insulating (low temperature) phase was definitely showed by Moon [66] using polarized neutron scattering. As the temperature is raised above 160 K, the resistivity of the crystal decreases by eight orders of magnitude [41], the monoclinic structure changes to a higher symmetry trigonal one [17] and the magnetic order disappears. This metallic (M) phase is isostructural with $\alpha - Al_2O_3$ (corundum). Dernier and Marezio studied the relation between the low and room temperature phases, showing that as the material is cooled below the

transition, each of the three equivalent $(110)_H$ axes in the hexagonally indexed trigonal cell becomes an unique $(010)_M$ axis in the monoclinic cell; therefore at low temperature there are three unique but spatially related monoclinic domains.

As the temperature is raised above 550 K, the resistivity shows a gradual increase related to a second transition to another metallic state (M'). In this case the transition is not coupled to any structural or magnetic transformation (see fig.2.18).

The addition of a small amount of chromium in V_2O_3, which substitutes some vanadium atoms, deeply affects the electrical properties [37]. At low temperature, the resulting $(Cr_xV_{1-x})_2O_3$ alloy for x up to ~ 0.3 is only slightly modified: it is monoclinic and presents the same magnetic arrangement of the undoped compound. On the other hand even a small percentage of Cr has a large effect on the phase between 160 K and 500 K.

For low Cr concentrations ($0.005 < x < 0.03$) an AFI phase to a M phase transition is observed, as in pure V_2O_3; as the dopant level is increased, the phase transition temperature also increases, while the variation of the resistivity through the transition decreases. At higher T, a second transition to a second non magnetic insulating state appears. The temperature of this M-I change depends on the Cr concentration. For concentration $x \geq 0.03$, a drop in resistivity at approximately 175 K of one order of magnitude is observed, while the system goes directly from the AFI phase to the I one and no M phase appears (fig.2.18).

There are similarities between doping with Cr and the application of a negative pressure. In fact, the application of a pressure on pure V_2O_3shifts the phase transition toward lower temperatures and the AF phase is completely suppressed by a pressure of ≈25 kbar. In the case of a 4% Cr-doped sample the needed pressure is ≈40 kbar, that is the doping acts as a negative pressure [50, 48]. As a matter of fact, in this sample an I-M transition occurs, at 298 K, at ≈10 kbar. Below 10 kbar there is an I-AF transition on cooling, while at pressures above 10 kbar there is a M-AF transition (fig.2.19).

If the dopant of $V_2O_3$is titanium, the transition temperatures are affected as well: at increasing Ti concentrations, the M-AFI phase transition temperature decreases; for x>0.055 the M state is stabilized and the AFI phase is completely suppressed (fig.2.17). Moreover, as T_{M-AFI} decreases, the jump in resistivity is reduced [51, 79].

Finally, if the stoichiometry of the $V_2O_3$is not perfect (for example, there are oxygen excess or metal deficiency) the transition temperature changes with respect to the pure compound: the M-AFI transition occurs at lower temperatures and for an excess of

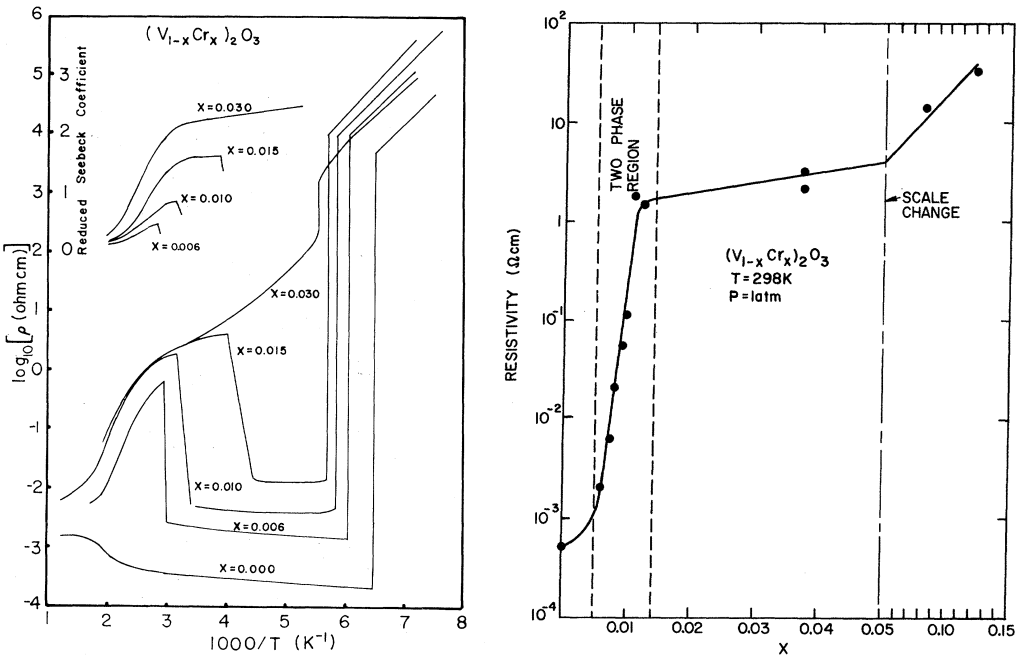

Figure 2.18: a) Resistivity vs 1000/T for some Cr-doped samples [41]; b) Resistivity vs Cr concentration at room temperature. The dashed lines indicate the two-phase region [49].

oxygen greater than 1% there is not transition at all [42]. The difference respect to the case of Ti-doping is that the discontinuity of the resistivity is bigger when the transition temperature is depressed. However, all the samples -pure or doped- have a common aspect: the AFI phase always has a monoclinic unit cell, whereas all the other phases (I, M or M') present a trigonal lattice symmetry without any long-range magnetic order.

2.2.2 Physical properties of pure and doped V_2O_3

Crystallographic structure and lattice properties

From a structural point of view, V_2O_3shows two different crystallographic symmetry. The high temperature phases (M, M' and I) have a corundum trigonal R3c lattice symmetry, similar to other metal sesquioxide systems such as $\alpha - Al_2O_3$, Fe_2O_3, Ti_2O_3 and Cr_2O_3. The corundum structure presents an approximate hexagonal close packing of the V atoms; the oxygens form an octahedron around the V sites; only $\frac{2}{3}$ of the octahedra centers are occupied by the metallic ion. The V atoms can be considered coupled to form dimers along the hexagonal c-axis (fig.2.20). The parameters of the hexagonal structure are found to be, at room temperature, a_H=4.95 Å, c_H=14.00 Å,

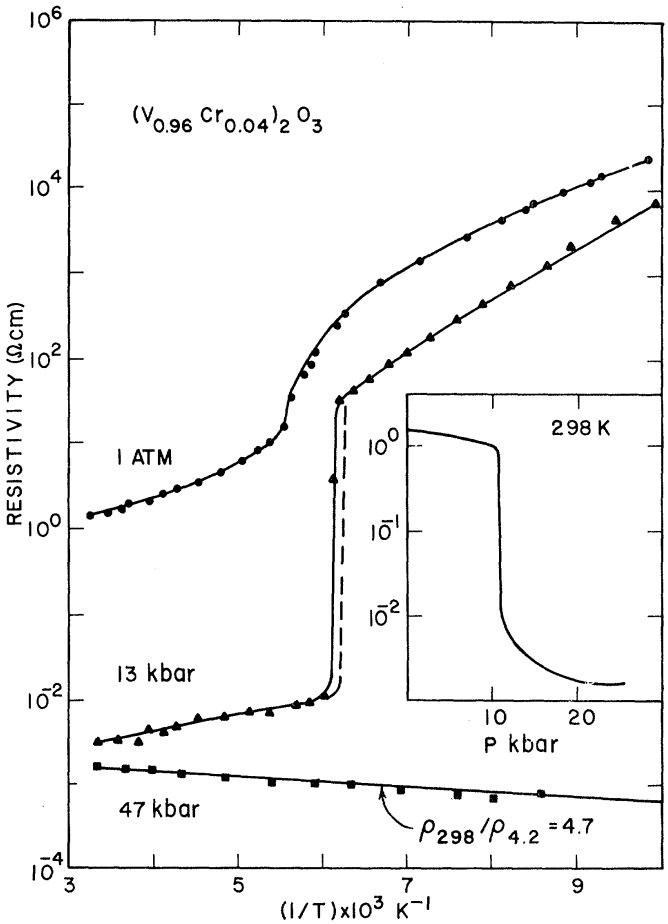

Figure 2.19: Resistivity vs 1000/T at different pressures for 4% Cr-doped V_2O_3. Inset shows I-M transition at 298 K as a function of pressure.

$\alpha = \beta = 90°$ and $\gamma = 120°$ [18, 29].

Pure V_2O_3[48] at room temperature shows a large value of the c/a ratio, which is anomalous compared to the other metal oxides with the same symmetry: it is 2.83, almost 4% larger than in corundum, for instance. McWhan et al. studied the behaviour of this c/a ratio as a function of temperature, Cr or dopant transition metal concentration. They found that the $(V_{1-x}Cr_x)_2O_3$ samples show a sharp drop in the c/a value (from 2.83 to 2.78, see also ref.[18]) and a volume expansion of 1% at x=0.009. The c/a ratio then decreases smoothly down to a value of 2.74 as the Cr concentration increases up to 100 per cent. Moreover anomalies occur in the ratio of the lattice parameters of the corundum structure by doping with the transition metals (fig.2.21, inset).

As said before, using X-ray diffraction techniques it was determined [18, 17] that, at the transition to the AFI phase, the trigonal unit cell having R3c symmetry undergoes a monoclinic distortion and the space group which best describes the unit cell is I2/a

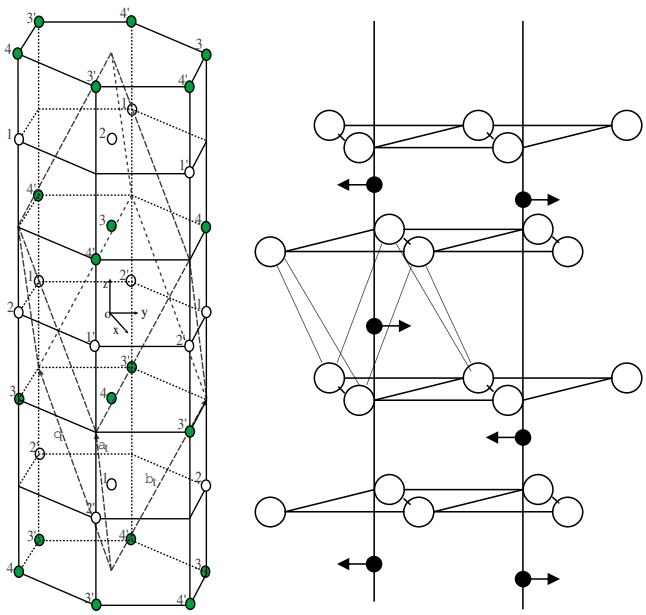

Figure 2.20: A schematic view of the V_2O_3lattice. a)The hexagonal (non primitive) cell and the trigonal (primitive) cell (inside). b) The vertical lines point along the c-axis and sheets of oxygen atoms (empty circles) lie in the basal plane. During the transition to the AFI phase the V atoms (plain circles) move as indicated by arrows: this movement is equivalent to the rotation of the V-V pairs respect to the c-axis by 1.8°.

(fig.2.22). at the transition, when the temperature decreases, the c-axis contracts and the a-axis expands but the V-V distance along the c-direction is actually about 5% larger than in the trigonal symmetry (∼2.74 Å). The metal-metal distances across the shared octahedral edge (within the $a_M - c_M$ plane) increases from ∼2.88 Å to ∼2.99 Å. The V-V distances between vanadium atoms belonging to the $a_M - c_M$ plane and those in adjacent layers do not change significantly. The distortion mechanism is a rotation of V pairs within the $a_M - c_M$ plane of approximately 1.8°. The pairs of V ions can rotate in three equivalent hexagonal-cell directions and this threefold degeneracy leads to the observation of the twinning of the monoclinic cell. Actually, if we consider the basal plane of the hexagonal cell, the monoclinic distortion corresponds to the elongation of one of the three equivalent V-V distances, while the other two remain almost unchanged (see fig.2.22).

Although individual V-O distances vary considerably, the overall average V-O distances slightly increase from 2.00 to 2.02 Å.

The monoclinic cell (body-centered) of the AFI phase in V_2O_3can be obtained from the hexagonal cell by the matrix

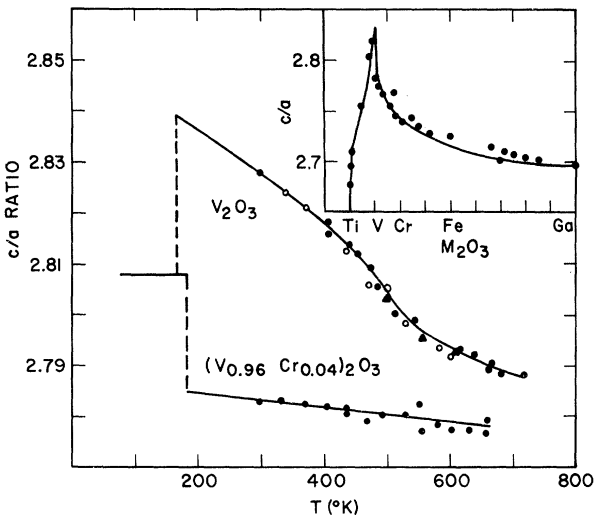

Figure 2.21: c/a ratio vs temperature for $V_2O_3$and 4% Cr-doped V_2O_3. Inset shows c/a ratio vs transition metal for corundum structure [48].

$$\begin{pmatrix} \vec{a}_M \\ \vec{b}_M \\ \vec{c}_M \end{pmatrix} = \begin{pmatrix} \frac{2}{3} & \frac{4}{3} & \frac{1}{3} \\ 1 & 0 & 0 \\ \frac{1}{3} & \frac{2}{3} & -\frac{1}{3} \end{pmatrix} \begin{pmatrix} \vec{a}_H \\ \vec{b}_H \\ \vec{c}_H \end{pmatrix}$$

with $\vec{a}_M$=7.255 Å, $\vec{b}_M$=5.002 Å, $\vec{c}_M$=5.548 Å and $\beta = 96.75°$ [17]. Corresponding to the lattice change at the M-AFI transition, there is also a big change in volume, since the cell's volume of the AFI phase is about 3.5% larger than the one of the M phase. This big variation in the volume causes samples to crack up on cycling through the M-AFI transition.

In Cr-doped specimens, as already said, the M, M' and I phases are trigonal. In samples where the AFI-M transition occurs, the lattice changes follow those in pure V_2O_3 and the lattice parameters are also very similar to the M phase in the undoped material. The volume of the I phase is also similar to that of the AFI phase, greater than the volume in the M state of about 1.5%. For this reason in samples where the transition to the I state occurs directly from the AFI phase the problem of sample cracking is no longer as severe, since the change in the unit cell volume is not as drastic as at the AFI-M change.

It is clear that the lattice structure and its dynamics play a significant role in these phase transformations. However, there are also other interactions that contribute to the features of this phase diagram.

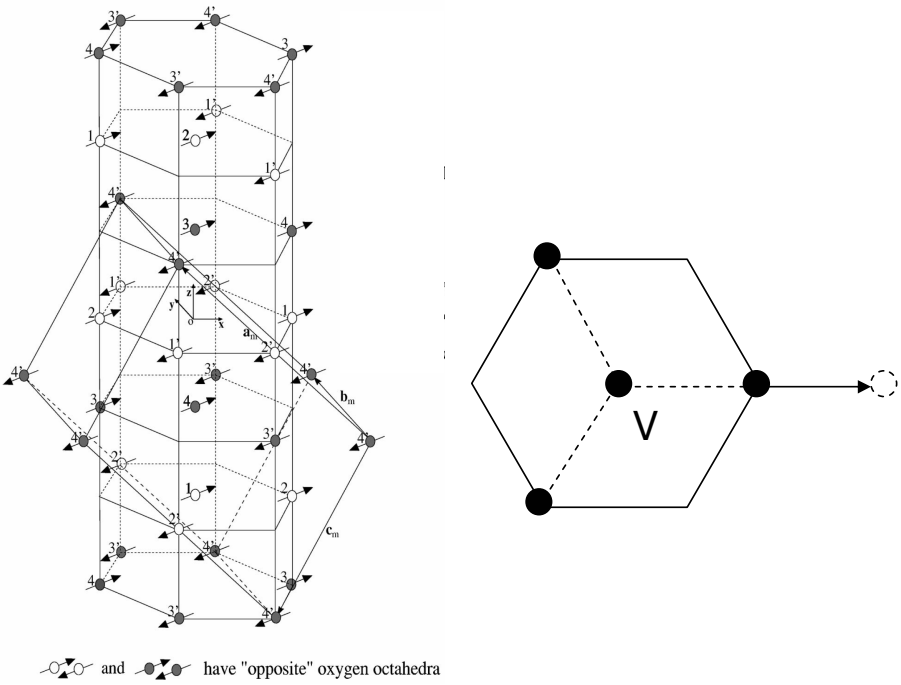

Figure 2.22: a) Corundum structure together with the unit cell for the monoclinic phase. b) The displacement of one of the three V atom in the basal plane in the monoclinic phase.

Magnetic properties

The magnetic order in V_2O_3at low temperature occurs in all compounds (pure or doped) that undergo a metal-insulator transition. Although early NMR [39] and Mössbauer [78] investigations provided evidence for magnetic ordering, the identification of a magnetic phase in V_2O_3 was controversial until the definitive experimental results by Moon in 1970 [66], who used polarized neutron scattering techniques to distinguish between nuclear and magnetic effects. In conventional neutron diffraction, in fact, it is not possible to definitely identify magnetic peaks when the magnetic transition occurs simultaneously with a structural one. On the other hand, the use of a polarized beam allows to detect separately neutrons which flip their spin on scattering (magnetically scattered neutrons) and those which do not.

The magnetic structure of V_2O_3 is unique among transition metal oxides, because a magnetic moment of $1.2\mu_B$ per V atom is observed as a saturation value, oriented about 71° from the hexagonal c-axis. The magnetic ordering-at low temperature- consists of ferromagnetic planes perpendicular to the b_M-axis (all the magnetic moments in these planes are parallel each other) and the planes along the $(110)_H$ are stacked antiferromagnetically, so that the space group of the AFI cell is $I2/a$. A published study

[89] reports the observation of intensity on the $(3/2\ 3/2\ 3)_H$ Bragg peak, indicative of a symmetry lower than the I2/a; however, this extra intensity is small.

Because of the magnetic order which sets in below the transition temperature, the monoclinic cell becomes primitive, due to the AF coupling of the magnetic moments on the V ions connected by the body-centered translation. In this situation the time-reversal operator $\hat{T}$ followed by the non-primitive translation $\frac{1}{2}(\vec{a}_m + \vec{b}_m + \vec{c}_m)$ is a symmetry operation of the magnetic structure, for this reason the magnetic point group is $C_{2h} \otimes \hat{T}$. As we shall see in next sections, this description of the magnetic order is not coherent with some reported experimental results [33].

From the phenomenological point of view, in pure V_2O_3 the magnetic transition is first-order and the intensity of the magnetic diffraction peaks reaches about 90% of its saturation value almost instantaneously. As T is lowered further below T_{M-AFI}, the intensity increases gradually. The first-order onset of magnetic long range order is observed in all samples which undergo the M-AFI transformation. On the contrary, in Cr-doped samples for which the transition to the AFI phase occurs directly from the I state, the magnetization sets in more gradually, even if the magnetic structure and the value of the ordered moments are the same as in V_2O_3. The Neel low temperature transition T_N, which coincides with the metal-insulator transition (M to AF) and associated crystallographic distortion, is shifted to higher temperature with increasing Cr content. Moreover, a hysteresis of about 12 K occurs at the M-I transition [54]. In addition, the susceptibility also shows anomalies for $T>T_N$. In the range 160 K-400 K the susceptibility obeys a Curie-Weiss law and neutron scattering results are consistent with a paramagnetic state in the M phase. For T in the range 500 K-650 K another Curie region exists and the only difference with the previous region is a small difference in the effective momentum for the M' phase.

It is clear that the role of electron correlations is basic in these systems, because one-electron band-structure calculations predict a metallic state for both the trigonal and the monoclinic crystal structures [65, 47].

Electronic structure

Vanadium has an electronic $3d^3 4s^2$ configuration. In V_2O_3 three electrons are engaged in forming bonds with the $2p$ states of the oxygens, so two magnetic electrons remain for each 3+ cation. The immediate surrounding of metal ions has an almost octahedral symmetry with point group O_h (6 oxygen atoms around V ion): in this symmetry the d orbitals split into t_{2g}-threefold and e_g-twofold symmetry levels. A slight trigonal

distortion and the influence of more distant cations in the lattice reduces the point group symmetry to D_{3d}, lifting the three-fold degeneracy of the t_{2g} orbitals. In this way the electronic configuration presents a higher non-degenerate a_{1g} orbital and a lower, doubly degenerate e_g orbital, separated by the distortion energy Δ_t (fig.2.23). The situation we just described should be exact from a theoretical point of view, nevertheless this electronic structure cannot explain all the phenomena occurring in V_2O_3 when the temperature changes. When the temperature is lowered the structural transition occurs and the magnetic order (AF) breaks the original trigonal symmetry. The electronic structure also must change, but it is not clear how it is influenced by the transition. Many different theoretical models have been considered to explain all the anomalous properties of this transition and the phase diagram, but nowadays a complete model which is able to explain all the experimental data and the complex phenomenology of the system V_2O_3 is still missing. In the following I will shortly report various attempts to elaborate a general theory of this system, which would describe the actual electronic structure of V_2O_3 and would explain all the aspects of the observed phase transitions.

2.2.3 Theoretical models

The first attempt to give a realistic description of this system , to explain the magnetic properties and the phase diagram, was performed by Castellani, Natoli and Ranninger [12, 13, 14], who realized that the peculiar structure observed in the AFI phase cannot be explained in terms of a single band Hubbard model and that it is necessary to introduce additional degrees of freedom in the model, taking into account the orbital degeneracy of the atomic $3d$ states involved. They considered a generalized Hubbard model for electrons in a twofold degenerate atomic state, because in $V_2O_3$the magnetic electrons belong to a degenerate atomic state.

Since the trigonal field splitting of the degenerate t_{2g} level is much smaller than the cubic splitting between t_{2g} and E_g levels (fig.2.23), the authors take the two e_g and the a_{1g} orbitals for each cation as the Hilbert subspace in which the Hamiltonian has to be diagonalized. In other words, the field operator is expanded in terms of a complete set of Wannier Functions of e_g and a_{1g} symmetry:

$$\psi_\sigma(\vec{x}) = \sum_{m=1}^{3} \sum_{j} w_j^m(\vec{x}) c_{jm\sigma} \tag{2.28}$$

where j runs over all the cation sites and $w_j^m(\vec{x})$ is the Wannier function centered on

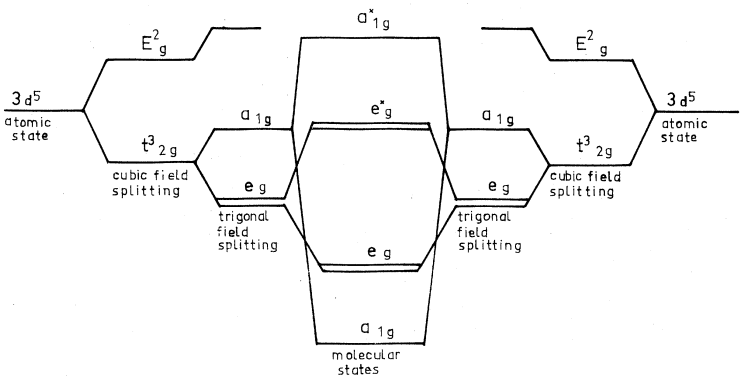

Figure 2.23: Schematic energy splitting of the $3d$ level in the corundum structure and formation of a stable bond between the a_{1g} orbitals of a vertical pair of cations [12].

site j and of symmetry type m. The Hamiltonian is written as:

$$H = \sum_{\sigma} \psi_{\sigma}^{+}(\vec{x})[-\frac{\hbar^2}{2m}\nabla^2 + V(\vec{x})]\psi_{\sigma}(\vec{x})d^3x + \frac{1}{2}\sum_{\sigma}\psi_{\sigma}^{+}(\vec{x})\psi_{\sigma'}^{+}(\vec{x'})V(\vec{x}-\vec{x'})\psi_{\sigma'}(\vec{x'})\psi_{\sigma}(\vec{x})d^3xd^3x' \tag{2.29}$$

where V is the potential of the Coulomb interaction among the electrons. In a Hubbard type approximation the authors retain in the interaction part of the Hamiltonian only terms on the same lattice site; in such a way the general Hamiltonian becomes:

$$\begin{aligned} H = &\sum_{jj'}\sum_{mm'\sigma} t_{jj'}^{mm'} c_{jm\sigma}^{+} c_{j'm'\sigma} + \frac{1}{2}\sum_{j}\sum_{mm'}\sum_{\sigma\sigma'}[(1-\delta_{mm'}\delta_{\sigma\sigma'})U_{mm'}n_{jm\sigma}n_{jm'\sigma'} \\ &-\delta_{\sigma\sigma'}(1-\delta_{mm'})J_{mm'}n_{jm\sigma}n_{jm'\sigma} - (1-\delta_{mm'})(1-\delta_{\sigma\sigma'})J_{mm'}c_{jm\sigma}^{+}c_{jm\sigma'}c_{jm'\sigma'}^{+}c_{jm'\sigma} \\ &+(1-\delta_{mm'})(1-\delta_{\sigma\sigma'})I_{mm'}c_{jm'\sigma'}^{+}c_{jm'\sigma}^{+}c_{jm\sigma}c_{jm\sigma'}] \end{aligned} \tag{2.30}$$

The first term in this expression corresponds to the hopping of an electron from the m' orbital belonging to the j' atom to the m orbital on j atom, without any change in spin; the other terms are different from zero if at least the orbitals or the spins are different ($m \neq m'$ or $\sigma \neq \sigma'$). The explicit expressions of t, U, J and I are:

$$t_{jj'}^{mm'} = \int w_j^m(\vec{x})H_0(\vec{x})w_{j'}^{m'}(\vec{x})d^3x, \tag{2.31}$$

$$U_{mm'} = \int |w_j^m(\vec{x})|^2 V(\vec{x}-\vec{x'})|w_j^{m'}(\vec{x'})|^2 d^3xd^3x', \tag{2.32}$$

$$J_{mm'} = I_{mm'} = \int w_j^m(\vec{x})w_j^{m'}(\vec{x})V(\vec{x}-\vec{x'})w_j^m(\vec{x'})w_j^{m'}(\vec{x'})d^3xd^3x'. \tag{2.33}$$

To simplify the solution of the problem, the authors consider that the corundum structure favors pairings of the cations along the z axis (*molecular approach*). In this way they assume that one a_{1g} electron per site is involved in a covalent non-magnetic bond between the vertical cations pairs (along z), whereas the other electron remains in a doubly-degenerate band that determines the magnetic structure (fig.2.23).

To apply the effective Hamiltonian to the particular case of V_2O_3, the authors have to specialize the value of the relevant transfer integrals to the symmetry of interest and to limit the parameters they consider to only nearest and next-nearest neighbors interaction, so that one atom interacts with only four neighboring atoms. To solve the problem they use a variational procedure taking a trial wave function of the type

$$|\Psi\rangle = \prod_j |\psi_j\rangle|\phi_j\rangle \tag{2.34}$$

where $|\psi_j\rangle$ refers to orbital occupancy on site j and $|\phi_j\rangle$ to spin occupancy on site j. Then they minimize the average value of the Hamiltonian in the state (2.34) with respect to $|\psi_j\rangle$ and $|\phi_j\rangle$. The calculation shows that the coupling along the z direction is antiferromagnetic in the orbital occupancy (that is the orbitals are occupied in an alternate way). The electrons can in this way minimize the kinetic energy and at the same time give up a little repulsive energy when two electrons happen to occupy the same site. The relative magnitude of the various transfer integrals may be essential to determine the actual orbital and spin ordering in the lattice. In this way the authors obtained a general phase diagram of V_2O_3, a plot of the region of stability of some orbital and spin structures as a function of the parameters appearing in H_{eff} (fig.2.24).

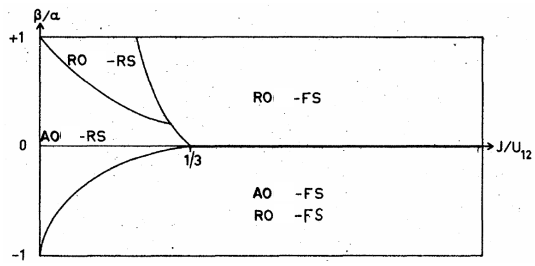

Figure 2.24: Phase diagram obtained from the CNR model for the orbital and spin ordering in the corundum structure in the atomic limit for first and second-nearest neighbors interactions: Fs, AS and RS stand for FM, AF and "real" spin structure (actual spin configuration realized in V_2O_3). AO and RO stand for AF and real orbital order [12].

In a second work [13] Castellani, Natoli and Ranninger attempted a more "realistic" calculation of V_2O_3, starting from the results of the first paper, considering the effect

of the O ligands [12]. Actually they try to achieve "realistic" results by introducing the complex band structure of the magnetic $3d$ electrons in the t_{2g} subband and takeing into account the role of the "diamagnetic" ligands. They succeeded to give a reasonable realistic calculation only in the low temperature AFI phase; however, from a correct interpretation of this AFI state, they obtained also valuable information about the correlations between electrons in the metallic phase.

Covalency effects are very important in determining the effective hopping rate of the electrons from site to site and can be a significant source of hopping between sites. The point of view adopted in this model to include the effect of the oxygen lattice on the magnetic electrons of the V atoms is based on the molecular orbital picture. In this description the a_{1g} electrons are engaged in a covalent bond in the vertical pairs, so they are nonmagnetic. Therefore only one magnetic electron is left on the V atom in an $e_g(\pi)$ state; there remains an empty $e_g(\pi)$ state nearly degenerate with the $e_g(\pi)$ occupied one and two empty $e_g(\sigma)$ states on the metal ion: there are two occupied σ orbitals which can make transitions to the empty metal orbitals of the same symmetry and one π orbital which can make transitions to the empty metal orbital of the same symmetry.

The conclusion of this study was that for reasonable values of the Hubbard parameters (U and J) the observed spin structure of V_2O_3together with an antiferromagnetic orbital order gives the lowest Hartree-Fock ground-state energy and shows a gap in the density of states. The value $J/U_1 \approx 0.2$, where U_1 is the intra-atomic Coulomb parameter within the same orbital, marks the transition between a V spin $S = \frac{1}{2}$ configuration and the $S = 1$ one. At the time of that work the possibility of S=1 was discarded in favor of the spin S=1/2 solution. The experimental data which show that the real state has S=1 in fact at that time were not available. Another aspect of this solution is the orbital ordering. The orbital ordering, referred to V_2O_3, is an ordered distribution of the electrons in the degenerate orbitals. This aspect will be treated in next paragraph .

Another more recent approach to the calculation of the electronic structure is the LDA+U method, that is not based on a molecular picture of the system but uses bands calculation. Using this method, Ezhov et al. [24] found that the model based on $S = \frac{1}{2}$ spin does not describe the metal-insulator transition.

According to the authors the small bandwidth of the a_{1g} levels would invalidate a molecular orbital-like approach such as the CNR one. They performed LDA+U calculations for different magnetic structures, since the important feature of the LDA+U

result is that the electronic structure strongly depends on the magnetic structure. Calculations were performed for both the monoclinic and trigonal structures, thus obtaining a description of the main properties of the AFI and PI phases. In contrast to the previous results [12], in both phases the electronic configuration is predominantly of the $e_g e_g$ type (which is in-plane symmetric and orbitally non-degenerate, but still with the complex real AFI magnetic structure), that is there are two d-electrons of V^{3+} occupying the doubly degenerate e_g orbitals, with only a small admixture of $e_g a_{1g}$. In addition the spins of the two electrons are parallel, leading to a high spin $S = 1$ local moment. The consequence is that there is not orbital ordering.

An intermediate approach between those of CNR and Ezhov et al. is the one followed by Mila et al. [55], who start from an atomic limit, considering first V-V pairs because the inter-site a_{1g} hopping matrix elements are the largest.

Since experimental evidences [4] indicate that the vertical bond is quite stable and coupled to total spin $S_{tot} = 2$ with non polar part of the orbital wave function, they consider a strong Hund's coupling ($J \sim 0.8eV$), as proposed by Ezhov, which leads to molecular orbitals for a V-V pair, consisting of a superposition of $(e_g e_g)$ on one V site and of $(e_g a_{1g})$ on the second site with a total spin $S = 2$. The atomic configuration is a mixture of $(e_g e_g)$ and $(e_g a_{1g})$. This delocalized molecular orbital has also a twofold degeneracy due to a choice in $(e_g a_{1g})$ among the e_g doublet. This means that there is an orbital degree of freedom which corresponds to choose between e_{g1} and e_{g2} for the V-V pairs. The physical picture that emerges from this model is promising because the observed magnetic arrangement is consistent with the calculated one and there is an orbital degree of freedom whose ordering is consistent with monoclinic distortion of the low temperature phase.

However, there still remain problems. The stability region of the magnetic phase is very small in the parameter space and the percentage of occupancy of the $|a_{1g}\rangle$ with respect to the $|e_g\rangle$ in the molecular state is different from that obtained experimentally [69]. Owing to these considerations, in 2002 Di Matteo et al. [19] reexamined the microscopic Hubbard Hamiltonian used to describe the ground state of V_2O_3 and studied the strong coupling limit of this Hamiltonian with three bands containing two electrons per site coupled to spin $S = 1$, following the patterns developed in [12] for $S = \frac{1}{2}$. They believe in fact that the LDA and LDA+U schemes are unable to catch the physics of V_2O_3.

According to their model, it is possible to construct the zeroth-order Hilbert subspace using only triplet states. The total ground state of H_0 can be written as a product

of the atomic states over the entire crystal:

$$|\Psi_0\rangle \equiv \prod_{j=1}^{N} |\alpha_j\rangle, \tag{2.35}$$

where $|\alpha_j\rangle$ denotes the degenerate atomic state on site j with spin $S = 1$ and N is the total number of sites. The perturbation H' partially removes the degeneracy of the $|\alpha_j\rangle$. Each atomic state $|\alpha_j\rangle$ can be characterized by two quantum numbers: the spin S and the pseudospin τ, an operator which describes the orbital occupation. Due to the ninefold degeneracy of each $|\alpha_j\rangle$ it is necessary a representation with both total $S_j = 1$ and $\tau_j = 1$. In this way it is possible to rewrite the effective Hamiltonian in terms of the spin and pseudospin operators. For the pseudospin quantum number τ_z there is no conservation law in the hopping process, whereas the spin part retains the usual spherical symmetry. The magnetic properties of the system are strongly affected by the orbital degrees of freedom because they determine the sign and the order of magnitude of the exchange constants and the authors show that it is impossible to obtain the ground state of each single bond in a configuration of total spin $\vec{S}_i + \vec{S}_j = 1$.

When the molecular correlation energy is greater than the exchange in-plane energy, the orbital part of the wave function (neglecting for the moment the spin degeneracy) for the doubly degenerate ground state can be written with $\tau_z^M = \pm 1$:

$$|\psi_{\pm}^{o}\rangle_{ab} = \frac{1}{\sqrt{2}}(|\pm 1\rangle_a |0\rangle_b + |\pm 1\rangle_b |0\rangle_a) \tag{2.36}$$

In this way the energy lowering of the ground state is due to three processes: the virtual hopping back and forth of an e_g electron, the same process for the a_{1g} electron and a sort of correlated hopping in which the e_g electron jumps from the a to the b atom while simultaneously an a_{1g} electron jumps from b to a, and vice versa. This latter phenomenon is due to the "entangled" orbital nature of the molecular state (eq.2.36). This implies that the molecular correlation energy is much bigger than the in-plane exchange energy and the best variational wave function for the entire crystal must be constructed in terms of molecular states. Di Matteo et al. found out that if the correlation energy is much higher than the interaction in the basal plane, then the appropriate variational wave function must be constructed in terms of molecular units, that is the crystal consists of some ordered sequences of molecular units, whose internal energy is so high that it is more convenient for the system, from the energetic point of view, not to break this structure. Otherwise, if it is the exchange energy in the basal plane to be bigger than the correlation energy, then the correct wave function is written in terms of single site atomic states.

They found also that the ratio $J/U_2 \approx 0.4$ almost marks the transition from a stable antiferromagnetic in-plane spin structure to a ferromagnetic one. This behaviour happens because for a low value of J the system tries to maximize the number of electron jumps (which occur more easily in an AF structure) with respect to the on-site Hund's energy gain, whereas for high J this last mechanism is dominant.

Finally, a very complete theoretical study has been performed by Tanaka [83], who improved the results of Di Matteo et al. [19] by the introduction of the spin-orbit interaction in the model Hamiltonian. He uses the molecular picture (the V atoms are coupled two by two along c_h), the a_{1g} orbitals point in the c_h direction and form tight molecular bonds σ, whereas the lower e_g states extend the lobes in directions perpendicular to c_h and give rise to π ligands with the three V atoms in the plane. Due to the Hund's coupling, the total spin on each V atoms is $S = 1$ because they use $J = 0.65$ eV. The choice of $J \sim 0.2$ eV in Castellani et al. [12] makes them find $S = \frac{1}{2}$, instead. When they study the occupation number of the a_{1g} orbital in the PM phase as a function of the intensity of the trigonal field, they found that in the range of interest for the value of the trigonal field (that is when the a_{1g} and the e_g become almost degenerate) the ground state is a superposition of the $(e^\pi e^\pi; e^\pi a_{1g})$ and $(e^\pi a_{1g}; e^\pi e^\pi)$ states, where the first two orbitals refer to the first V atom and the other two to the second V atom in the couple. In this case the wave functions which describe the fundamental state are degenerate and can be written as follows:

$$|g+\rangle = \frac{1}{\sqrt{2}}(|e^\pi_{+\uparrow} a_{1g\uparrow}; e^\pi_{+\uparrow} e^\pi_{-\uparrow}\rangle + |e^\pi_{+\uparrow} e^\pi_{-\uparrow}; e^\pi_{+\uparrow} a_{1g\uparrow}\rangle) \tag{2.37}$$

$$|g-\rangle = -\frac{1}{\sqrt{2}}(|e^\pi_{-\downarrow} a_{1g\downarrow}; e^\pi_{+\downarrow} e^\pi_{-\downarrow}\rangle + |e^\pi_{+\downarrow} e^\pi_{-\downarrow}; e^\pi_{-\downarrow} a_{1g\downarrow}\rangle) \tag{2.38}$$

where $\uparrow$ or $\downarrow$ means $s_z = \pm\frac{1}{2}$, whereas $|e^\pi_\pm\rangle = \frac{1}{\sqrt{2}}(\mp|e^\pi_u\rangle - i|e^\pi_v\rangle)$, where u, v indicate two different types of base functions, on each atom, with e symmetry; these states have the property: $\langle e^\pi_\pm|L_z|e^\pi_\pm\rangle = \mp 1$.

From the model Tanaka found out that the degeneration of the ground state is magnetic, therefore there is no orbital degree of freedom. If we compare this model with the one of Mila et al. or Di Matteo et al. [55, 19], who did not take into account the spin-orbit interaction among the $3d$ electrons, the wave functions of Tanaka for the ground state can be rewritten in terms of the wave functions given in the other model: if ψ_1 and ψ_2 are the states in which the orbital degree of freedom is separated by the spin degree of freedom (no spin-orbit coupling),

$$\psi_1 = \frac{1}{\sqrt{2}}(|e_u^\pi a_{1g}; e_u^\pi e_v^\pi\rangle + |e_u^\pi e_v^\pi; e_u^\pi a_{1g}\rangle) \tag{2.39}$$

$$\psi_2 = \frac{1}{\sqrt{2}}(|e_v^\pi a_{1g}; e_u^\pi e_v^\pi\rangle + |e_u^\pi e_v^\pi; e_v^\pi a_{1g}\rangle) \tag{2.40}$$

the states of Tanaka become $|g_\pm\rangle = \frac{1}{\sqrt{2}}(-i\psi_1 \pm \psi_2)$.

In the AFI phase, the spin-orbit interaction strongly affects the ground state; the occupation numbers of the e_u and e_v orbitals, in fact, change considerably with or without the spin-orbit coupling of the $3d$ electrons on the V site and there is an immediate effect on the problem of orbital ordering. The conclusion by Tanaka, in fact, excludes the possibility of orbital ordering in V_2O_3, therefore experimental data which have been interpreted as the effect of orbital ordering, as we will see in the next section, must be examined by the light of this consideration.

2.2.4 The problem of Orbital Ordering

The term "orbital ordering" is used in conjunction with different phenomena. In the case of V_2O_3, orbital order regards the distribution of orbital occupation; in fact the removal of the degeneration of the molecular orbitals, due to the spin-orbit interaction, makes possible for the electron to occupy only one particular orbital.

In other cases, as in manganites, the orbital order corresponds to a particular spatial distribution of the charges: that is, the orbitals have particular orientations with a certain spatial periodicity.

Orbital ordering in V_2O_3 has a rather formal meaning, because it corresponds to determine in which orbital the unpaired electron settles. In this picture the determination of orbital ordering in V_2O_3 corresponds to understand how to write the ground state of the system. Recently, the debate about the presence of orbital ordering in V_2O_3 has grown after some experimental evidences on its existence by Resonant X-ray Scattering. This technique is able to give direct information on magnetic and orbital order. RXS is sensitive to the occupancy of electronic orbitals because it probes the symmetry of empty electronic states through resonant multipole electric transitions: the variation of the resonant scattering cross section with the direction of the incident polarization reflects the spatial symmetry of ordered orbitals. The possibility to observe orbital ordering (OO) in $V_2O_3$by RXS was suggested by Fabrizio et al. [25] who predicted the dependence of the resonant Bragg reflections on the polarization of the incident radiation and on the azimuthal angle of the scattering plane.

In 1999 Paolasini et al. [67] presented resonant x-ray scattering (RXS) experiments at the K edge of vanadium in V_2O_3, showing the existence of orbital order in this system and providing information on the kind of ordering. In fact the resonance at the vanadium K edge provides observable cross sections due to the ordering of the $3d$ V states. If h, k, l are the monoclinic Miller indices, the Bragg peaks due to the crystal structure follow the selection rule:

$$h + k + l = even \tag{2.41}$$

Since the vanadium sites form ferromagnetic planes, with magnetic moment tilted away from the trigonal c axis, the resulting magnetic structure is such that the magnetic Bragg peaks (h, k, l) satisfy a different extinction rule:

$$k - l = odd \qquad \text{and } h = even \tag{2.42}$$

In the monoclinic phase the resonant scattering experimental data show the presence of two different sets of Bragg reflections, which are forbidden according to the first selection law (2.41). The first set satisfies the second rule (2.42), therefore these peaks have magnetic origin. The second set of peaks, instead, follows the rule

$$k - l = even \qquad \text{and } h = odd. \tag{2.43}$$

These peaks are observed both in the $\sigma-\sigma$ and $\sigma-\pi$ polarization channels.The authors associate these extra Bragg reflections with the long-range order of orbital occupancy in V_2O_3, because the observed propagation wave vector is one of the possible solutions suggested in [12, 13, 14] and the energy dependence points to the d orbital ordering of vanadium orbitals as the origin of the scattering; moreover the angular dependance of the resonant intensity presents similarities with the theoretical calculations of the work by Fabrizio et al. [25].

On the contrary, the analysis performed by Tanaka [83] contested these results. Using the theory explained above, the author studies theoretically the dependence of the intensity of the reflection (1,1,1) on the azimuthal angle ϕ in the AFI phase for different value of the crystal field parameter. The dependence on ϕ is greatly influenced by the direction of the orbital magnetic moment. In the presence of the $3d$ spin-orbit interaction, spin and orbital degrees of freedom are strongly coupled and this removes the orbital degeneracy of the ground state, resulting in no orbital ordering. As a consequence, the peak observed by Paolasini t al. must have magnetic origin: it is the ordering of the orbital part of the magnetic moment. Also Lovesey et al. [44, 45]

had already interpreted the forbidden Bragg reflections as due to scattering originating only from the orbital component of the magnetic moment. Moreover, if the spin-orbit interaction is not considered in the theory, Tanaka finds that the scattering intensity for the reflection is zero, even if in this case a ferro-orbital molecular order should exist in the ground state, as found in [55]. Therefore this reflection has a pure magnetic origin and derives from the AF order.

2.2.5 Experimental evidences on local structure in V_2O_3

The relevant role of possible electron-lattice interactions has been stressed by recent theoretical work [83], because it is not clear whether electronic correlations alone can completely account for the metal-insulator transition in V_2O_3. To completely understand the interplay of structural and electronic degrees of freedom, both information on the global structure (by X-Ray Diffraction measurements) and on the local structure of the compound are required. Interatomic distances and symmetries, in fact, can deviate locally from the long-range symmetry, therefore indicating the presence of an order-disorder component in the transitions or of structural fluctuations. An open problem is the understanding of the temperature evolution of the local structure in the vicinity of the transition, as shown hereafter.

XAFS and RXS results

The local structure can be studied by X-ray Absorption Fine Structure (XAFS) method. A XAFS study was performed by Frenkel et al. [30], who made fits on absorption spectra of V_2O_3at various temperatures and found that the local structure of the samples is monoclinic also above the phase transition temperature. The experimentally observed decrease in volume of the system was explained mainly by the shortening of the V-V vertical distances in the monoclinic unit cell. The average trigonal structure, instead, was explained as resulting from an averaging over unoriented monoclinic regions, which are so small, that do not produce sharp monoclinic diffraction peaks. In this frame, while the monoclinic region size is big enough to be detected by diffraction in the AFI phase, it changes abruptly above the transition. Therefore, according to the authors, there is a significant order-disorder component in the transition.

In a very recent work Pfalzer et al. [70] studied V_2O_3 using the Extended X-ray Absorption Fine Structure technique (EXAFS), investigating the presence of precursory elements in the vicinity of the transition. They show that structural changes precede the changes in transport and magnetic properties. Their analysis of the po-

larization dependence reveals that two distinct distortions with different temperature dependencies must be distinguished: one is due to the movement of the vanadium ions within the basal plane and the other concerns the change of the V-V pair distance along the c_h axis. The first movement determines the rotation of these V pairs, which are parallel to c_h in the PM phase and tilted away from this axis in the AFI state. They observe a continuously increasing tilt, starting above the metal-insulator transition and continuing also in the AFI phase. According to the authors the V-V distance (vertical) expands after the tilt of the pair has adopted its maximum value. Moreover they also find that on a local scale the trigonal symmetry is not fully recovered in the metallic phase, thus meaning the trigonal and monoclinic structures are very close in energy, allowing fluctuations between the two. In conclusion, they can distinguish between two structural effects with different temperature characteristics: at the onset of the electronic and magnetic transition temperature, the next vanadium neighbours along the c axis abruptly increase their distance; however, a continuous increase of the monoclinic distortion in the basal plane is already observed far above the MIT reaching its maximum value at the onset of the electronic and magnetic transition. As we will see in the last chapter of our work, the results found by Pfalzer et al. are at least in part in contrast with the ones found by means of our analysis on Cr-doped V_2O_3 absorption spectra. Recently, an RXS experiment [9] has presented very interesting features about the presence of forerunners of the transition in Cr-doped V_2O_3. They mainly analyzed the resonant scattering in both the PI and AFI phases of the system. When they observe the forbidden reflection $(0\ 0\ 3)_h$ in the PI phase, they tune the energy of the incident photons in correspondence of the quadrupolar channel E_2, $1s \rightarrow 3d$, and they find that a large signal is present also at higher energies, corresponding to the dipolar transitions (dipolar channel E_1, $1s \rightarrow 4p$). To interpret the data they assume that the dipolar signal is due to the presence, above the transition temperature, of a second phase of lower symmetry, which could be monoclinic. To study the symmetry of this phase they perform azimuthal scans and compare the angular dependence of this signal with the one of the quadrupolar signal. In this way they find that the dipolar signal is completely independent of the azimuthal angle, whereas the quadrupolar signal still reminds the six-fold azimuthal dependence of the trigonal symmetry. Instead when they consider the low temperature phase, this reflection is allowed in the monoclinic structure in both the dipolar and quadrupolar transitions and the new symmetry is revealed in the change in the azimuthal dependence of the two signals, which are both two-fold. A possible explanation for the different azimuthal dependence of the dipolar channel

below and above the transition, is that the diffracted intensity in the long range ordered AFI phase originates from one specific monoclinic domain, whereas above the transition temperature there are three almost equipopulated pseudo-monoclinic domains and the expected signal becomes a constant.

The hypothesis of the existence of the pseudo-monoclinic domains is just a possible solution to the problem of the presence of the dipolar signal even at high temperature. These domains must be interpreted as dynamical distortions of the V-V bonds in the hexagonal plane and each domain corresponds to the elongation of one of the three V-V distances. In this frame the frequency of the distortions should be too high to be detected by XRD, that would reveal only the average static corundum structure.

Another significant feature that emerges from the work by Bombardi et al. [9] regards the temperature dependence of the integrated intensity of the peak at the dipolar position: while the integrated intensity at the E_2 position is almost constant, when cooling the sample in all the range of temperatures 190-270 K, and decreases abruptly near to the transition T_N, the integrated intensity at E_1, instead, increases by one order of magnitude when T decreases, then close to the first-order transition there is a sharp increase again by one order of magnitude. A possible explanation could be that the distortion of the pseudo-monoclinic domains starts above the transition temperature, therefore there are precursory elements of the transition. This is very peculiar of Cr-doped V_2O_3, because in the pure system these phenomena have not been observed.

Chapter 3

The Multiple Scattering theory for X-ray radiation spectroscopy

Spectroscopies are among the most widely used techniques to investigate the physical and chemical properties of materials and now are largely present in many field of science such as physics, chemistry, biology, etc. Spectroscopies are based on the interaction of incident particles (photons, atoms, neutrons, electrons, ions) with a sample and on the analysis of the outgoing particles. Depending on the type of spectroscopy, this provides information on the crystallographic, electronic or magnetic structure of the sample. In this chapter I will restrict to some spectroscopies in which the incident particle are photons, in particular X-ray photons. The main physical processes that happen when the photon beam hits the target are represented schematically in fig.3.1.

Historically, electromagnetic radiation has been largely used to investigate the properties of matter in its different physical states. The coupling constant between radiation and matter is very small ($\alpha = 1/137$), therefore measurements can be interpreted in the framework of the linear response theory. Moreover the system is weakly perturbed by the electromagnetic field and it is possible to study the properties of the unperturbed system. The use of synchrotron radiation (SR) has given a great contribution to the study of matter by X-rays and stimulated the interest in new spectroscopic techniques that make use of the unique properties of this radiation such as its high brilliance, intensity, polarization and high collimation. In next sections I will focus on X-ray Absorption Spectroscopy (XAS), which gives information on the geometrical and electronic structure of a system, even if it does not show long range spatial order. The XAS technique, in fact, uses the strong coupling of the emitted photoelectron with atoms to gather information about the surrounding of the absorber atom.

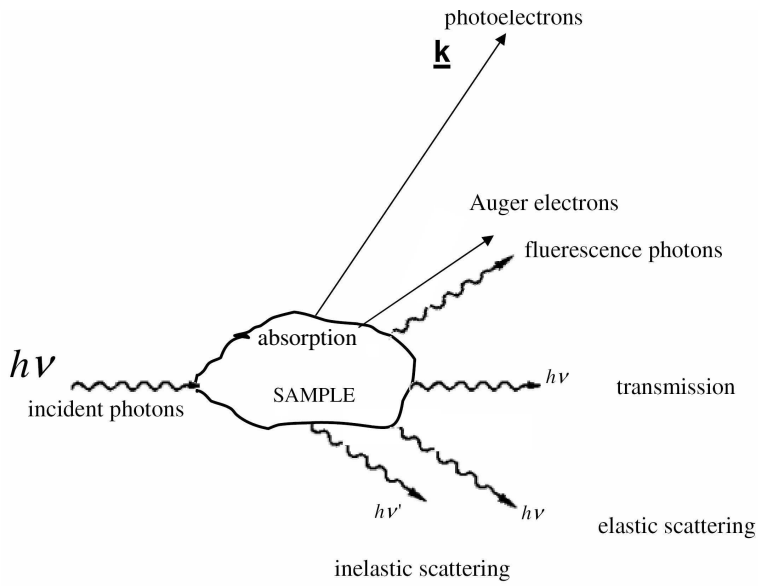

Figure 3.1: The different physical processes deriving from the interaction of an X-ray photon beam with matter.

As illustrated in Fig.3.1, part of the incident photons is absorbed in the sample and, if the beam is collimated and monochromatic, the intensity of the outgoing radiation from an infinitesimal thickness dx of the sample is proportional to the initial intensity and to dx: $dI = -\mu I dx$. This means that the beam intensity has an exponentially decreasing behaviour when the photons go through a material of thickness x, of the type $I = I_0 e^{-\mu x}$, where μ is the absorption coefficient and depends on the photon energy. Also other processes like elastic and inelastic scattering, photoemission, photons and electrons decay take place together with absorption. All these physical processes are part of the same phenomenon and consequence of the interaction between matter and radiation. In the case of XAS, the absorption coefficient contains the physics of the system, because it is related to the absorption cross section $\sigma_{ass}(E)$:

$$\mu(E) = n_{abs}\sigma_{ass}(E), \tag{3.1}$$

where n_{abs} is the density of absorbing atoms. Using the *Fermi golden rule* the cross section is given by:

$$\sigma(E) = 4\pi^2 E\alpha \sum_f |\langle\psi_f|\hat{\epsilon}\cdot\vec{r}|\psi_i\rangle|^2 \delta(E - E_f + E_i) \tag{3.2}$$

where $E = \hbar\omega$ is the photon energy and ϵ the polarization vector.

Generally, the information contained in the recorded spectra cannot be extracted

directly from them with enough accuracy, which can only be achieved through the systematic comparison to spectra calculated assuming a postulated structure. As it is evident from eq.3.2, we must know the initial and final wave functions to calculate the spectra. Multiple Scattering (MS) theory allows to write these wave functions, by solving the Schroedinger equation, taking into account the interactions of the photoelectron with the surrounding atoms.

3.1 The Multiple Scattering method

The Multiple Scattering (MS) theory is the base of a cluster approach useful to describe a variety of structural techniques, like photoelectron diffraction, electron diffraction, x-ray scattering, x-ray absorption, etc. A common aspect of all these spectroscopic techniques is the presence of a quasi-free electron in the final state, whose wave function is described by the MS method, that calculates it through an effective Schroedinger equation with an optical potential. The main advantage of such a unitary approach is the possibility of comparing the various techniques in a very direct way: it becomes also the evident the common origin of all those phenomena, based on scattering or absorption of photons. By the application of the MS method, in fact, it becomes clear that the various spectroscopies investigate different aspects of the same physical process.

Moreover the use of complex optical potentials - of the Hedin-Lunqvist type - for electron self-energy, whose imaginary part describes the inelastic losses of the electron in the final state and automatically takes into account the finite mean free path of the electron probe.

In the following I will describe in some details the MS theory in a non-relativistic approach; this is not a limitation because relativistic effects can be taken into account very easily. All the calculation details are developed in App.A.1.

3.1.1 The wave function for a single scattering center

The MS theory calculate the electronic structure of polyatomic molecules and solids in real space, without the need of any spatial symmetry or translational invariance. The method is based on the division of the system in subsets (clusters), which can be a whole polyatomic molecule, part of a molecule or part of a solid. Each cluster is divided in three geometrical different but contiguous regions (Fig.3.2):

- **atomic region**: spherical region centered on each atom of the cluster;

- **interatomic region**: region between the atomic sphere and the outer sphere that contains the whole molecule;
- **extra-molecular region**: external region outside the outer sphere.

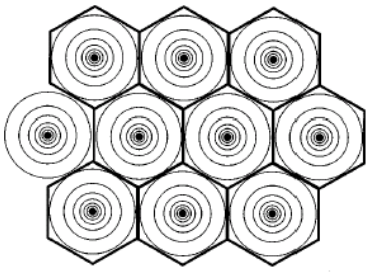

Figure 3.2: Partition of the solids in different but contiguous regions.

The Schroedinger equation is solved in each region, then the wave functions, along with their derivatives, are matched at the boundaries of the different regions of the cluster. The boundary conditions contain the information about the effects of the local environment on the cluster. In an ordered crystal the polyatomic cluster can be chosen as the unitary cell: in this way the boundary conditions on the wave functions are exactly the Bloch's conditions and the theoretical model reduces to the bands theory [61]. Anyway, the theoretical formalism is suitable for many problems related to the structure of complex systems, because the boundary conditions are chosen according to the problem and it is possible to treat even clusters with a high number of atoms.

The MS gives a set of secular equations and by solving them the energies and wave functions of the molecular orbitals can be obtained, using an iterative self-consistent procedure.

If we first consider the case of a single scattering center, the Schroedinger equation to be solved is the following:

$$(\nabla^2 + E - V(\vec{r}))\psi_k = 0, \tag{3.3}$$

where $V(\vec{r})$ is the potential due to the scattering center (atom or cluster) and ψ_k the single particle wave function. For the sake of simplicity we will assume the potential is spherically symmetric: this hypothesis is good for core states in the atom, whereas the potential of valence states does not show a spherical symmetry. Moreover we suppose that V is short-ranged so that in this approximation (muffin-tin approximation) the potential V in the atomic region is $V(r) \neq 0$, for $r < r_s$, whereas $V(r) = 0$ in $r > r_s$.

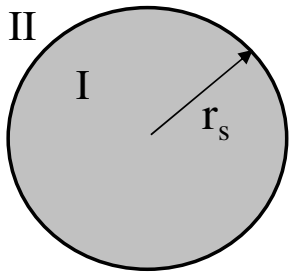

Figure 3.3: Muffin-tin approximation: inside the region with $r < r_s$ the potential is non zero, whereas it is zero for $r > r_s$.

In this way it is possible to rewrite the radial part of the Schroedinger equation, because the potential depends only on r:

$$[\frac{1}{r^2}\frac{\partial^2}{\partial r^2} + \frac{2}{r}\frac{\partial}{\partial r} - \frac{L^2}{r^2} + E - V(r)]\psi_k = 0 \tag{3.4}$$

and there are two solutions depending on the value of $V(R)$, that must match on the boundaries: ψ_k^I and ψ_k^{II} (fig.3.3). The total wave function will be the sum of the two partial solutions. Since in region II the potential is zero, the solution for $r \to \infty$ is the free wave function, that is it contains spherical waves:

$$\psi_k \sim e^{i\vec{k}\cdot\vec{r}} - f(\vec{k},\hat{r})\frac{e^{ikr}}{r}. \tag{3.5}$$

The two solutions thus become:

$$\psi_k^I(\vec{r}) = \sum_L 4\pi i^l R_l(r) Y_L(\hat{r}) C_L Y_L(\hat{k}) \tag{3.6}$$

$$\psi_k^{II}(\vec{r}) = \sum_L 4\pi i^l Y_L(\hat{k})[J_L(\vec{r}) - ikt_l H_L^+(\vec{r})]. \tag{3.7}$$

Here $L = (l, m)$; $Y_L(\hat{r})$ are the spherical harmonics solutions of the non-radial part of the Schroedinger equation, whereas $R_l(r)$ are the radial solutions in the case of $V \neq 0$; $Y_L(\hat{k})$ are the solid harmonics; C_L are coefficients that must be determined by the matching conditions between ψ_k^I and ψ_k^{II} and t_l are the scattering amplitudes which represent the strength of the scattering potential. The functions $J_L(\vec{r})$ and $H_L^+(\vec{r})$ are related to the Bessel j_l and Hankel h_l^+ functions through the spherical harmonics:

$$J_L(\vec{r}) = j_l(kr)Y_L(\hat{r}) \qquad \text{and } H_L^+(\vec{r}) = h_l^+(kr)Y_L(\hat{r}).$$

The Bessel functions j_l are regular solutions in the origin $r = 0$ of the free Schroedinger equation and they show a plane wave behaviour, whereas the Hankel functions h_l^+ are irregular in the origin and for $r \to \infty$ behave as spherical waves.

Since the total wave function and its first derivative must be continuous, we impose these conditions and determine the scattering amplitudes:

$$t_l = \frac{W[j_l, R_l]}{[-ikh_l^+, R_l]} = -\frac{1}{k} e^{i\delta_l} sin\delta_l \tag{3.8}$$

where δ_l is the phase shift due to the scattering potential: the effect of the scattering potential is to shift the phase of each outgoing partial wave. If the potential is real, the phase is real, otherwise δ_l becomes complex and a damping factor appears in the scattering amplitude. The coefficients C_L are:

$$C_L = \frac{t_l}{r_s^2 W[j_l, R_l]_{r_s}}, \tag{3.9}$$

where $W[j_l, R_l] = j_l R_l' - R_l j_l'$. Using the renormalization $\bar{R}_l = \frac{R_l}{r_s^2 W[j_l, R_l]_{r_s}}$, we can rewrite

$$\psi_k^I(\vec{r}) = \sum_L 4\pi i^l \bar{R}_l(r) Y_L(\hat{r}) t_l Y_L(\hat{k}). \tag{3.10}$$

The differential cross section, using the *Fermi Golden Rule*, for the photoemission process can be written using the wave function just found:

$$\begin{aligned} \frac{d\sigma}{d\hat{k}} &= 4\pi\alpha\hbar\omega \sum_{m_0} |\psi_k(\vec{r})\langle|\hat{\epsilon}\cdot\vec{r}|R_{l_0}^{core}(r) Y_{l_0 m_0}(\hat{r})\rangle|^2 \\ &= 4\pi\alpha\hbar\omega \sum_{m_0} |\sum_{lm} \langle \bar{R}_l(r) Y_{lm_i}(\hat{r}) t_l 4\pi i^l Y_L(\hat{k}) | r Y_{1m_i} | R_{l_0}^{core}(r) Y_{l_0 m_0}(\hat{r})\rangle|^2. \end{aligned} \tag{3.11}$$

By the separation of the integrals on r and Ω the differential photoemission cross section can be rewritten as follows:

$$\frac{d\sigma}{d\hat{k}} = 4\pi\alpha\hbar\omega \sum_{m_0} |\sum_L M_{Ll_0} C(L, 1m_i, L_0) i^l Y_L(\hat{k}) t_l(E)|^2 \tag{3.12}$$

where $M_{Ll_0} = \int_0^{r_s} dr r^3 \bar{R}_l(r) R_{l_0}^{core}(r)$ is the dipole matrix element and $C(L, 1m_i, L_0) = \int d\Omega Y_L(\hat{r}) Y_{lm_i}(\hat{r}) Y_{l_0 m_0}(\hat{r})$ gives the dipole selection rules. Since the selection rules allow just $l = l_0 \pm 1$ and taking into account the fact that the $l = l_0 + 1$ is the most probable channel, one can neglect the interference between the two channels and rewrite the cross section as follows:

$$\frac{d\sigma}{d\hat{k}} = 4\pi\alpha\hbar\omega \sum_{m_0} |M_{l_0,l_0+1} C(l_0+1m, 1m_i, l_0m_0) i^l Y_{l_0+1m}(\hat{k}) t_{l_0+1}(E)|^2. \tag{3.13}$$

The M_{l_0,l_0+1} amplitude has a very weak dependence on the energy E, whereas all the structures in the signal that depend on E are contained in the scattering amplitude $t_{l_0+1}(E)$.

The total cross section is obtained by the integration of the differential cross section and it is found that $\sigma_{tot} \propto |t_l|^2$. If the potential is real, conservation of the flux requires that $|t_l|^2 = \Im[t_l]$ and we find the optical theorem, because $\sigma_{tot} \propto \Im[t_l]$, so that δ_l is real; otherwise $k|t_l|^2 < \Im[t_l]$, implying that δ_l is complex, and the difference $\Im[t_l] - k|t_l|^2 \neq 0$ is related to the loss of flux due to the absorptive part of the potential.

The same results can be obtained introducing the Green function, as it is shown in App.A.1.

3.1.2 Multicenter scattering theory

When we consider a realistic system made up of many scattering centers, we have to extend the approach used in the case of the atomic scattering, making use of the Green's function method (App.A.1). The MS theory I am going to describe is a single particle approach, therefore it is well suited when multielectronic interactions are weak and it is possible to reduce the whole process to the interaction of only one electron with its atom and the surrounding centers. The validity of this hypothesis might break down when core wave functions overlap significantly with valence wave functions, as in 3d transition metals. In this case, in the low energy part of the spectra, many body effects should be included.

The main difference from the atomic case is that the position of the potentials, with respect to a given origin of space, have to be taken into account in the theoretical description. From now on, we will assume that the sample potential can be partitioned into a superposition of atomic potentials (each atomic potential can contain an exchange and correlation part). We must solve the Schroedinger equation

$$[\nabla^2 + E - V(\vec{r})]\psi_k(\vec{r}) \tag{3.14}$$

with the boundary condition

$$\psi_k(\vec{r}) \sim_{r\to\infty} e^{i\vec{k}\cdot\vec{r}} - kf(\vec{k},\vec{r})\frac{e^{ikr}}{kr}. \tag{3.15}$$

It is possible to transform the differential Schroedinger equation in an integral equation, the so called Lippmann-Schwinger equation; the Schroedinger equation of the full system can be rewritten as

$$(\nabla^2 + E)\psi_k(\vec{r}) = V(\vec{r})\psi_k(\vec{r}) \tag{3.16}$$

which is an inhomogeneous equation. The general solution of such an equation is simply the sum of the general solution of the corresponding homogeneous equation - that is a plane wave - and of a particular solution of the inhomogeneous equation.

If we introduce a complete set of basis local functions $\phi_L(\vec{r}_i)$, which are regular for $r \to 0$, we rewrite the wave function referred to the cell Ω_i as a linear combination of these functions:

$$\psi_k^i(\vec{r}_i) = \sum_L A_L^i(\vec{k})\phi_L(\vec{r}_i), \tag{3.17}$$

where i indicates the i-th cell. Using eq.(3.17), the solution of the Lippmann-Schwinger equation leads to the following general equation for the coefficients $A_L^j(\vec{k})$:

$$\sum_{j\neq i}\sum_{L'}\Big\{\delta_{ij}E_{LL'}^i + \sum_{L''} G_{LL''}^{ij} S_{L''L'}^j\Big\}A_{L'}^j(\vec{k}) = -A_L^0(\vec{k}). \tag{3.18}$$

where we defined the coefficients $A_L^0(\vec{k}) = \sqrt{\frac{k}{\pi}}i^l Y_L(\hat{k})e^{i\vec{k}\cdot\vec{R}_{i0}}$. The factors $G_{LL''}^{ij}$ in these equations are the real space structure factors, which gives the probability of a wave, with angular momentum l, to go from the site i to the site j with angular momentum l'. The structure factors are the propagators, that is the projections of the free propagator in partial waves.

This formalism can be used both for states in the continuum and for bound states, because we can treat $E < 0$ just by taking the analytic continuation of the functions of energy appearing in the definition of the Green's function (App.A.1), provided we put to zero the incoming plane wave in the definition of the wave function.

The Multiple Scattering equation.

To solve the equation (3.18), which allows to determine the coefficients of the wave functions, we must evaluate the expressions of $E_{LL'}^i$ and $S_{L''L'}^j$ (App.A.4). To do this, we must know the wave function ϕ in each single atomic center, that is the wave function referred to the single atom. In the muffin-tin approximation we consider that the potential is spherical inside the atomic region, which is a sphere, whereas it is

constant in the space between the atoms and the outer sphere. In our case we put this constant to zero. For each muffin-tin sphere the radius is ρ_i.

We introduce the quantities:

$$B_L^i(\vec{k}) = \sum_{L'}(-S_{LL'}^i)A_L^i(\vec{k}) \tag{3.19}$$

so that

$$\psi_k^i(\vec{r}) = \sum_L A_L^i(\vec{k})\phi_L(\vec{r}) = \sum_L B_L^i(\vec{k})\bar{\phi}_L(\vec{r}) \tag{3.20}$$

where $\bar{\phi}_L(\vec{r}) = \frac{\phi_L(\vec{r})}{W[j_l(\tilde{k}\rho_i),R_l^i(\rho_i)]\rho_i^2}$.

If we define the Multiple Scattering matrix as the operator $(T^{-1}+G)$, whose elements are $((t_l^i)^{-1}\delta_{LL'}\delta_{ij} + G_{LL'}^{ij})$, and the full scattering path operator, which is the inverse of the MS matrix:

$$\tau_{LL'}^{ij} = [(T^{-1}+G)]_{LL'}^{ij} = [(t_l^i)^{-1}\delta_{LL'}\delta_{ij} + G_{LL'}^{ij}]^{-1}, \tag{3.21}$$

the full scattering path operator gives the total amplitude of propagation from site i to site j, starting with angular momentum L and arriving with angular momentum L', after having been scattered by all the possible atoms. With this notation the multiple scattering equation becomes:

$$\begin{aligned}
&\sum_j\sum_{L'}(\tau_{LL'}^{ij})^{-1}B_{L'}^j(\vec{k}) = A_L^0(\vec{k})\\
&B_L^i(\vec{k}) = \sum_j\sum_{L'}\tau_{LL'}^{ij}A_L^0(\vec{k})\\
&B_L^i(\vec{k}) = \sum_j\sum_{L'}\tau_{LL'}^{ij}\sqrt{\frac{k}{\pi}}i^{l'}Y_{L'}(\hat{k})e^{i\vec{k}\cdot\vec{R}_{j0}}.
\end{aligned} \tag{3.22}$$

The coefficient $B_L^i(\vec{k})$ is a scattering amplitude impinging on the potential located in the cell i in response to a plane wave excitation of momentum $\vec{k}$. Therefore, (3.22) are nothing else but the self-consistent equations for these amplitudes.

For these amplitudes there exist a generalization of the optical theorem, which relates the scattering amplitudes $B_L^i(\vec{k})$ to the imaginary part of the scattering path operator τ; in the case of a real potential one can show [63] that as a consequence of the MS equation (3.22) the following relation holds:

$$\int d\hat{k}B_L^i(\vec{k})^*B_{L'}^j(\vec{k}) = -\frac{1}{k}\Im[\tau_{LL'}^{ij}]. \tag{3.23}$$

This relation is a consequence of the conservation of the particles flux and is not valid in the case of losses, that is when the potential is complex. It can be used to connect the integrated photoemission cross section with the photoabsorption cross section derived from the Green's function expression, as we will see in the following.

3.1.3 Cross section in MS theory

Once the scattering amplitudes have been determined, the wave function is known and we can use it to calculate the differential cross section for the various processes. In particular the photoemission differential cross section is:

$$\begin{aligned}\frac{d\sigma}{d\hat{k}} &= 4\pi^2\alpha\hbar\omega\sum_{m_c}\left|\langle\psi_k(\vec{r})|\hat{\epsilon}\cdot\vec{r}|R^c_{l_c}(r)Y^c_{L_c}(\hat{r})\rangle\right|^2 = \\ &= 4\pi^2\alpha\hbar\omega\sum_{m_c}\left|\langle\sum_L B^i_L(\vec{k})\bar{\phi}_L(\vec{r})|\hat{\epsilon}\cdot\vec{r}|R^c_{l_c}(r)Y^c_{L_c}(\hat{r})\rangle\right|^2 = \\ &= 4\pi^2\alpha\hbar\omega\sum_{m_c}\left|\langle\sum_L B^i_L(\vec{k})R^i_l(r)Y_L(\hat{r})|\hat{\epsilon}\cdot\vec{r}|R^c_{l_c}(r)Y^c_{L_c}(\hat{r})\rangle\right|^2. \end{aligned} \tag{3.24}$$

Since the initial angular momentum is l_c and the final one is l, in dipole approximation $l = l_c \pm 1$:

$$\begin{aligned}\frac{d\sigma}{d\hat{k}} &= 4\pi^2\alpha\hbar\omega\frac{4\pi}{3}\sum_{m_c}\left|\sum_L\int drr^3R^i_{l_c\pm1}(r)R_{l_c}(r)\int d\Omega Y_{l_c\pm1,m_c}(\hat{r})Y_{1,m_\sigma}(\hat{r})Y_{L_c}(\hat{r})B^i_L(\vec{k})\right|^2 = \\ &= 4\pi^2\alpha\hbar\omega\frac{4\pi}{3}\sum_{m_c}\left|\sum_L M_{LL_c}B^i_L(\vec{k})\right|^2 = \\ &= 4\pi^2\alpha\hbar\omega\frac{4\pi}{3}\frac{k}{\pi}\sum_{m_c}\left|\sum_L M_{LL_c}\sum_{jL'}i^{l'}Y_{L'}(\hat{k})e^{i\vec{k}\cdot\vec{R}_{0j}}\tau^{0j}_{LL'}\right|^2, \end{aligned} \tag{3.25}$$

if we consider $i = 0$, that is the photoabsorbing atom is in the origin of the outer sphere. We then see that the photoemission current along the direction $\hat{k}$ is the square modulus of the sum of all possible composite amplitudes obtained as products of an amplitude M_{LL_c} for exciting a core electron at site 0 with angular momentum L, times the amplitude of propagation $\tau^{0j}_{LL'}$ from this site to any other site (cell) j with final angular momentum L', times the amplitude $Y_{L'}(\hat{k})$ for emission along $\hat{k}$, times the phase factor $e^{i\vec{k}\cdot\vec{R}_{0j}}$ that takes into account the phase relation of the electronic wave between site 0 and j. It is therefore the result of a complicated interference process that strongly depends on the reliability of the optical potential.

In this case the primary wave is the photoelectron which leaves the absorber and goes directly to the detector; otherwise the photoelectron can be scattered by the

surrounding atoms before being detected, therefore the amplitudes corresponding to all these processes must be summed and give rise to interference phenomena.

3.2 XAS (X-ray Absorption Spectroscopy) in MS approach

The photoabsorption cross section is nothing more than the integration of the photoemission cross section over all the emission angles and all the final channels (elastic plus inelastic) with the same final energy. The reasons the two cases can be treated together are mainly two: firstly, the mathematical formalism is the same; secondly, we can think of photoabsorption as a kind of photoemission that has the same electron source (the photoabsorber), in which the detector, instead of being outside the measured system, coincides with the source. In the formalism developed above, this means that in all the expressions in which the full path scattering operator appears, we have to take $j = 0$. By treating photoabsorption and photoemission together, one can judge the sensitivity to structural details of a particular potential in absorption by looking at its performance in photoelectron diffraction. In photoabsorption, because of the impossibility to control the measured variables (except total energy), we must sum over all the final states at a given energy.

We integrate the photoemission cross section (A.59) over the whole solid angle and consider $j = 0$ in order to find the absorption cross section, because we want the photoelectron, after having been scattered by the other atoms, to return to the absorber (that is, we consider a closed path):

$$\begin{aligned}\sigma_{abs} &= \int d\hat{k}\frac{d\sigma}{d\hat{k}} = 4\pi^2\alpha\hbar\omega\frac{k}{\pi}\frac{4\pi}{3}\sum_{m_c}\int\sum_{LL'}M_{LL_c}B^0_L(\vec{k})B^{0*}_{L'}(\vec{k})M^*_{L'L_c}d\hat{k} = \\ &= -4\pi^2\alpha\hbar\omega\frac{k}{\pi}\frac{1}{k}\frac{4\pi}{3}\sum_{m_c}\sum_{LL'}M_{LL_c}\Im[\tau^{00}_{LL'}]M_{LL_c},\end{aligned} \tag{3.26}$$

where we used the generalization of the optical theorem (3.23). If we use the explicit expression for M_{LL_c}, the relation becomes:

$$\begin{aligned}\sigma_{abs} = &-4\pi^2\alpha\hbar\omega\frac{1}{\pi}\frac{4\pi}{3}\sum_{LL'}\sum_{m_c}\langle R^0_{l_c}(r)Y_{L_c}(\hat{r})|rY^*_{1m_p}(\hat{r})|R_l(r)Y_L(\hat{r})\rangle\Im[\tau^{00}_{LL'}] \\ &\cdot\ \langle R_{l'}(r')Y_{L'}(\hat{r'})|rY_{1m_p}(\hat{r})|R^0_{l_c}(r)Y_{L_c}(\hat{r})\rangle =\end{aligned}$$

$$= -4\pi\alpha\hbar\omega\frac{4\pi}{3}\sum_{LL'}\sum_{m_c} M_{ll_c}M_{l'l_c}\langle Y_{L_c}(\hat{r})|Y^*_{1m_p}(\hat{r})|Y_L(\hat{r})\rangle\Im[\tau^{00}_{LL'}]\langle Y_{L'}(\hat{r})|Y_{1m_p}(\hat{r})|Y_{L_c}(\hat{r})\rangle =$$
$$= -4\pi\alpha\hbar\omega\sum_m M^2_{ll_c}\Im[\tau^{00}_{lmlm}]\Big(\frac{l_c+1}{2l+1}\delta_{l,l_c+1}+\frac{l_c}{2l+1}\delta_{l,l_c-1}\Big), \tag{3.27}$$

where the properties of the spherical harmonics have been used to simplify the expression of the absorption cross section (see. appendix A.5).

If we remember that the absorption cross section of a single atom is:

$$\sigma_{at} = -4\pi\alpha\hbar\omega\sum_{lm} M^2_{ll_c}\Im[t_l] = -4\pi\alpha\hbar\omega\sum_{lm} M^2_{ll_c}\frac{\sin^2\delta_l}{k}, \tag{3.28}$$

the (3.27) can be factored as the atomic cross section, times a coefficient depending on the contribution of all the other atoms:

$$\sigma_{abs} = \sigma^{at}_l\Big[(l_c+1)\delta_{l,l_c+1}+l_c\delta_{l,l_c-1}\Big]\frac{1}{\sin^2\delta_l(2l+1)}\sum_m k\Im[\tau^{00}_{lmlm}] =$$
$$= \Big[(l_c+1)\delta_{l,l_c+1}+l_c\delta_{l,l_c-1}\Big]\sigma^{at}_l\chi_l \tag{3.29}$$

where χ_l contains the multiple scattering signal, because it is

$$\chi_l = \frac{1}{\sin^2\delta_l(2l+1)}\sum_m k\Im[\tau^{00}_{lmlm}]. \tag{3.30}$$

χ_l is a structure factor that gives the information about the atomic cluster around the absorber atom and if we remember that $\tau = (T^{-1}+G)^{-1}$, we see that when $G = 0$, that is the absorber is isolated, then $\chi_l = 1$ and the total absorption cross section is reduced to the atomic one. The factorization between structural term and atomic absorption in (3.29) is possible only if the potential is real, otherwise the structural signal must be obtained as shown in par.3.2.2.

To enlighten the physical meaning of the photoabsorption process, matrix inversion in (3.30) must be performed. It is possible to rewrite the scattering path operator as

$$\tau = (T^{-1}+G)^{-1} = (I+TG)^{-1}T. \tag{3.31}$$

Provided that the spectral radius $\rho(TG)$ is less than one - that is the photons energy is quite high, because $T \to 0$ for $E \to \infty$ - inversion is obtained by series expansion:

$$(I+TG)^{-1} = \sum_{n=0}(TG)^n \tag{3.32}$$

which gives

$$\tau = \sum_{n=0} (TG)^n T. \tag{3.33}$$

When the photons energy is sufficiently high, the structure factor thus becomes:

$$\begin{aligned}\chi_l &= \frac{1}{\sin^2\delta_l(2l+1)} \sum_m k\Im[\tau^{00}_{lmlm}] = \frac{1}{\sin^2\delta_l(2l+1)} \sum_m k\Im[\sum_n (TG)^n T\Big|^{00}_{lmlm}] = \\ &= \sum_n \frac{1}{\sin^2\delta_l(2l+1)} \sum_m k\Im[(TG)^n T\Big|^{00}_{lmlm}] = \sum_n \chi_l^{(n)}. \end{aligned} \tag{3.34}$$

$\chi_l^{(n)}(E)$ represents the partial contribution of order n to the photoabsorption coefficient of the cluster under study, coming from all processes where the photoelectron emitted from the absorbing site 0 is scattered $n-1$ times by the surrounding atoms before escaping to free space after returning to site 0.

If we consider the first contributions of order n, we find that for $n = 0$ $\chi_l^{(n)} = 1$, since

$$\begin{aligned}\chi_l^{(0)} &= \frac{1}{\sin^2\delta_l(2l+1)} \sum_m k\Im[T^{00}_{lmlm}] = \frac{1}{\sin^2\delta_l(2l+1)} \sum_m k\Im[t_l(2l+1)] = \\ &= \frac{1}{\sin^2\delta_l(2l+1)} \sin^2\delta_l(2l+1) = 1. \end{aligned} \tag{3.35}$$

The contribution of order 1 instead is zero, since it is

$$\chi_l^{(1)} = \frac{1}{\sin^2\delta_l(2l+1)} \sum_m k\Im[TGT]\Big|^{00}_{lmlm} \tag{3.36}$$

but G is off-diagonal in the site indices, so $G^{00} = 0$. The contribution of order 2 is the first non trivial term, because it is

$$\begin{aligned}\chi_l^{(2)} &= \frac{1}{\sin^2\delta_l(2l+1)} \sum_m k\Im[TGTGT]\Big|^{00}_{lmlm} = \\ &= \frac{1}{\sin^2\delta_l(2l+1)} \sum_m k\Im[\sum_{jl'm'} t^0_l G^{0j}_{lml'm'} t^j_{l'} G^{j0}_{l'm'lm} t^0_l]. \end{aligned} \tag{3.37}$$

This term is a single-scattering contribution, because the photoelectron is emitted from the atom 0, arrives to atom j and comes back to 0.

Due to the localization of the initial core state, only closed paths beginning and ending to the absorbing atom are possible. It is this peculiarity that entails the site

specificity of the XAS spectroscopy and makes it a unique tool for studying structural problems and for probing higher order correlation functions in condensed matter. The interpretation of the XAS spectrum in terms of MS pathways of the photoelectron in the final state is meaningful only if it is possible the series expansion of the MS matrix. From the matrix theory the absolute convergence is ensured if $\rho(TG) < 1$. This criterion is very useful since the convergence entails the property that terms of order n in the series higher than a certain n_0 do not contribute appreciably to the sum. Now $\rho(TG)$ is a continuous function of the photoelectron energy, which goes to zero when E goes to infinity and tends to the infinity as E goes to zero, because G is singular at $E = 0$ due to the presence of the Hankel function in the definition of the propagators. As a consequence it must cross at least once the value $\rho = 1$; the nearer to 1 is its value the slower is the convergence of the series. For this reason, according to the size of the spectral radius, one can roughly divide the photoabsorption spectrum into three regions:

- **Full multiple scattering (FMS) region**: region characterized by $\rho(TG) > 1$, where an infinite number of paths contribute to the shape of the spectrum. This is the region of the shape resonances where the scattering power of the environment is strong enough that it can scatter the photoelectron many times. Global information can be extracted such as point group symmetry and electronic structure information.

- **Intermediate multiple scattering (IMS) region**: where $0.5 \leq \rho(TG) \leq 0.8$: only a limited number of paths of low order contributes, due to convergence of the MS series. It is the region where information on bond lengths and and angles between bonds are contained, since the photoelectron is sensitive to the relative position of two or more atoms at the time via the MS paths.

- **Single-scattering (SS) region**: in this case $\rho(TG) < 0.5$, only paths of order $n = 2$ contribute significantly. This is the region where the photoelectron is sensitive only to pair-correlation function, that is the relative positions of the central atom and the backscattering atoms.

The general picture of a XAS spectrum that emerges from this discussion is one in which oscillating signals with variable amplitudes are superimposed on a background of a more or less smooth atomic absorption. The oscillating signals are the so called X-ray absorption fine structures (XAFS) and originate from the interference of the scattered

waves with the primary wave of the photoelectron. In the region of convergence of the MS series the SS signal is the strongest and acts as a carrier wave that supports all of the other MS waves. In principle any XAS spectrum contains all the three regions. In the limit of high energy the IMS region should continuously merge into the SS region and finally reduce to pure atomic absorption. This picture is the basis for almost all modern methods of analysis of the experimental XAS data.

3.2.1 XAFS (X-ray Absorption Fine Structure) technique

Now we concentrate on the oscillating signals contained in the absorption coefficient. It is possible, in fact, to write the paths contributions $\chi_l^{(n)}$ in useful functional form to analyze the experimental spectra:

$$\chi_l^{(n)} = \sum_{p_n} A_n^{(l)}(k, R_{ij}^{p_n}) \sin[kR_{p_n}^{tot} + \varphi_n^{(l)}(R_{ij}^{p_n})] \tag{3.38}$$

where the sum is over all possible paths p_n of order n and $R_{p_n}^{tot}$ is the corresponding path length. This form follows from the fact that each spherical wave propagator G carries a factor $e^{ikR_{ij}}$ independent from L and L', contained in the Hankel functions of the propagators, that can be factorized. It is the form expected on the basis of interference process between the outgoing and the backscattered photoelectron wave at the absorbing site. As a consequence, under the assumption that the MS series converges, one can always fit an experimental spectrum with a series of EXAFS like functions. The EXAFS (Extended X-ray Absorption Fine Structure) function is the analytical expression of the SS signal and it is obtained by the approximation of the spherical propagators with plane waves. Actually, from a theoretical point of view, this approximation is not correct because the distance between the absorber (source) and the scatterer is comparable to the interatomic distances, so spherical waves should be used. Nevertheless, this approximation leads to good experimental results. Since the Hankel function is:

$$h_{l''}^{+}(\rho) = i^{-(l''+1)} \frac{e^{i\rho}}{\rho} P(\frac{1}{i\rho}), \tag{3.39}$$

where $P = \sum_{k=0}^{l} \frac{1}{k!} (\frac{i}{2\rho})^k \prod_{m=0}^{k-1} [l(l+1) - m(m+1)]$, and the plane wave approximation corresponds to taking $P = 1$, as if we considered only one spherical wave. This should be correct if it were $\rho \to \infty$. In this way the propagator becomes:

$$G_{LL'}^{ij} = -4\pi i^{l-l'} \frac{e^{ikR_{ij}}}{kR_{ij}} Y_L(\hat{R}_{ij}) Y_{L'}^{*}(\hat{R}_{ij}) \tag{3.40}$$

end if we substitute (3.40) in (3.37) the second order contribution to the XAFS signal becomes:

$$\begin{aligned}\chi_l^{(2)} &= \frac{1}{\sin^2\delta_l(2l+1)}\sum_m k\Im[\sum_{jl'm'} t_l^0 G_{lml'm'}^{0j} t_{l'}^j G_{l'm'lm}^{j0} t_l^0] = \\ &= \frac{1}{\sin^2\delta_l(2l+1)}\sum_m k\Im\Big[(\sin\delta_l e^{i\delta_l})^2 \sum_{jl'm'}(4\pi)^2\frac{e^{ikR_{0j}}}{kR_{0j}}Y_{lm}(\hat{R}_{0j})Y_{l'm'}^*(\hat{R}_{0j}) \\ &\quad t_{l'}^j\frac{e^{ikR_{j0}}}{kR_{j0}}Y_{l'm'}(\hat{R}_{j0})Y_{lm}^*(\hat{R}_{j0}))\Big].\end{aligned} \tag{3.41}$$

According to the addition theorem for spherical harmonics

$$\sum_m Y_{lm}(\hat{R}_{0j})Y_{lm}^*(\hat{R}_{j0}) = \frac{2l+1}{4\pi}P_l(-1) \tag{3.42}$$

and $P_l(-1) = (-1)^l$, therefore (3.41) is:

$$\begin{aligned}\chi_l^{(2)} &= \frac{1}{2l+1}k\Im\Big[(4\pi)^2\sum_j e^{2i\delta_l}\frac{e^{2ikR_{0j}}}{(kR_{0j})^2}\sum_{l'}\frac{2l'+1}{4\pi}P_{l'}(-1)\frac{2l+1}{4\pi}t_{l'}^j(-1)^l\Big] = \\ &= (-1)^l\Im\Big[e^{2i\delta_l}\sum_j\frac{e^{2ikR_{0j}}}{k(R_{0j})^2}\sum_{l'}(2l'+1)P_{l'}(-1)t_{l'}^j\Big].\end{aligned} \tag{3.43}$$

If we remember the expression for the scattering factor in atomic physics, $f(\cos\vartheta) = \sum_l(-1)^l(2l+1)P_l(\cos\vartheta)t_l$, we rewrite (3.43) as

$$\begin{aligned}\chi_l^{(2)} &= \Im\Big[e^{2i\delta_l}\sum_j\frac{e^{2ikR_{0j}}}{k(R_{0j})^2}f_j(\pi)\Big] = \Im\Big[\sum_j\frac{e^{2i\delta_l+2ikR_{0j}}}{k(R_{0j})^2}|f_j(\pi)|e^{i\phi_j}\Big] = \\ &= \sum_j\frac{|f_j(\pi)|}{k(R_{0j})^2}\sin(2kR_{0j}+2\delta_l+\phi_j) = \sum_j\frac{|f_j(\pi)|}{k(R_{0j})^2}\sin(2kR_{0j}+\phi_t^{(j)}(k))\end{aligned} \tag{3.44}$$

where ϕ_j is the phase-shift due to the scattering event and $\phi_t^{(j)}(k)$ is the total phase-shift. This is the EXAFS formula, which describes the oscillatory signal originated by the interference between the single-scattering paths. Basically, the EXAFS signal has a sinusoidal behaviour, with frequency $2R_{0j}$ proportional to the interatomic distance. The phase of the sine function is perturbed by the phase-shift $\phi_t^{(j)}(k)$, while the amplitude is modulated by $|f_j(\pi)|$.

In this treatment I have neglected to consider inelastic effects, that are essentially of two type: intrinsic and extrinsic, referring to many-body interactions within and outside the absorber atom, respectively. These inelastic channels drain away amplitude from the elastic channel, which alone gives structural information, and must be included in a realistic calculation to make comparison with experimental data. This situation calls for a many-body treatment of the photoabsorption process. Actually, a formal exact solution of this problem can be found in the language of configuration interaction or channels giving a generalization of the MS theory in terms of multi-channels [62]. I will not report the treatment but just give some arguments which will enable us to achieve a reasonable guess for a possible complex one-electron potential to be used in an effective one-electron theory.

The intrinsic inelastic effects are the multiple excitations within the absorber atom, which modify the photoelectron energy and hence the interference conditions between outgoing and incoming waves. The net effect is a reduction of the coherent EXAFS signal with respect to that expected for purely elastic excitations. The fraction of total absorption giving rise to elastic excitations is measured by the superposition factor S_0^2 defined as

$$S_0^2 = |\langle \Psi_i^{N-1} | \Psi_f^{N-1} \rangle|^2 \tag{3.45}$$

assuming the "sudden approximation", that is it is possible to neglect the passive electrons of the absorbing atoms so that the wave functions can be factorized in the contributions ψ_i and ψ_f of the active electron and Ψ_i^{N-1} and Ψ_f^{N-1} of the passive electrons. The value of S_0^2 is generally between 0.7 and 0.9 and gives the probability amplitude that the excited state Ψ_i^{N-1} of the spectator (N-1) electrons with a core hole relaxes to the state Ψ_f^{N-1}, eigenstate of the (N-1) particles Hamiltonian.

The extrinsic inelastic effects instead are taken into account as a mean free path λ, to which two distinct phenomena contribute: the core-hole life-time τ_h, depending on the atomic number Z, which establishes the distance λ_h the photoelectron can travel before the absorber atom de-excitation; the energy-dependent photoelectron mean free path λ_e, determined by the inelastic interactions with other electrons outside the absorber atom. The smaller of the two contributions determines the actual value of λ:

$$\frac{1}{\lambda} = \frac{1}{\lambda_h} + \frac{1}{\lambda_e}. \tag{3.46}$$

At low energies, in the XANES region, the mean free path is determined by λ_h, while in the EXAFS region the contribution of λ_e is predominant. The extrinsic effects are

generally taken into account by a phenomenological factor $e^{-2R_{0j}/\lambda}$, with $\lambda \simeq 5 \div 15$ Å. The mean free path factor progressively reduces the amplitude of EXAFS oscillations when R_{0j} increases, contributing to make EXAFS insensitive to long range order.

Another effect that we have not discussed yet is the Debye-Waller factor, which is given to a good approximation by $e^{-2\sigma^2 k^2}$. This factor is due partly to thermal effects, which cause all of the atoms to oscillate around their equilibrium atomic positions. These slight movements "soil" the sharp interference pattern of the varying $\sin(2kR)$ term, that would be seen if the atoms were unmoving. Effects of structural disorder are similar and they give an additional contribution to σ^2. In formal terms, the Debye-Waller contribution originates from the representation of disorder through a distribution of the atomic distances: this means that the distance between absorber and back-scatterer atoms, instead of having a value R_{0j}, varies according to a probability distribution $\rho(r)$ normalized to unity. Thus we must substitute in (3.44) the terms where there is R_{0j} with the probability distribution $\rho(r)$:

$$\begin{aligned}\chi_l^{(2)} &= S_0^2 \Im\Big[\sum_j \frac{e^{2i\delta_l + 2ikR_{0j}}}{k(R_{0j})^2} e^{-2R_{0j}/\lambda} |f_j(\pi)| e^{i\phi_j}\Big] = S_0^2 \Im\Big[\sum_j \frac{e^{2ikR_{0j}}}{k(R_{0j})^2} e^{-2R_{0j}/\lambda} e^{2i\delta_l} |f_j(\pi)| e^{i\phi_j}\Big] = \\ &= \frac{S_0^2}{k} \Im\Big[\sum_j e^{2i\delta_l} |f_j(\pi)| e^{i\phi_j} \int_0^\infty \rho(r) \frac{e^{-2r/\lambda}}{r^2} e^{2ikr} dr\Big].\end{aligned} \tag{3.47}$$

The fundamental problem of EXAFS analysis is to recover the distribution $\rho(r)$ from the experimental spectrum $\chi(k)$. No exact solution can be given to this problem, since every experimental spectrum has a finite extension in k. An approximate solution to the inversion problem from $\chi(k)$ to $\rho(r)$ consists in assuming physical structural models and in fitting the parameters of their distributions $\rho(r)$ to experimental EXAFS signal. when the effects of disorder can be treated within the harmonic approximation, the distribution has a gaussian shape with only two parameters, the mean value R and the variance σ^2:

$$\rho(r) = \frac{1}{\sigma\sqrt{2\pi}} e^{-\frac{(r-R)^2}{2\sigma^2}}. \tag{3.48}$$

An alternative approach is based on the cumulant method, which makes a series expansion of the integral in (3.47) and under the assumption of weak disorder coincides to considering a gaussian probability distribution. This method leads to the final EXAFS formula, after we make a last consideration: if atoms can be grouped into coordination shells, each one containing N_s atoms of the same species at the same mean distance R_s

from the absorber atom, it is possible to rewrite the EXAFS signal separating the contributions of different coordination shells, and we find the so called *Standard EXAFS Formula*:

$$\chi_l^{(2)} = \frac{S_0^2}{k} \sum_s |f_s(\pi)| \frac{e^{-2R_s/\lambda}}{R_s^2} e^{-2k^2\sigma^2} \sin\left(2kR_s + \phi_t^{(j)}(k)\right). \tag{3.49}$$

3.2.2 Inelastic energy loss: use of optical potentials

As we said above, the inelastic losses are the cause of a reduction in the signal amplitude and they are caused by both the relaxation of the system around the core hole and the effects due to the outgoing photoelectron. A complete solution should take into account all the possible processes of energy loss but this way would be impracticable from the computational point of view. For this reason it is necessary to reduce the processes to fewer channels and this procedure would lead to a single equation for the propagator G_{00} in presence of a complex, energy dependent, non-local optical potential. The nature of this complex potential must be determined by some simple physical considerations: first of all, in a metal one obtains very good agreement with experimental data using a one-particle approach with an X_α potential -that is, a potential which is proportional to the charge density- and convoluting the calculated spectrum with a Lorentzian broadening function having an energy-dependent width related to the mean free path of the photoelectron in the system ($\Gamma(E) = \hbar\sqrt{(E/2m)}/\lambda(E)$); then one can consider that double-electron excitations are normally very weak, therefore an optical potential given by $V_{X_\alpha} + i\Gamma(E)$ is able to give a satisfactory picture of the absorption process. Moreover, according to a statistical approximation suggested by the opening of many channels with the same weight, the optical potential must be approximated by the self-energy of a uniform interacting electron gas with density given by the local density of the system. Thus we find the Hedin-Lundqvist (HL) potential [34, 46], with its energy-dependent exchange and its imaginary part that is able to reproduce the observed mean-free path at least for metals and semiconductors. This potential can be interpreted as an effective optical potential that controls the propagation and the damping of the photoelectron everywhere in the system, even in the atomic core region. The complicated many-body problem is reduced to an effective one-electron problem where the plasmon excitations exhaust all the possible inelastic excitations of the system. In keeping with this interpretation no $|S_0(E)^2|$ correction is needed. The application of these ideas to the calculation of K-edge XAS spectra of many transition metals and semiconductors has yielded results in good agreement with the experimental data. In

particular, amplitudes and phases of the MS signals in the IMS and SS regions are very well reproduced.

If one uses a complex potential the atomic cross section does not factorize out from the structural contribution. Therefore the total structural signal in a final angular momentum channel l is defined as:

$$\chi_l(E) = \frac{\sigma_l(E)}{[\sigma_{at}(E)]} - 1 \tag{3.50}$$

and the various MS signals of order n are given by:

$$\chi_l^n(E) = \frac{\sigma_l^n(E)}{[\sigma_{at}(E)]}. \tag{3.51}$$

To better understand the effect of using the complex potential, one can observe that the MS series is formed by the product of the propagator $G^{ij}_{LL'}$ between sites i and j and the and the l-wave atomic t-matrix t^i_l of the atom at site i. The general term of the MS series is built by several repetitions of the product $t^i_l G^{ij}_{LL'}$, that brings out a factor $e^{-2\delta_l} e^{-k_2 R_{ij}}$ when complex potential is used, where δ_2 is the imaginary part of the atomic phase shift and k_2 the complex part of the wave vector. As a consequence, the complex potential gives rise to a damping factor that reduces the amplitude of the elastic signal, therefore there are fewer scattering paths and atoms which contribute to the measurable physical signal. This is the origin of the mean free path of the photoelectron, that appears as a factor in the form $e^{-2R_{ij}/\lambda(k)}$.

Chapter 4

Experimental setup

Since X-ray absorption spectroscopy is based on the analysis of the absorption coefficient as a function of photons' energy, the radiation source must have a continuous energy spectrum in the X-ray region. Synchrotron light is therefore the ideal source to perform such a spectroscopy, thanks to its wide energy spectrum, high intensity and collimation. In the following, I will briefly give some elements about the properties of synchrotron radiation and the characteristics of the ESRF facility where we performed the experiments. Then I will shortly describe the experimental XAS beam-lines.

4.1 Synchrotron radiation

Synchrotron light is the electromagnetic radiation emitted by charged particles (electrons) which are accelerated on a circular orbit. First, the charges are accelerated with an energy of the order of some GeV, then they are constrained by bending magnets to move on circular paths. The bending magnets (BM) and other magnetic devices that are along the accumulation ring, such as wigglers and undulators (ID, insertion devices), give the electrons an acceleration which is perpendicular to the motion's direction. In this way the electrons emit electromagnetic radiation, which is called synchrotron radiation.

The main properties of this radiation source are the following:

- a continuous energy spectrum from infrared to X-ray energies;
- high intensity;
- high collimation along the flight direction of the accelerated particles;

- high brilliance (emitted power per solid angle unit and per surface unit normal to the direction of propagation);
- well defined polarization: the polarization is linear in the orbital plane and elliptical out of plane;
- pulsed structure of the radiation: the light is formed by impulses which have a duration < 100ps, with repetition time from a few ns to μs.

When the electrons are accelerated and they reach a velocity v close to that of light (c), these properties can be obtained using a relativistic approach to the process. In this case, in fact, the emitted power is given by the *relativistic Larmor's Formula*:

$$W = \frac{2}{3}\frac{e^2}{4\pi\epsilon_0}\frac{c}{r^2}\gamma^4 \qquad [eVs^{-1}] \tag{4.1}$$

The total power is proportional to γ^4 ($\gamma = 1/\sqrt{1-(v/c)^2}$), that is to E^4, and it is inversely proportional to r^2 (orbital radius). In this way the radiation is emitted in a cone tangent to the flight direction of the particle, with a width $1/\gamma$. Since $\gamma = E/mc^2 \simeq 2000 \cdot E(GeV)$, if we consider a particle with E=6 GeV we find a value $1/\gamma \sim 10^{-5}$ rad, that is the degree of collimation increases with increasing energy.

A characteristic connected to the performance of a synchrotron is the critic energy, ε_c, given by the expression:

$$\varepsilon_c = \frac{3\hbar c}{4\pi}\frac{\gamma^3}{R} \tag{4.2}$$

where R is the radius of the accumulation ring. It represents the energy below which the spectrum is independent of energy with an exponential decrease of its intensity at higher E values.

4.2 European Synchrotron Radiation Facility (ESRF)

The X- ray absorption spectra analyzed in this work were collected at the European Synchrotron Radiation Facility (ESRF) at Grenoble (France). This facility is a third generation synchrotron and its scientific purposes range from physics to chemistry and biology.

The synchrotron (Fig.4.1) is made of a pre-injector LINAC which at the beginning produces and accelerates the electrons with energy of 200 MeV; then there is a circular accelerator (booster) that accelerates the electrons until they reach the required energy; finally the electrons are injected in the accumulation ring where they are kept

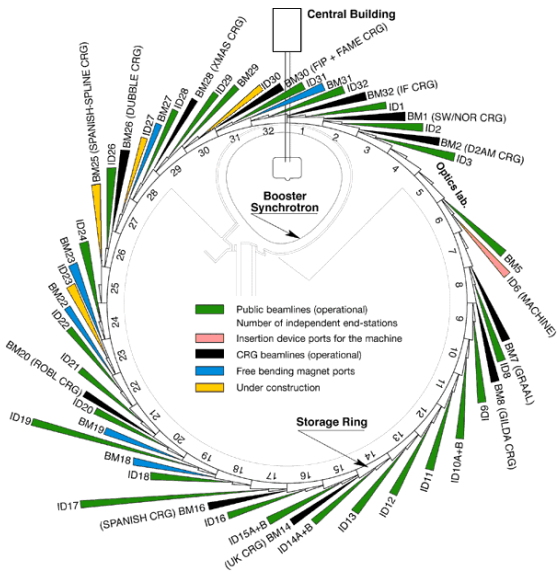

Figure 4.1: Scheme of the ESRF.

at constant energy and circulate at 6 GeV. The bending magnets induce the electrons to move following the ring and then to emit radiation, because they undergo the centripetal acceleration. Actually the ring is not perfectly circular but it has got some linear parts, where there are insertion devices (wigglers and undulators). The electrons, which pass through the ID, oscillate in a direction perpendicular to their velocity and for this reason emit radiation with different characteristics from those of the radiation emitted in the BM.

In Tab.4.1 the technical information about the acceleration ring of ESRF is reported.

4.3 The XAS beam-line: general features

The experiments of absorption spectroscopy were performed on the beam-line BM8 (GILDA) and ID26. The beam-line is made of two sections: in the first, the optical hutch, the photons beam is monochromatized and focalized; in the second, the experimental hutch, the instruments for X-ray absorption spectroscopy are installed.

Optics. A sketch of the optical hutch for a beam-line is shown in Fig.4.2. To protect the machine front end from vacuum failures the beam-line is equipped with a thick Be window following the front end shutter.

The first element of the beam-line after the front end shutter are the standard ESRF

Parameters	Units	2006
Current	mA	200
Kinetic energy	GeV	6.03
Mean life	hours	75
Horizontal emittance	nm	4
Vertical emittance	nm	0.03
Revolution frequency	kHz	355
Number of bunches		1 to 992
Time between bunches	ns	2816 to 2.82
Brilliance at 10 keV	ph/s/$mm^2/mrad^2$/0.1%Bwidth	$3 \cdot 10^{20}$
Brilliance at 60 keV	ph/s/$mm^2/mrad^2$/0.1%Bwidth	10^{19}

Table 4.1: Characteristics of ESRF.

primary slits. These are used to define the white-beam profile which is incident on the monochromator crystals. These slits can provide a beam profile by moving both in the horizontal and in the vertical planes. In particular the primary slits vertical aperture is an important parameter, as it largely defines the energy resolution of the instrument for a given set of monochromator crystals. Following the primary slits the beam-line is equipped with a series of beam attenuators, consisting of Al and Cu plates of various thickness.

A fundamental element of the optics is the monochromator. This device is used to select from the continuous spectrum of the synchrotron radiation a defined energy $E = \hbar\omega$ in a band of energies of width ΔE (resolution). In our experiments the monochromator is a double crystals of Si with fixed exit, that is the vertical position of the beam does not change as a function of the energy. The monochromators for X-ray energies are based on the Bragg diffraction from perfect crystals (*Bragg Law*):

$$2d_{hkl} \sin\theta_{hkl} = n\lambda \tag{4.3}$$

where d_{hkl} is the distance between the crystallographic planes in the lattice, θ_{hkl} is the angle between the incident beam (and the diffracted beam) and the crystallographic planes hkl (Bragg angle), n is an integer number. The energy scan is performed by rotating the crystal around an axis which is parallel to the Bragg planes and perpendicular to the beam direction.

Following the monochromator there are secondary slits, to control the energy reso-

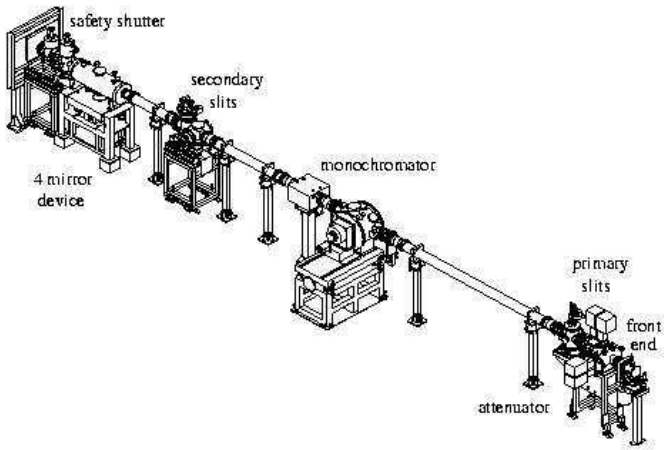

Figure 4.2: Scheme of the components of the optical hutch.

lution and to eliminate possible parasitic reflections from the monochromator. In most operating modes the slits are used to define the horizontal and vertical focalization of the beam. The next optical elements are mirrors, which are used to reduce higher harmonics. The use of the mirrors, anyway, is not compulsory, since the reduction of the contribution of higher harmonics can be performed also by mean of the "detuning": in this case, the Bragg angle of one of the crystal of the monochromator respect to the other is varied so that to select only the fundamental wave length. This operation is possible because of the intrinsic width (*Darwin width*) of any Bragg reflection from a perfect crystal; this width determines the intrinsic resolution of the monochromator and is much larger for the fundamental wave length than for the higher harmonics. The energy resolution ΔE of the photons beam after the monochromator depends on two factors: the Darwin width and the angular divergence Ω of the incident beam on the monochromator. The latter is determined by the geometrical characteristics of the source and by the slits; in first approximation, $\Omega \approx d/l$, where d is the vertical aperture of the primary slits and l the distance between the source and the monochromator. From the Bragg law the expression of the relative energetic resolution can be obtained as:

$$\frac{\Delta E}{E} = \Delta\Theta \cot\theta_B \tag{4.4}$$

where Θ is the convolution of the Darwin width $\Delta\Theta_D$ and the divergence Ω

$$\Delta\Theta = \sqrt{(\Delta\Theta)_D^2 + \Omega^2} \tag{4.5}$$

The final element in the beam-line optics hutch is the beam shutter that isolates the experimental hutch from the now monochromatic source. This shutter allows work to be performed at the experimental end station of the beam-line while beam is taken in the optics hutch. The heatload on the monochromator is therefore kept constant during experimental procedures and this is important for maintaining the stability offered by the beam-line.

Experimental XAS hutch. The experiment is separated from the optics section by a Be window. A general scheme of the experimental equipment for a XAS experiment is given by the experimental chamber where the sample is mounted, which is equipped with a cryostat to vary the temperature of the sample and with a vacuum system; then there are the detectors to measure the initial photons beam and the final flux of particles. The detectors and the geometry of the experiment depends on the kind of measurement, that is if the experiment is performed in transmission, fluorescence or total electrons yield mode. In the first and second mode, the particles detected after the interaction with the sample are photons; in the latter the electrons emitted by the sample are revealed.

In our case, we performed different sets of experiments, one on the GILDA-BM8 beam-line to measure the absorption spectra of $LaMnO_3$ and $CaMnO_3$ in transmission mode; another one on the ID26 beam-line in fluorescence geometry to measure the absorption coefficients in V_2O_3. Here follow the details of the three beam-lines.

4.3.1 GILDA beam-line

The GILDA beam-line (General purpose Italian Line for Diffraction and Absorption) exploits the emission from a bending magnet and uses photons in the energy range 5-80 keV with high energy resolution, high flux on the sample and small beam spot. The monochromator is formed by two independent crystals, the first is flat and the second can be curved on a cylindric surface in order to focus the beam in the horizontal plane: in this way the incident beam is 2 mm wide. To cover the entire energy range (5-80 keV), there are three couples of crystals: Si(111), Si(311) for the low energy measurements and Si(511) for higher energy experiments. The energy resolution obtained is $\simeq 5 \cdot 10^{-5}$ keV. In our experiment we used the Si(311) double-crystal. A couple of grazing incidence mirrors placed before the sample were used to clean the x-ray beam from higher-order harmonics (energy cut-off at about 10 keV). The mirrors have manifold uses: they collimate the beam before the monochromator in such a way to better the resolution, they eliminate the higher-order harmonics, they reduce the incident power

on the monochromator and vertically focus the beam. In the X-ray range, mirrors use the property of the refraction index $n = 1 - \delta - i\beta$, which has the real part $1 - \delta$ minor than 1 ($\delta \simeq 10^{-4} - 10^{-5}$). This fact implies that the refraction index for X-rays is smaller than that in vacuum, thus there exist a critical angle below which the incident radiation is totally reflected. Since the critical angle depends on the wave length, it is possible to make the beam arrive on the mirror's surface with such an angle that the higher-order harmonics are cut off. The mirrors are made of a Glydcop alloy and they are divided in three planar sections, with a total length of 1.5 m. The reflecting surfaces are made of two stripes of Pt and Pd, which can cover the whole energy range 5-30 keV. We performed the XAS experiments in transmission mode. Vacuum is obtained by means of two turbo-molecular pumps and reaches 10^{-6} Torr. A N_2 cryostat allows the temperature to reach T=77 K. The sample is placed in an adjustable (vertically and horizontally) sampler holder. The detectors are two ionization chambers, with planar and parallel electrodes, of about 15 cm and 40 cm length, respectively. The measured currents are typically of $10^{-8} - 10^{-10}$ A. The ionizations chambers are placed one before and the other after the sample and are filled with N_2.

4.3.2 ID26 beam-line

ID26 is an insertion device source consisting of three mechanically independent undulators (two of 42-mm period and one of 35-mm period). The insertion devices present a very bright x-ray emission centered at an energy that is a function of its opening. At ID26 two different scanning modes are available: one consists on discrete movements of the undulator gap; the other is the quick scans mode, consisting on a synchronous movement of the undulator gap and the Bragg angle of the monochromator. Of course more scans are necessary to obtain enough statistics. The x-ray beam energies were selected by double crystal Si(220), a fixed exit monochromator with an energy resolution of about 0.3 eV at the V K-edge. We used two silicon mirrors for the rejection of the harmonics coming from the incident X-ray beam and they also provided a small (diameter $\sim 300\mu$m), intense x-ray spot size on the sample. The experiment was performed in total-fluorescence mode, that is measuring the intensity of the fluorescence emission from the sample due to the absorption of the incident photons. A schematic picture of the experimental geometry in a fluorescence mode experiment is shown in Fig.4.3.

The fluorescence intensity emitted from the sample was collected by measuring the current from two photodiodes, mounted parallel to the polarization of the incoming

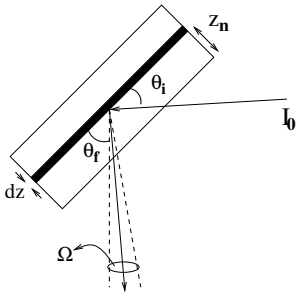

Figure 4.3: Schematic representation of fluorescence experimental setup.

beam in order to minimize the elastic contribution to the spectrum. I_0 was recorded by another Si photo-diode from the fluorescence signal of a titanium foil.

Chapter 5

Results

In this chapter I will present the results obtained from the XAS analysis of the transition metal oxide systems $LaMnO_3$, $CaMnO_3$ and Cr-V_2O_3. As said before, the XAS spectroscopy allows us to investigate the local structure surrounding the absorber atom, in our case Mn and V, respectively.

The open problem in manganites regards the knowledge of the surrounding of Mn from a topological point of view. In this thesis we extensively studied the XANES spectra of the two end compounds $LaMnO_3$ and $CaMnO_3$, with the plan to extend in the future this study to the whole series $La_{1-x}Ca_xMnO_3$. These systems have been studied with a recent fitting code, the MXAN code, that allows to perform a best fitting procedure on the absorption experimental spectra in the edge region and not only a theoretical simulation of the data, as it is usually done. At the moment, this code has been tested on small molecules but never on a crystalline system, in particular a highly correlated system as manganites are. The interest in the application of this software on such systems is due also to the complexity of the distortion phenomenon shown by $LaMnO_3$; the idea is to study quantitatively the Jahn-Teller distortions which are fundamental to explain the electronic and magnetic properties of manganites, by fitting the XANES regions of the spectrum of $LaMnO_3$. In this way we can verify the usability of the XANES spectroscopy.

On the other hand V_2O_3 is another system which has been largely studied as a Mott-Hubbard system but that still offers problems to the full comprehension of its basic properties. The evolution of the structural transition with temperature is still unclear, as also the origin of the dichroic signal under particular external conditions [33]. For this reason, to obtain local information about the structure surrounding the Mn ion, we performed X-ray absorption experiments to investigate both the EXAFS

region of the spectrum as a function of temperature and the dichroic signal using linearly polarized X-ray synchrotron radiation.

In the following, the data analysis of the spectra and the results obtained on these systems are reported.

5.1 X-ray Absorption Spectroscopy in $LaMnO_3$ and $CaMnO_3$

The local atomic structure around Mn ions plays a crucial role in the determination of the complex phenomena observed in manganites. This is especially due to the electron-phonon coupling, which involves a dynamical Jahn-Teller deformation of the Mn local surrounding. For this reason short-range order techniques like X-ray absorption spectroscopy (XAS) are very well suited for studying these compounds.

The conjectures about the mixed compound $La_{1-x}Ca_xMnO_3$ concern the possible local structure around the Mn ions and the contribution of the two "separate" compounds $LaMnO_3$ and $CaMnO_3$ when the mixed one is formed, that is to say if the final system can be obtained as a simple "sum" of the two or it cannot. For this reason it is very important to clarify which is the local structure around the Mn atoms in the end compounds and this can be achieved by means of highly accurate XAS analysis. In particular, we focused on the XANES region of the XAS spectra of $LaMnO_3$ and $CaMnO_3$, because it allows to determine the local geometry of the atoms around the absorber, including also the orientation of the atoms with respect to the central one. We quantitatively studied the spectra using a new fitting code, the MXAN code, which refines the structure obtained from a long-range order technique such as X-ray diffraction. In the following I will describe the analysis of the XANES spectra of $LaMnO_3$ and $CaMnO_3$ at room temperature.

The Mn K-edge X-ray absorption spectra were recorded at the GILDA-BM8 beamline of the European Synchrotron Radiation Facility (ESRF).

5.1.1 Sample preparation

The stoichiometric $LaMnO_3$ and $CaMnO_3$ oxides were prepared at the "Indian Institute of Science" in Bangalore, India. Stoichiometric amounts of analytical-grade La_2O_3, $Ca(NO_3)_2$ and $MnCO_3$ were dissolved in citric acid. The citrate solutions were slowly evaporated and all organic materials were eliminated in a treatment at 700 °C in air,

for 12 h. This treatment gave highly reactive precursor materials: $LaMnO_3$ precursor was then treated at 1100 °C in a N_2 flow for 12 h to avoid the oxidation of the samples. $CaMnO_3$ precursor was annealed in air at 1100 °C for 12 h. All compounds appeared well crystallized and single phase at standard XRD analysis.

The experiment was performed in transmission mode, therefore the samples must have some requirements: ideally the jump edge must be $\simeq 1$, with the total absorption of the sample $\mu x \approx 2 \div 3$, because the ratio between the edge and background must be optimized; secondly, the sample must be as homogeneous as possible to avoid artificial changes in the absorption signal due to non linearity between I_1 and μ. For these reasons sample pellets were ground by hand in agate mortar under ethylic alcohol and the powders were suspended in ethylic alcohol under an ultrasonic bath, then the finest powders were deposited onto a Millipore membrane and enclosed between two Kapton tape films. In our samples we have $\mu x \approx 2.6$ and $\Delta\mu x = 0.9$ for $CaMnO_3$ and $\Delta\mu x = 1.1$ for $LaMnO_3$.

We measured the I_0 and I_1 currents as a function of the energy in the range 6150-7700 eV, choosing a difference ΔE, among the measured energy points, different for the different parts of the spectrum: in the pre-edge region ΔE is wider (ΔE=10 eV) since we are not interested in this part of the spectrum, it is thinner in the XANES region (ΔE=1 eV) and intermediate in the remaining part of the spectrum (ΔE=2 eV). The integration time is 3 s, sufficient to have a good statistics.

5.1.2 XANES analysis in $LaMnO_3$and $CaMnO_3$

We used the ATOMS software to determine the atomic positions coordinates, starting from the crystallographic Pnma symmetry group. The lattice distances found by ATOMS are reported in Tab.5.1. These initial coordinates are used as input data of the fitting code.

The XANES analysis concerned the energy region from 10 eV below the edge up to 180 eV above the edge. The experimental spectra, after subtraction of the pre-edge, were normalized to the jump edge. The MXAN code was used to fit the calculated x-ray absorption cross section $\mu_{th}(E)$ to the experimental data. It is a new code (see App.B) based on the multiple scattering theory (see Chap.3) and able to calculate the cross section in the full multiple scattering framework, i.e. it solves exactly the scattering operator, without any series expansion; therefore it calculates the edge region, where the multiple scattering matrix does not converge. So far MXAN has been applied only to systems with no long-range order, in particular to complex molecules [5, 6, 7]; at

$LaMnO_3$		$CaMnO_3$	
legame	dist.(Å)	legame	dist.(Å)
Mn-O(2)	1.906	Mn-O(2)	1.885
Mn-O(2)	1.971	Mn-O(2)	1.887
Mn-O(2)	2.174	Mn-O(2)	1.917
Mn-La(2)	3.232	Mn-Ca(2)	3.114
Mn-La(2)	3.346	Mn-Ca(2)	3.198
Mn-La(2)	3.419	Mn-Ca(2)	3.258
Mn-La(2)	3.684	Mn-Ca(2)	3.348
Mn-Mn(2)	3.850	Mn-Mn(2)	3.725
Mn-Mn(4)	3.986	Mn-Mn(4)	3.727
Mn-Mn(2)	5.536	Mn-Mn(2)	5.264
Mn-Mn(8)	5.541	Mn-Mn(8)	5.269
Mn-Mn(2)	5.736	Mn-Mn(2)	5.277
Mn-Mn(4)	6.743	Mn-Mn(4)	6.449
Mn-Mn(4)	6.908	Mn-Mn(4)	6.459

Table 5.1: Distances from the central Mn in $LaMnO_3$ e $CaMnO_3$: The number in parenthesis is the number of atoms placed at that distance.

the moment it has not been applied to solids. Our aim is to test this computational method studying crystalline systems such as $LaMnO_3$ and $CaMnO_3$. In the future, we will extend its application to the whole manganite series.

To perform a fitting MXAN calculates the parameters which describe the potential and the structure: the former are the muffin-tin radii of the atomic potentials, the line-width, the number of scatterers and the maximum angular momentum of the scattered waves (l_{max}), the values of the MT potentials and the charge densities. Actually, in a fitting procedure only the overlapping factor is minimized, while the numbers of scatterers and l_{max} are chosen according to convergence criteria; the other non-structural parameters generally are automatically calculated by the software. The structural parameters, then, are the interatomic distances and the angles between bonds. After the calculation, to take into account broadening effects, the calculated spectra $\mu_{th}(E)$ are convoluted with an energy-dependent Lorentzian function of width $\Gamma(E) = \Gamma_r + \Gamma_p(E)$. The constant term Γ_r takes into account the core-hole lifetime and the experimental resolution, the energy-dependent term Γ_p considers the inelastic processes. It is assumed to be zero below the plasmon excitation energy E_p and above

it varies from an initial value A_p according to the universal function of the mean free path in solids. The numerical values for Γ_r, E_p and A_p are optimized at each refinement step of the structural parameters using a simulated annealing procedure, based on a Monte Carlo search. Slope correction and normalization are also refinable parameters.

The first step in the refinement procedure was the choice of the cluster dimension, that is the number of atoms, around the absorber. This has been performed by progressively adding neighbor shells around the central atom while assuming crystallographic structure for $LaMnO_3$ and $CaMnO_3$. The procedure is stopped when the increase of the cluster size do not change the calculated potential. In our case the optimal balance between computation time and cluster size resulted in an 85 atoms cluster for $LaMnO_3$ and 87 for $CaMnO_3$. The shells considered are shown in Fig.5.1.

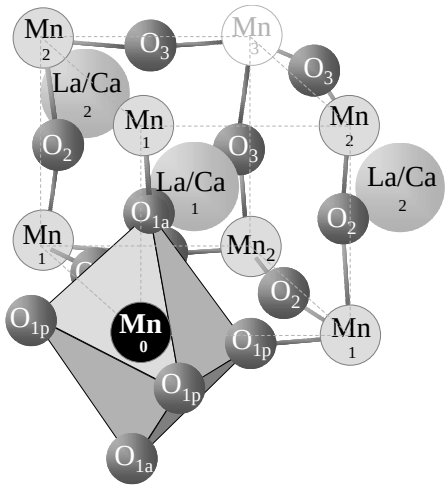

Figure 5.1: Schematic view of $La(Ca)MnO_3$ structure. The generic Mn absorber (Mn_0) is shown in black.

The next step was the minimization of the potential parameters (using the OPTN option of the code). This OPTN option carries out a statistical minimization keeping the assigned structure fixed; the parameters that are determined are:

- Ovlp, the overlapping of the MT radii; the MT radii are calculated according to the Norman criterion and their choice fixes the constant MT potential and the charge density;
- Fermi, the Fermi energy;
- Broad, the line-width;
- Epl1, the plasmon energy;

- Apl1, the plasmon amplitude;
- Slope, the slope of the spectrum;
- Norm, the normalization coefficient of the calculated spectrum with respect to the experimental one;
- Ensh, energy shift of the calculated spectrum with respect to the experimental one.

To calculate the absorption cross section of $LaMnO_3$ it was necessary to take l_{max}=4, due to the presence of La, whereas for $CaMnO_3$ it was sufficient l_{max}=3. We verified that it is not necessary to consider waves with angular momentum greater than 4, because the spectrum does not change increasing further the angular momentum.

For what concerns the number of scatterers to be considered during the calculation of the spectra, the fitting was obtained with 63 atoms for $LaMnO_3$ and 59 for $CaMnO_3$, thus including the 12 Mn atoms of the second coordination sphere. In fact we found that, if we considered less scatterers, the spectral features after the main line were not sufficiently resolved.

The minimization of the potential parameters has been performed considering a complex Hedin-Lundqvist potential for $LaMnO_3$, whereas for $CaMnO_3$ it was sufficient to use the real Hedin-Lundqvist potential (see Cap.3). The values of the potential parameters obtained by the fitting are reported in Tab.5.2.

$LaMnO_3$		$CaMnO_3$	
Ovlp	-0.081	Ovlp	-0.054
Fermi	-9.10 eV	Fermi	-10.1 eV
Broad	2.0 eV	Broad	2.3 eV
Epl1	2.4 eV	Epl1	1.0 eV
Apl1	7.8 eV	Apl1	6.5 eV
Slope	0.0005	Slope	0.0003
Norm	0.036	Norm	0.062
Ensh	2.46 eV	Ensh	8.51 eV

Table 5.2: Values of the potential parameters used for the structural fittings.

The results obtained by this procedure, that is by fitting only the potential parameters are shown in the first panels of Fig.5.3(a); the structure used in this calculation is fixed and equal to the crystallographic one.

Finally, the atomic structure was refined and, using the potential parameters found in the previous step, we let the structural parameters vary. Our aim is to find the distances between the central Mn atom and the other ions. After some preliminary tests we chose the groups of atoms to be refined together at each step, because the MXAN code allows to refine, at each run, the atomic coordinates of 12 ions at the maximum; in large systems these "free ions" must be suitably chosen and several runs must be reiterated. We grouped the atoms in the following way: (i) the 6 O_1 atoms bound to Mn, (ii) the 8 $La_1(Ca_1)$ ions at the cube center and (iii) the 6 Mn_1 ions on the cube edges. We found that the refinement of the position of the faraway ions produces large instability of the fitting procedure while having only a weak effect on the best accuracy, since their degree of disorder is higher and hence their effect in multiple scattering is negligible; thus the positions of these atoms were kept fixed at the crystallographic positions. The fitting proceeded cyclically through the refinement of (i), (ii) and (iii). When a stable configuration is achieved, the potential parameters are recalculated and a new refinement cycle restarted. In our case the 87-atom cluster requires about 24-48 h on a Linux-based workstation equipped with 3 Ghz PIV processor. A complete refinement is achieved in 20-25 cycles - that is, about 800 h. At the state of the art the long computing time prevents one from fully exploiting the capabilities of MINUIT subroutines for an accurate analysis of statistical errors taking into account the correlations among the parameters. Therefore, the error bars on the refined parameters were estimated as the variance on a set of different structures producing similar fittings ($\chi^2_\nu < \chi^2_\nu(min)+5\%$). In the near future the parallelization of the MXAN code will allow an improvement of the treatment of errors. In Fig.5.2 we show the first fittings obtained: we can see that the main structural features of the spectra are present even if the broadening is not taken into account, but the differences between the calculation and the experimental data are too large. After many trials we concluded that a systematic mismatch between experimental and calculated spectra existed, which prevented a satisfactory refinement (Fig.5.3(b)): we can see that the structural features of the experimental spectra are reproduced by the fitting, but the slopes of the calculations and the data are very different. This effect did not depend on the calculated potential or the input structure. The large residuals found either in $LaMnO_3$ and $CaMnO_3$ XANES suggests, instead, that a secondary absorption edge contributes to our spectra, originated by multiple excitation effects. The relevance of multiple excitation in the XAS spectra has been widely discussed in the literature [26, 27, 28]; in the extended region of a XAS spectrum additional edges can be partially taken into account or masked by a proper choice of

the splines, that mimic the atomic background; on the contrary, in the XANES region the effect of a secondary edge can be dramatic and must be explicitly considered.

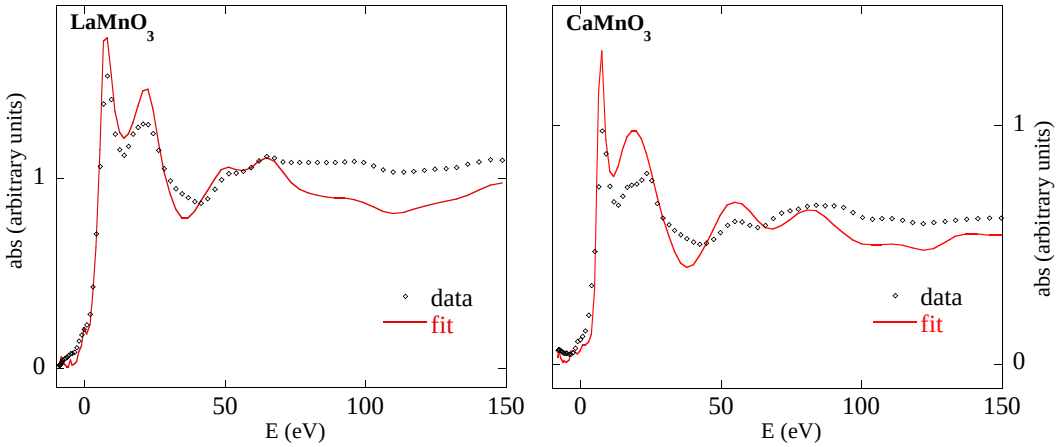

Figure 5.2: First fittings obtained on $LaMnO_3$ and $CaMnO_3$, without adding any broadening. The open diamonds are the experimental points, the continuous line is the calculation.

In order to take into account multiple excitations the MXAN code was modified adding the possibility to introduce a secondary edge, that was parameterized with an arctangent function, thus introducing three additional nonstructural parameters to the fitting: the onset energy (E_{de}), the amplitude (A_{de}) and the width (W_{de}) of the secondary edge. The addition of the contribution of a multiple excitation in this form drastically reduces the residual (Fig.5.3(c)).

The refined values of the parameters of the secondary edge are reported in Tab.5.3:

$LaMnO_3$		$CaMnO_3$	
E_{de}	69±4 eV	E_{de}	75±4
A_{de}	0.19±0.01	A_{de}	0.09±0.01
W_{de}	6±1	W_{de}	4±1

Table 5.3: Values of the secondary edge parameters.

These values must be compared with the energy positions of the M_I and M_{II} edges of Fe, which in the simple Z+1 approximation amounts to about 53 eV [85]. Considering that an additional shift towards higher energy values is certainly present (but not evaluated) for the valence status of Mn in our samples (Mn^{3+} in $LaMnO_3$ and Mn^{4+} in $CaMnO_3$), we can consider satisfactory the agreement between the values found (69 and 75 eV) and the approximated one (53 eV). Moreover, the positive shift between the

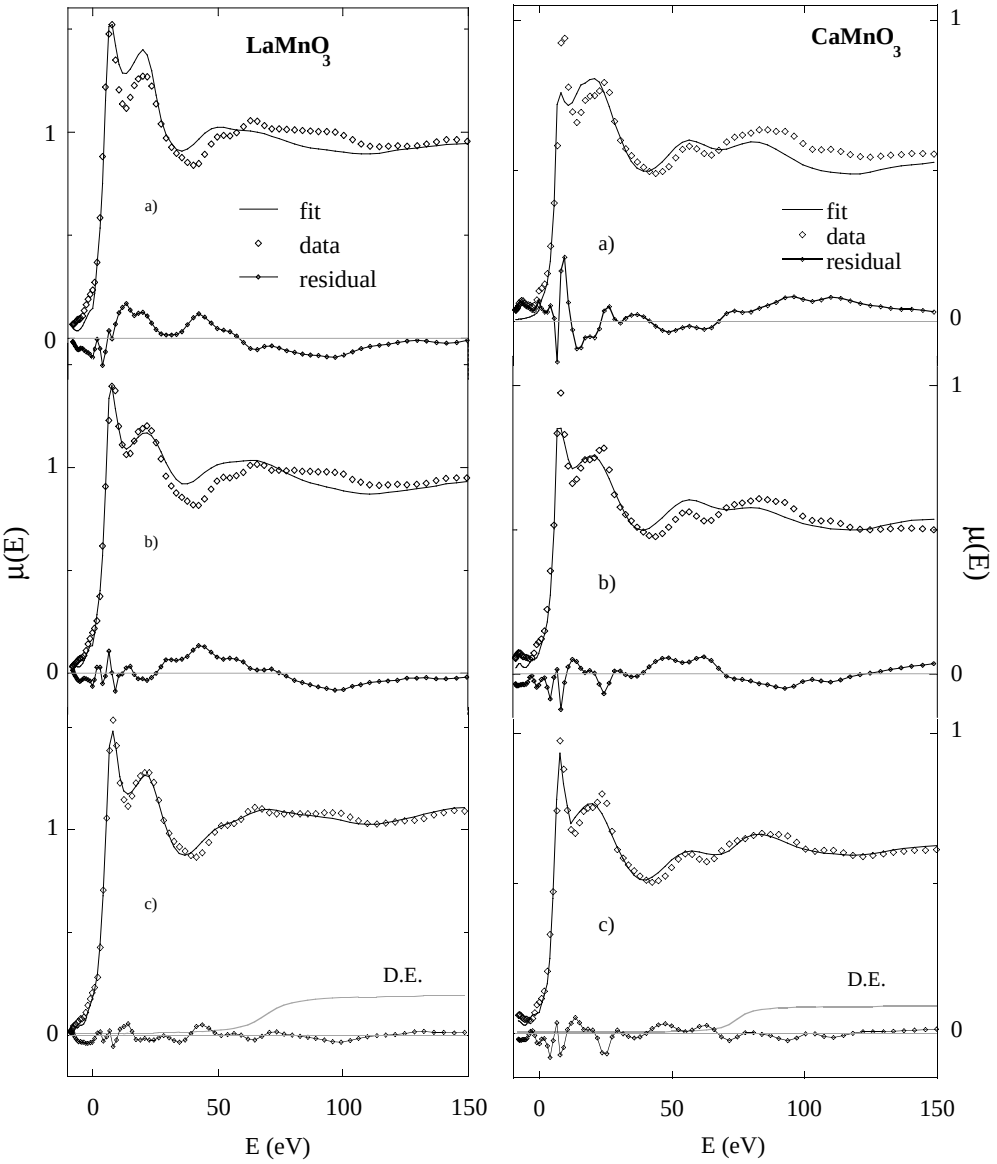

Figure 5.3: XANES fitting for $LaMnO_3$ (left panels) and $CaMnO_3$ (right panels): the experimental data (diamonds), the theoretical (solid lines), residuals (experimental - theory) are shown, shifted for clarity. Panels (a to c) show some relevant steps of the refinement procedure (full lines): (a) the initial model obtained from the crystallographic structure; (b) the best fitting without secondary edge; (c) the final best fittings are shown; the secondary edge contributions are also shown, shifted for clarity.

$E_{de}(CaMnO_3)$ and $E_{de}(LaMnO_3)$ is qualitatively consistent with the higher valence status of Mn in $CaMnO_3$.

The potential parameters were calculated again with the addition of the double excitation (DE) and they are reported in Tab.5.4.

We can notice that the inclusion of a secondary edge in the fitting reduces the

$LaMnO_3$		$CaMnO_3$	
Ovlp	-0.067	Ovlp	-0.048
Fermi	-8.90	Fermi	-9.80
Broad	1.2 eV	Broad	1.4 eV
Epl1	1.6 eV	Epl1	1.1
Apl1	4.3	Apl1	7.6
Slope	0.0004	Slope	0.0004
Norm	0.037	Norm	0.062
Ensh	2.48 eV	Ensh	8.48 eV

Table 5.4: Values of the potential parameters calculated with the secondary edge.

parameter Γ_r in both samples: in $LaMnO_3$ the Γ_r decreases from about 2 eV (without secondary edge) to 1.2 eV (with secondary edge) and in $CaMnO_3$ it decreases from about 2.3 eV to about 1.4 eV. These values match well with the Mn core-hole width of 1.16 eV, definitively confirming the hypothesis and the relevance of the multiple excitation effect in these spectra. The best fitting of XANES spectra achieved for $LaMnO_3$ and $CaMnO_3$ samples are shown in Fig.5.3, while the main structural parameters are reported in Tab.5.5 and 5.6. The χ^2_ν value obtained for the two fittings is $\sim$4 for both samples.

5.1.3 $LaMnO_3$ and $CaMnO_3$: results and discussion

The complete fittings of the XANES data are shown in Fig.5.3(c): it is evident that, once included the secondary edge, the agreement between the calculation and the experimental spectra is very good. The structural parameters that change during the fitting are the distances, the polar and azimuthal angles of the 6 O_1, the 8 La_1/Ca_1 and the 6 Mn_1. The coordination system of the parameters is shown in Fig.5.4. The structural data obtained from the fitting are in rather good agreement with the crystallographic data of Ref.[73, 35] and are compatible with those obtained from the extended region of the XAS spectrum [60].

$R_{Mn-O} \pm 0.02$ (Å)	$\theta_{MnO_1Mn_1} \pm 5$ (deg)	$R_{MnCa/La} \pm 0.04$ (Å)
	$LaMnO_3$	
1.93	149	3.23
1.93	153	3.25
1.94	158	3.25
1.94	161	3.41
2.10	163	3.49
2.10	165	3.55
		3.78
		3.82
	$CaMnO_3$	
1.90	149	3.02
1.90	151	3.11
1.91	159	3.12
1.92	164	3.21
1.93	163	3.22
1.93	169	3.30
		3.33
		3.36

Table 5.5: The main structural features characterizing the Mn local environment in $CaMnO_3$ and $LaMnO_3$ samples as obtained by the XANES structural refinement.

The Mn-O_1 distance found in $CaMnO_3$ is in good agreement with the average crystallographic distance, and it is slightly longer than the EXAFS one. In addition, the XANES results suggest a bimodal Mn-O_1 distance distribution with three shorter (average value $\sim$ 1.903 Å, with two distances at 1.90 Å and one at 1.91 Å) and three longer (average value $\sim$ 1.926 Å, with one distance at 1.92 Å and two O at 1.93 Å) bonds (Tab.5.6), in agreement with the crystallographic structure, which shows four shorter bonds at $\sim$ 1.89 Å and two longer bonds at $\sim$ 1.92 Å. If we define the JT distortion of the oxygens octahedron as:

$$\sigma_{JT} = \sqrt{\frac{1}{6}\sum_{i=1}^{6}(R_i - \bar{R})^2}, \tag{5.1}$$

the JT distortions given by XANES and by crystallography are the same: 0.01 Å.

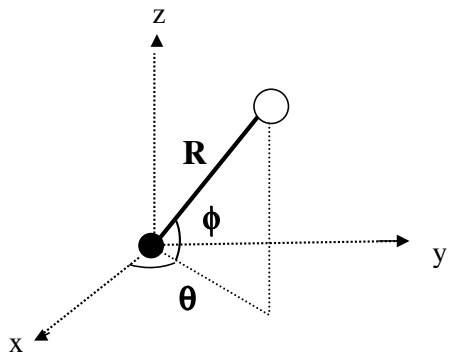

Figure 5.4: Coordination system used by MXAN: R is the distance of each atom with respect to the absorbing atom; ϕ is the azimuthal angle and θ the polar one.

	Crystal	EXAFS	XANES
		$CaMnO_3$	
$\overline{R}_{O_1}$(Å)	1.90	1.895	1.91
σ_{JT} (Å)	0.01	-	0.01
$\overline{\theta}_{O_1}$(deg.)	159.2	156.6	159.1
$\overline{\sigma}_{\theta}$(deg.)	4.8	-	7.1
$\overline{R}_{Ca_1}$(Å)	3.23	3.18	3.21
$\overline{\sigma}_{Ca_1}$(Å)	0.09	-	0.11
		$LaMnO_3$	
R_{O_p}(Å)	1.938	1.925	1.935
R_{O_a}(Å)	2.174	2.129	2.100
$\overline{R}_{O_1}$(Å)	2.017	1.99	1.990
σ_{JT} (Å)	0.125	0.096	0.084
$\overline{\theta}_{O_1}$(deg.)	155.3	161	158.1
$\overline{\sigma}_{\theta}$(deg.)	0.05	-	5.6
$\overline{R}_{La_1}$(Å)	3.42	3.43	3.47
$\overline{\sigma}_{La_1}$(Å)	0.18	-	0.22

Table 5.6: The main structural features of $LaMnO_3$ and $CaMnO_3$ samples as obtained by XANES analysis are compared with the crystallographic structure and the EXAFS results. In the table, $\overline{R}_{O_1}$ is the average value of the distances reported in Tab.5.5, σ_{JT} is the JT distortion as defined in eq.5.1, $\overline{\theta}_{O_1}$ is the mean value of the $\theta_{MnO_1Mn_1}$ angles reported in Tab.5.5, $\overline{\sigma}_{\theta}$ is the standard deviation of the θ angles reported in Tab.5.5 and so on.

The XANES analysis also confirms that the six O_1 neighbours are effectively in an octahedral configuration around Mn with O_1-Mn_0-O_1 bond angles, θ_{Mn}, equal to 90°, with a sharp distribution $\sigma_\theta^2 \sim 3°$. Even the average Mn-O_1-Mn_1 bond angles (θ_{O_1}) found by XANES and diffraction are the same as well as the bond angle distribution width (σ_θ). For what concerns the Mn-Ca_1 distance, the fitting results point out an asymmetric Mn-Ca_1 distribution, in very good agreement with the diffraction results (Fig. 5.5).

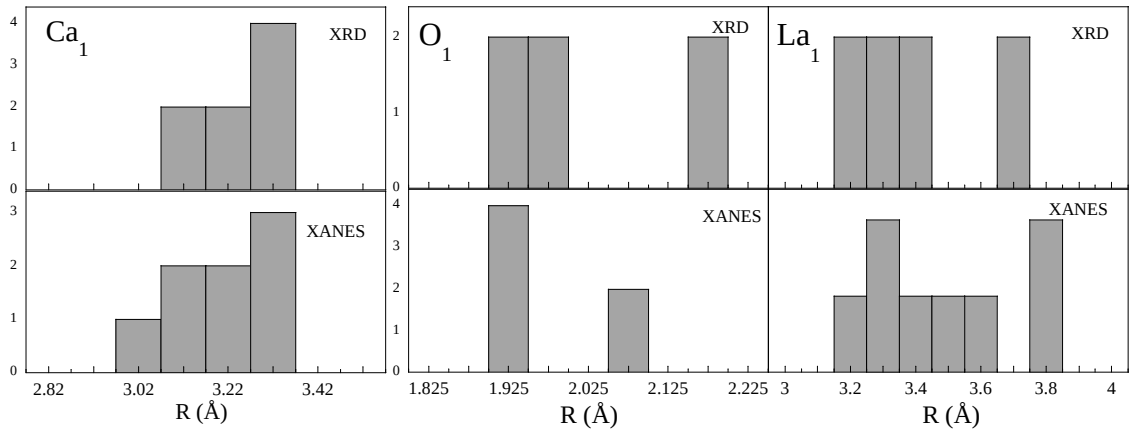

Figure 5.5: Pictorial view of the Mn-Ca_1 distribution in $CaMnO_3$ and Mn-O_1 Mn-La_1 distributions in $LaMnO_3$, as derived from diffraction data (upper panel) compared to XANES results (lower panel).

In conclusion the results of the analysis of $CaMnO_3$ depict a good agreement between the XANES structure and the known crystallographic one and demonstrate the accuracy of the MXAN approach.

In the $LaMnO_3$ samples the main structural features derived from XANES are in good agreement with the EXAFS results reported in [60], confirming the consistency of the XANES fitting even in this complex case (Tab.5.6). The XANES analysis shows a bimodal distribution of Mn-O_1 distances with four nearest-neighbours and two longer bonds. The shorter Mn-O_{1p} distances found by the analysis ($R_{O_p} \sim 1.935$ Å, average value of the four distances found by MXAN) are in good agreement with the crystallographic distance ($R_{O_p} \sim 1.938$ Å) (Tab.5.6). However, the XANES analysis suggests all the planar oxygen ions to be at the same distance, while the crystallographic structure points out two well defined distances at 1.907 Å and 1.971 Å; moreover the Mn-O_{1a} distance found with the fitting is shorter than the diffraction value (Fig. 5.5).

Let us discuss in detail these results, since precise knowledge of the local structure in Jahn-Teller- distorted MnO_6 is relevant for the still open discussion on the peculiar

physical properties of manganites. Discrepancies between XAS and diffraction results are often reported in literature: they may arise from either physical or fictitious effects. In fact, on the one hand, large differences between local and long-range coherent structure are often documented in these compounds. On the other hand, XANES results can be affected by the choice of the interatomic potentials. We underline that in our case the contraction is observed only for one distance, the long Mn-O_{1a} bond, while all the other structural parameters show a general agreement between XANES and crystallographic results. This points towards the presence of a real shorter distance of the Mn-O_{1a} bonds. We notice that a similar contraction of the apical Mn-O bond has been reported in Ref.[77] as a result of slightly not stoichiometric $LaMnO_3$ phases. Therefore the contraction of the apical Mn-O bond length can be at least partially due to local deviations from ideal stoichiometry in this sample.

Also in $LaMnO_3$ case XANES data show that the six O_1 neighbours are effectively in an octahedral configuration around Mn_0 with O_1-Mn_0-O_1 bond angles θ_{Mn_0} equal to 90°, with $\sigma_\theta^2 \sim 4°$. The average Mn-O_1-Mn_1 bond angles found by XAS are a little larger ($\sim 5°$) than the average crystallographic value; the XANES show a broad θ_{O_1} distribution with a bimodal trend (as for $CaMnO_3$ sample) with two smaller angles (around 151°) and four larger angles (around 162°). This finding differs from the sharp distribution of the crystallographic structure.

For what concerns the Mn-La_1 distances, the XANES results are the same than the diffraction ones within the errors and show a bimodal distribution with six nearest La ions and two far away which is in quite good agreement with the crystallographic structure (Fig.5.5). It is just to be noted that XANES results show a long Mn-La distance slightly elongated with respect to EXAFS and XRD.

The local structure derived from the XANES analysis somewhat differs from the crystallographic one and this fact suggests that there exist a difference in the actual local structure with respect to the one inferred from diffraction measurements. The good results obtained in these two reference manganite compounds encourage us to extend this approach to doped manganites as well, in which the details of the local structure are a fundamental issue to the comprehension of their magnetotransport properties. However, in that case to fully characterize the local order and to get a reliable structural refinement from XANES spectra, a large number of different contributions should be considered, since there should be different Mn ion sites. This prohibitively enlarges the computation time, making this problem capable of being addressed only when a parallelized MXAN version will be available.

5.2 X-ray Absorption Spectroscopy in V_2O_3

Using the XAS technique we have studied the local structure of V_2O_3 to understand the evolution of the structural transition with the temperature variation, to see if the transition is a sharp one or there is still the presence of monoclinic domains above the transition temperature. Moreover we have studied the origin of the dichroism measured in V_2O_3 and reported in Ref.[33].

All the X-ray absorption spectroscopy measurements were performed on a single crystal of V_2O_3, doped with 2.8% of chromium, whose dimensions are about $5 \times 5 \times 2mm^3$. Experiments were carried out at the European Synchrotron Radiation Facility in Grenoble, at beam-line ID26. X-ray absorption spectra at the V K edge, corresponding to edge-energy $E_0 = 5465$ eV, were collected in fluorescence mode. In the experiment at ID26 the sample was mounted in a closed-cycle He refrigerator, properly oriented with respect to the horizontal linear polarization of the x-ray beam. The sample, in fact, was rotated, collecting the absorption spectra with the polarization vector along three orthogonal directions, that is along the corundum c axis (z), and in the hexagonal plane, along the monoclinic b axis (y) and the a axis perpendicular to it (x), according to fig.5.6.

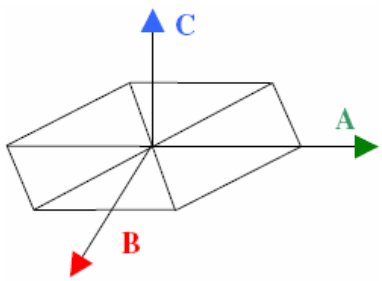

Figure 5.6: Coordination system used in the following: A corresponds to the x axis, B to the y axis and C to the z axis.

Absorption spectra were collected in the energy range 5300-6300 eV, in the temperature range 80 K up to 300 K. Spectra were collected at T=80, 100, 120, 140, 160, 200, 220, 230, 260 and 300 K for x polarization; at T=80, 100, 120, 140, 160, 200, 215 and 300 K along y polarization direction; at T=100, 120, 140, 160, 215, 230 and 260 K in the z polarization. The geometrical setup allowed to have very narrow Bragg peaks at some energies, due to the elastic scattering of the fluorescence radiation with the crystal. In order to remove these peaks, several spectra (about 20-60) were collected at different angles by rocking the sample ($\pm 2°$) around the vertical axis. With this procedure

the Bragg peaks were shifted and could be easily distinguished from the true spectral features and removed. Since the data were collected in quick EXAFS mode (each scan required about 20 s), after eliminating the Bragg contributions we averaged up all the scans in order to reduce the noise-to-signal ratio. Each spectrum consists of $\simeq$ 4000 points. The spectra obtained in this way were then used for a XAS analysis, both in the XANES energy range and in the EXAFS one.

An EXAFS analysis has been performed on the polarized spectra, where we studied also the changes in the pre-edge and XANES part of the spectrum when the sample is rotated with respect to the polarization vector of the X-ray beam.

5.2.1 Structural dichroism in V_2O_3

The analysis of the dichroic signal in V_2O_3 was performed at T=80 K, that is in the monoclinic phase [53]. We measured the two absorption spectra with x and y polarizations (in the hexagonal plane), then we subtracted a straight line simulating the background given by the atomic absorption coefficient; to normalize the spectra we divided them to a polynomial function that fits the average data at high energy. Then we made the difference between the data with y polarization and that one with x polarization: $\sigma_y - \sigma_x$. We focused on the XANES energy region to take into account both the electronic and structural differences. The experimental XANES spectra are reported in Fig.5.7. The A and B spectra are an average of 61 spectra, while C is an average of 16 spectra.
When the X-ray polarization is along the c (z) axis, the difference with respect to the other spectra is evident; the difference between the two spectra with polarizations in the hexagonal is instead less manifest. The dichroism within the hexagonal plane is nevertheless still clear, as it is shown in Fig.5.9.

We compared these XANES data and the dichroic signal ($\sigma_y - \sigma_x$) to theoretical calculations performed by the FDMNES program [38]. This software calculates the absorption cross section of photons around the absorption edge. The calculation can be performed with a specific linear polarization of the incident photons. The numerical simulation is calculated in the framework of the multiple scattering theory within the muffin-tin approximation.

At the V K-edge, the X-ray absorption cross section for the ith vanadium ion in the unit cell is given by

$$\sigma_i = 4\pi\alpha^2\hbar\omega \sum_n |\langle\Psi_n^{(i)}|\hat{O}|\Psi_0^{(i)}\rangle|^2 \delta[\hbar\omega - (E_n - E_0)]. \tag{5.2}$$

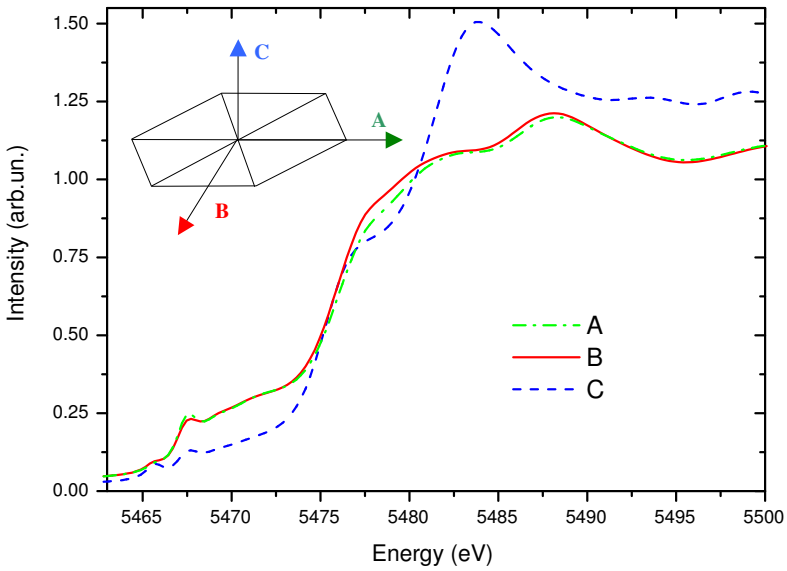

Figure 5.7: Experimental XANES spectra A, B have the polarization along the in-plane axis and C has polarization along the out-of-plane axis. A and B are an average of 61 spectra; C is an average of 16 spectra.

The operator $\hat{O}$ is the usual matter-radiation interaction operator; $\Psi_n^{(i)}$ and $\Psi_0^{(i)}$ are the ground and the excited states, respectively, of the crystal and E_0 and E_n their energy. The sum is extended over all the excited states of the system. The total cross section is obtained by summing up, overall, eight V ions in the unit cell: $\sigma = \sum_{i=1}^{8} \sigma_i$.

To calculate the total cross section we chose a cluster containing 135 atoms, that is 54 vanadium and 81 oxygen atoms in the correct ratio 2:3; the cluster has a radius of 6.9 Å, which is the limit to get convergence with the cluster size. The spectrum calculated with the real part of the Hedin-Lunqvist potential [34, 46] is convoluted with a Lorentzian function, with a width given by an energy-dependent damping $\Gamma(E)$, derived from the universal mean free path curve by the relation:

$$\lambda(E) = \frac{1}{k_e} \frac{E}{\Gamma(E)} \tag{5.3}$$

where E is the photoelectron kinetic energy in Rydberg and $k_e = \sqrt{E}$ its wave vector.

In Fig.5.8 we have plotted the numerical simulation of the in-plane XANES as calculated by FDMNES. The (a) and (b) curves are the calculated spectra corresponding to the experimental spectra A and B in Fig.5.7, while the (c) spectrum is the experimental

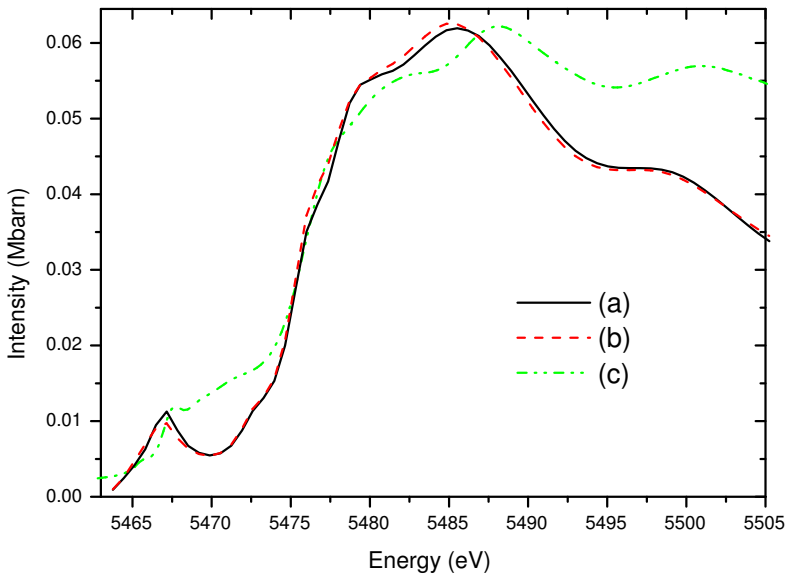

Figure 5.8: (a) and (b) are the calculated A and B spectra; (c) is the experimental curve A.

curve A, the edge peak of the spectra were normalized for a better comparison.

The agreement between experimental measurements and numerical simulations is rather good, even though the theory underestimate the energy distance between the peak at 5467 eV and the main peak (18 eV vs 20.5 eV). This may be a consequence of the potential we used to describe the electron-atom scattering in the MS equations, because it is known that the Hedin-Lundqvist exchange-correlation part is too attractive near the edge [64]. This compression of the energy scale in the theoretical spectrum is evident also from Fig.5.9, where experimental and theoretical in-plane linear dichroism are compared. Here (a) is the experimental dichroic signal calculated as $\sigma_y - \sigma_x$ (B-A) and (b) is the signal calculated from the numerical simulations in the same way. We can see that the energy scale of the latter is compressed with respect to the former, anyway all other main features of the experimental signal are well described by the calculation. We expanded the energy scale, in fact, by a factor of 1.14 in Fig.5.9(c) in order to better guide the eye and in this case it is evident that all the main peaks and valleys are correctly reproduced at almost all energies. The same observations could be made on Fig.5.8. About this figure we must also notice that the theoretical spectra differ from the experimental one around 5470 eV, as if there were a missing of density of states in the pre-edge region. This problem could arise from the single-particle ap-

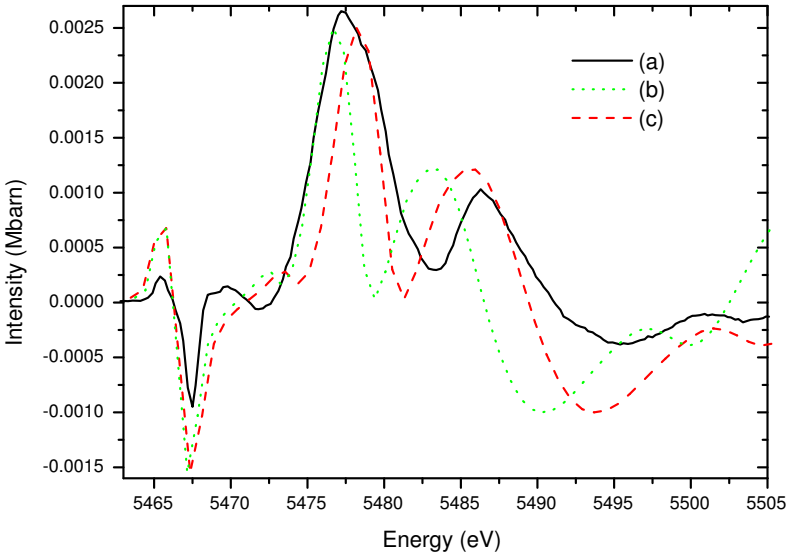

Figure 5.9: Experimental and theoretical in-plane linear dichroism. (a) Experimental plot, (b) curve obtained from the simulations, (c) theoretical curve with an expanded energy scale.

proach of our calculation, because in this way the upper Hubbard band is missed, that would require a many-particle theory to be taken into account.

Another important feature is that no extra scale factors are needed to describe the relative intensity of linear dichroism and XANES spectra, as both experimental absorption coefficients and theoretical signals show a ratio of about 3%.

Finally, we underline that the signal is found to be of purely dipolar origin (E1-E1), because our calculation contains only the E1-E1 term and neglects the interference terms (E1-E2) and the pure quadrupolar term. This means that the experimental dichroic signal has a pure structural origin: it is the structural monoclinic distortion to originate the signal and not a magnetic effect [53]. This result clashes with a previous work [33]; this could be due either to fact that the authors, using a magnetoelectric annealing during the experiment, had a transition into another monoclinic domain, or by an accidental geometrical setup with the two orthogonal polarizations at 45° from the monoclinic b axis. In this latter case in fact they would not find structural dichroism. For what concerns the first hypothesis, we are sure we did not change monoclinic domain during the experiment, as it will explained in next sections.

Once we checked the structural origin of the dichroic signal, we calculated the

difference $\sigma_y - \sigma_x$ in all the temperature range, to study the evolution of the structural changes when the temperature varies. In Fig.5.10 the experimental dichroic spectra are plotted. We can see that also for $T > 180$ K in the trigonal phase there is a non zero dichroic signal. This fact seems to point to a different description of the structural changes so as they are reported in literature, since from a local point of view the transition appears not so sharp but a residual anisotropy remains also above the transition temperature. This evidence points towards the hypothesis put forward by RXS experiments [9], therefore a more accurate local investigation must be carried out. A study of the local structure of V_2O_3 by means of EXAFS analysis is reported in the next sections in order to understand the structural evolution of this system.

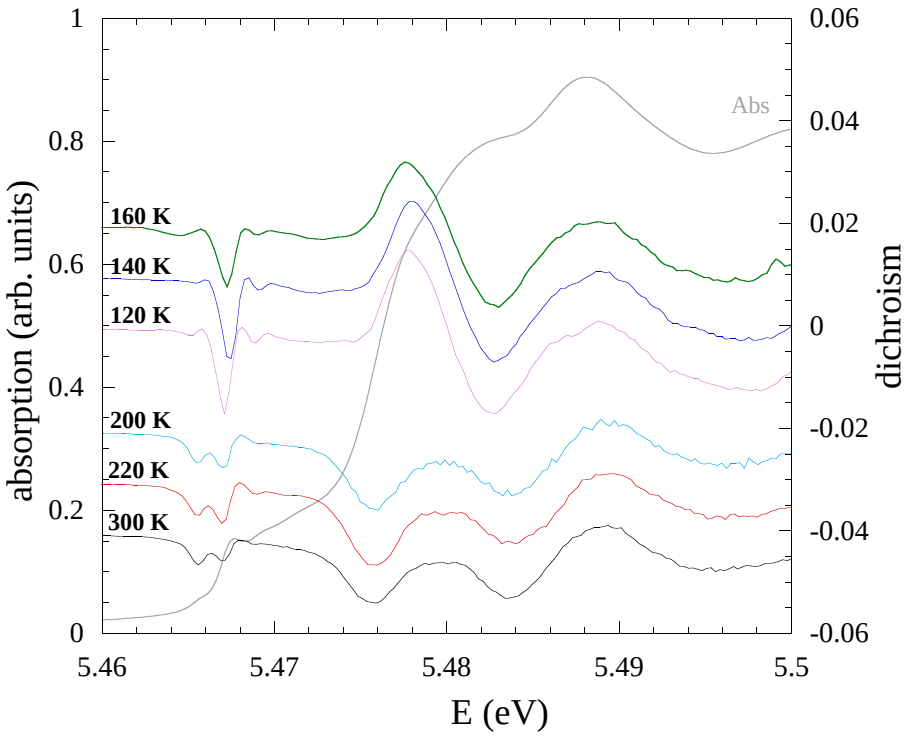

Figure 5.10: Spectra of dichroism ($\sigma_y - \sigma_x$) at different temperatures, above and below the transition temperature.

5.2.2 Analysis of the polarized EXAFS signals

The analysis of the EXAFS spectra follows two steps: first we have to extract the EXAFS signal, in order to isolate the structural contributions from the atomic background, then we quantitatively analyze the extracted signal through the simulation of the spectra and the minimization of the difference between the simulation and the

experimental one.

Extraction of the EXAFS signal

As explained in Chap.3, the total absorption cross section contains both the contribution due to the atomic absorption and the structural features due to the interaction of the photoelectron with the surrounding atoms. By a linear fitting of the spectrum at energies in the range 5320-5410 eV, we simulated the pre-edge behaviour and subtracted this line from the spectrum to isolate the K absorption edge of vanadium. Then, we determined the energy E_0 corresponding to the origin of the photoelectron energy scale, as the maximum of the first derivative of $\mu(E)$. The discrepancy between the effective bond energy of the electron and E_0 is unknown and this difference is a free parameter to be optimized in the best fitting procedure. Using this energy value, we calculated the absorption atomic coefficient μ_0 by a polynomial curve with three splines. The nodes and order of the splines determine the curve that approximates μ_0 and which is subtracted from the total spectrum. The remaining properly normalized spectrum is the XAFS signal. In our case the polynomial splines fit to the data in the k range 2.3-11.6 $\mathring{A}^{-1}$, being $k = \hbar^{-1}\sqrt{2m(E - E_0)}$; we used three splines with degree 3. In Fig.5.11 the XAFS signals extracted for the three polarizations at different T are shown. We describe first the fitting of the data collected on ID26 beam-line, which have been measured with linearly polarized light on a crystal sample.

Fitting of the EXAFS signal: significant scattering contributions

The extracted EXAFS data were analyzed quantitatively. In the best fitting procedure, the experimental EXAFS signal is "compared" with the theoretical Standard EXAFS Formula (eq.3.49). In order to do this, we use a software which optimizes several parameters, by minimization procedure. Throughout the analysis, we always fitted the theoretical formula to the experimental EXAFS signal, without any Fourier filtering.

In order to obtain the structural parameters from the fitting, that is the mean interatomic distances R_s, the coordination numbers N_s and the widths of the distances distributions σ_s, it is necessary to know the non structural parameters contained in the Standard EXAFS Formula: the scattering amplitudes $|f_s(\pi)|$, the phase shifts $\phi_t^{(s)}(k)$ and the inelastic contributions S_0^2 and λ. These parameters can be either calculated theoretically or extracted from the EXAFS signal of a reference sample. In our case the amplitude and phase functions were calculated by FEFF8.2 [2]. This software uses the complex Hedin-Lunqvist empirical potentials in the muffin-tin approximation and

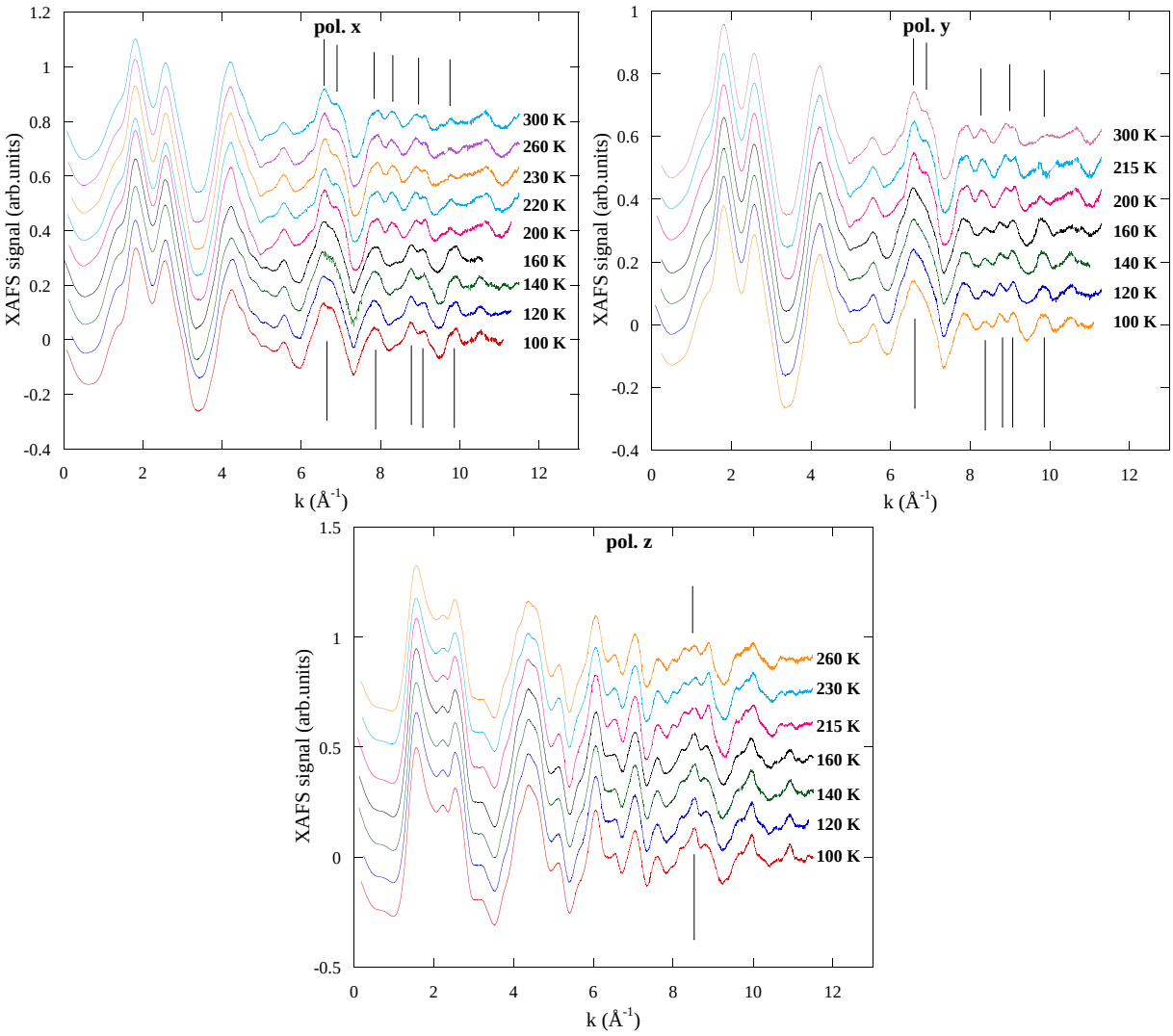

Figure 5.11: XAFS signals extracted for the three polarizations at different T.

solves the multiple-scattering equation, according to the crystallographic structure of the system to be studied. In our case, amplitudes and phases of V_2O_3 were calculated using the trigonal symmetry for the PI state and the monoclinic one for the AFI phase. These are the two reference structures for the following analysis. To take into account the polarization dependence of the absorption spectra, we used the option of FEFF8.2 which allows to calculate amplitudes and phases for a specific polarization vector, for this reason we have six sets of $|f_s(\pi)|$ and $\phi_t^{(s)}(k)$ corresponding to x, y and z polarizations, for each of the two reference structures.

FEFF8.2 generates amplitude and phase functions for each possible scattering path, which contributes to the total spectrum. For this reason it is necessary to choose only the most important contributions to the EXAFS signal, to simplify the calculation of

the theoretical signal. In order to verify which are the significant paths, we performed a series of simulations. We chose the scattering paths which reproduce the main features of the spectra in the k range 3-11 $\mathring{A}^{-1}$ and we took into account all the two-body signals corresponding to atomic distances up to $\sim 7\mathring{A}$. In Fig.5.13 the chosen paths are illustrated; Fig.5.12 shows the sections of the cell in the xy and xz planes. In a first stage, we considered more contributions than those which are shown here. To evaluate the importance of the various contributions we made many trials fitting the data in the k range 3-11 $\mathring{A}^{-1}$, then the signals with a difference in R_s minor than 5% are gathered together in a single one. The significance of weak contributions (i.e., with a large σ_s^2) is statistically checked by means of the F-test and eventually removed. As a final step, all the parameters for the remaining signals are refined at the same time: first all the R_s, than the σ_s^2 altogether. At the end of this procedure we get the final values for the structural parameters using the signals reported in Tab.5.7 and 5.8 and shown in Fig.5.13).

At low temperature the crystallographic structure is monoclinic and the significant contributions used to simulate the EXAFS signal are the following:

a. x and y polarizations: the first contribution is due to the single-scattering from the O_6 octahedron, that is the nearest-neighbours oxygen ions, with a crystallographic mean value R=2.013 Å; then there is the effect of the 3 V ions in the hexagonal plane, the V atoms nearest-neighbours, with R=2.862 Å, R=2.876 Å and R=2.986 Å (Fig.5.13a). These shells are the strongest contributions to the spectra; the others we considered correspond to the second, third and fourth shell of oxygen ions (Fig.5.13g) and to three shells of V ions (Fig.5.13c,d). Therefore in the case of monoclinic symmetry, with x and y polarizations we have 8 signals which determine the main features of the spectra. We described these paths according to the hexagonal symmetry just for the sake of simplicity, since in the monoclinic structure those ligands are only distorted with respect to the trigonal one.

b. z polarization: the significant signals are 9; the strongest, as in the previous geometry, are $V-O_1$ and $V-V_1$, where V_1 in this case is the vanadium atom along the vertical axis, out of the hexagonal plane, with R=2.745 Å (Fig.5.13a). Then there are 5 shells of V atoms and other two contributions from the oxygen ions, that we labels as O_2 and O_6 since they are the second and the sixth coordination sphere of oxygens (Fig.5.13b).

At high temperature we used as a starting atomic configuration the trigonal structure and the significant paths to the spectra are:

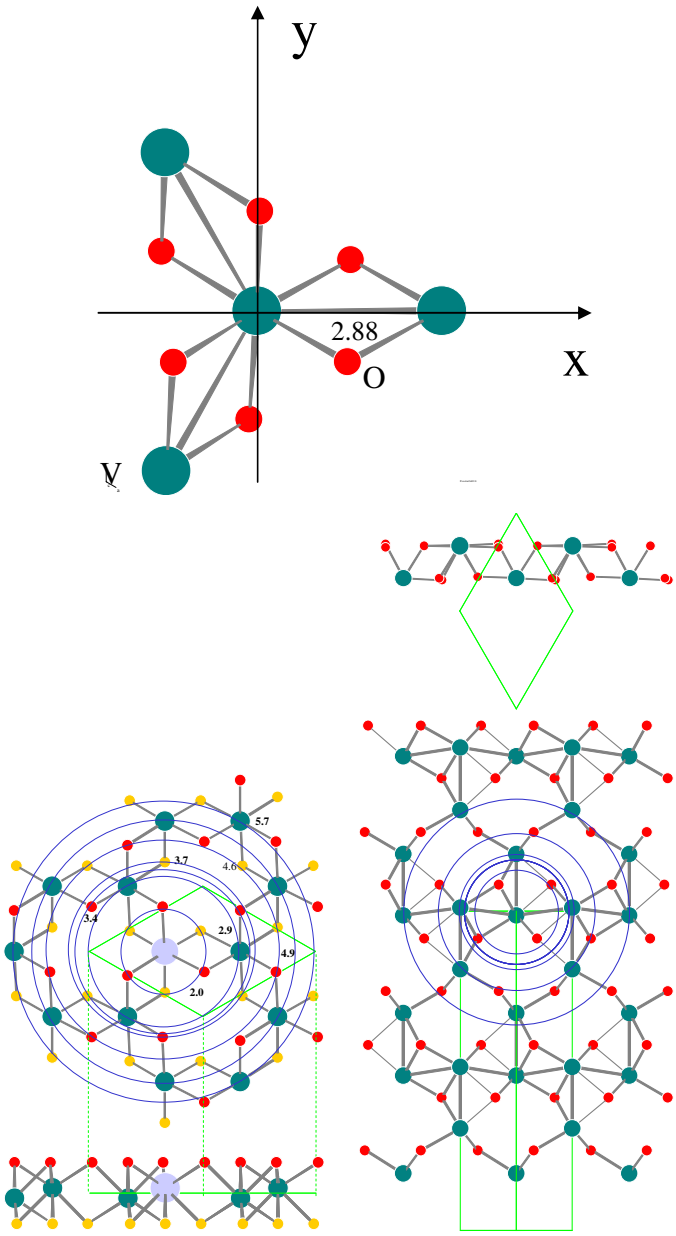

Figure 5.12: The first picture shows the SECTION of the first and second shell (O_6 octahedron and nearest-neighbours V atoms) in the xy plane; the second picture shows the section in the same plane of the trigonal cell of V_2O_3: the red circles represent the O atoms above the xy plane, while the yellow ones represent the O atoms below this plane. The last picture shows the section of this cell in the xz plane.

c. x and y polarizations: the most important signals are those corresponding to the distances $V - O_1$ (mean value R=2.007 Å) and $V - V_1$ (R=2.887 Å) (Fig.5.13a); then there are the contributions from the atoms labelled V_2 and V_3 in Fig.5.13c, with R=3.449 Å and R=3.690 Å; from the third and fourth shell of oxygen ions (O_3 with R=3.704 Å and O_4 with R=4.343 Å, Fig.5.13e); from the V ions in the hexagonal

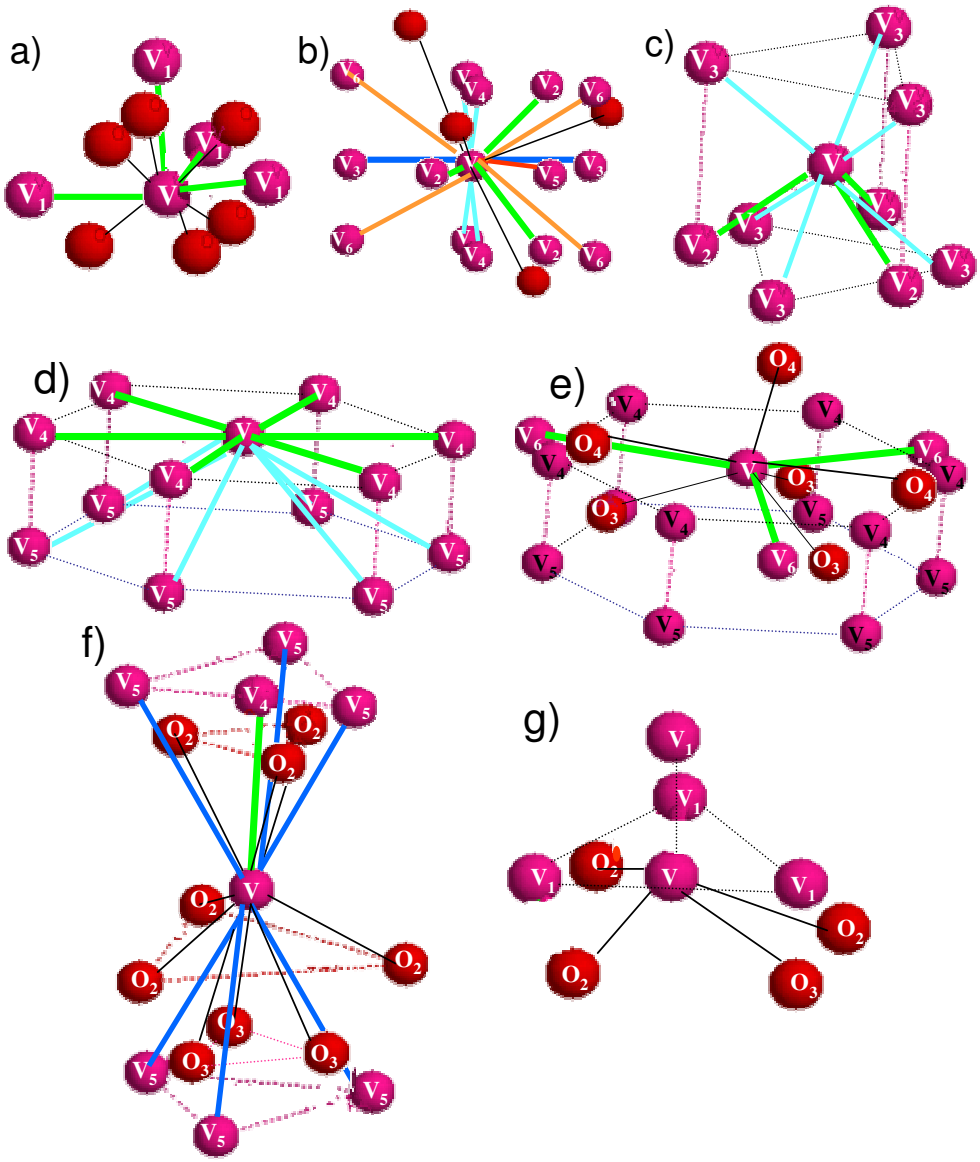

Figure 5.13: Contributions to experimental data in the monoclinic phase, with polarizations along x and y are represented in figures a),c), d) and g); paths for spectrum in the monoclinic phase with polarization along z are in a) and b); significant contributions to signals in the trigonal phase, with polarizations x and y, are described in fig. a), c), d) and e), whereas the contributions to the signal with z-polarization above the transition temperature are those in a), c) and f). The paths corresponding to the low temperature spectra with x and y polarizations are described according to the hexagonal symmetry just for the sake of simplicity, since in the monoclinic structure those ligands are only distorted.

plane coplanar to the V absorbing atom ($V - V_4$, with R=4.952 Å) and those in the lower hexagonal plane (V_5 with R=5.658 Å, Fig.5.13d). Finally, there is one more signal which is significant to the x and y polarized spectra, which corresponds to $V - V_6$ in Fig.5.13e (R=5.732 Å).

d. z **polarization:** in these spectra the contributions that are different, with respect to those in the x or y-polarized data, are $V - O_3$ (R=4.085), $V - V_4$ (R=4.263 Å) and $V - V_5$ (R=5.473 Å) (Fig.5.13f), while the $V - O_2$ shell contains more O atoms than the same shell in the x or y-polarized spectra. Moreover, if we compare these contributions with those in the monoclinic phase, we see that the one due to V-V_3 is split, in the low T phase, into two contributions: V-V_{3A} and V-V_{3B}.

As regards the effect of multiple scattering paths on the EXAFS signal, all those indicated by FEFF8.2 are less significant than the single-scattering contributions we chose. This can be explained by the observation that there are no paths which can contribute to the so-called "focusing effect", that is configurations with almost aligned atoms, for whom the probability of multiple scattering is strongly enhanced (Fig.5.14).

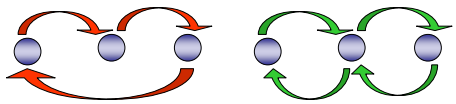

Figure 5.14: Focusing effect.

Since many coordination shells contribute to the EXAFS spectra, we fixed the coordination numbers N_s in the fitting to their crystallographic values, because we do not expect them to change. We calculated the multiplicity N_s of each shell according to the formula

$$N_s = 3 \sum_j \cos^2 \vartheta_j, \tag{5.4}$$

where ϑ_j is the angle between the polarization vector ϵ and the position vector $\vec{r}_j$ of the jth atom of the sth shell. In this way the closer is the position vector to the polarization direction, the larger is the contribution of the atom to the EXAFS signal. The value of N_s for each shell is reported in Tab.5.7 and Tab.5.8, together with the corresponding crystallographic distances, for the three polarization vectors in the monoclinic or trigonal symmetry. We must underline that the reported distances refer to the pure V_2O_3 and not to the Cr-doped compound, because crystallographic data on $(V_{1-x}Cr_x)_2O_3$ in the monoclinic phase are not available, whereas Dernier and Marezio [17] in 1970 reported only the interatomic distances in the corundum phase of $(V_{1-x}Cr_x)_2O_3$. In their work, the only difference between the distances of $(V_{1-x}Cr_x)_2O_3$ and pure V_2O_3 in the corundum structure is a very slight extension of the bonds due to the addition of Cr: for example, the V-V_{1z} distance becomes 2.745

Å instead of 2.700 Å and V-V_{1xy} is 2.914 Å instead of 2.887 Å. This difference is not important in the fitting procedure, because the crystallographic values are just a starting point of the calculation.

								T < 180 K
x			y			z		
path	N	R_s (Å)	path	N	R_s (Å)	path	N	R_s (Å)
V-O_1	5.9	2.013	V-O_1	5.9	2.013	V-O_1	6.1	2.013
V-V_1	4.2	2.908	V-V_1	4.6	2.869	V-V_1	3.0	2.745
V-O_2	4.1	3.395	V-O_2	2.8	3.416	V-V_2	2.8	3.453
V-V_2	3.1	3.453	V-V_2	3.2	3.461	V-V_{3A}	2.5	3.625
V-O_3	2.5	3.762	V-O_3	2.6	3.722	V-O_2	4.7	3.679
V-V_{3x}	3.5	3.625	V-V_{3y}	5.4	3.726	V-V_{3B}	4.6	3.735
V-O_4	3.9	4.384	V-O_4	4.2	4.391	V-V_4	3.0	4.233
V-V_4	8.9	4.974	V-V_4	6.0	5.002	V-O_6	4.8	4.625
						V-V_5	8.8	5.429

Table 5.7: Scattering paths taken into account for the fitting of the low temperature data.

								T > 180 K
x			y			z		
path	N	R_s (Å)	path	N	R_s (Å)	path	N	R_s (Å)
V-O_1	5.9	2.007	V-O_1	5.9	2.007	V-O_1	6.2	2.007
V-V_1	4.4	2.887	V-V_1	4.4	2.887	V-V_1	3.0	2.700
V-O_2	4.1	3.374	V-O_2	4.1	3.374	V-V_2	2.8	3.449
V-V_2	3.1	3.449	V-V_2	3.1	3.449	V-V_3	7.2	3.690
V-V_3	5.4	3.690	V-V_3	5.4	3.690	V-O_2	8.3	3.713
V-O_3	3.9	3.704	V-O_3	3.9	3.704	V-O_3	7.4	4.085
V-O_4	2.8	4.343	V-O_4	2.8	4.343	V-V_4	3.0	4.263
V-V_4	9.0	4.952	V-V_4	9.0	4.952	V-V_5	13.	5.473
V-V_5	6.9	5.658	V-V_5	6.9	5.658			
V-V_6	4.5	5.732	V-V_6	4.5	5.732			

Table 5.8: Scattering paths taken into account for the fitting of the high temperature data.

Having determined the paths to use in the theoretical calculation of EXAFS spectra,

we proceeded with the fitting procedure to obtain the structural parameters.

Fitting procedure

The fitting software minimizes the k^n-weighted square residual function:

$$Res_\chi^2 = \frac{1}{N}\sum_j \Big(\frac{k^n(\chi_j^{th}(k,P_i) - \chi_j^{expt}(k))}{w_j(k)}\Big)^2 \tag{5.5}$$

as a function of the parameters P_i. The sum runs over the N experimental points, $\chi_j^{expt}(k)$ is the experimental value in the k_j point, $w_j(k)$ is the uncertainty associated to each measured data point and k is the weight. We used n=1 for all the spectra. The uncertainty $w_j(k)$ was calculated as

$$w_j(k) = |\chi_j^{expt}(k) - \bar{\chi}_j(k)| \tag{5.6}$$

where $\bar{\chi}_j(k)$ is a smooth high degree polynomial spline through the experimental data. The average uncertainty in the experimental data $\bar{w}$ resulted in being better than 10^{-3}.

The minimization of (5.5) is performed by the MINUIT package of the CERN library [36]. The free parameters are the structural parameters R_s and σ_s^2 and the non structural ones ΔE_0 and S_0^2 for each coordination shell contributing to the signal. The mean free path λ was calculated by FEFF8.2 and used without further corrections.

The total number of parameters we have to refine is too high to let them all free to vary, because in this case the fitting would not give an accurate output. This is due to the strong correlations among the parameters, therefore we proceeded following some intermediate steps that consisted in fixing, from time to time, some of them, then releasing these and fixing the others. First we fixed all the structural parameters and refined the energy scale ΔE_0 and the S_0^2; then ΔE_0 and S_0^2 were fixed and the interatomic distances R_s were adjusted keeping fixed the Debye-Waller factors σ_s^2; the refinement cycles through these steps so that all the R_s and σ_s^2 of each considered signal vary.

The errors on the optimized parameters have been evaluated using the MINOS routine of the MINUIT package, that takes into account also the correlation between parameters. The correlation between two parameters of the fitting is highlighted by the option of MINUIT named "contour", which plots the curves corresponding to a constant value of χ^2 when two parameters vary. For example, the curve in Fig.5.15 shows different curves with constant χ^2 created by MINUIT, where the concentric ellipses correspond to different values of χ^2 and from them we calculated the errors. Examples

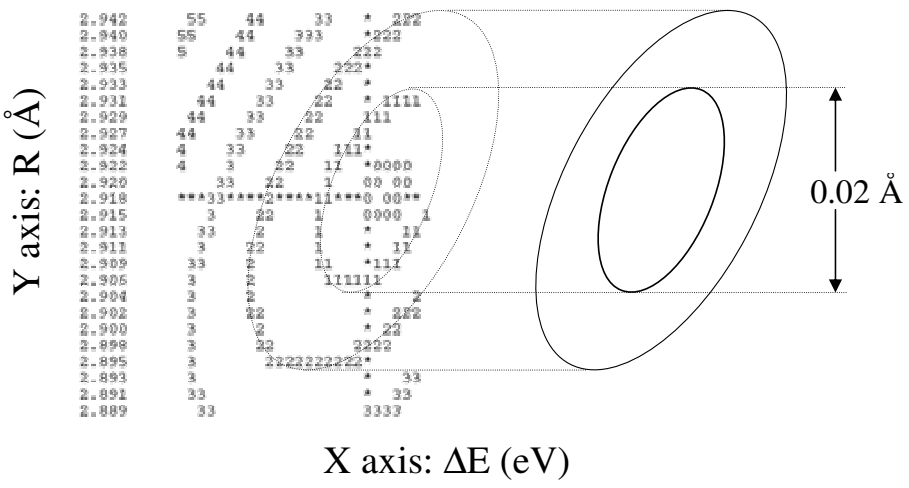

Figure 5.15: Examples of calculation of the errors: concentric ellipses correspond to different values of χ^2 and from their distance we calculated the errors.

of fittings for the three polarizations, above and below the transition temperature, are reported in Fig.5.16 and 5.17.

For each spectrum we report also the corresponding Fourier transformation. From them we can identify the peaks corresponding to the various shells; the position of the peak corresponds to the distance of the shell from the absorber. The intensity of the peak is proportional to the coordination number. During the fitting procedure, we found that not all the shells we chose contribute to the experimental spectra in a significant way. This means that the reduced χ^2 does not change if some of these signals are not considered. This fact is due to the strong correlations among the signals and also to the structure of the system, because some shells are very close to each other and the distributions of distances can be described by a single disordered shell in an equivalent way. Therefore, in the final fittings we neglected some contributions in order to make the calculation more stable.

In particular, in the monoclinic phase the V-O_3 contribution in the x-polarized spectra and the V-O_4 in the y-polarized ones do not strongly affect the fitting and so does the V-O_2 contribution in the z-polarized spectra. In the high temperature phase we found that we can neglect the effect of V-O_2 in the x and y-polarized spectra.

Of all the contributions that fitted the EXAFS data, the most stable for what concerns the dependence on the initial conditions are those due to: the scattering from the shell of the oxygen octahedron; the scattering from the nearest-neighbours V ions (V_1: planar V for x and y polarization and vertical V atom for the z polarization) and the scattering from the 6 V ions in the hexagonal configuration, coplanar to the central

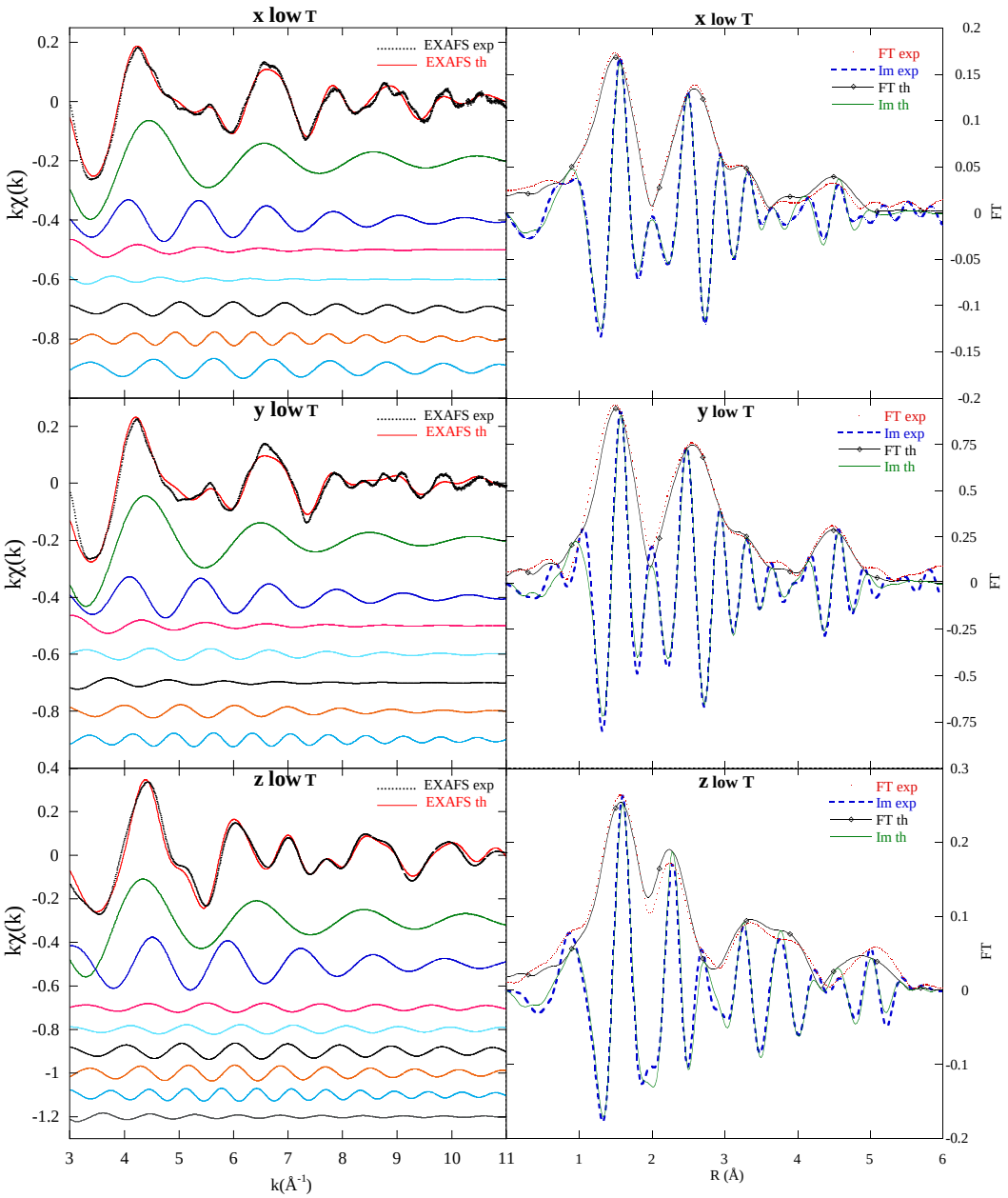

Figure 5.16: Examples of fittings of EXAFS signal and its FT below the transition temperature, for polarizations x, y and z.

absorber in the case of x and y polarizations (V-V_4 for x and y, V-V_5 for z). The other signals reproduce quite well the structural features both in the EXAFS data and in its Fourier transformation (Fig.5.16, 5.17), but they are too correlated among themselves and probably tend to compensate all the other weak contributions that we neglected in our analysis because their amplitudes were too small. For this reason we think that their absolute values obtained from the fitting are not reliable; on the other hand the

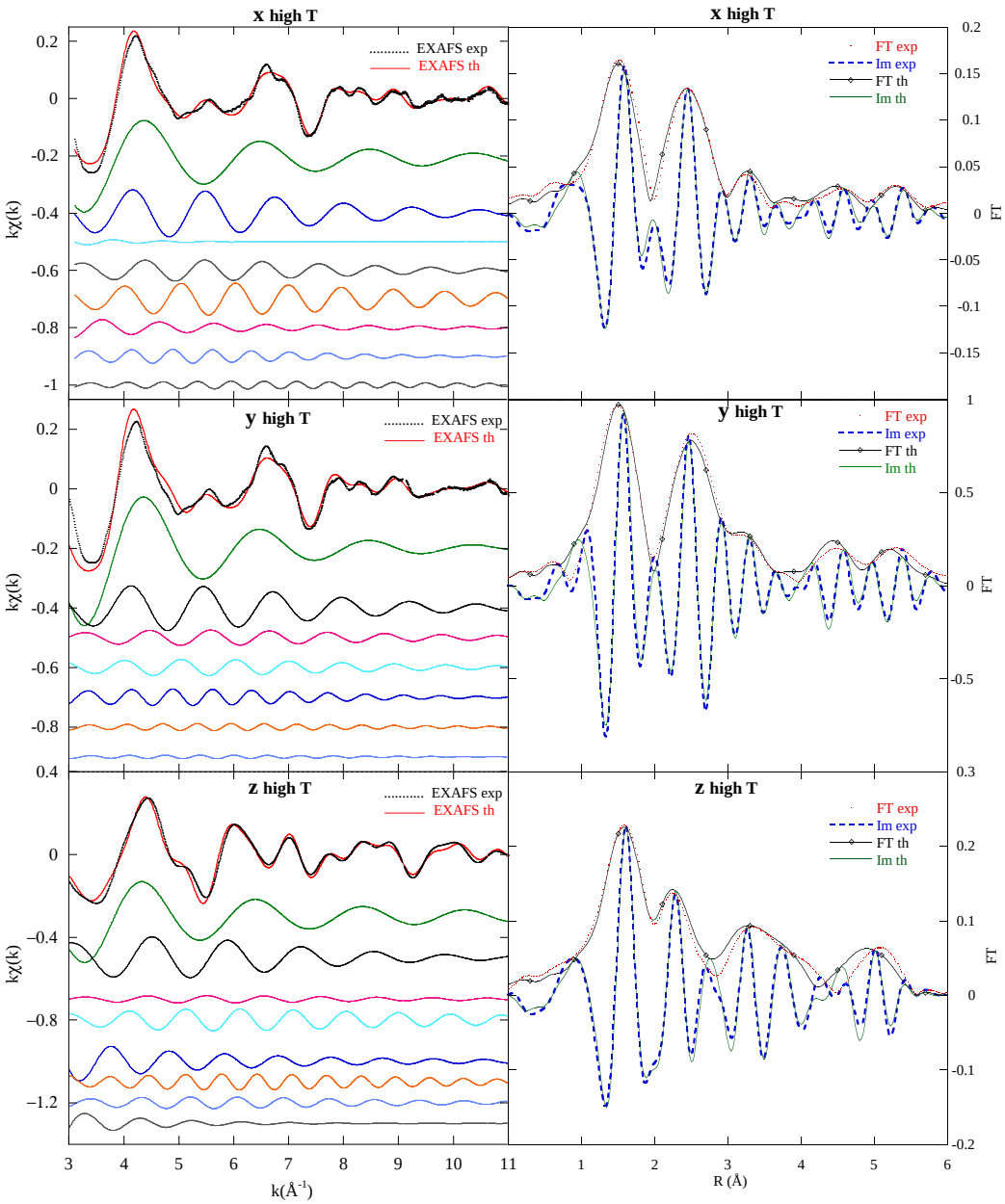

Figure 5.17: Examples of fittings of EXAFS signal and its FT above the transition temperature, for polarizations x, y and z.

results for the V-O_1, V-V_1 and V-V_4 (or V-V_5) shells show a very good reproducibility, because they are independent from the initial conditions. Therefore, in the following we will show only the results for these signals. As can be observed in Tab.5.7, 5.8, in the x, y-polarized case, at high T we used V-contributions until ∼5.7 Å (V-V_5, V-V_6), whereas at low T we stopped at ∼5 Å (V-V_4): we can see from Fig.5.16 and 5.17 that at high T there are two peaks instead of one. We can explain this evidence by

considering that in the trigonal structure there are 9 V atoms sharply distributed into two shells at ∼5.65 Å (6 V) and ∼5.73 Å (3V), therefore their Debye-Waller factor is due to thermal effects. On the contrary, the V atoms in the monoclinic structure are spread over a wider range of distances: there are not two well defined shells, therefore they have a high σ^2 which sums to the thermal disorder. For this reason the peak at ∼5.7 Å does not appear in the low temperature data.

5.2.3 EXAFS results and discussion

First of all we must comment on the choice of the crystallographic symmetry we used to fit our data. After many trials using the monoclinic or the trigonal structure as input starting configurations, we concluded that it is not possible to discriminate between these two symmetries fitting the signal and its Fourier transformation until ∼ 5 Å; nevertheless the trigonal structure can reproduce better the contributions to the signal in a range longer than 5 Å. A quite clear indication of this fact comes from the EXAFS signals (Fig.5.11) and their Fourier transformations (Fig.5.18).

In fact, looking at the extracted XAFS signals (Fig.5.11) and their Fourier transformations (Fig.5.18), it is evident that there is a structural change at the transition temperature. The XAFS signals both with x and y polarizations, for energies above 6 $Å^{-1}$, show clear differences in the spectral features above and below the transition temperature, as indicated in the figures. Moreover if we compare the signals with x and y polarizations among themselves, we can see that above T_N they are almost the same, indicating that at high temperature the in-plane local symmetry is not broken and there is not difference between the x or y observation direction. At low temperature, instead, for energies higher than 6 $Å^{-1}$ the spectra corresponding to the two directions are different, because the in-plane symmetry is broken. From these first observations we can find that also locally the structure around V is different above and below T_N. As expected, the z-polarized spectrum shows just little differences at high or low temperature.

We find a confirmation to these observations looking at the Fourier transformation of the spectra (Fig.5.18). We can see that for atomic distances shorter than 5 Å, the FT of the x-polarized spectra below and above the transition temperature does not present differences, except for a very slight shift of the second peak towards higher R values decreasing T; there is an evident difference, instead, for R> 5 Å, where a peak, which is present at high T, disappears at low T. A similar behaviour is displayed by the FT of the y-polarized spectra, while the z-polarized FT does not show clear

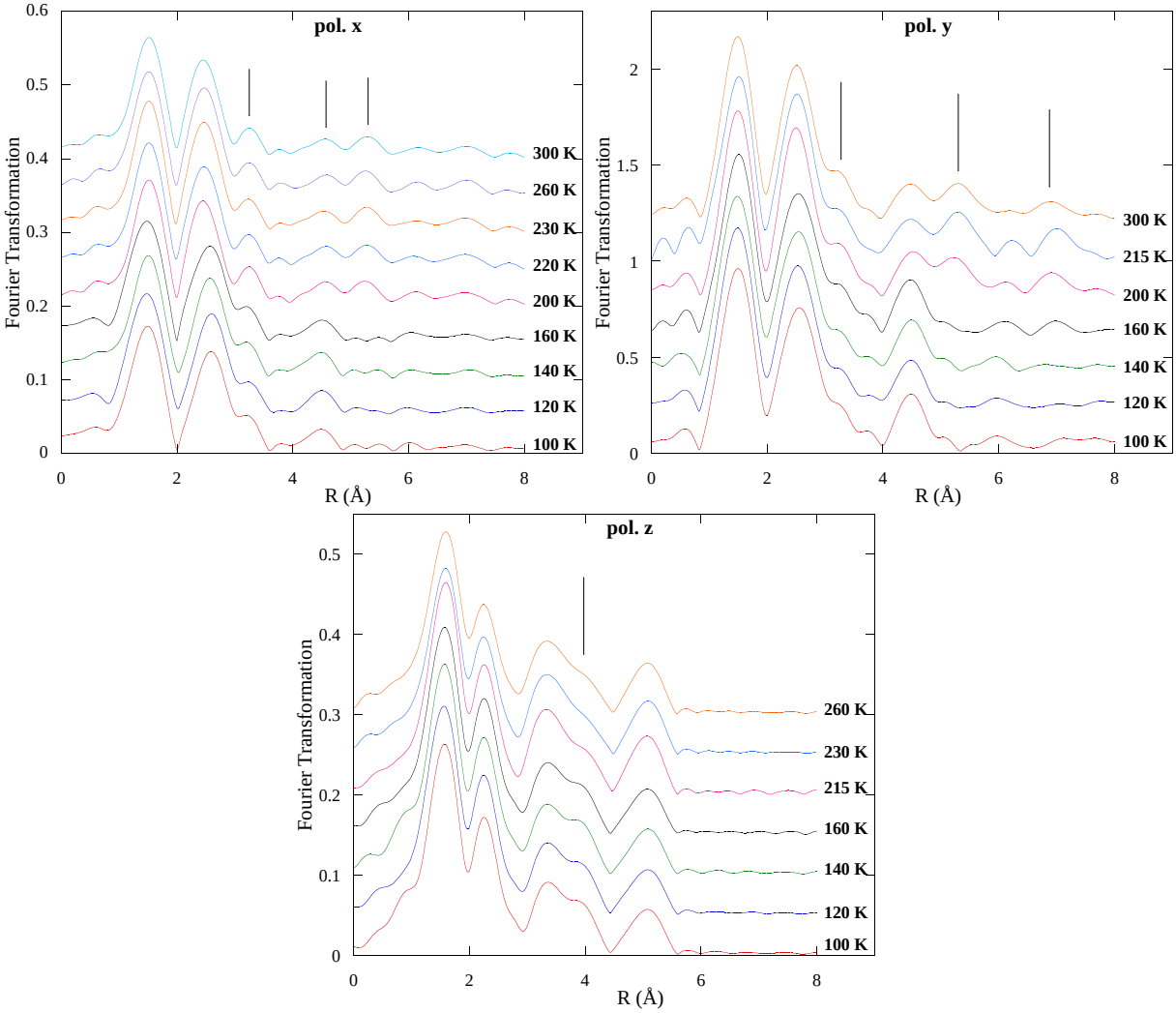

Figure 5.18: Fourier transformations of the EXAFS signals extracted for the three polarizations at different T.

variations changing T. From these qualitative considerations we can conclude that the local surrounding of the central V ion can be described by both the monoclinic and the trigonal symmetry if we look at the nearest-neighbour atoms; we can say that the monoclinic cell is necessary to describe the local structure at low T, while at high T the probe see the trigonal cell.

The fittings of the EXAFS signals, however, give us a quantitative insight on the local structure through the transition. The main information can be achieved from the trend of V-V_1 distance with T. The V_1 atoms are the nearest-neighbours vanadium ions around the absorber, therefore this distance describes the local structure of the first coordination shell and gives a measure of the local distortions of the fundamental units of the V_2O_3 structure, that is the V-V couples.

If we look at the V-V_1 distance in the x direction, we find that the effect of the transition on this bond is evident (Fig.5.19). The distance increases from about 2.91±0.01 Å above the transition temperature up to 2.97±0.01 Å below T_N. The transition is sharp, because V-V_1 shows a plateau above T_N, then there is a steep increase in the distance and then another plateau for $T > T_N$. Therefore the effect of the drop in temperature on the V_1 atom, along the x direction, is the elongation of this ligand.

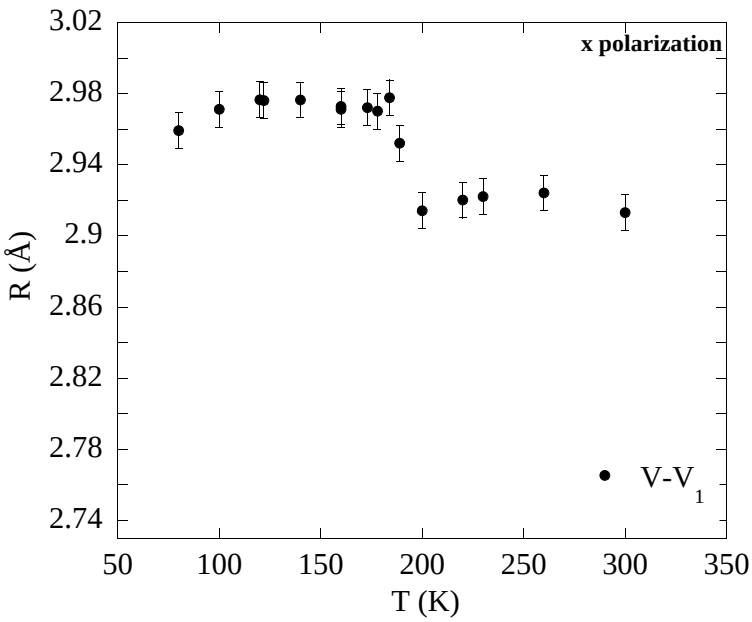

Figure 5.19: Values of the V-V_1 distance along the x direction as the temperature changes.

Looking at the other V-V_1 distance, instead, we find that there is no local change along the trigonal axis (z) when passing through the transition (Fig.5.20). The average distance does not change in a wide temperature range far above and below the transition temperature. A similar behaviour has been measured in the y direction (i.e. the direction of the AFM propagation vector): no significant changes are observed in the average V-V_1 distance along this axis.

If we consider the results of the other neighbour shells, that is the oxygen octahedron and the 6 V atoms in the hexagonal plane of the cell (or along the trigonal axis for the z-polarized spectra), we can see (Fig.5.21) that the distance of the V-O_1 ligand does not change significantly at the transition temperature and the mean value of the oxygen atoms' distance in the octahedron follows what observed by diffraction experiments [48]. Even the V-V_4 (V-V_5) distance does not show significant changes as the temperature decreases and the average value present just a very slight decreasing, as reported also by diffraction.

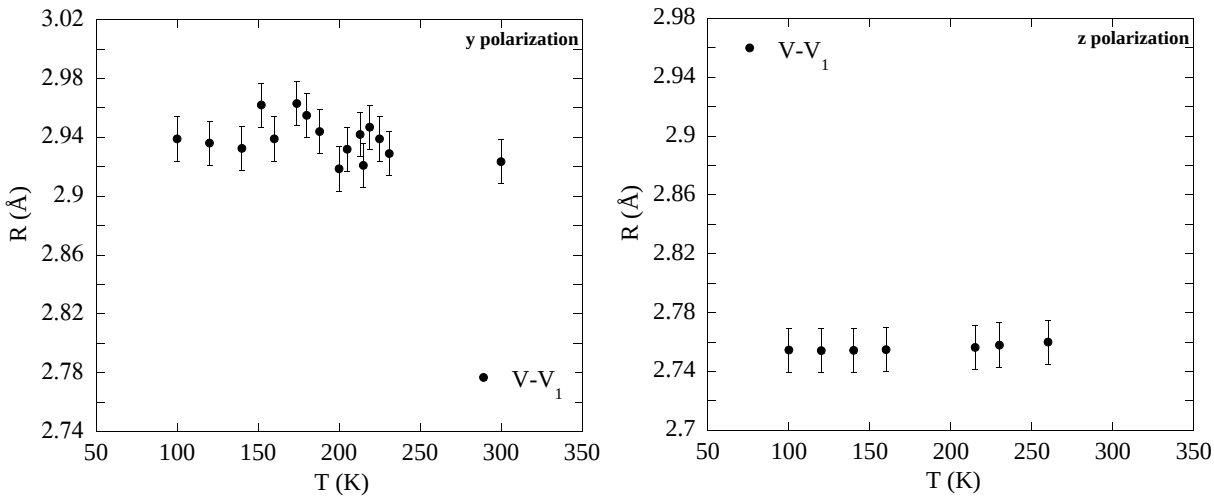

Figure 5.20: Values of the V-V_1 distance along the y and z directions as the temperature changes.

The main results obtained from the compared analysis of Fig.5.19, 5.20 and 5.21 suggest that the PI-AFI transition is strongly different from the PM-AFI transition as determined by the EXAFS analysis in Ref.[70], because the authors identify two distinct movements: the positioning of the V atoms in the basal plane and the change of the V-V pair distance along the c-axis; in fact they see an increase both in the in-plane V-V_1 distance and in the vertical V-V_1 distance; in addition the transition in the basal plane is not sharp as we found. Moreover the behaviour is also definitively different from that recorded in Ref.[71] for the same PI-AFI transition in the Al-doped compound.

A possible distortion mechanism for the structural transition as observed in our study is the following: the central V_0 atom rotates in the xz plane, around the y axis, and simultaneously the V_1 atom in the x direction (V_{1x}) rotates in the opposite way of the same angle, so that at the end of the rotation the net effect is the elongation of the V_0-V_{1x} ligand (Fig.5.22).

This implies that along the y direction the V_0-V_1 distance (V_0-V_{1y}) remains unchanged and so does the vertical distance V_0-V_1 (V_0-V_{1z}). In fact also V_{1z} is at the center of another hexagon and it performs the same movement as V_0 around the y axis in the specular direction with respect to V_0, so that the V_0-V_{1z} distance does not change but the net effect is the rotation of this ligand around the y axis, as reported also in literature from diffraction studies. In this framework, therefore, the elongation of the V_0-V_1 distance along x is a measure of the tilting of the V-V vertical molecule in the xz plane.

The invariance of the V_0-V_{1z} distance shows also that, when the V-V ligands

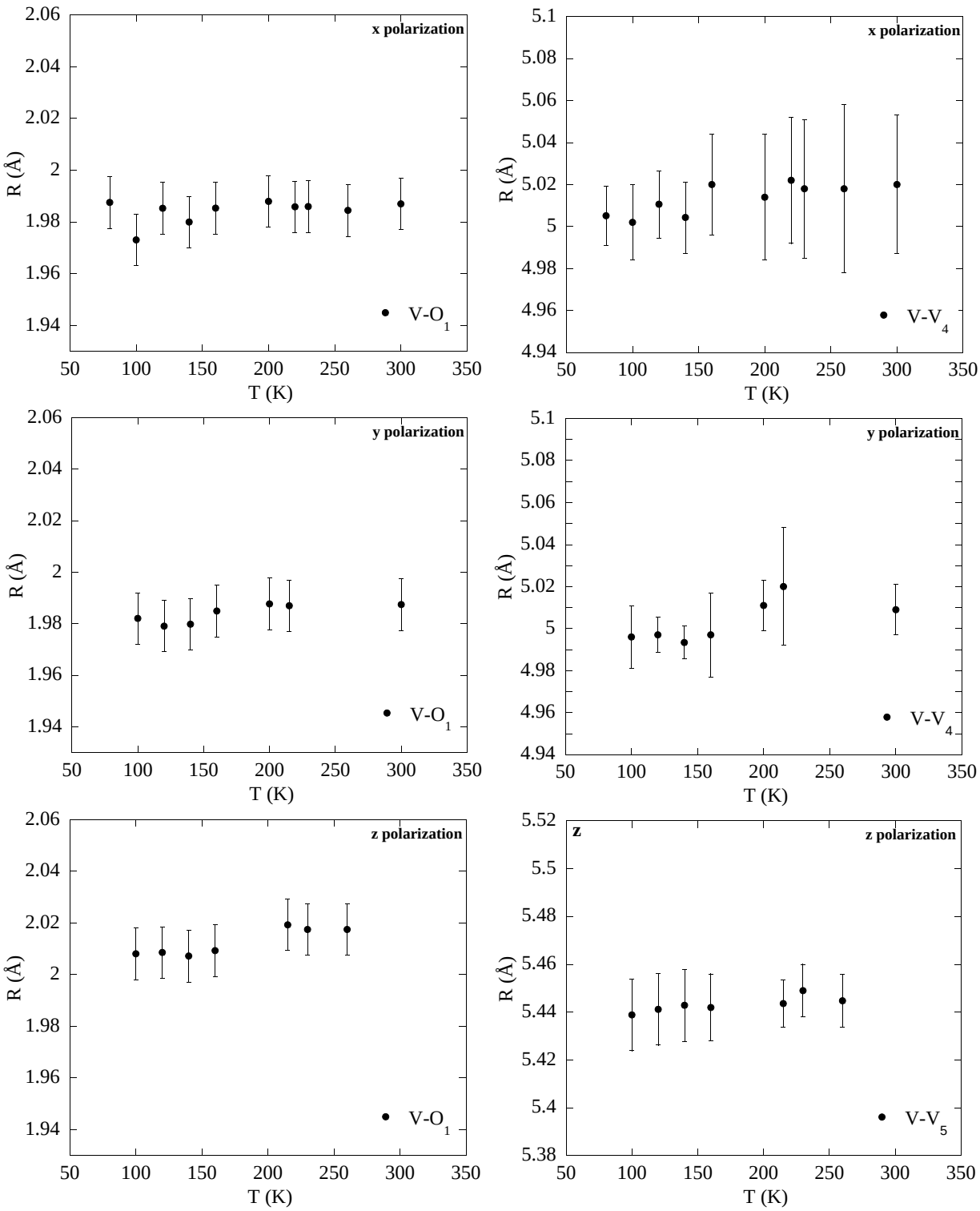

Figure 5.21: Values of the V-O_1 and V-V_4 (V-V_5) distances along the x, y and z directions as the temperature changes.

lengthen due the Cr addition to the compound, the transition does not cause a further increasing of the cell's volume but only the tilting of the vertical molecule.

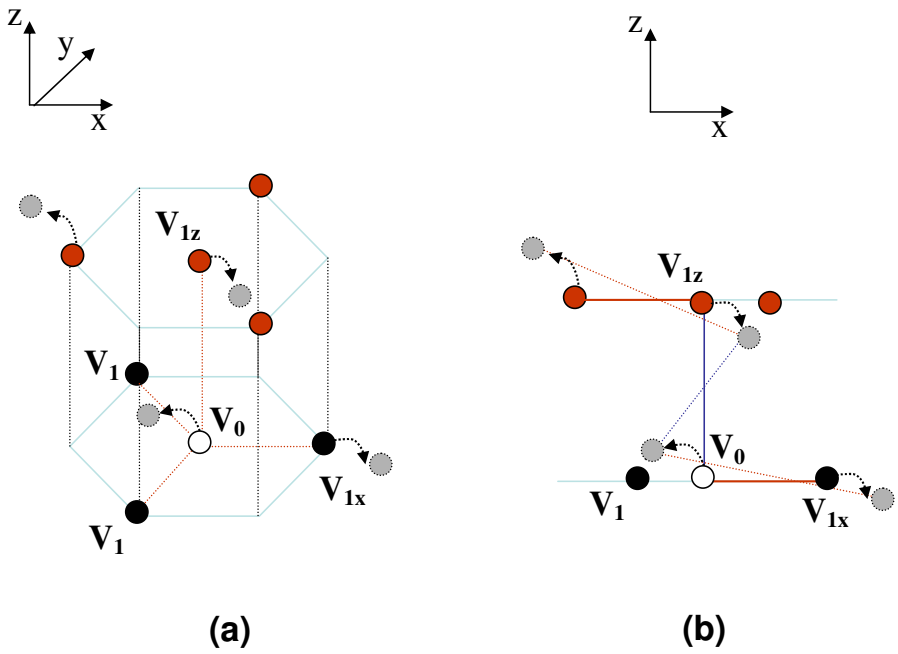

Figure 5.22: The arrows indicate the rotation of the V atom around the y axis. The net effect of this rotation is the elongation of the V-V_{1x} distance and the titling of the V-V_{1z} vertical molecule.

This situation is coherent with the tilting of the molecule measured by diffraction experiments, which report a rotation around the y axis of about 1.8°, which means that if the V_{1x} atom rotates of the same amount in the apposite way, we should expect an increasing of the V_0-V_{1x} distance of $\sim$ 0.08 Å and hence the value we found ($\sim 2.97 \pm 0.01$ Å) is consistent with the one expected ($\sim 2.90 + 0.08$ Å).

Moreover observing the results achieved from these fittings, we can also conclude that our system presents only one big macro-domain, or at least a mono-domain sufficiently larger than the photons beam-spot. At low temperature in fact the monoclinic domain is large enough that we always see the longer V-V_1 ligand in the same direction (x in our coordinate system), otherwise we should observe an average distance over all the different micro-domains. Finally we can discard the hypothesis suggested by RXS studies [9] about the presence of both distorted and undistorted sites (i.e. monoclinic and hexagonal sites) just above the transition temperature, as if the transition would not be sharp. We cannot discard another hypothesis presented in this work [9], instead, about the existence in the high temperature phase of many different monoclinic domains which could be differently oriented, so producing an average trigonal symmetry.

A possible way to check this second hypothesis can be to analyze the XANES region of the spectra by means of numerical simulations and fittings of the V K-edge.

As I said previously, the XANES part of the absorption spectrum contains all the information related to the topology of the sample, that is XANES are sensitive to the orientation of the atoms around the absorber. Therefore, if differently oriented monoclinic domains would exist in the high temperature phase, XANES spectroscopy would allow to achieve this information. At the moment we started the simulation of the XANES spectra of V_2O_3 in the high and low temperature phases, using the FEFF8.2 software. Moreover we are fitting this region of the spectra using the MXAN code, because as we saw it allows a more complete and detailed refinement of the local structure, for what concerns both the ligands' distances and angles. In this way we are confident we can verify the hypothetic domains distribution suggested in Ref.[9]. Finally, the analysis of the XANES will permit also to further check the results we obtained from our EXAFS study.

5.2.4 Cr K-edge

In spite of the huge amount of publication on V_2O_3 and its phase diagram, there are very little investigations about the role of chromium in Cr-doped samples. In most cases, the problem is dealt with qualitatively, by stating that the role of Cr is to increase the average cation-cation distance, which leads to a mechanism for the metal-insulator transition that is the one traditionally described by Mott. However, the mechanism that leads to the effective increase in the cation-cation distance is usually not explained. The original thinking that Cr^{3+}-ion has a longer average radius than V^{3+}-ion does not hold, because it is known that the same average increase in the cation-cation distance can be obtained by doping with Al^{3+}-ion [71], which is definitively smaller. The mechanism behind the localization of the two $3d$ electrons of V^{3+}-ion is more probably determined by the relative position of electronic levels in V^{3+}-ion and Cr^{3+}-ion. In the case of Cr^{3+}-ion, each ion carries three $3d$ electrons occupying the t_{2g} subband coupled to spin 3/2, according to the intra-atomic Hund's rule. Setting another electron on a site occupied by a Cr ion would require the occupancy of one of the upper e_g levels with the same spin, due to the high value of the Hund's coupling $J \simeq 1$ eV. Even though the reference $3d$ level is lower for Cr ions than for V ions and even though there can be intra-atomic exchange energy gain if the electron occupying the e_g levels has the right spin polarization, the process might easily cost some fractions of eV. In this way, it is as if the Cr-occupied site has to be counted as a site onto which the V-$3d$ electrons cannot jump, due to the presence of an effective repulsive potential barrier. Hence, increasing the Cr percentage leads to an effective reduction

of conductivity. Actually we are facing a percolation problem, therefore it becomes interesting to know whether Cr^{3+} ions are distributed randomly in the crystal or a kind of local correlation sets in, in such a way that there is a strong probability that a Cr^{3+} ion has another Cr^{3+} ion as a first or second nearest neighbour.

In order to settle this problem, we have performed near-edge absorption measurements at the Cr K-edge, as well as a series of numerical calculations through the FDMNES program [38], with several clusters characterized by the presence of one or more Cr^{3+} ions in different positions. We considered the following cases:

- **one** Cr atom per unitary cell;
- **two** Cr atoms per unitary cell; in this case the simulations differ among themselves according to the position of the second Cr atom, that replaces V_2, V_3, V_4, etc.

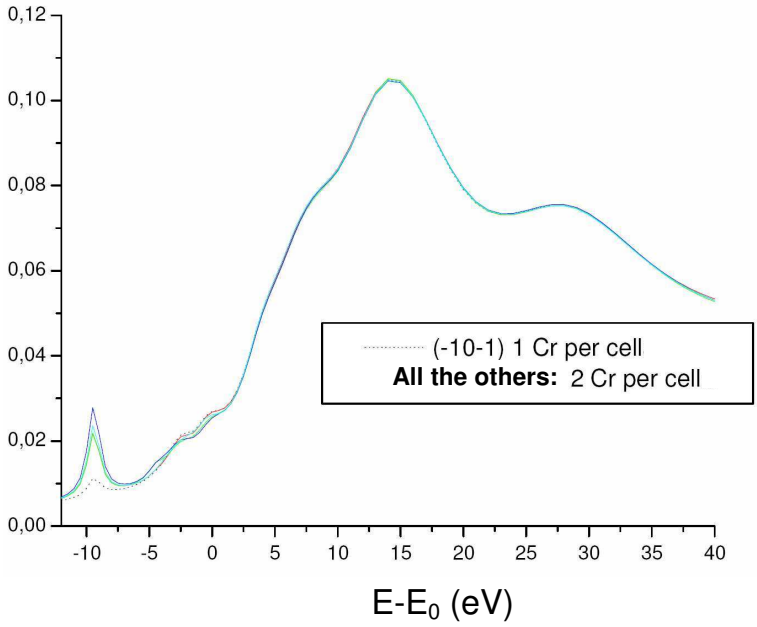

Figure 5.23: Numerical simulations of the Cr K-edge: the dotted line is the calculation obtained with one Cr atom per unitary cell; all the others are obtained adding a second Cr atom replacing different V positions.

The calculations are shown in Fig.5.23. We can see that if we consider only one Cr atom per unitary cell, then the pre-edge region of the Cr K-edge presents just a very low peak at about 10 eV before the edge. Instead if we add a second Cr atom in another V position, then a very clear peak appears in that region. Let us compare these

calculations with the experimental absorption edges of Cr, both below the transition temperature (T=100 K), and above (T=300 K), in the unpolarized and polarized cases. Figures 5.24, 5.25 and 5.26 show the experimental data.

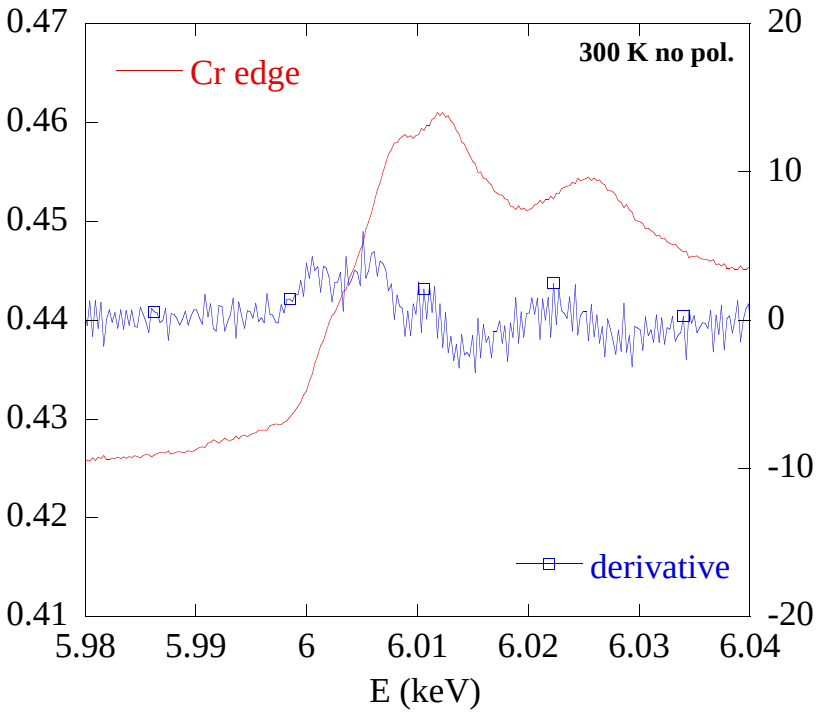

Figure 5.24: Cr K-edge at room temperature and its derivative. The spectrum is not polarized.

First of all we see that the Cr edges in the x and y polarization condition, at both 100 K and 300 K, present some small differences among themselves, while the difference becomes evident when they are compared to the z polarized XANES: this is the same situation we found for the K-edge of the vanadium absorber and then depends on the symmetry of the system.

A more important observation concerns instead the pre-edge region, where we can see that there is not any peak in any polarization or temperature condition. Therefore, considering what we obtained from the numerical simulation, we can deduce that in the real system the Cr atoms arrange themselves in such a way that no more than one atom settles in each unitary cell.

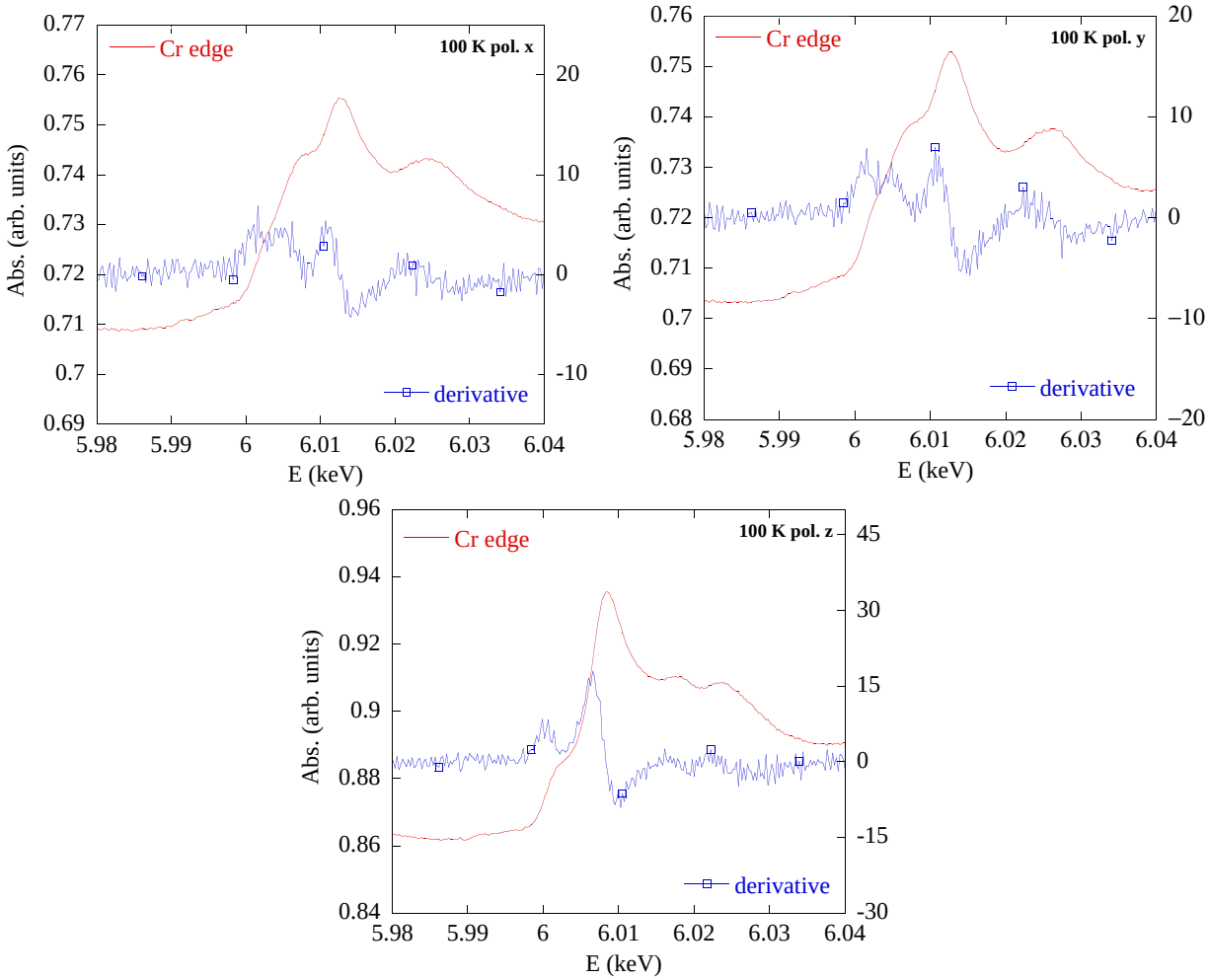

Figure 5.25: Cr K-edge at T=100 K and its derivative for the x, y and z polarized spectra.

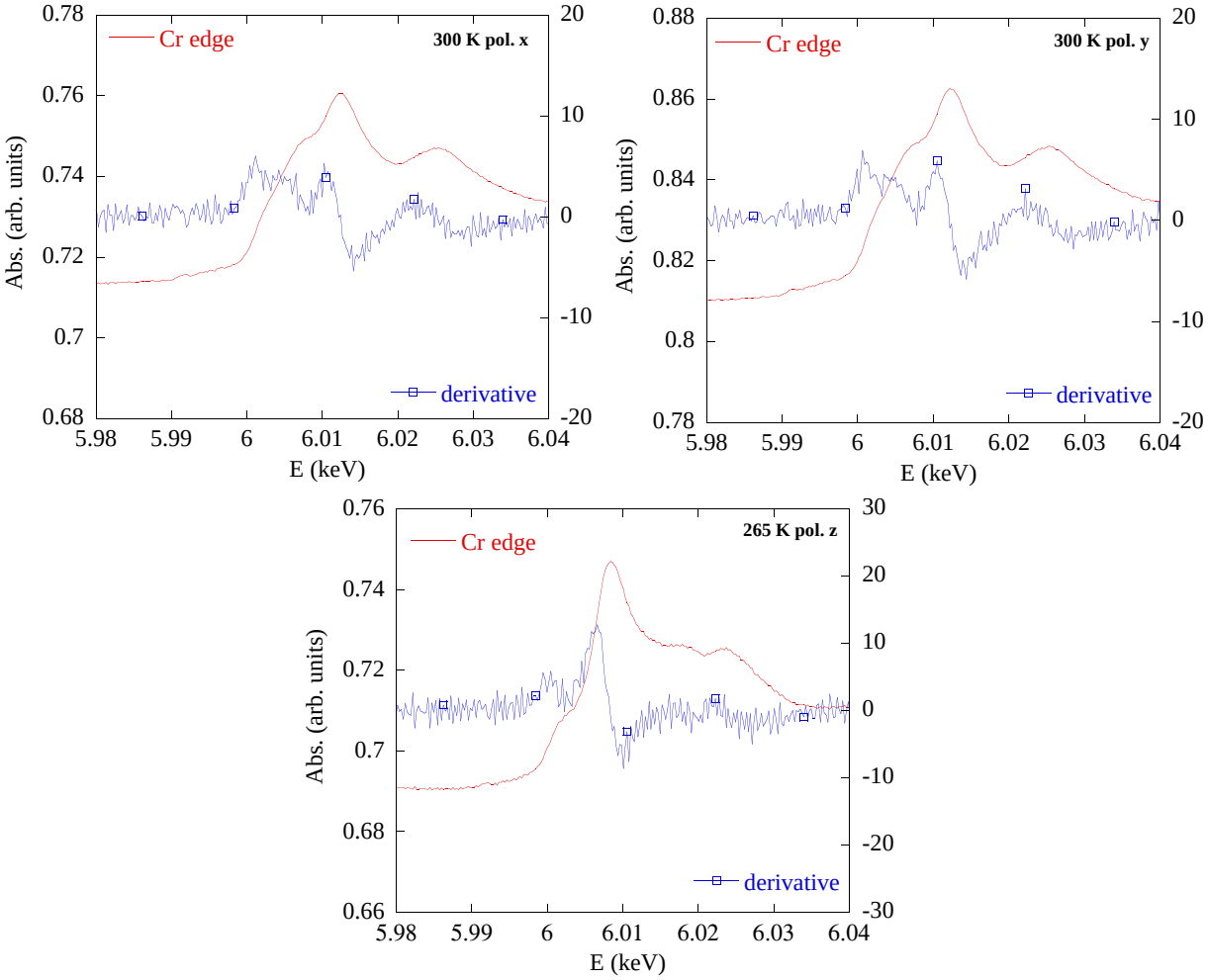

Figure 5.26: Cr K-edge at T=300 K and its derivative for the x, y and z polarized spectra.

Conclusions

In this thesis I presented the study of three transition metal oxides, $LaMnO_3$, $CaMnO_3$ and Cr-doped V_2O_3. Although these systems show different properties, nevertheless all of them exhibit various phase transitions that are strongly connected to their local structure. X-ray absorption spectroscopy was used for this study, due to its high sensitivity in investigating the structure around the transition metal ion: Mn in the case of manganites and V and Cr in Cr-doped V_2O_3.

The importance of the structure around the manganese atom is due to its role in the Jahn-Teller effect, that takes place as a consequence of the electronic structure of Mn^{3+} in $LaMnO_3$: since the e_g energy levels in Mn^{3+} are degenerate and half-occupied, the ion undergoes the Jahn-Teller distortion that removes the degeneration and, as a consequence, deforms the oxygen octahedron MnO_6 around Mn.

The importance of the local structure around the vanadium ion is due to the fact that the V atoms couple along the c-axis of the hexagonal cell forming a sort of molecule which is the fundamental unit of the crystal. Thus the properties of the systems depend on the electronic structure of this "molecule" and hence they are related to the local structure around V, determined by this bond.

The Mn K-edge X-ray absorption spectra were recorded at the GILDA-BM8 beamline of the European Synchrotron Radiation Facility (ESRF); the experiment was performed in transmission mode at T=298 K. The XANES analysis concerned the energy region from 10 eV below the edge up to 180 eV above the edge. In order to obtain information from the XANES, we used a recent code named MXAN. This software is based on the multiple scattering theory, therefore it allows to calculate the absorption cross section taking into account the full multiple scattering of the photoelectron emitted by the absorbing atom, which is the probe of this experimental technique. Moreover MXAN performs the fitting of the theoretical calculation to the experimental data, thus it allows a quantitative refinement of the local structure around the absorber.

The complete fitting of the XANES data shows that the agreement between the

calculations and the experimental spectra is very good. Moreover the structural data obtained from the fitting are in rather good agreement with the crystallographic data and compatible with those obtained in literature from the extended region of the XAS spectrum. In $CaMnO_3$ the average Mn-O_1 distance is in good agreement with the average crystallographic distance. The XANES results suggest that there are three shorter ($\sim$ 1.904 Å) and three longer ($\sim$ 1.924 Å) bonds, in agreement with the crystallographic structure. Even the Mn-O_1-Mn bond angle found by XANES and diffraction are the same, as well as the bond angle distribution width. For what concerns the Mn-Ca_1 distance, the fitting results point out an asymmetric Mn-Ca_1 distribution, in very good agreement with the diffraction results.

In the $LaMnO_3$ samples the main structural features derived from XANES are in good agreement with the EXAFS results reported in literature, confirming the consistency of the XANES fitting even in this complex case. The XANES analysis shows a bimodal distribution of Mn-O_1 distances with four nearest-neighbours and two longer bonds. The shorter Mn-O_{1p} distances found by the analysis are in good agreement with the crystallographic distance. However, the XANES analysis suggests all the planar oxygen ions to be at the same distance, while the crystallographic structure points out two different distances, and the Mn-O_{1a} distance found with the fitting is shorter than the diffraction value. In our case the contraction is observed only for one distance, the long Mn-O_{1a} bond, while all the other structural parameters show a general agreement between XANES and crystallographic results. This points towards the presence of a real shorter distance of the Mn-O_{1a} bonds. The contraction of the apical Mn-O bond length could be at least partially due to local deviations from ideal stoichiometry in this sample. The average Mn-O_1-Mn_1 bond angles found by XAS are a little larger than the average crystallographic value; the XANES show a broad θ_{O_1} distribution with a bimodal trend (as for $CaMnO_3$ sample) with two smaller and four larger angles. This finding differs from the sharp distribution of the crystallographic structure. The Mn-La_1 distances found by our analysis, instead, are the same as those obtained by diffraction. We can state that there exist a difference in the actual local structure of $LaMnO_3$ with respect to the one inferred from diffraction measurements. The good results obtained in these two reference manganite compounds encourage us to extend this approach to doped manganites as well, in which the details of local structure are a fundamental issue to the comprehension of their magnetotransport properties. Up till now this is not possible yet, because a parallelized version of MXAN is needed which is still not available.

X-ray absorption spectra at the V K edge were collected in fluorescence mode at the ID26 beam-line at the ESRF in Grenoble. The absorption spectra were collected for three orthogonal directions of polarization, that is along the corundum c axis (z), and in the hexagonal plane, along the monoclinic b axis (y) and the a axis perpendicular to it (x), in a temperature range from 80 K up to 300 K. We used these data to study the structural dichroism in the sample at low temperature and to analyze the EXAFS signal in the whole temperature range. The EXAFS analysis was performed both on the polarized spectra and on the unpolarized ones. Moreover we calculated the XANES of the K-absorption edge of Cr and compared the simulations to the experimental spectra above and below the transition temperature.

The dichroic signal was obtained as the difference between the data with y polarization and that one with x polarization, $\sigma_y - \sigma_x$. We focused on the XANES energy region to take into account both the electronic and structural differences. The calculation of the absorption cross sections σ_y and σ_x was performed in dipole approximation, therefore no magnetic effect was considered. The comparison of the experimental dichroic signal with the calculated one evidences that the agreement between experimental measurements and numerical simulations is rather good. In fact the main differences between the two dichroic spectra- the compression of the energy scale and the missing of density of states in the pre-edge region- can be ascribed to the potential used for the calculation. If we expand the energy scale, we find that all main features of the experimental signal are well described by the calculation. Moreover the intensity of the dichroic signal is very well reproduced by the theoretical simulation. We can conclude that this signal is of purely dipolar origin, that means that the experimental dichroic signal has a pure structural origin: it is the structural monoclinic distortion to originate the signal and not a magnetic effect, as stated in previous literature.

From the polarized-EXAFS analysis we found that at high temperature it is not possible to discriminate between the monoclinic and the trigonal symmetry fitting the signal and its Fourier transformation until $\sim$ 5 Å; nevertheless the trigonal structure can reproduce better the contributions to the signal in a range longer than 5 Å. The V-V_1 distance in the x direction increases when the temperature decreases through the transition temperature. Moreover the transition is sharp. Looking at the other V-V_1 distance, instead, we find that there is no local change along the trigonal axis (z) when passing through the transition. The average distance does not change in a wide temperature range far above and below the transition temperature. A similar behaviour has been measured in the y direction (i.e. the direction of the AFM propagation vector):

no significant changes are observed in the average V-V_1 distance along this axis. The distances of the other shells do not change significantly changing T, instead.

A possible distortion mechanism for the structural transition can be described as follows: the central V_0 atom rotates in the xz plane, around the y axis, and simultaneously the V_1 atom in the x direction (V_{1x}) rotates in the opposite way of the same angle, so that at the end of the rotation the net effect is the elongation of the V_0-V_{1x} ligand. This means that along the y direction the V-V_1 distance (V_0-V_{1y}) remains unchanged and so does the vertical distance (V_0-V_{1z}). In this framework, therefore, the elongation of the V-V_1 distance along x is a measure of the tilting of the V-V vertical molecule in the xz plane. The invariance of the V_0-V_{1z} distance shows also that, when the V-V ligands lengthen due to the Cr addition to the compound, the transition does not cause a further increase of the cell's volume but only the tilting of the vertical molecule. This situation is coherent with the tilting of the molecule measured by diffraction experiments, which report a rotation around the y axis of about 1.8°.

Moreover observing the results achieved from these fittings, we can also conclude that our system presents only one big macro-domain: at low temperature, in fact, the monoclinic domain is large enough that we always see the longer V-V_1 ligand in the same direction (x in our coordinate system). Finally we can discard the hypothesis suggested by RXS studies [9] about the presence of both distorted and undistorted sites (i.e., monoclinic and hexagonal sites) just above the transition temperature, as if the transition would not be sharp. We cannot discard another hypothesis presented in that work, instead, about the existence in the high temperature phase of many different monoclinic domains which could be differently oriented, so producing an average trigonal symmetry.

Appendix A

Multiple scattering equation: calculation details

A.1 Atomic scattering

The Hamiltonian of the system is $H = H_0 + V$, where H_0 is the Hamiltonian in the absence of the potential. Solving the Schroedinger equation

$$(E - H)\psi = 0 \tag{A.1}$$

is equivalent to solve the Green equation

$$(E - H)G(r - r'; E) = \delta(r - r') \tag{A.2}$$

with $G(r - r'; E) = \sum_n \frac{\psi_n(\vec{r})\psi_n^*(\vec{r}')}{E - E_n}$.

If we define the operator

$$G(E) = \frac{1}{E - H}, \tag{A.3}$$

the application of $G(E)$ to an eigenstate of H $|\psi_k\rangle$ gives (in units of $\frac{\hbar^2}{2m}$)

$$G(E)|\psi_k\rangle = \frac{1}{E - k^2}|\psi_k\rangle, \tag{A.4}$$

for each $E \neq k^2$. Therefore the eigenstates of H are also eigenstates of G and the eigenvalues of H are poles of $G(E)$, so that both the eigenstates and eigenvalues of H can be obtained from $G(E)$.

Now we consider the states in the continuum because we want the scattering states, not the bound states, that is $E > 0$ and in particular the values of $E = k^2$; it is possible to define $G(E)$ as

$$G(E) = \lim_{\varepsilon^+ \to 0} \frac{1}{E - k^2 \pm i\varepsilon} = G^{\pm}(k^2). \tag{A.5}$$

When H reduces to H_0, $G^{\pm}(k^2) = G_0^{\pm}(k^2)$, with k solution for V=0. In this case the Green function corresponds to that obtained for $\psi_n = \frac{1}{\sqrt{V}} e^{i\vec{k}\cdot\vec{r}}$, that is a plane wave solution of the free equation. With these wave functions the Green function becomes:

$$G_0(r - r'; E) = \sum_n \frac{\psi_n(\vec{r})\psi_n^*(\vec{r}')}{E - k^2 \pm i\varepsilon} \to \frac{1}{(2\pi)^3} \int d^3k \frac{e^{i\vec{k}\cdot(\vec{r}-\vec{r}')}}{E - k^2 \pm i\varepsilon} \tag{A.6}$$

The double sign in $\pm i\varepsilon$ corresponds to the outgoing and ingoing waves, because through the choice of the sign the integral in the complex plane can be solved taking into account the right physical conditions on the wave function.

Since we are interested only in the outgoing wave, and there are two poles corresponding to $k = \pm\sqrt{E}$, we have to choose the pole in $k = \sqrt{E}$; in this way the solution becomes:

$$G_0^+(r - r'; E) = -\frac{1}{4\pi} \frac{e^{i\sqrt{E}|\vec{r}-\vec{r}'|}}{|\vec{r} - \vec{r}'|}. \tag{A.7}$$

This expression shows that $G_0^+(r - r'; E)$ is the amplitude at $\vec{r}$ of a spherical wave created at $\vec{r}'$. For this reason, when the eigenvalues of H_0 are positive, $G_0^{\pm}$ is usually termed the free electron propagator. G_0^+ describes outgoing waves, while the time-reversed G_0^-corresponds to ingoing waves. Likewise, the resolvent $G^{\pm}$ is called the propagator of the electron in the presence of the potential V.

A.2 Expansion of the propagator in partial waves

It is very useful to develop the propagator G in partial waves [62], to apply successfully this method to the solution of the Schroedinger equation in the MS approach.

Let's consider the expression of G_0 (eq.A.6 in A.1). Since it is possible to expand a plane wave in spherical waves

$$e^{i\vec{k}\cdot\vec{r}} = \sum_L 4\pi i^l j_l kr Y_L(\hat{k}) Y_L(\hat{r}), \tag{A.8}$$

we can rewrite the integral in G_0:

$$G_0^+(r-r';E) = \frac{1}{(2\pi)^3}\int d^3k \frac{e^{i\vec{k}\cdot(\vec{r}-\vec{r}')}}{E-k^2+i\varepsilon} =$$
$$= \frac{1}{(2\pi)^3}\int_0^\infty \frac{k^2dk}{E-k^2+i\varepsilon}\int d\Omega_k \sum_{LL'}(4\pi)^2 i^{l-l'} j_l(kr)j_{l'}(kr')\cdot Y_L(\hat{r})Y_{L'}(\hat{r'})Y_L(\hat{k})Y_{L'}(\hat{k}) =$$
$$= \frac{2}{\pi}\sum_L Y_L(\hat{r})Y_L(\hat{r'})\int_0^\infty \frac{k^2dk}{E-k^2+i\varepsilon} j_l(kr)j_{l'}(kr') \tag{A.9}$$

because $\int d\Omega_k Y_L(\hat{k})Y_{L'}(\hat{k}) = \delta_{LL'}$.

Remembering the properties of the Bessel functions $h_l^\pm = j_l \pm in_l$, $j_l(-kr) = (-1)^l j_l(kr)$ and $h_l^-(-kr) = (-1)^l h_l^+(kr)$, the integral becomes:

$$\begin{aligned} G_0^+(r-r';E) &= \frac{2}{\pi}\sum_L Y_L(\hat{r})Y_L(\hat{r'})\int_0^\infty \frac{k^2dk}{E-k^2+i\varepsilon} j_l(kr)\frac{(h_l^+(kr')+h_l^-(kr'))}{2} \\ &= \frac{1}{\pi}\sum_L Y_L(\hat{r})Y_L(\hat{r'})\Big\{\int_0^\infty \frac{k^2dk}{E-k^2+i\varepsilon} j_l(kr)h_l^+(kr') + \\ &\quad \int_{-\infty}^0 \frac{k^2dk}{E-k^2+i\varepsilon}(-1)^l j_l(kr)(-1)^l h_l^+(kr')\Big\} \\ &= \frac{1}{\pi}\sum_L Y_L(\hat{r})Y_L(\hat{r'})\int_{-\infty}^\infty \frac{k^2dk}{E-k^2+i\varepsilon} j_l(kr)h_l^+(kr'). \end{aligned} \tag{A.10}$$

Through the integration in the complex plane, we can solve the integral and we leave out the solution corresponding to the negative pole, since we are searching for the outgoing waves. We finally find:

$$\begin{aligned} G_0^+(r-r';E) &= -i\sqrt{E}\sum_L Y_L(\hat{r})Y_L(\hat{r'})j_l(\sqrt{E}r)h_l^+(\sqrt{E}r') \\ &= -i\sqrt{E}\sum_L J_L(\sqrt{E}\vec{r}_<)H_L^+(\sqrt{E}\vec{r}_>) \end{aligned} \tag{A.11}$$

where $r_<$ and $r_>$ indicate $r' > r$, the condition for the integral to be convergent. This condition just means that in the calculation, when we have the product $j_l(kr)j_l(kr')$, we must transform in a combination of $h_l^\pm$ the j_l with the biggest $\vec{r}$ among r and r'. This condition assures that for $k \to \infty$ the integral goes to zero.

A.3 Multicenter expansion of the propagator

We consider Fig.A.1 to define our framework: R_i and R_j are the distances of the centers of two atoms i and j from an origin O external to the atoms; R_{ij} is the distance among

i and j; r_i and r_j are the distances of points on i and j respect to the centers of i and j, whereas r and r' are the distances of these same points respect to O.

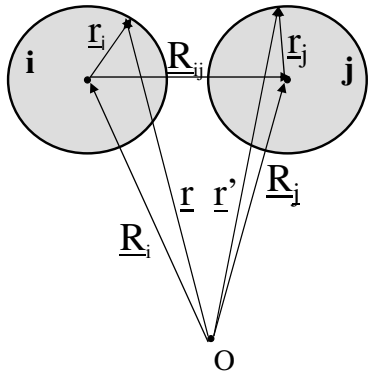

Figure A.1: Scheme of a two atoms system, in which the atoms are labelled i and j.

We want to expand the propagator G_0^+ according to this vector diagram, considering two ions at R_i and R_j respect to O. Since G_0^+ is given by (eq.A.6), we can rewrite it considering the following relation among the position vectors:

$$\vec{r} - \vec{r'} = \vec{r} - \vec{R}_i + \vec{R}_i + \vec{R}_j - \vec{R}_j - \vec{r'} = \vec{r_i} - \vec{r_j} + \vec{R}_{ij} \tag{A.12}$$

and G_0^+ becomes:

$$G_0^+(\vec{r} - \vec{r'}) = \frac{1}{(2\pi)^3} \int \frac{d^3k}{E - k^2 + i\varepsilon} e^{i\vec{k}\cdot\vec{r}_i} e^{-i\vec{k}\cdot\vec{r}_j} e^{i\vec{k}\cdot\vec{R}_{ij}}. \tag{A.13}$$

Through the expansion of a plane wave in spherical waves A.8, the propagator becomes:

$$\begin{aligned} G_0^+(\vec{r} - \vec{r'}) &= 8 \sum_{LL'L''} i^{l-l'+l''} Y_L(\hat{r}_i) Y_{L'}(\hat{r}_j) Y_{L''}(\hat{R}_{ij}) \int d\Omega_k Y_L(\hat{k}) Y_{L'}(\hat{k}) Y_{L''}(\hat{k}) \cdot \\ &\quad \int_0^\infty \frac{k^2 dk}{E - k^2 + i\varepsilon} j_l(kr_i) j_{l'}(kr_j) j_{l''}(kR_{ij}) \\ &= 8 \sum_{LL'L''} i^{l-l'+l''} C(L, L', L'') Y_L(\hat{r}_i) Y_{L'}(\hat{r}_j) Y_{L''}(\hat{R}_{ij}) \cdot \\ &\quad \int_0^\infty \frac{k^2 dk}{E - k^2 + i\varepsilon} j_l(kr_i) j_{l'}(kr_j) j_{l''}(kR_{ij}). \end{aligned} \tag{A.14}$$

where $C(L, L', L'')$ are the Gaunt coefficients. According to the choice of $\vec{r}_i$, $\vec{r}_j$ and R_{ij}, one of the Bessel functions is transformed in Hankel function, likewise to (A.10). For our purpose, we consider two conditions [62] which guarantee the convergence of the integral: first $R_{ij} > \vec{r}_i + \vec{r}_j$ (that is, the spheres of the ions i and j do not overlap),

secondly the case of $j \equiv O$ with $\vec{r}_0 > \vec{r}_i + R_{i0}$ (that is, $\vec{r} \in \Omega_i$ volume of i and $\vec{r}'$ on S_{Ω_0}, surface of the volume Ω_0 centered in O, which contains all the atomic volumes).

Let's consider first the condition $R_{ij} > \vec{r}_i + \vec{r}_j$: in this case we transform the function $j_{l''}(kR_{ij}) = \frac{h^+_{l''}(kR_{ij}) + h^-_{l''}(kR_{ij})}{2}$:

$$\begin{aligned}
&\int_0^\infty \frac{k^2 dk}{E - k^2 + i\varepsilon} j_l(kr_i) j_{l'}(kr_j) j_{l''}(kR_{ij}) = \int_0^\infty \frac{k^2 dk}{E - k^2 + i\varepsilon} j_l(kr_i) j_{l'}(kr_j) \frac{h^+_{l''}(kR_{ij}) + h^-_{l''}(kR_{ij})}{2} \\
&= \int_0^\infty \frac{k^2 dk}{E - k^2 + i\varepsilon} j_l(kr_i) j_{l'}(kr_j) \frac{h^+_{l''}(kR_{ij})}{2} + \int_\infty^0 \frac{k^2 dk}{E - k^2 + i\varepsilon} j_l(-kr_i) j_{l'}(-kr_j) \frac{h^-_{l''}(-kR_{ij})}{2} \\
&= \frac{1}{2} \int_{-\infty}^\infty \frac{k^2 dk}{E - k^2 + i\varepsilon} i^{l+l'+l''} j_l(kr_i) j_{l'}(kr_j) h^+_{l''}(kR_{ij}) \\
&= -\frac{1}{2} \pi i \tilde{k} j_l(\tilde{k} r_i) j_{l'}(\tilde{k} r_j) h^+_{l''}(\tilde{k} R_{ij})
\end{aligned} \tag{A.15}$$

where the condition $l + l' + l'' = 2n$ is applied and $\tilde{k} = \sqrt{E}$. Including A.15 in A.14 G_0^+ becomes:

$$G_0^+(\vec{r} - \vec{r'}) = -4\pi i \tilde{k} \sum_{LL'} \sum_{L''} i^{l-l'+l''} C(L, L', L'') J_L(\tilde{k}\vec{r}_i) J_{L'}(\tilde{k}\vec{r}_j) H^+_{L''}(\tilde{k}\vec{R}_{ij}), \tag{A.16}$$

where $J_L(\tilde{k}\vec{r}_i) = j_l(\tilde{k} r_i) Y_L(\hat{r}_i)$, $J_{L'}(\tilde{k}\vec{r}_j) = j_{l'}(\tilde{k} r_j) Y_{L'}(\hat{r}_j)$ and $H^+_{L''}(\tilde{k}\vec{R}_{ij}) = h^+_{l''}(\tilde{k} R_{ij}) Y_{L''}(\hat{R}_{ij})$.

The (A.16) is usually rewritten in terms of structural factors $G^{ij}_{LL'}$ when the following definition is applied:

$$G^{ij}_{LL'} = -4\pi i \tilde{k} \sum_{L''} i^{l-l'+l''} C(L, L', L'') H^+_{L''}(\tilde{k}\vec{R}_{ij}) \tag{A.17}$$

and (A.16) becomes:

$$G_0^+(\vec{r} - \vec{r'}) = \sum_{LL'} J_L(\tilde{k}\vec{r}_i) G^{ij}_{LL'} J_{L'}(\tilde{k}\vec{r}_j). \tag{A.18}$$

In the second case, when $\vec{r}_0 > \vec{r}_i + R_{i0}$, we transform in Hankel functions the Bessel function j which depends on $\vec{r}_0$ and consider the relation $\vec{r}_i - \vec{r}_0 + \vec{R}_{i0}$:

$$\begin{aligned}
G_0^+(\vec{r} - \vec{r'}) &= 8 \sum_{LL'} \sum_{L''} i^{l-l'+l''} C(L, L', L'') \int_0^\infty \frac{k^2 dk}{E - k^2 + i\varepsilon} J_L(k\vec{r}_i) J_{L'}(k\vec{r}_0) J_{L''}(k\vec{R}_{i0}) \\
&= -4\pi i \tilde{k} \sum_{LL'} \sum_{L''} i^{l-l'+l''} C(L, L', L'') J_L(\tilde{k}\vec{r}_i) J_{L''}(\tilde{k}\vec{R}_{i0}) H^+_{L'}(\tilde{k}\vec{r}_0)
\end{aligned} \tag{A.19}$$

If we define the structural factor

$$J^{i0}_{LL'} = 4\pi \sum_{L''} i^{l-l'+l''} C(L, L', L'') J_{L''}(\tilde{k}\vec{R}_{i0}) \tag{A.20}$$

the propagator becomes:

$$G_0^+(\vec{r} - \vec{r'}) = -i\tilde{k} \sum_{LL'} J_L(\tilde{k}\vec{r}_i) J^{i0}_{LL'} H^+_{L'}(\tilde{k}\vec{r}_0). \tag{A.21}$$

A.4 Multiple scattering theory

We must consider a realistic model of our system. Since the sample is composed of numerous atoms, the electron (probe) will be elastically scattered by several atoms and this must be accounted by the theory. The position of the potentials, with respect to a given origin of space, must be taken into account. We will consider the potential in the sample as the sum of the atomic potentials:

$$V = \sum_i V_i. \tag{A.22}$$

As I already said, we must solve the Schroedinger equation

$$[\nabla^2 + E - V(\vec{r})]\psi_k(\vec{r}) \tag{A.23}$$

with the boundary condition

$$\psi_k(\vec{r}) \sim_{r\to\infty} e^{i\vec{k}\cdot\vec{r}} - kf(\vec{k}, \vec{r})\frac{e^{ikr}}{kr}. \tag{A.24}$$

Using the property of the free propagator G_0^+

$$(\nabla^2 + E)G_0^+(\vec{r} - \vec{r'}) = \delta(\vec{r} - \vec{r'}), \tag{A.25}$$

we can transform the differential Schroedinger equation in an integral equation, the Lippmann-Schwinger equation; the Schroedinger equation of the full system is then rewritten as

$$(\nabla^2 + E)\psi_k(\vec{r}) = V(\vec{r})\psi_k(\vec{r}) \tag{A.26}$$

which is an inhomogeneous equation. It is easy to verify that a particular solution of the inhomogeneous equation is

$$\tilde{\psi_k}(\vec{r}) = \int_V d^3r' G_0^+(\vec{r} - \vec{r'}; E) V(\vec{r'})\psi_k(\vec{r'}) \tag{A.27}$$

so that the Lippmann-Schwinger solution for the wave function is:

$$\psi_k(\vec{r}) = e^{i\vec{k}\cdot\vec{r}} + \int_V d^3r' G_0^+(\vec{r}-\vec{r'};E)V(\vec{r'})\psi_k(\vec{r'}). \tag{A.28}$$

The equation could be then iterate leading to its Born series expansion.

The volume Ω_0 encloses all the atoms of the system and it is so big that in the complement of Ω_0 the solution of the Schroedinger equation has the form (3.5). We partition the "molecular" volume in N non-overlapping cells Ω_j with centers at $\vec{r}_j$, contained in Ω_0.

We use the Green's theorem in the form

$$\int_V d^3r[F(\nabla^2+E)G - G(\nabla^2+E)F] = \int_S (F\vec{\nabla}G - G\vec{\nabla}F)\cdot\hat{n}d\sigma \tag{A.29}$$

where S is the surface enclosing the volume V, and we apply it to the volume of space $\Delta\Omega$ between the atomic regions ($\sum_j \Omega_j$) and the outer sphere (Ω_0), where $V(r)=0$. In this case $G=G_0$ and $F=\psi_k \sim e^{i\vec{k}\cdot\vec{r}} + f(k,r)\frac{e^{ikr}}{r}$ and the left-hand member of (A.29) becomes:

$$\int_{\Delta\Omega} d^3r'\psi_k(\vec{r'})\delta(\vec{r'}-\vec{r}) - \int_{\Delta\Omega} d^3r' G_0(\vec{r'}-\vec{r})(\nabla^2+E)\psi_k(\vec{r'}) = 0 \tag{A.30}$$

because r never coincides with r'. For the Green's theorem equation (A.30) is also equal to the second part of (A.29), in this way we find:

$$\int_{S_0}(\psi_k(\vec{r'})\vec{\nabla}G_0 - G_0\vec{\nabla}\psi_k(\vec{r'}))\cdot\hat{n}d\sigma - \int_{S_\Omega}(\psi_k(\vec{r'})\vec{\nabla}G_0 - G_0\vec{\nabla}\psi_k(\vec{r'}))\cdot\hat{n}d\sigma = 0 \tag{A.31}$$

that is

$$\int_{S_0}(\psi_k(\vec{r'})\vec{\nabla}G_0 - G_0\vec{\nabla}\psi_k(\vec{r'}))\cdot\hat{n}d\sigma = \sum_j \int_{S_{\Omega_j}}(\psi_k(\vec{r'})\vec{\nabla}G_0 - G_0\vec{\nabla}\psi_k(\vec{r'}))\cdot\hat{n}_i d\sigma_i \tag{A.32}$$

with S_0 surface surrounding Ω_0 and S_{Ω_j} surface around the cell j; S_Ω is the total surface surrounding the atoms.

We now introduce a complete set of basis local functions $\phi_L(\vec{r}_i)$, which are regular for $r\to 0$, and write the wave function referred to the cell Ω_i as a linear combination of these functions:

$$\psi_k^i(\vec{r}_i) = \sum_L A_L^i(\vec{k})\phi_L(\vec{r}_i) \tag{A.33}$$

We take $\vec{r} \in \Omega_i$: the left-hand member of equation (A.30) becomes:

$$\sum_j \int_{\Omega_j} [\psi_k(\vec{r'}_j)(\nabla^2 + E)G_0^+(\vec{r} - \vec{r'}_j) - G_0^+(\vec{r} - \vec{r'}_j)(\nabla^2 + E)\psi_k(\vec{r'}_j)d^3r'_j] =$$
$$= \int_{\Omega_i} [\psi_k(\vec{r'}_j)(\nabla^2 + E)G_0^+(\vec{r} - \vec{r'}_j)d^3r'_j - \int_{\Omega_i} G_0^+(\vec{r} - \vec{r'}_j)(\nabla^2 + E)\psi_k(\vec{r'}_j)d^3r'_j +$$
$$\sum_{j\neq i} \int_{\Omega_j} d^3r'_j\psi_k(\vec{r'}_j)(\nabla^2 + E)G_0^+(\vec{r} - \vec{r'}_j) - \sum_{j\neq i} \int_{\Omega_j} d^3r'_j G_0^+(\vec{r} - \vec{r'}_j)(\nabla^2 + E)\psi_k(\vec{r'}_j) \tag{A.34}$$

and we could add the expression $\sum_{j\neq i} \int_{\Omega_j} d^3r'_j\psi_k(\vec{r'}_j)(\nabla^2 + E)G_0^+(\vec{r} - \vec{r'}_j)$ because it is zero, since $\vec{r} \neq \vec{r'}_j$. Now we can apply the Green's theorem to the integrals over Ω_i and Ω_j so that (A.34) is equal to the following:

$$\int_{S_{\Omega_i}} [\psi_k^i(\vec{r'}_i)\vec{\nabla}G_0^+(\vec{r} - \vec{r'}_i) - G_0^+(\vec{r} - \vec{r'}_i)\vec{\nabla}\psi_k^i(\vec{r'}_i)] \cdot \hat{n}_i d\sigma'_i +$$
$$\sum_{j\neq i} \int_{S_{\Omega_j}} [\psi_k(\vec{r'})\vec{\nabla}G_0^+(\vec{r} - \vec{r'}) - G_0^+(\vec{r} - \vec{r'})\vec{\nabla}\psi_k^i(\vec{r'})] \cdot \hat{n}_j d\sigma'_j =$$
$$= \int_{S_0} [\psi_k^0(\vec{r'})\vec{\nabla}G_0^+(\vec{r} - \vec{r'}) - G_0^+(\vec{r} - \vec{r'})\vec{\nabla}\psi_k^0(\vec{r'})] \cdot \hat{n}_0 d\sigma'_0. \tag{A.35}$$

In eq.(A.35) the first part of the left-hand member corresponds to the expansion of the propagator respect to just one scattering center (App.A.2, that is $\vec{r}$ in Ω_i and $\vec{r'}$ on S_{Ω_i}), whereas the second part corresponds to the expansion respect to more than one atom in the situation with $\vec{r}$ in Ω_i but $\vec{r'}$ on S_{Ω_j} (App.A.3, eq.(A.18)); the right-hand member corresponds to $\vec{r}$ in Ω_i and $\vec{r'}$ on S_0) (App.A.3, eq.(A.61)). Eq.(A.35) is obtained taking into account (A.32).

Now we have to substitute in the various terms of the equation (A.35) the corresponding expressions for the propagator G_0^+ and the right expansions of the wave function ψ_k. We evaluate separately the three terms in (A.35), that is the integrals over S_{Ω_i}, S_{Ω_j} and S_0.

1. If we put (A.33) and (A.11) in the integral over S_{Ω_i}, it becomes:

$$\int_{S_{\Omega_i}} \Big[\sum_L A_L^i(\vec{k})\phi_L(\vec{r'}_i)\vec{\nabla}_{\underline{r}'_i}(\sum_{L'}(-i\tilde{k})J_{L'}(\tilde{k}\vec{r}_i)H_{L'}^+(\tilde{k}\vec{r'}_i)) -$$
$$\sum_{L'}(-i\tilde{k})J_{L'}(\tilde{k}\vec{r}_i)H_{L'}^+(\tilde{k}\vec{r'}_i)\vec{\nabla}_{\underline{r}'_i}(\sum_L A_L^i(\vec{k})\phi_L(\vec{r'}_i))\Big] \cdot \hat{n}_i d\sigma'_i =$$
$$= \sum_L J_L(\vec{r}_i)\sum_{L'} A_{L'}^i(\vec{k}) \int_{S_{\Omega_i}} \Big[\phi_{L'}(\vec{r'}_i)\vec{\nabla}_{\underline{r}'_i}\tilde{H}_L^+(\tilde{k}\vec{r'}_i)) - \tilde{H}_L^+(\tilde{k}\vec{r'}_i))\vec{\nabla}_{\underline{r}'_i}\phi_{L'}(\vec{r'}_i)\Big] \cdot \hat{n}_i d\sigma'_i =$$

$$= \sum_L J_L(\vec{r}_i) \sum_{L'} A^i_{L'}(\vec{k}) E^i_{LL'} \tag{A.36}$$

with $\tilde{H}^+_L(\tilde{k}\vec{r}) = -i\tilde{k}H^+_L(\tilde{k}\vec{r})$ and

$$E^i_{LL'} = \int_{S_{\Omega_i}} \Big[\phi_{L'}(\vec{r'}_i)\overrightarrow{\nabla}_{\underline{r}'_i}\tilde{H}^+_L(\tilde{k}\vec{r'}_i)) - \tilde{H}^+_L(\tilde{k}\vec{r'}_i))\overrightarrow{\nabla}_{\underline{r}'_i}\phi_{L'}(\vec{r'}_i)\Big] \cdot \hat{n}_i d\sigma'_i. \tag{A.37}$$

2. If we put (A.33) and (A.18) in the integral over S_{Ω_j} in (A.35), it becomes:

$$\begin{aligned}
&\sum_{j\neq i}\int_{S_{\Omega_j}} \Big[\sum_{L'''} A^j_{L'''}\phi_{L'''}(\vec{r'}_j)\overrightarrow{\nabla}_{\underline{r}'_j}(\sum_{LL''} J_L(\tilde{k}\vec{r}_i)G^{ij}_{LL''}J_{L''}(\tilde{k}\vec{r'}_j)) - \\
&\sum_{LL''} J_L(\tilde{k}\vec{r}_i)G^{ij}_{LL''}J_{L''}(\tilde{k}\vec{r'}_j)\overrightarrow{\nabla}_{\underline{r}'_j}(\sum_{L'''} A^j_{L'''}\phi_{L'''}(\vec{r'}_j))\Big] \cdot \hat{n}_j d\sigma'_j = \\
= &\sum_{j\neq i}\sum_L J_L(\tilde{k}\vec{r}_i)\sum_{L''} G^{ij}_{LL''}\sum_{L'''} A^j_{L'''}\int_{S_{\Omega_j}} \Big[\phi_{L'''}(\vec{r'}_j)\overrightarrow{\nabla}_{\underline{r}'_j}J_{L''}(\tilde{k}\vec{r'}_j) - \\
&J_{L''}(\tilde{k}\vec{r'}_j)\overrightarrow{\nabla}_{\underline{r}'_j}\phi_{L'''}(\vec{r'}_j)\Big] \cdot \hat{n}_j d\sigma'_j = \\
= &\sum_{j\neq i}\sum_L J_L(\tilde{k}\vec{r}_i)\sum_{L''} G^{ij}_{LL''}\sum_{L'''} A^j_{L'''}S^j_{L''L'''}.
\end{aligned} \tag{A.38}$$

with

$$S^j_{L''L'''} = \int_{S_{\Omega_j}} \Big[\phi_{L'''}(\vec{r'}_j)\overrightarrow{\nabla}_{\underline{r}'_j}J_{L''}(\tilde{k}\vec{r'}_j) - J_{L''}(\tilde{k}\vec{r'}_j)\overrightarrow{\nabla}_{\underline{r}'_j}\phi_{L'''}(\vec{r'}_j)\Big] \cdot \hat{n}_j d\sigma'_j. \tag{A.39}$$

3. Finally, we put (3.7) and (A.61) in the integral over S_0 in (A.35); it becomes:

$$\begin{aligned}
&\int_{S_0} \Big[\sum_{L'''} 4\pi i^{l'''}Y_{L'''}(\hat{k})(J_{L'''}(\vec{r'}_0) + \sum_{L'} H^+_{L'}(\vec{r'}_0)T_{L'L'''})\overrightarrow{\nabla}_{\underline{r}'_0}(\sum_{LL''} J_L(\tilde{k}\vec{r}_i)J^{i0}_{LL''}\tilde{H}^+_{L''}(\vec{r'}_0)) - \\
&\sum_{LL''} J_L(\tilde{k}\vec{r}_i)J^{i0}_{LL''}\tilde{H}^+_{L''}(\vec{r'}_0)\overrightarrow{\nabla}_{\underline{r}'_0}(\sum_{L'''} 4\pi i^{l'''}Y_{L'''}(\hat{k})(J_{L'''}(\vec{r'}_0) + \sum_{L'} H^+_{L'}(\vec{r'}_0)T_{L'L'''}))\Big] \cdot \hat{n}d\sigma'_0 = \\
= &\sum_L J_L(\tilde{k}\vec{r}_i)\sum_{L''} J^{i0}_{LL''}\int_{S_0}\sum_{L'''} 4\pi i^{l'''}Y_{L'''}(\hat{k})\Big[(J_{L'''}(\vec{r'}_0) + \sum_{L'} H^+_{L'}(\vec{r'}_0)T_{L'L'''})\overrightarrow{\nabla}_{\underline{r}'_0}\tilde{H}^+_{L''}(\vec{r'}_0) - \\
&\tilde{H}^+_{L''}(\vec{r'}_0)\overrightarrow{\nabla}_{\underline{r}'_0}(J_{L'''}(\vec{r'}_0) + \sum_{L'} H^+_{L'}(\vec{r'}_0)T_{L'L'''})\Big] \cdot \hat{n}d\sigma'_0 = \\
= &\sum_L J_L(\tilde{k}\vec{r}_i)\sum_{L''} J^{i0}_{LL''}\sum_{L'''} 4\pi i^{l'''}Y_{L'''}(\hat{k})\int_{S_0}\Big[\Big(J_{L'''}(\vec{r'}_0)\overrightarrow{\nabla}_{\underline{r}'_0}\tilde{H}^+_{L''}(\vec{r'}_0) - \tilde{H}^+_{L''}(\vec{r'}_0)\overrightarrow{\nabla}_{\underline{r}'_0}J_{L'''}(\vec{r'}_0)\Big) + \\
&\sum_{L'} H^+_{L'}(\vec{r'}_0)T_{L'L'''}\overrightarrow{\nabla}_{\underline{r}'_0}\tilde{H}^+_{L''}(\vec{r'}_0) - \tilde{H}^+_{L''}(\vec{r'}_0)\overrightarrow{\nabla}_{\underline{r}'_0}\sum_{L'} H^+_{L'}(\vec{r'}_0)T_{L'L'''}\Big] \cdot \hat{n}d\sigma'_0.
\end{aligned} \tag{A.40}$$

The terms in (A.40), remembering that $d\sigma_0' = R_0^2 d\Omega$ and considering a spherical symmetry, can be reduced as follows:
the second term gives

$$\begin{aligned}
&\int_{S_0} \sum_{L'} H^+_{L'}(\vec{r'}_0) T_{L'L'''} \overrightarrow{\nabla}_{\underline{r}_0'} \tilde{H}^+_{L''}(\vec{r'}_0) \cdot \hat{n} d\sigma_0' = \\
&= \int_{S_0} \sum_{L'} h^+_{l'}(r_0') Y_{L'}(\hat{r'}_0) T_{L'L'''} \overrightarrow{\nabla}_{\underline{r}_0'} (-i\tilde{k}) [h^+_{l''}(r_0') Y_{L''}(\hat{r'}_0)] \cdot \hat{n} R_0^2 d\Omega = \\
&= -i\tilde{k} R_0^2 \sum_{L'} T_{L'L'''} h^+_{l'}(r_0') \overrightarrow{\nabla}_{\underline{r}_0'} h^+_{l'}(r_0') \cdot \hat{n},
\end{aligned} \tag{A.41}$$

the third term is equal to the second, therefore they give zero as a final result; the first term instead gives:

$$\begin{aligned}
&\sum_L J_L(\tilde{k}\vec{r}_i) \sum_{L''} J^{i0}_{LL''} \sum_{L'''} 4\pi i^{l'''} Y_{L'''}(\hat{k}) \int_{S_0} \Big[J_{L'''}(\vec{r'}_0) \overrightarrow{\nabla}_{\underline{r}_0'} \tilde{H}^+_{L''}(\tilde{k}\vec{r'}_0) - \\
&\tilde{H}^+_{L''}(\tilde{k}\vec{r'}_0) \overrightarrow{\nabla}_{\underline{r}_0'} J_{L'''}(\vec{r'}_0) \Big] \cdot \hat{n} d\sigma_0' = \\
&= -i\tilde{k} \sum_L J_L(\tilde{k}\vec{r}_i) \sum_{L''} J^{i0}_{LL''} \sum_{L'''} 4\pi i^{l'''} Y_{L'''}(\hat{k}) \int d\Omega \Big\{ j_{l'''}(kr_0') Y_{L'''}(\hat{r'}_0) Y_{L''}(\hat{r'}_0) \overrightarrow{\nabla}_{\underline{r}_0'} h^+_{l''}(kr_0') \\
&- h^+_{l''}(kr_0') Y_{L''}(\hat{r'}_0) Y_{L'''}(\hat{r'}_0) \overrightarrow{\nabla}_{\underline{r}_0'} j_{l'''}(kr_0') \Big\} R_0^2 = \\
&= \sum_L J_L(\tilde{k}\vec{r}_i) \sum_{L''} J^{i0}_{LL''} \sum_{L'''} 4\pi i^{l'''} Y_{L'''}(\hat{k}) W[j_{l''}(kr_0'), -i\tilde{k} h^+_{l''}(kr_0')] \Big|_{R_0} R_0^2 \delta_{l'''l''} = \\
&= \sum_L J_L(\tilde{k}\vec{r}_i) \sum_{L''} J^{i0}_{LL''} \sum_{L'''} 4\pi i^{l'''} Y_{L'''}(\hat{k}) (-\frac{1}{R_0^2}) R_0^2 \delta_{l'''l''} = \\
&= -\sum_L J_L(\tilde{k}\vec{r}_i) \sum_{L'} J^{i0}_{LL'} 4\pi i^{l'} Y_{L'}(\hat{k}).
\end{aligned} \tag{A.42}$$

Now we can rewrite (A.35) using (A.36), (A.38) and (A.42), and it becomes:

$$\begin{aligned}
&\sum_L J_L(\vec{r}_i) \sum_{L'} A^i_{L'}(\vec{k}) E^i_{LL'} + \sum_{j \neq i} \sum_L J_L(\tilde{k}\vec{r}_i) \sum_{L''} G^{ij}_{LL''} \sum_{L'''} A^j_{L'''} S^j_{L''L'''} = \\
&= -\sum_L J_L(\tilde{k}\vec{r}_i) \sum_{L'} J^{i0}_{LL'} 4\pi i^{l'} Y_{L'}(\hat{k}).
\end{aligned} \tag{A.43}$$

If we remind that $e^{i\vec{k}\cdot\vec{r}} = 4\pi \sum_L i^l J_L(\vec{r}) Y_L(\hat{k})$ and $\sum_{L'} C(L, L', L'') Y'_L(\hat{k}) = Y_L(\hat{k}) Y_{L''}(\hat{k})$, and if we take into account the usually normalization of ψ_k^0 in (3.7) (it should be multiplied by $\sqrt{\frac{k}{\pi}} \frac{1}{4\pi}$), equation (A.43) becomes:

$$\sum_L J_L(\vec{r}_i)\sum_{L'} A^i_{L'}(\vec{k})E^i_{LL'} + \sum_{j\neq i}\sum_L J_L(\tilde{k}\vec{r}_i)\sum_{L''} G^{ij}_{LL''}\sum_{L'''} A^j_{L'''}(\vec{k})S^j_{L''L'''} =$$
$$= -\sum_L J_L(\tilde{k}\vec{r}_i)\sum_{L'} 4\pi\sum_{L''} i^{l-l'+l''}C(L,L',L'')J_{L''}(\tilde{k}\vec{R}_{i0})4\pi i^{l'}Y_{L'}(\hat{k})\sqrt{\frac{k}{\pi}}\frac{1}{4\pi} =$$
$$= -\sum_L J_L(\tilde{k}\vec{r}_i)\sqrt{\frac{k}{\pi}}i^l Y_L(\hat{k})e^{i\vec{k}\cdot\vec{R}_{i0}}. \tag{A.44}$$

If we define the coefficients $A^0_L(\vec{k}) = \sqrt{\frac{k}{\pi}}i^l Y_L(\hat{k})e^{i\vec{k}\cdot\vec{R}_{i0}}$ we obtain:

$$\sum_L J_L(\vec{r}_i)\Big\{\sum_{L'} A^i_{L'}(\vec{k})E^i_{LL'} + \sum_{j\neq i}\sum_{L'L''} G^{ij}_{LL''}A^j_{L'}(\vec{k})S^j_{L''L'}\Big\} = -\sum_L J_L(\vec{r}_i)A^0_L(\vec{k})$$
$$\sum_{j\neq i}\sum_{L'}\Big\{\delta_{ij}E^i_{LL'} + \sum_{L''} G^{ij}_{LL''}S^j_{L''L'}\Big\}A^j_{L'}(\vec{k}) = -A^0_L(\vec{k}). \tag{A.45}$$

The factors $G^{ij}_{LL''}$ in these equations are the real space structure factors, which gives the probability of a wave, with angular momentum l, to go from the site i to the site j with angular momentum l'. The structure factors are the propagators, that is the projections of the free propagator in partial waves.

A.4.1 The Multiple Scattering equation

To solve the equation (A.45), which allows to determine the coefficients of the wave functions, we must evaluate the expressions contained in (A.37) and (A.39). To do this, we must know the wave function ϕ in each single atomic center, that is the wave function referred to the single atom. We solve the problem in muffin-tin approximation; for each muffin-tin sphere the radius is ρ_i and outside this region the potential is zero.

Inside the atomic sphere the wave function must be regular, therefore we take its radial part for $r \to 0$ as

$$\phi_L(\vec{r}_i) \sim J_L(\vec{r}_i) = R^i_l(r_i)Y_L(\hat{r}_i) \tag{A.46}$$

and we write explicitly the expressions for $E^i_{LL'}$ and $S^j_{LL'}$ (eq. A.37 and A.39):

$$E^i_{LL'} = \int_{S_{\Omega_i}} \Big[\phi_{L'}(\vec{r'}_i)\vec{\nabla}_{\underline{r}'_i}\tilde{H}^+_L(\tilde{k}\vec{r'}_i)) - \tilde{H}^+_L(\tilde{k}\vec{r'}_i))\vec{\nabla}_{\underline{r}'_i}\phi_{L'}(\vec{r'}_i)\Big]\cdot\hat{n}_i d\sigma'_i =$$
$$= -i\tilde{k}\int_{S_{\Omega_i}} \Big\{R^i_{l'}(r'_i)Y_{L'}(\hat{r'}_i)[\vec{\nabla}_{\vec{r'}_i}h^+_l(\tilde{k}r'_i)Y_L(\hat{r'}_i) + h^+_l(\tilde{k}r'_i)\vec{\nabla}_{\vec{r'}_i}Y_L(\hat{r'}_i)] -$$

$$
\begin{aligned}
&+ h_l^+(\tilde{k}r_i')Y_L(\hat{r'}_i)[\overrightarrow{\nabla}_{\vec{r'}_i} R_{l'}^i(r_i') \cdot Y_{L'}(\hat{r'}_i) + R_{l'}^i(r_i')\overrightarrow{\nabla}_{\vec{r'}_i} Y_{L'}(\hat{r'}_i)]\Big\} \cdot \hat{n}_i d\sigma_i' = \\
&= -i\tilde{k}\int_{S_{\Omega_i}} W[R_{l'}^i(r_i'), h_l^+(\tilde{k}r_i')]Y_{L'}(\hat{r'}_i)Y_L(\hat{r'}_i)\rho_i^2 d\Omega = \\
&= W[R_l^i(r_i'), \tilde{h}_l^+(\tilde{k}r_i')]\Big|_{r_i'=\rho_i}\rho_i^2\delta_{LL'}.
\end{aligned}
\tag{A.47}
$$

In the same way we find

$$
\begin{aligned}
S_{LL'}^j &= \int_{S_{\Omega_j}} \Big[\phi_{L'}(\vec{r'}_j)\overrightarrow{\nabla}_{\underline{r}_j'} J_L(\tilde{k}\vec{r'}_j) - J_L(\tilde{k}\vec{r'}_j)\overrightarrow{\nabla}_{\underline{r}_j'}\phi_{L'}(\vec{r'}_j)\Big] \cdot \hat{n}_j d\sigma_j' = \\
&= W[R_{l'}^j(r_j'), j_l(\tilde{k}r_j')]\Big|_{r_j'=\rho_j}\rho_j^2\delta_{LL'}.
\end{aligned}
\tag{A.48}
$$

We find that both $E_{LL'}^i$ and $S_{LL'}^j$ are diagonal, since the potential has spherical symmetry. Equation (A.45) thus becomes:

$$
\sum_j\sum_{L'}\Big\{W[R_l^i(\rho_i), \tilde{h}_l^+(\tilde{k}\rho_i)] \cdot \rho_i^2\delta_{LL'}\delta_{ij} + G_{LL'}^{ij}W[R_{l'}^j(\rho_j), j_{l'}(\tilde{k}\rho_j)]\rho_j^2\Big\} \cdot A_{L'}^j(\vec{k}) = -A_L^0(\vec{k}).
\tag{A.49}
$$

To arrive to the usually employed formalism in multiple scattering theory, we introduce the quantities:

$$
B_L^i(\vec{k}) = \sum_{L'}(-S_{LL'}^i)A_L^i(\vec{k})
\tag{A.50}
$$

that is

$$
B_L^i(\vec{k}) = W[j_l(\tilde{k}\rho_i), R_l^i(\rho_i)]\rho_i^2 A_L^i(\vec{k})
\tag{A.51}
$$

and renormalize the local wave functions in this way:

$$
\bar{\phi}_L(\vec{r}) = \frac{\phi_L(\vec{r})}{W[j_l(\tilde{k}\rho_i), R_l^i(\rho_i)]\rho_i^2}
\tag{A.52}
$$

so that

$$
\psi_k^i(\vec{r}) = \sum_L A_L^i(\vec{k})\phi_L(\vec{r}) = \sum_L B_L^i(\vec{k})\bar{\phi}_L(\vec{r}).
\tag{A.53}
$$

We rewrite eq. (A.49) as follows:

$$\sum_{jL'}\Big\{\frac{W[\tilde{h}_l^+(\tilde{k}\rho_i),R_l^i(\rho_i)]}{W[j_l(\tilde{k}\rho_i),R_l^i(\rho_i)]}W[j_l(\tilde{k}\rho_i),R_l^i(\rho_i)]\rho_i^2\delta_{LL'}\delta_{ij}+G_{LL'}^{ij}W[j_{l'}(\tilde{k}\rho_j),R_{l'}^j(\rho_j)]\rho_j^2\Big\}A_{L'}^j(\vec{k})=$$
$$=A_L^0(\vec{k}). \tag{A.54}$$

Looking at the (A.54) and remembering that the scattering amplitude, for a single atomic center as obtained by the continuity of the wave function and its first derivative (3.8), is $t_l^i=\frac{W[j_l(\rho_i),R_l(\rho_i)]}{W[\tilde{h}_l^+(\rho_i),R_l(\rho_i)]}$, the equation for the coefficients becomes:

$$\sum_j\sum_{L'}\Big\{(t_l^i)^{-1}\delta_{LL'}\delta_{ij}W[j_l(\tilde{k}\rho_i),R_l^i(\rho_i)]\cdot\rho_i^2+G_{LL'}^{ij}W[j_{l'}(\tilde{k}\rho_j),R_{l'}^j(\rho_j)]\rho_j^2\Big\}\cdot A_{L'}^j(\vec{k})=A_L^0(\vec{k})$$
$$\sum_j\sum_{L'}\Big\{(t_l^i)^{-1}\delta_{LL'}\delta_{ij}+G_{LL'}^{ij}\Big\}\cdot B_{L'}^j(\vec{k})=A_L^0(\vec{k}). \tag{A.55}$$

We have found the Multiple Scattering equation. In this expression the MS matrix is given by the operator $(T^{-1}+G)$, whose elements are $((t_l^i)^{-1}\delta_{LL'}\delta_{ij}+G_{LL'}^{ij})$, and the full scattering path operator, which is the inverse of the MS matrix, is:

$$\tau_{LL'}^{ij}=[(T^{-1}+G)]_{LL'}^{ij}=[(t_l^i)^{-1}\delta_{LL'}\delta_{ij}+G_{LL'}^{ij}]^{-1}. \tag{A.56}$$

Since $T_{LL'}^i$ is the scattering matrix of the non-spherical potential located inside the i-th cell and G is the propagator of the free spherical wave, the full scattering path operator gives the total amplitude of propagation from site i to site j, starting with angular momentum L and arriving with angular momentum L', after having been scattered by all the possible atoms. With this notation the multiple scattering equation becomes:

$$\sum_j\sum_{L'}(\tau_{LL'}^{ij})^{-1}B_{L'}^j(\vec{k})=A_L^0(\vec{k})$$
$$B_L^i(\vec{k})=\sum_j\sum_{L'}\tau_{LL'}^{ij}A_L^0(\vec{k})$$
$$B_L^i(\vec{k})=\sum_j\sum_{L'}\tau_{LL'}^{ij}\sqrt{\frac{k}{\pi}}i^{l'}Y_{L'}(\hat{k})e^{i\vec{k}\cdot\vec{R}_{j0}}. \tag{A.57}$$

The coefficient $B_L^i(\vec{k})$ is a scattering amplitude impinging on the potential located in the cell i in response to a plane wave excitation of momentum $\vec{k}$. Therefore, (A.57) are nothing else but the self-consistent equations for these amplitudes.

A.4.2 Cross section in MS theory

Once the scattering amplitudes have been determined, the wave function is known and we can use it to calculate the differential cross section for the various processes, in our case we first calculate the photoemission differential cross section:

$$\begin{aligned}\frac{d\sigma}{d\hat{k}} &= 4\pi^2\alpha\hbar\omega\sum_{m_c}\left|\langle\psi_k(\vec{r})|\hat{\epsilon}\cdot\vec{r}|R^c_{l_c}(r)Y^c_{L_c}(\hat{r})\rangle\right|^2 = \\ &= 4\pi^2\alpha\hbar\omega\sum_{m_c}\left|\langle\sum_L B^i_L(\vec{k})R^i_l(r)Y_L(\hat{r})|\hat{\epsilon}\cdot\vec{r}|R^c_{l_c}(r)Y^c_{L_c}(\hat{r})\rangle\right|^2. \end{aligned} \tag{A.58}$$

Since the initial angular momentum is l_c and the final one is l, in dipole approximation $l = l_c \pm 1$:

$$\begin{aligned}\frac{d\sigma}{d\hat{k}} &= 4\pi^2\alpha\hbar\omega\frac{4\pi}{3}\sum_{m_c}\Big|\sum_L\int drr^3R^i_{l_c\pm1}(r)R_{l_c}(r)\int d\Omega Y_{l_c\pm1,m_c}(\hat{r})Y_{1,m_\sigma}(\hat{r})Y_{L_c}(\hat{r})B^i_L(\vec{k})\Big|^2 = \\ &= 4\pi^2\alpha\hbar\omega\frac{4\pi}{3}\frac{k}{\pi}\sum_{m_c}\Big|\sum_L M_{LL_c}\sum_{jL'}i^{l'}Y_{L'}(\hat{k})e^{i\vec{k}\cdot\vec{R}_{0j}}\tau^{0j}_{LL'}\Big|^2, \end{aligned} \tag{A.59}$$

if we consider $i = 0$, that is the photoabsorbing atom is in the origin of the outer sphere. We then see that the photoemission current along the direction $\hat{k}$ is the square modulus of the sum of all possible composite amplitudes obtained as products of an amplitude M_{LL_c} for exciting a core electron at site 0 with angular momentum L, times the amplitude of propagation $\tau^{0j}_{LL'}$ from this site to any other site (cell) j with final angular momentum L', times the amplitude $Y_{L'}(\hat{k})$ for emission along $\hat{k}$, times the phase factor $e^{i\vec{k}\cdot\vec{R}_{0j}}$ that takes into account the phase relation of the electronic wave between site 0 and j. It is therefore the result of a complicated interference process that strongly depends on the reliability of the optical potential.

In this case the primary wave is the photoelectron which leaves the absorber and goes directly to the detector; otherwise the photoelectron can be scattered by the surrounding atoms before being detected, therefore the amplitudes corresponding to all these processes must be summed and give rise to interference phenomena.

A.5 Absorption cross section

The absorption cross section can be obtained from the photoemission differential cross section by integration of the latter over the solid angle $d\hat{k}$. From a physical point of view, in fact, the absorption process can be interpreted as a photoemitted electron

that returns to the absorbing atom. Therefore we write the absorption cross section as follows:

$$\begin{aligned}\sigma_{abs} &= \int d\hat{k}\frac{d\sigma}{d\hat{k}} = 4\pi^2\alpha\hbar\omega\frac{k}{\pi}\sum_{m_c}\int d\hat{k}\langle R^0_{l_c}(r)Y_{L_c}(\hat{r})|(\hat{\epsilon}\cdot\vec{r})^*|\psi^0_k(\vec{r})\rangle\langle\psi^0_k(\vec{r})|\hat{\epsilon}\cdot\vec{r}|R^0_{l_c}(r)Y_{L_c}(\hat{r})\rangle = \\ &= -4\pi^2\alpha\hbar\omega\frac{k}{\pi}\frac{1}{k}\frac{4\pi}{3}\sum_{m_c}\sum_{LL'}\langle R^0_{l_c}(r)Y_{L_c}(\hat{r})|rY^*_{1m_p}(\hat{r})|R_l(r)Y_L(\hat{r})\rangle\Im[\tau^{00}_{LL'}] \\ &\cdot\ \langle R_{l'}(r)Y_{L'}(\hat{r})|rY_{1m_p}(\hat{r})|R^0_{l_c}(r)Y_{L_c}(\hat{r})\rangle = \\ &= -4\pi\alpha\hbar\omega\frac{4\pi}{3}\sum_{m_c}\sum_{LL'}M_{ll_c}M_{l'l_c}\langle Y_{L_c}(\hat{r})|Y^*_{1m_p}(\hat{r})|Y_{lm}(\hat{r})\rangle\Im[\tau^{00}_{LL'}]\langle Y_{l'm'}(\hat{r})|Y_{1m_p}(\hat{r})|Y_{L_c}(\hat{r})\rangle.\end{aligned} \tag{A.60}$$

Since the behaviour of the spherical harmonics under inversion symmetry operation is $Y_{lm}(-\hat{r}) = (-1)^l Y_{lm}(\hat{r})$, the integrals $\langle Y_{L_c}(\hat{r})|Y^*_{1m_p}(\hat{r})|Y_{lm}(\hat{r})\rangle$ and $\langle Y_{l'm'}(\hat{r})|Y_{1m_p}(\hat{r})|Y_{L_c}(\hat{r})\rangle$ are not zero only if $l_c + l + 1 = 2n$. Moreover, $Y^*_{lm} = (-1)^m Y_{l,-m}$, so it is possible to rewrite, using the Wigner notation,

$$\begin{aligned}\langle Y_{L_c}(\hat{r})|Y^*_{1m_p}(\hat{r})|Y_{lm}(\hat{r})\rangle &= \int d\Omega Y^*_{L_c}(\hat{r})Y^*_{1m_p}(\hat{r})Y_{lm}(\hat{r}) = \\ &= (-1)^{m_c+m_p}\int d\Omega Y_{l_c,-m_c}(\hat{r})Y_{1,-m_p}(\hat{r})Y_{lm}(\hat{r}) = \\ &= (-1)^{-m}\Big[\frac{3(2l_c+1)(2l+1)}{4\pi}\Big]^{\frac{1}{2}}\begin{pmatrix} l_c & 1 & l \\ 0 & 0 & 0\end{pmatrix}\begin{pmatrix} l_c & 1 & l \\ -m_c & -m_p & m\end{pmatrix},\end{aligned} \tag{A.61}$$

because $-m_c - m_p + m = 0$, due to the conservation of the angular momentum projection. Moreover $l_c - 1 \leq l \leq l_c + 1$. The same can be obtained for the other integral. Through the use of this relation the absorption cross section can be rewritten as

$$\begin{aligned}\sigma_{abs} = \sum_{m_p m_c}\sum_{LL'}M_{ll_c}M_{l'l_c}(-1)^{-m}\Big[\frac{3(2l_c+1)(2l+1)}{4\pi}\Big]^{\frac{1}{2}}\begin{pmatrix} l_c & 1 & l \\ 0 & 0 & 0\end{pmatrix}\begin{pmatrix} l_c & 1 & l \\ -m_c & -m_p & m\end{pmatrix}\cdot \\ (-1)^{m}\Big[\frac{3(2l_c+1)(2l'+1)}{4\pi}\Big]^{\frac{1}{2}}\begin{pmatrix} l_c & 1 & l' \\ 0 & 0 & 0\end{pmatrix}\begin{pmatrix} l_c & 1 & l' \\ m_c & m_p & -m'\end{pmatrix}\Im[\tau^{00}_{LL'}].\end{aligned} \tag{A.62}$$

We can use the following rule to reduce expression (A.62):

$$\sum_{m_p m_c}\begin{pmatrix} l_c & 1 & l \\ -m_c & -m_p & m\end{pmatrix}\begin{pmatrix} l_c & 1 & l' \\ m_c & m_p & -m'\end{pmatrix} =$$

$$= \begin{pmatrix} l_c & 1 & l \\ m_c & m_p & -m \end{pmatrix} \cdot (-1)^{l_c+1+l'} \begin{pmatrix} l_c & 1 & l' \\ m_c & m_p & -m' \end{pmatrix} = \frac{\delta_{ll'}\delta_{mm'}}{2l+1} \tag{A.63}$$

therefore the cross section becomes

$$\begin{aligned} \sigma_{abs} &= -4\pi\alpha\hbar\omega \frac{4\pi}{3} \sum_{LL'} M_{ll_c} M_{l'l_c} \Im[\tau^{00}_{LL'}] \frac{\delta_{ll'}\delta_{mm'}}{2l+1} \frac{3}{4\pi}(2l_c+1)(2l+1) \begin{pmatrix} l_c & 1 & l \\ 0 & 0 & 0 \end{pmatrix}^2 = \\ &= -4\pi\alpha\hbar\omega \sum_{lm} M^2_{ll_c} \Im[\tau^{00}_{lm,lm}](2l_c+1) \begin{pmatrix} l_c & 1 & l \\ 0 & 0 & 0 \end{pmatrix}^2 . \end{aligned} \tag{A.64}$$

Actually, the final angular momentum can assume only two possible values in the dipole approximation: $l = l_c \pm 1$. As a consequence the Wigner coefficients in (A.64) are:

$$\begin{aligned} \sum_l \begin{pmatrix} l_c & 1 & l \\ 0 & 0 & 0 \end{pmatrix}^2 &= \begin{pmatrix} l_c & 1 & l_c+1 \\ 0 & 0 & 0 \end{pmatrix}^2 + \begin{pmatrix} l_c & 1 & l_c-1 \\ 0 & 0 & 0 \end{pmatrix}^2 = \\ &= \frac{l_c+1}{(2l_c+3)(2l_c+1)} + \frac{l_c}{(2l_c+1)(2l_c-1)}. \end{aligned} \tag{A.65}$$

Finally, using (A.65) the absorption cross section is:

$$\begin{aligned} \sigma_{abs} &= -4\pi\alpha\hbar\omega \sum_m M^2_{ll_c} \Im[\tau^{00}_{lm,lm}](2l_c+1)\Big\{ \frac{l_c+1}{(2l_c+3)(2l_c+1)}\delta_{l,l_c+1} + \frac{l_c}{(2l_c+1)(2l_c-1)}\delta_{l,l_c-1} \Big\} \\ &= -4\pi\alpha\hbar\omega \sum_m \Im[\tau^{00}_{lm,lm}] M^2_{ll_c} \Big\{ \frac{l_c+1}{(2l+1)}\delta_{l,l_c+1} + \frac{l_c}{(2l+1)}\delta_{l,l_c-1} \Big\} = \\ &= -4\pi\alpha\hbar\omega \sum_m \Im[\tau^{00}_{lm,lm}] M^2_{ll_c} \frac{1}{2l+1} \Big[(l_c+1)\delta_{l,l_c+1} + l_c\delta_{l,l_c-1} \Big]. \end{aligned} \tag{A.66}$$

Eq. (A.66) gives the total non polarized absorption cross section in the one-electron model.

Appendix B

MXAN

MXAN is a recent fitting procedure of the XANES region of the X-ray absorption spectrum. This method compares the experimental spectrum with numerous calculated spectra, which are produced by changing the relevant geometrical parameters of the region around the absorbing atom. Hundreds of different geometrical configurations are necessary in order to obtains the best fitting of the experimental spectrum. The absorption cross section is calculated in the framework of the Full Multiple Scattering. MXAN is able to give information on the symmetry of the system and on the interatomic distances; the calculated solution is independent of the initial conditions. The MXAN procedure exploits a package developed by the Frascati theory group, in particular:

- VGEN, that generates the muffin-tin potentials;
- CONTINUUM, that calculates the full multiple scattering cross section.

MXAN uses the MINUIT package of CERN (MINUIT on WEB: http://wwwinfo.cern.ch/asdoc/minuit/minmain/minmain.html) to search the minimum of the square residue function in the space of the parameters defined as:

$$S^2 = n\frac{\sum_{i=1}^{m} w_i[(y_i^{th} - y_i^{exp})\varepsilon_i^{-1}]^2}{\sum_{i=1}^{m} w_i} \tag{B.1}$$

where n is the number of independent parameters, m is the number of experimental points, y_i^{th} and y_i^{exp} are respectively the theoretical and experimental value of the absorption coefficient, ε_i is the experimental error of the i-th experimental point and w_i is the statistical weight (for $w_i = cost = 1$, S^2 is the statistical function χ^2).

The MXAN procedure needs three input files containing respectively the experimental data to be fitted, the starting atomic coordinates of the cluster (the putative

structure), and the commands and options necessary for the chosen minimization strategy (Fig.B.1).

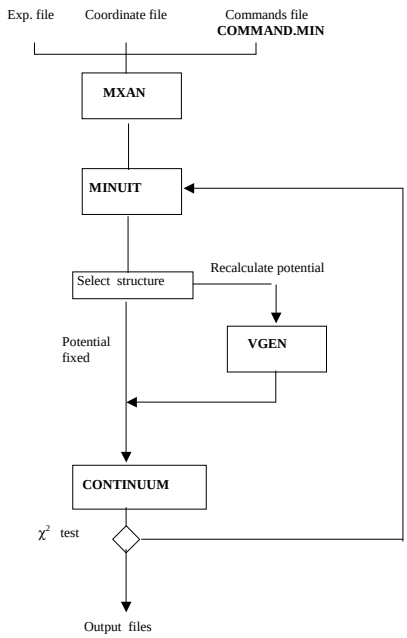

Figure B.1: Sketch of the MXAN procedure to calculate the XANES spectrum; the main steps are shown.

MXAN uses the MT approximation, with a complex optical potential. The real part of the self-energy is calculated either from the the X_α approximation or using the Hedin-Lundqvist potential. In the former case, inelastic processes are taken into account by a convolution with a broadening lorentzian function, with a full Γ_c includes the core hole lifetime and the experimental resolution, while the energy dependent term $\Gamma(E)$ represents all the inelastic processes. The $\Gamma(E)$ function is zero below an onset energy E_s, and it begins to increase from a value A_s following the universal functional form of the mean free path in solid. This method introduces three non-structural parameters that are refined on the basis of Monte Carlo search at each step of optimization of the structural parameters. In such a way, together with the MT radii, the MXAN method uses only four non-structural parameters for the optimization of the potential, with the OPTN option: the MT radii (by means of the overlapping factor), the broadening, the number of scatterers and the maximum angular momentum of the scattered waves (l_{max}), the values of the MT potentials and the charge density. The potential can be calculated for each intermediate structural configuration produced during the optimization, or else it can be fixed: this option allows the use of more

sophisticated external potentials. The MT radii are calculated from the overlapping factor ovlp, using the Norman criterion. By means of this criterion the ratio between the radii of the atomic spheres is chosen using the concept of "charge radius". The charge radius- corresponding to an atomic site occupied by an atom with Z atomic number- is the radius of the sphere which contains exactly Z electrons. In this way we fix the relative values of the atomic spheres' radii: if R_1 and R_2 are the radii of the atomic spheres with Z_1 and Z_2 electrons, then the ratio between the MT radii is given by $\frac{R_{MT2}}{R_{MT1}} = \frac{R_2}{R_1}$. The final choice of the MT radii is performed imposing the right ionization energy levels and complying the virial theorem -2⟨T⟩/⟨V⟩=1. Sometimes these conditions requires overlapping among the atomic spheres. The overlapping factor ovlp is exactly the "amount" of overlapping:

$$R_{MT1} + R_{MT2} = d(1 + \alpha)$$

where d is the distance between the centers of the MT spheres. The MT potential v0imp and the charge density rhoimp are automatically calculated by the program. During the minimization of the structural parameters MXAN calculates also some non-structural parameters:

- **Normalization** Norm: this value is calculated approximately as the ratio between the jump of the theoretical spectrum and the experimental jump;
- **Alignment** Ensh: it is the energy shift between the experimental spectrum and the theoretical one;
- **Energy independent broadening** Broad: each calculated spectrum is convoluted with a lorentzian function. This is the Γ_c value, which takes into account the core hole width and the experimental resolution;
- **Energy dependent broadening** plasmons: it simulates the electrons' mean free path, due to inelastic losses, and adds this value to the width of the lorentzian function.

Finally, there are other options that allow to consider correlations among the fitting parameters.

Bibliography

[1] P.W. Anderson, H. Hasegawa, Phys. Rev. **100**, 675 (1955)

[2] A.L. Ankudinov, B. Ravel, J.J. Rehr, S.D. Conradson, Phys. Rev. B, **58**, 7565 (1998)

[3] V.I. Anisimov, F. Aryasetiawan, A. Lichtenstein, J. Phys.: Condens. Matter **9**, 767 (1997)

[4] W. Bao, C. Broholm, G. Aeppli, S.A. Carter, P. Dai, T.F. Rosenbaum, J.M. Honig, P. Metcalf, S.F. Trevino, Phys. Rev. B**58**, 12727 (1998)

[5] M.Benfatto et al., J. Synchrotron Rad., 10, 51 (2003)

[6] M.Benfatto et al., J. Synchrotron Rad., 8, 1087 (2001)

[7] M.Benfatto et al., J. Synchrotron Rad., 8, 267 (2001)

[8] S.J.L. Billinge et al., Phys. Rev. Lett. **77**, 715 (1996)

[9] A. Bombardi, F. de Bergevin, S. Di Matteo, L. Paolasini, P.A. Metcalf, J.M. Honig, Physica B **345** , 40 (2004)

[10] C.H. Booth, F. Bridges, G. H. Kwei, J. M. Lawrence, A. L. Cornelius, J. J. Neumeier, Phys. Rev. B**57**, 10440, (1998)

[11] P. Carra, B.T. Thole, M. Altarelli, X. Wang, Phys. Rev. Lett.**70**, 694 (1993)

[12] C. Castellani, C.R. Natoli, J. Ranninger, Phys. Rev. B**18**, 4945 (1978)

[13] C. Castellani, C.R. Natoli, J. Ranninger, Phys. Rev. B**18**, 4967 (1978)

[14] C. Castellani, C.R. Natoli, J. Ranninger, Phys. Rev. B**18**, 5001 (1978)

[15] J.M. Coey et al., Advances in Physics **48**, 2 (1999)

[16] P.G. de Gennes, Phys. Rev. **118**, 141 (1960)

[17] P.D. Dernier, M. Marezio, Phys. Rev. B**2**, 3771 (1970)

[18] P.D. Dernier, J. Phys. Chem. Solids **31**, 2569 (1970)

[19] S. Di Matteo, N.B. Perkins, C.R. Natoli, Phys. Rev. B**65**, 054413 (2002)

[20] S. Di Matteo, Y.Joly, C.R. Natoli, Phys. Rev. B**67**, 195105 (2003)

[21] S. Di Matteo, Physica B **318**, 321 (2002)

[22] J.B. Elemans, J. Solid State Chem. **3**, 238 (1971)

[23] I.S. Elfimov, T. Saha-Dasgupta, M.A. korotin, Phys. Rev. B**68**, 113105 (2003)

[24] S.Yu. Ezhov, V.I. Anisimov, D.I. Khomskii, G.A. Sawatzky, Phys. Rev. Lett.**83**, 4136 (1999)

[25] M. Fabrizio, M. Altarelli, M. Benfatto Phys. Rev. Lett.**80**, 3400 (1998)

[26] A. Filipponi, E. Bernieri, S. Mobilio, Phys. Rev. B, **38**, 3298 (1988)

[27] A. Filipponi, A. Di Cicco, Phys. Rev. A, **52**, 1072 (1995)

[28] A. Filipponi, A. Di Cicco, P. Pianetta, T. Kendelewicz, Phys. Rev. B, **53**, 15571 (1996)

[29] L.W. Finger, R.H. Hazen, J. Appl. Phys. **51**, 5362 (1980)

[30] A.I. Frenkel, E.A. Stern, F.A. Chudnovsky, Solid State Communication **9**, No.9, 637 (1997)

[31] J. García, M.C. Sanchez, G. Subías, J. Blasco, J. Phys. Cond. Matter **13**, 3229 (2001)

[32] F. Gebhard, pag.34 *"The Mott Metal-Insulator Transition"* (Springer-Verlag, Berlin Heidelberg 1997)

[33] J. Goulon, A. Rogalev, C. Goulon-Ginet, G. Benayoun, L. Paolasini, C. Brouder, C. Malgrange, P.A. Metcalf, Phys. Rev. Lett.**85**, 4385 (2000)

[34] L. Hedin, B.I. Lundqvist, J. Phys. C **4**, 2064 (1971)

[35] Q. Huang, A. Santoro, J.W. Lynn, R.W. Erwin, J.A. Borchers, J.L. Peng, R.L. Green, Phys. Rev. B, **55**, 14987 (1997)

[36] F. James, CERN 506,*Program Library* (1994)

[37] A. Jayaraman, D.B. McWhan, J.P. Remeika, P.D. Dernier, Phys. Rev. B**2**, 3751 (1970)

[38] Y. Joly, Phys. Rev. B**63**, 125120 (2001)

[39] E.D. Jones, Phys. Rev. **137**, A978 (1965)

[40] K. Kubo, N: Ohata, J. Phys. Soc. Jpn. **33**, 21 (1972)

[41] H. Kuwamoto, J.M. Honig, J. Appel, Phys. Rev. B**22**, 2626 (1980)

[42] H. Kuwamoto, J.M. Honig, J. Solid State Chem. **32**, 335 (1980)

[43] A. Lanzara, N. L. Saini, M. Brunelli, F. Natali, A. Bianconi, P. G. Radaelli, S.W. Cheong, Phys. Rev. Lett.**81**, 878 (1998)

[44] S.W. Lovesey, K.S. Knight, J. Phys.: Condens. Matter **12**, L367 (2000)

[45] S.W. Lovesey, K.S. Knight, D.S. Sivia Phys. Rev. B**65**, 224402 (2002)

[46] B.I. Lundqvist, Phys. Kondens. Mater **6**, 206 (1977)

[47] L.F. Mattheiss, J. Phys.: Condens. Matter **6**, 6477 (1994)

[48] D.B. McWhan, T.M. Rice, J.P. Remeika, Phys. Rev. Lett.**23**, 1384 (1969)

[49] D.B. McWhan, J.P. Remeika, Phys. Rev. B**2**, 3734 (1970)

[50] D.B. McWhan, T.M. Rice, Phys. Rev. Lett.**22**, 887 (1969)

[51] D.B. McWhan, A. Menth, T.M. Remeika, W.F. Brinkman, T.M. Rice Phys. Rev. B**7**, 1920 (1973)

[52] C. Meneghini, R. Cimino, S. Pascarelli, S. Mobilio, C. Raghu, D. D. Sarma, Phys. Rev. B**56**, 3520 (1997)

[53] C. Meneghini, S. Di Matteo, C. Monesi, T. Neisius, L. Paolasini, S. mobilio, C.R. Natoli, P.A. Metcalf, J.M. Honig, Phys. Rev. B**72**, 033111 (2005)

[54] A. Menth, J.P. Remeika, Phys. Rev. B**2**, 3756 (1970)

[55] F. Mila, R. Shiina, F.C. Zhang, A. Joshi, M. Ma, V.I. Anisimov, T. Rice, Phys. Rev. Lett.**85**, 1714 (2000)

[56] A.J. Millis et al., Phys. Rev. Lett. **74**, 5144 (1995)

[57] A.J. Millis et al., Phys. Rev. Lett. **77**, 175 (1996)

[58] A.J. Millis et al., Phys. Rev. B**53**, 8434 (1996)

[59] A.J. Millis et al., Phys. Rev. B**54**, 5405 (1996)

[60] C. Monesi, C. Meneghini, F. Bardelli, M. Benfatto, S. mobilio, U. Manju, D.D. Sarma, Phys. Rev. B**72**, 174104 (2005)

[61] C.R. Natoli, M. Benfatto, J. Phys. (Paris) **C8**,11 (1986)

[62] C.R. Natoli, M. Benfatto, C. Brouder, M.F. Ruiz Lpez, D.L. Foulis, Phys. Rev. B**42**, 1944 (1990)

[63] C.R. Natoli, M. Benfatto, S. Doniach, Phys. Rev. A**34**, 4682 (1986)

[64] C.R. Natoli, M. Benfatto, S. Della Longa, K. Hatada, J. Synchrotron Radiat. **10**, 26 (2003)

[65] I. Nebenzahl, M. Weger, Phys. Rev.**184**, 936 (1969)

[66] R.M. Moon, Phys. Rev. Lett.**25**, 527 (1970)

[67] L. Paolasini, C. Vettier, F. de Bergevin, F. Yakhou, D. Mannix, A. Stunault, W. Neubeck, M. Altarelli, M. Fabrizio, P.A. Metcalf, J.M. Honig, Phys. Rev. Lett.**82**, 4719 (1999)

[68] L. Paolasini, S. Di Matteo, C. Vettier, F. de Bergevin, A. Sollier, W. Neubeck, F. Yakhou, P.A. Metcalf, J.M. Honig, Journal of Electron Spectroscopy and Related Phenomena **120**, 1-10 (2001)

[69] J.H. Park, L.H. Tjeng, A. Tanaka, J.W. Allen, C.T. Chen, P. Metcalf, J.M. Honig, F.M.F. de Groot, G.A. Sawatzky, Phys. Rev. B, **61**, 11506 (2000)

[70] P. Pfalzer, G. Obermeier, M. Klemm, S. Horn, M.L. denBoer, Phys. Rev. B, **73**, 144106 (2006)

[71] P. Pfalzer, J. Will, A. Jr. Nateprov, M. Klemm, V. Eyert, S. Horn, A.I. Frenkel, S. Calvin, and M.L. denBoer, Phys. Rev. B, **66**, 85119 (2002)

[72] E. Pollert et al., J. Phys. Chem. Solids **43**, 1137 (1982)

[73] K.R. Poeppelmeier, M.E. Leonowicz, J.C. Scanlon, J.M.L.W.B.Yelon, Solid State Chem., **45**, 71 (1982)

[74] Q. Quian et al., Phys. Rev. B**64**, 024430 (2001)

[75] H. Roder et al., Phys. Rev. Lett.**76**, 1356 (1996)

[76] M.C. Sanchez, G. Subías, J. García, J. Blasco, Phys. Rev. Lett.**90**, 045503 (2003)

[77] T. Shibata, B.A. Bunker, J.F. Mitchell, Phys. Rev. B, **68**, 024103 (2003)

[78] T. Shinjo, K. Kosuge, J. Phys. Soc. Jap. **21**, 2622 (1966)

[79] S.A. Shivashankar, J.M. Honig, Phys. Rev. B**28**, 5695 (1983)

[80] G. Subías, J. García, M. G. Proietti, J. Blasco, Phys. Rev. B**56**, 8183 (1997)

[81] G. Subías, J. García, J. Blasco, M. G. Proietti, Phys. Rev. B**57**, 748 (1998)

[82] G. Subías, J. García, J. Blasco, M.C. Sanchez, M.G. Proietti, J. Phys. Cond. Matter **14**, 5017 (2002)

[83] A. Tanaka, J. Phys. Soc. Jpn., **71**, 1091 (2002)

[84] B.T. Thole, P. Carra, F. Sette, G. van der Laan, Phys. Rev. Lett.**68**, 1943 (1992)

[85] A.C. Thompson et al., *X-RAY DATA BOOKLET* (Lawrence Berkeley National Laboratory, University of California, Berkeley, 2001)

[86] T.A. Tyson, J.M. de Leon, S. D. Conradson, A. R. Bishop, J. J. Neumeier, H. Rder, Jun Zang Phys. Rev. B**53**, 13985 (1996)

[87] T.A. Tyson, Phys. Rev. B**49**, 12578 (1994)

[88] R. Von Helmolt et al., Phys. Rev. Lett. **71**, 2331 (1993)

[89] W.B. Yelon, S.A. Werner, R.E. Word, J. Appl. Phys. **52**, 2237 (1981)

[90] S.I. Zabinsky, J. J. Rehr, A. Ankudinov, R. C. Albers, M. J. Eller, Phys. Rev. B**52**, 2995, (1995)

[91] C. Zener, Phys. Rev. **81**, 440 (1951)

[92] C. Zener, Phys. Rev. **82**, 403 (1951)